UNIVERSITÀ DEGLI STUDI DI TRIESTE

XXXVIII CICLO DEL DOTTORATO DI RICERCA IN CHIMICA

Exploring the Pyrazine Scaffold to Develop Inhibitors towards Casein Kinase 1δ

Settore scientifico-disciplinare: **CHIMICA FARMACEUTICA - CHIM/08**

DOTTORANDA
LETIZIA TREVISAN

COORDINATORE
PROF. ENZO ALESSIO

SUPERVISORE DI TESI
PROF. STEPHANIE FEDERICO

ANNO ACCADEMICO 2024/2025

Abstract

Protein kinases (PKs) are a family of 518 enzymes that catalyze the phosphorylation of substrates containing serine, threonine, or tyrosine residues (Ser/Thr/Tyr). Among these, Casein Kinase 1 (CK1) represents a distinct subgroup composed of six isoforms. This PhD thesis focuses on the δ isoform (CK1δ), which plays a crucial role in several physiological processes by modulating different signaling pathways. Dysregulation of CK1δ activity has been associated with various pathological conditions, including cancer, circadian rhythm disorders, and neurodegenerative diseases. In particular, CK1δ has been implicated in Alzheimer's disease (AD), Parkinson's disease (PD), and Amyotrophic Lateral Sclerosis (ALS), all characterized by aberrant protein hyperphosphorylation and aggregation, leading to neuroinflammatory and neurodegenerative processes. Given its involvement in these disorders, CK1δ represents an attractive therapeutic target for detailed investigation.

In this thesis, a series of pyrazine-based inhibitors of CK1δ were developed to identify promising candidates that could serve as both pharmacological tools in neurodegenerative disease research and chemical probes to elucidate the kinase's mechanism of action. An initial screening of in-house compounds highlighted several pyrazine derivatives of interest,

particularly one bearing two fluorophenyl groups at positions 5 and 6 of the pyrazine scaffold. Following preliminary structural optimization at position 5, where various substituted aryl groups were introduced, a new hit compound (compound **V**) was identified, bearing a pyridine moiety at position 5 and achieving an IC_{50} of 110 nM.

Subsequent optimization focused on position 3, where the introduction of diverse amine substituents yielded several potent compounds with nanomolar inhibitory activity. The role of the amino group at position 2 was explored by modulating its hydrogen-bonding capacity through mono- and dimethyl substitutions. These derivatives remained active but displayed reduced potency compared to their free amino analogues. Finally, position 6 was investigated to identify alternatives to the para-fluorophenyl substituent, while maintaining the most promising groups at other positions. Although several active compounds were obtained, none of the newly optimized derivatives displayed significantly enhanced activities compared to the derivatives containing the 4-fluorophenyl substituent.

After completing the structure–activity relationship (SAR) studies, four promising derivatives, along with the parent compound (**V**), were selected for an in-depth multidisciplinary characterization. ATP-competition assays confirmed the

hypothesized ATP-competitive binding mode, while biophysical analyses, performed in collaboration with the group of Paola Storici at Elettra Sincrotrone Trieste, demonstrated strong target affinities via thermal shift assays (TSA). Kinetic characterization, particularly through Grating-Coupled Interferometry (GCI), revealed compound **20** as a tight binder with a very slow dissociation rate. Co-crystallization experiments provided valuable structural insights into the ligand–protein interactions, guiding future compound design.

An important aspect of this study concerns the isoform selectivity of the developed inhibitors. CK1δ and its closely related isoform CK1ε share approximately 98% sequence identity, making the design of isoform-selective inhibitors particularly challenging. Remarkably, compound **20** displayed a 100-fold selectivity for CK1δ over CK1ε, a degree of discrimination that has not been previously reported in the literature. This grade of selectivity underlines the novelty of the compound and highlights its potential as a highly valuable chemical probe for selectively investigating CK1δ biological functions.

From a pharmacokinetic perspective, PAMPA assays showed that all selected compounds displayed moderate to good passive permeability across the blood–brain barrier (BBB), a critical property for central nervous system (CNS) targeting.

Microsomal stability assays indicated good clearance profiles for compounds **20** and **21** in mouse liver microsomes. Biologically, all compounds demonstrated a favorable safety profile on the human neuroblastoma SH-SY5Y cell line. Moreover, in an *in vitro* ALS model using the same cell line, the compounds effectively reduced phosphorylated TDP-43 (pTDP-43) levels, a key hallmark of ALS pathology. Consistent results were obtained *in vivo* on Drosophilae by the group of Marco Bisaglia at the University of Padua, where the experiments show again a marked reduction in pTDP-43 levels.

In summary, this work reports the design, synthesis, and comprehensive characterization of a novel series of pyrazine-based CK1δ inhibitors with potent activity, and good selectivity, favorable pharmacokinetic properties, and efficacy both on *in vitro* and *in vivo* ALS models. These compounds represent valuable tools for studying CK1δ biology and hold promise as leads for the development of therapeutics targeting neurodegenerative disorders.

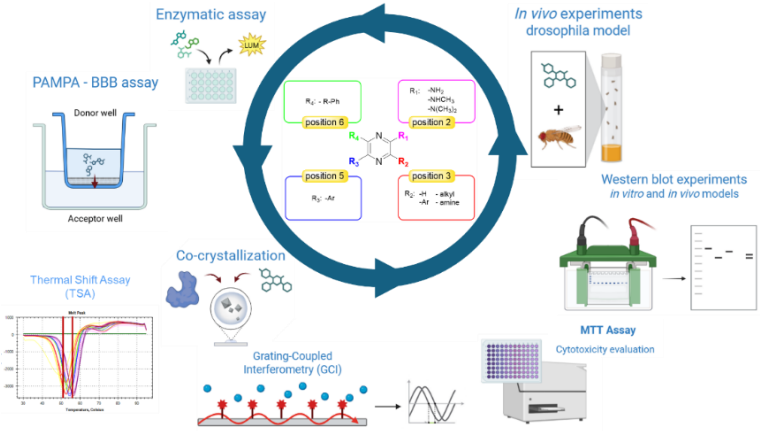
Enzymatic assay
LUM
PAMPA - BBB assay
Donor well
Acceptor well
position 6
position 2
position 5
position 3
In vivo experiments
drosophila model
Western blot experiments
in vitro and in vivo models
Co-crystallization
Thermal Shift Assay
(TSA)
MTT Assay
Cytotoxicity evaluation
Grating-Coupled
Interferometry (GCI)

Riassunto

Le proteine chinasi (PK) costituiscono una famiglia di 518 enzimi che catalizzano la fosforilazione di substrati contenenti residui di serina, treonina o tirosina (Ser/Thr/Tyr). Tra queste, la Caseina Chinasi 1 (CK1) rappresenta un sottogruppo distinto composto da sei isoforme. Questo progetto si concentra su CK1δ, la quale svolge un ruolo cruciale in numerosi processi biologici e modulando differenti vie di segnalazione. La deregolazione dell'attività di CK1δ è stata associata a diverse condizioni patologiche, tra cui l'insorgenza di tumori, disturbi del ritmo circadiano e malattie neurodegenerative. In particolare, CK1δ è implicata nella malattia di Alzheimer (AD), nel morbo di Parkinson (PD) e nella sclerosi laterale amiotrofica (SLA), tutte caratterizzate da iperfosforilazione proteica e accumulo di aggregati che contribuiscono all'insorgenza di processi neuroinfiammatori e neurodegenerativi. Data la sua rilevanza in questi disordini, CK1δ rappresenta un bersaglio terapeutico di grande interesse per lo sviluppo di nuovi agenti terapeutici e per ulteriori studi dei suoi meccanismi di azione.

In questo progetto è stata sviluppata una serie di inibitori di CK1δ basati su uno scaffold pirazinico, con l'obiettivo di identificare candidati promettenti utilizzabili sia come strumenti farmacologici per lo studio delle malattie neurodegenerative, sia come *chemical probes* per chiarire il meccanismo d'azione della

chinasi in esame. L'idea deriva da uno *screening in house* iniziale che ha evidenziato diversi derivati pirazinici di interesse, in particolare uno (**IV**) contenente due gruppi fluorofenilici nelle posizioni 5 e 6 dello *scaffold*. Dopo un'ottimizzazione preliminare della struttura in posizione 5, introducendo vari sostituenti arilici, è stato identificato un nuovo composto *hit* (composto **V**) caratterizzato dalla presenza di un anello piridinico in posizione 5 e da un'attività con IC_{50} di 110 nM**.**

L'ottimizzazione successiva si è concentrata sulla posizione 3, dove l'introduzione di diverse ammine ha portato all'individuazione di composti potenti con attività nell'ordine del nanomolare. Il ruolo del gruppo amminico in posizione 2 è stato studiato riducendone la capacità di formare legami a idrogeno mediante sostituzione con gruppi metilici; tali derivati sono risultati attivi ma con una potenza inferiore rispetto ai corrispettivi con l'ammina libera. Infine, la posizione 6 è stata esplorata al fine di trovare un'alternativa al gruppo *para*-fluorofenile, mantenendo le sostituzioni più promettenti nelle altre posizioni. Sebbene siano stati ottenuti composti molto attivi, nessuno ha superato in efficacia i composti **10** e **20** con il gruppo 4-fluorofenile in posizione 6 dello *scaffold*.

Completati gli studi di relazione struttura–attività (*Structure Ativity Relationship* - SAR), quattro derivati promettenti,

insieme al composto capostipite (**V**), sono stati selezionati per una caratterizzazione multidisciplinare approfondita. Tramite saggi di competizione con ATP è stato confermato il meccanismo di legame ATP-competitivo già ipotizzato, mentre le analisi biofisiche, condotte in collaborazione con il gruppo di Paola Storici presso Elettra Sincrotrone Trieste, hanno mostrato una forte affinità verso il target attraverso **i** *thermal shift assay* (TSA). La caratterizzazione cinetica, effettuata principalmente mediante la tecnica *Grating-Coupled Interferometry* (GCI), ha evidenziato che il composto **20** è un legante particolarmente stabile, con una lenta dissociazione, per questo definito *tight binder*. Gli esperimenti di co-cristallizzazione hanno fornito preziose informazioni sul modo in cui i composti si posizionano nel sito attivo e che legami instaurano, fornendo informazioni utili anche per la progettazione di future molecole.

Un aspetto importante di questo studio riguarda la selettività verso le isoforme degli inibitori sviluppati. CK1δ e la sua isoforma strettamente correlata CK1ε condividono circa il 98% di identità di sequenza, rendendo la progettazione di inibitori selettivi per isoforma una sfida particolarmente complessa. In modo sorprendente, il composto **20** ha mostrato una selettività di 100 volte per CK1δ rispetto a CK1ε, un grado di discriminazione che non era stato precedentemente riportato in letteratura.

Questo livello di selettività sottolinea la novità del composto e ne evidenzia il potenziale come sonda chimica di grande valore per studiare in modo selettivo le funzioni biologiche di CK1δ.

Dal punto di vista farmacocinetico, i saggi PAMPA hanno dimostrato una permeabilità passiva moderata-buona attraverso la barriera ematoencefalica (BBB), una proprietà cruciale per i target del sistema nervoso centrale. I test di stabilità microsomiale hanno evidenziato un buon profilo di *clearance* per i composti **20** e **21** nei microsomi epatici di topo. Dal punto di vista biologico, tutti i composti hanno mostrato un buon profilo di sicurezza sulla linea cellulare di neuroblastoma umano SH-SY5Y. Inoltre, in un modello *in vitro* di SLA sulla stessa linea cellulare, i composti si sono dimostrati efficaci nel ridurre i livelli di TDP-43 fosforilata (pTDP-43), un marcatore chiave della patologia. Risultati coerenti sono stati ottenuti *in vivo* dal gruppo di Marco Bisaglia presso l'Università di Padova, dove i composti sono stati testati su *Drosophila* e hanno nuovamente portato a una significativa riduzione dei livelli di pTDP-43.

In sintesi, questo lavoro descrive la progettazione, sintesi e caratterizzazione approfondita di una nuova serie di inibitori pirazinici di CK1δ con elevata potenza, selettività eccezionale, buone proprietà farmacocinetiche ed efficacia in modelli cellulari e animali di malattie neurodegenerative. Questi composti rappresentano strumenti preziosi per lo studio dei

meccanismi di azione di CK1δ e costituiscono potenziali candidati guida per lo sviluppo di nuove terapie rivolte ai disturbi neurodegenerativi.

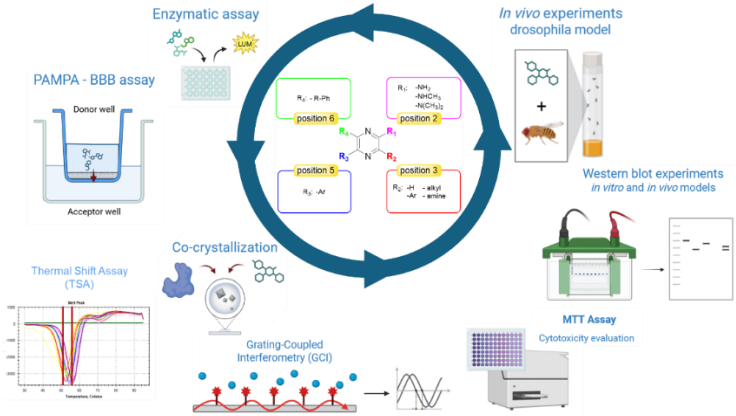

Table of Contents

List of abbreviations

Protein Kinases	**PKs**	Upper motor neuron	**UMN**
Adenosine Triphosphate	**ATP**	Lower motor neuron	**LMN**
Eukaryotic protein kinase	**ePKs**	Frontotemporal dementia	**FTD**
Atypical protein kinases	**aPKs**	Transactive response DNA-binding protein 43 kDa	**TDP-43**
Tyrosine kinases	**TK**	RNA-recognition motifs	**RRM1**
Tyrosine kinase-like	**TKL**	Nuclear localization signal	**NLS**
Casein kinase 1	**CK1**	Tunneling nanotubes	**TNT**
Ca^{2+}/calmodulin-dependent kinases	**CAMK**	N-bromosuccinimide	**NBS**
Receptor guanylyl cyclase	**RGC**	Dichloromethane	**DCM**
Aspartate	**Asp**	Ethanol	**EtOH**
Phenylalanine	**Phe**	Room Temperature	**RT**
Glycine	**Gly**	Acetonitrile	**ACN**
Glutamate	**Glu**	Dimethylformamide	**DMF**
Lysine	**Lys**	tert-Butyloxycarbonyl	**Boc**
Phosphate loop	**(P-loop**	Tetrahydrofuran	**THF**
Hydrogen Bond	**H-bond**	Structure activity relationship	**SAR**
Pharmacokinetic	**PK**	Nuclear Magnetic Resonance	**NMR**
Serine	**Ser**	Nuclear Overhauser Effect	**NOE**

Threonine	**Thr**	Adenosine diphosphate	**ADP**
Vaccinia-Related Kinases	**VRK**	Half maximal inhibitory concentration	**IC_{50}**
Tau Tubulin Kinases	**TTBK**	Thermal Shift Assay	***TSA***
Arginine	**Arg**	Melting temperature	**T_m**
Murine double-minute clone 2 protein	**MDM 2**	Grating Coupled Interferometry	***GCI***
Death-inducing signaling complex	**DISC**	Association constant	**K_{on}**
Galectin-3	**Gal-3**	Dissociation contants	**K_{off}**
Hedgehog	**Hh**	Parallel Artificial Membrane Permeability Assay – Blood Brain Barrier	**PAMPA – BBB**
Sonic Hedgehog	**Shh**	Central nervous system	**CNS**
Indian Hedgehog	**Ihh**	Absorption, Distribution, Metabolism and Excretion	**ADME**
Desert Hedgehog	**Dhh**	Intrinsic clearance	**CL_{intr}**
Patched 1 receptor	**PTCH 1**	Half-life	**$T_{1/2}$**
Seven-pass transmembrane protein Smoothened	**SMO**	Brain-derived neurotrophic factor	**BDNF**
Protein Suppressor of Fused	**SUFU**	4,5-dimethylthiazol-2-yl)-2,5-diphenyltetrazolium bromide	**MTT**

Planar cell polarity	**PCP**	Ethacrynic Acid	**EA**
Adenomatous polyposis coli	**APC**	Reactive oxygen species	**ROS**
Frizzled	**Fz**	Thin Layer Chromatography	**TLC**
Low-density lipoprotein receptor-related protein 5/6	**LRP5/6**	Parts per million	**ppm**
Protein disheveled	**Dvl**	Singlet	**s**
T-cell factor and lymphoid-enhancing factor	**Tcf/Lef**	Doublet	**d**
Smad ubiquitination regulatory factor	**Smurf**	Doublet of doublets	**dd**
Ras homologue gene-family member A	**RhoA**	Doublet of triplets	**dt**
Receptor tyrosine kinases	**RTKs**	Triplet	**t**
Phospholipase C	**PLC**	Multiplet	**m**
Period proteins	**PER**	Broad signal	**bs**
Cryptochromes	**CRY**	High Resolution Mass Spectrometry	**HRMS**
Alzheimer's disease	**AD**	Electrospray Ionization – Mass Spectrometry	**ESI-MS**
Parkinson's Disease	**PD**	Time of Flight	**TOF**

Amyotrophic Lateral Sclerosis	**ALS**	4-Dimethylaminopyridine	**DMAP**
Neurofibrillary Tangles	**NFT**	Relative Light Units	**RLU**
Microtubule-associated protein Tau	**MAPT**	Absorption Units	**AU**
Post-translational modifications	**PTMs**	Fetal bovine serum	**FBS**
Amyloid protein precursor	**APP**	Bovine serum albumin	**BSA**
presenilin	**psen**	Phosphate-Buffered Saline	**PBS**
β-site APP cleaving enzyme 1	**BACE 1**	Sodium Dodecyl Sulfate – Polyacrylamide Gel Electrophoresis	**SDS–PAGE**
Lewy bodies	**LB**	Tris-Buffered Saline with Tween 20	**TBST**
Tyrosine	**Tyr**	Horseradish peroxidase	**HRP**
Compound	**Cmpd**	Doubletime	**DBT**

1. INTRODUCTION

1.1. The Human Kinome

Phosphorylation is one of the most common and relevant post-translational modifications in eukaryotic cells. By reversibly modulating cell growth and cell differentiation, protein activity, stability, subcellular localization, and molecular interactions, phosphorylation regulates many aspects of cellular physiology[1,2].

This modification is catalyzed by Protein Kinases (PKs), a vast superfamily of enzymes that transfer phosphate groups from Adenosine Triphosphate (ATP) to serine, threonine, or tyrosine residues of their substrates. Accordingly, kinases are broadly classified as serine/threonine (ser/thr) kinases or tyrosine (tyr) kinases, depending on the amino acid residues they preferentially phosphorylate[3,4]. Along with lipid kinases, human protein kinases collectively constitute the human kinome, one of the largest enzyme families in the genome, and counts more than 500 hundred protein kinases encoded by 1.7% of the coding genes. Among the protein kinases, 478 contain a eukaryotic protein kinase (ePKs) domain while the other 40 kinases are classified as atypical protein kinases (aPKs) since they still have kinase activity, but lack in similarity within the kinasedomain sequence[5]. The ePKs can be further classified in smaller families depending on their substrate specificity and

mode of regulation[3,6]. Even though all kinases catalyze the same phosphoryl-transfer reaction, they display different structures, substrate specificity, and take part in a wide variety of cellular pathways.

As represented in Figure 1, ePKs can be classified into eight major groups based on sequence similarity within this domain:

- Tyrosine kinases (TK);
- Tyrosine kinase-like (TKL);
- STE20, STE11, and STE7 related (STE);
- Casein kinase 1 (CK1);
- Protein kinase A, protein kinase G and protein kinase C related (AGC);
- Ca^{2+}/calmodulin-dependent kinases (CAMK);
- Cdk, MAPK, GSK, Cdk-like related (CMGC);
- Receptor guanylyl cyclase (RGC)[5].

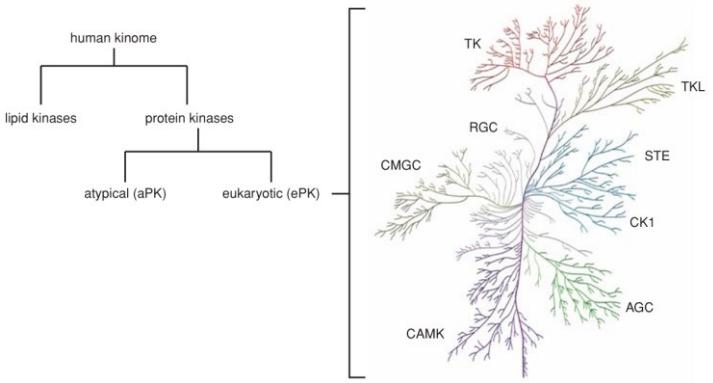

Figure 1: representation of the human kinome and classification of the kinases in groups[5].

1.2. Kinases Structure and common features

Despite the differences in their biological role and function, kinases display some common structural features. For example, they are commonly folded in a bilobed tertiary structure, with a smaller N-terminal lobe connected to a larger C-terminal lobe where ATP binding occurs. Several kinases possess also a metal ion, usually magnesium, that contributes to the correct positioning of the phosphoryl group.

The N-lobe is usually composed by several β-strands and one main helix, called C-helix while the C-lobe is constituted by α-helixes and key residues responsible for the protein substrate correct positioning and interaction. The short and flexile loop that separates the two lobes are responsible for the ATP correct binding and it is the so-called *hinge region.* Other common

features present in most of the kinases are the conformational states active and inactive. Regarding this the majority of kinases possess a conserved activation motif, named DGF loop, which is composed by the triad Aspartate- Phenylalanine and Glycine (Asp-Phe-Gly), located in the C-terminal domain. In the active state, this motif extends away from the ATP pocket, with the Asp residue that coordinates the magnesium ion responsible for the positioning of the ATP for the catalytic reaction. This conformational state is called DGF-in, due to the protrusion of the Asp residue towards the ATP substrate. The active state can be stabilized by multiple phosphorylation states, promoted by other kinases or *via* autophosphorylation (cis-autophosphorylation with an intramolecular phosphoryl transfer or trans-autophosphorylation when another molecule of the same kinase catalyzes the phosphoryl motion). A polar interaction between a glutamate (Glu) at the level of the C-lobe and a lysine (Lys) present in N-lobe, further contributes to stabilizing the active state, this Lys also interacts with the α- and β-phosphate of the ATP. On the other hand, the inactive state (DGF-out) varies among the kinases, but the most common mechanism consists in the occlusion of the ATP pocket and substrate binding site by the activation loop. This situation is characterized by the disruption of the bridge between the Glu in the C-term and the Lys located in the N-loop and the mislocalization of the P-loop. Another conserved loop is the

glycine-loop, named *phosphate- loop* (P-loop) that again contributes to the specific positioning of the ATP mediated by the coordination of the phosphate mediated by the Glycine (Gly) residue[5].

1.3. Kinase inhibitors and mechanism of action

Phosphorylation can activate or inactivate substrates, create docking sites for protein recruitment, or induce conformational changes that shift proteins between ordered and disordered states[7,8]. Thus kinases are responsible of the regulation of many essential processes such as signal transduction, cell cycle progression, apoptosis, and metabolic regulation[9]. For these reasons their regulation is very strict, and dysregulation of kinase activity is a hallmark of many human diseases, including cancer, inflammatory conditions, metabolic disorders, and neurodegenerative diseases. Because kinases regulate a wide variety of cellular processes and are implicated in numerous pathologies, they represent one of the most extensively studied therapeutic targets, but their conserved ATP domain makes the design of selective inhibitors quite challenging[2,10].

The interactions between kinases and ATP can be resumed as reported in Figure 2. The adenine core is positioned in the so-called adenine region and interacts with the hinge region through H-bond interactions, while the sugar moiety fits in a

pocket named after it (sugar pocket). The phosphates are positioned by polar residues in the phosphate region.

In the last years a lot of kinase inhibitors were developed, and they have been classified based on their mode of action and site of interaction.

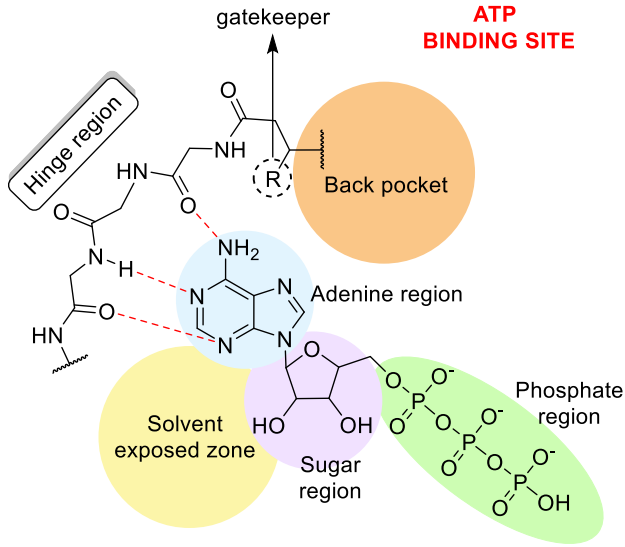

Figure 2: ATP binding mode and most representative parts of the binding pocket.

- Type I inhibitors: consist of small molecules capable of interacting with the active conformation of the kinase (DGF-in). This class of inhibitors commonly exhibits a heterocycle scaffold that mimics the interactions of the adenine-core of the ATP as represented in Figure 3,

usually through the formation of one to three hydrogen bonds within the catalytic cleft. The scaffold of the inhibitors is then decorated with substituents capable of interacting both through polar and hydrophobic interactions with the aminoacids surrounding the pocket. In this context, the gatekeeper residue, an amino acid located in the hydrophobic back pocket of the ATP-binding site, is fundamental in regulating ligand migration within the pocket. Ligands that specifically target this residue often result in efficient inhibition of kinase activity. These kind of inhibitors occupy the ATP binding site preventing the phosphorylation reaction[11–14].

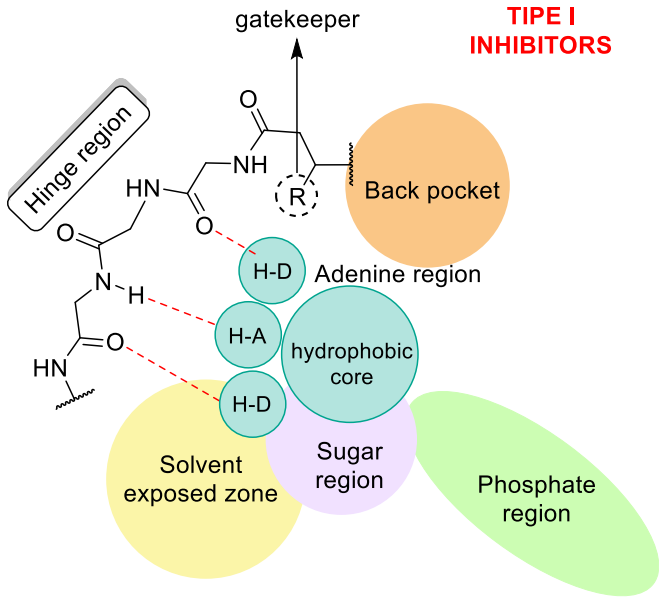

Figure 3: Type I inhibitors and mode of binding.

- Type II inhibitors: small molecules that disturb the enzyme catalysis by inducing the inactive DGF-out conformation. This mode of action, as represented in Figure 4, usually exploits hydrophobic interactions between the kinase and the inhibitors, that occupies an allosteric hydrophobic site generated by this peculiar DGF-out state, where the phenylalanine (Phe) of the motif partially occludes the ATP pocket[11–13,15,16].

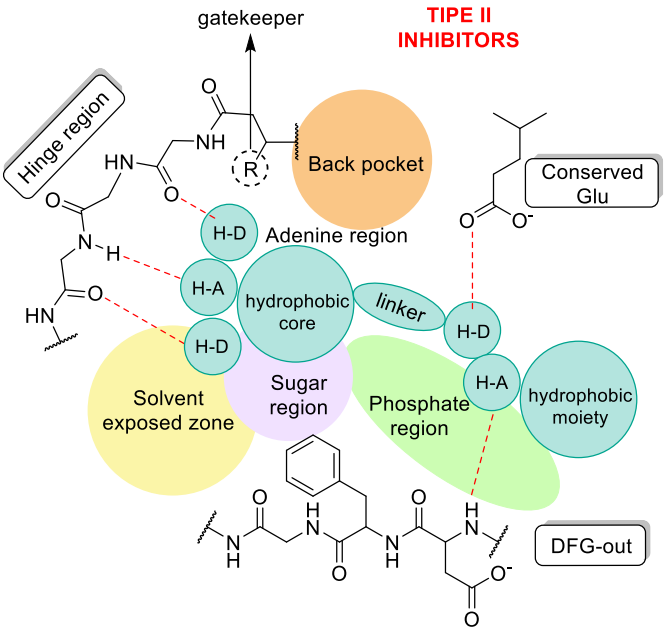

Figure 4: Type II inhibitors and mode of binding.

It is worth to mention that in the last years also hybrid inhibitors where identified, for example type ½ inhibitors that have an intermediate behavior between type I and type II. In fact, these kinds of small molecules are capable of binding an inactive conformation of the enzyme but still in a DFG-in state, this situation is characterized by a mislocalization of the αC-helix, enabling interaction within the hydrophobic back pocket[11,12].

- Type III inhibitors: this kind of inhibition mechanism is adopted by compounds that interact with an allosteric site located adjacent to the ATP binding site in the

catalytic pocket between the two lobes, thus disrupting the interactions between the enzyme and the ATP, as represented in Figure 5. This class of inhibitors is characterized by higher selectivity compared to class I/II inhibitors, as they bind to pockets that are less conserved than the catalytic one[17,18]. They are also more resistant to mutations, especially if these involve the gatekeeper residue[19].

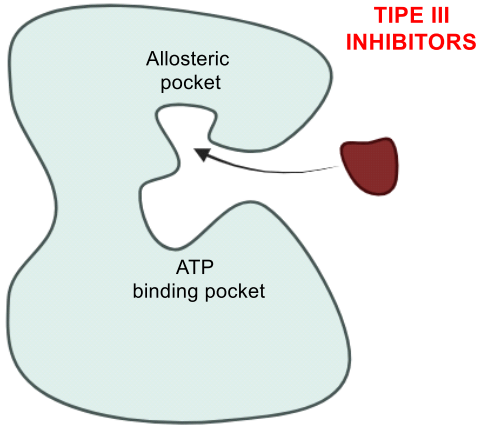

Figure 5: Type III inhibitors and their binding mode.

- Type IV inhibitors: these inhibitors, schematically represented in Figure 6, are allosteric inhibitors, capable of interaction within an allosteric site that is localized far from the kinase domain, and the interaction between the molecules and the residues in the pocket causes a conformational modification that avoids the substrate correct positioning and thus the catalytic reaction[20,21].

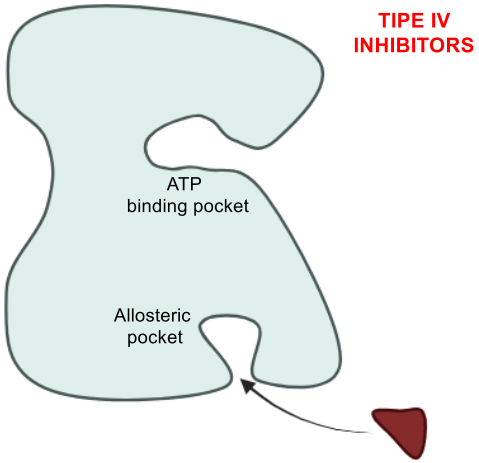

Figure 6: Type IV inhibitors and their mechanism of action.

- Type V inhibitors: small molecules that have a bifunctional structure and are able to target both the ATP binding pocket and an allosteric site, as reported in Figure 7. This allows us to overcome the main problem of the allosteric inhibitors that consist in low

potencies, even though they are highly selective [22]. This approach consists in developing an appropriate linker that could connect the two parts of the molecule in order to have a more potent inhibitor compared to type III/IV ones and with improved selectivity thanks to the non-ATP cleft directed inhibitor[22,23].

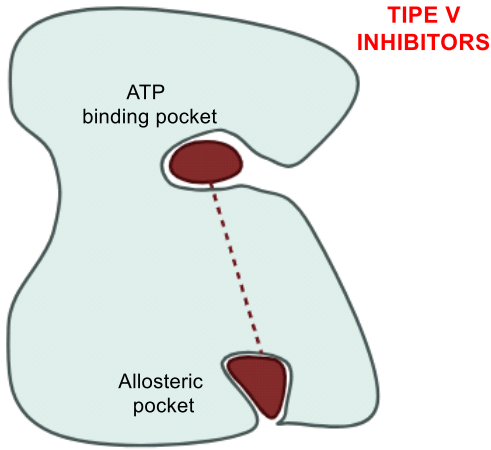

Figure 7: Type V inhibitors and their binding mode, the red dotted line represents the linker connecting the two parts of the inhibitor.

- Type VI inhibitors: these are represented by covalent inhibitors, that could interact both within the catalytic site and allosteric pockets (Figure 8). Of course, when developing a drug, the highest potencies possible is desirable, but this depends on the target engagements

and thermodynamics. Non-covalent inhibitors interact with the target exploiting intermolecular forces, that could increase by increasing the molecules dimensions, but this can be translated into poor pharmacokinetic (PK) properties. Covalent inhibitors are capable of forming stronger interactions (covalent bonds) with specific aminoacidic residues, thus guaranteeing improved PK profiles. Furthermore, covalent binding enables higher potencies and thus lower required concentration of the drug, resulting in less toxicity issues. This is due to the strength of the bond, in contrast with non-covalent inhibitors, which interactions can be affected by physiological substrate concentrations (e.g. ATP)[24].

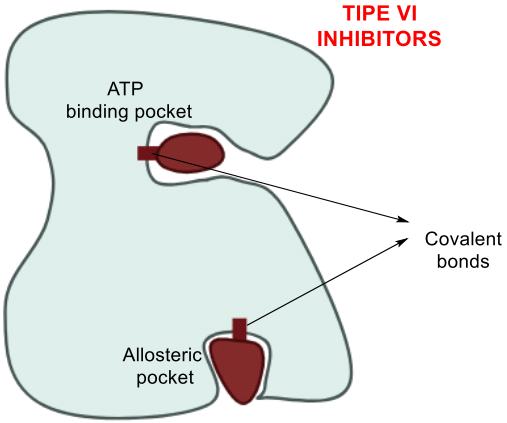

Figure 8: Type VI inhibitors and their binding mode.

1.4. Casein Kinase 1 (CK1) family

One of the earliest kinase families described is Casein Kinase 1 (CK1), although casein is not its physiological substrate. The enzyme's preference for phosphorylating specific serine and threonine residues places it within the serine/threonine kinase (Ser/Thr kinase) group. The CK1 family is highly conserved in eukaryotic cells, and in humans includes seven paralogs encoded by distinct genes (α, α-like, γ1, γ2, γ3, δ, and ε), along with several splice variants[25–27]. The family also encompasses Vaccinia-Related Kinases 1–3 (VRK1–3) and Tau Tubulin Kinases 1 and 2 (TTBK1/2), which are structurally related to CK1 paralogs. As shown in Figure 9, CK1 proteins share high homology in their kinase domain, while a more variable C-terminal domain differing in both length and amino acid composition, influencing substrate selectivity[28–30].

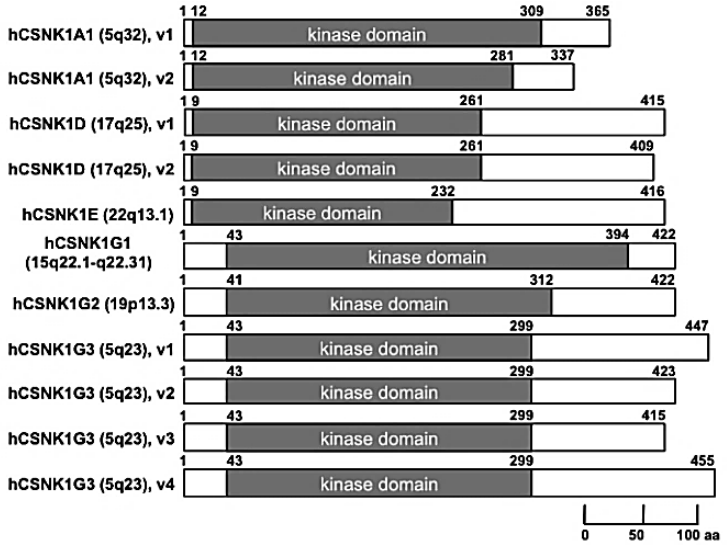

Figure 9: Homology in the kinase domain of Casein Kinase 1 isoforms [28].

CK1 proteins are pleiotropic regulators capable of phosphorylating diverse substrates, making them key players in numerous cellular pathways[26,31,32]. CK1δ has attracted particular attention due to its involvement in the regulation of circadian rhythms[33–37], Wnt signaling[38], and neurodegenerative disease progression[39–42] . More broadly, CK1 functions extend to mitotic checkpoint signaling[43], DNA repair[32,44], endocytosis[45], Hedgehog signaling[46], and Hippo pathway regulation[47].

1.5. Structure and Regulation

Like other kinases, the CK1 family displays a typical bilobed structure: the smaller N-terminal lobe, composed mainly of β-

sheets, and the larger C-terminal lobe, containing mostly α-helixes and loop structures. The two lobes are connected by the hinge region, which hosts the catalytic cleft responsible for binding both ATP and substrate proteins[48,49].

Within this conserved kinase architecture, CK1 isoforms display some common structural features represented in Figure 10. A prominent α-helix (C-helix) in the N-terminal lobe that plays a key role in regulating their conformational state and, consequently, catalytic activity[32]. CK1 isoforms also show variations in the C-terminal region, where differences in length and amino acid composition influence substrate specificity and regulatory interactions[28–30,32]. Moreover, in CK1δ the conserved Alanine-Proline-Glutamate (APE) motif is replaced by the Serine-Isoleucine-Asparagine (SIN) motif, which contributes, together with the P-loop, to the correct positioning of ATP[3,49]. Additional elements such as the L-78 loop, located below the hinge region, are implicated in substrate selectivity[50], while the T-loop (L-9D) can interact with the catalytic cleft and interfere with substrate binding.

These distinctive features highlight how CK1 isoforms integrate the common kinase fold with specialized elements that direct their functional diversity[51].

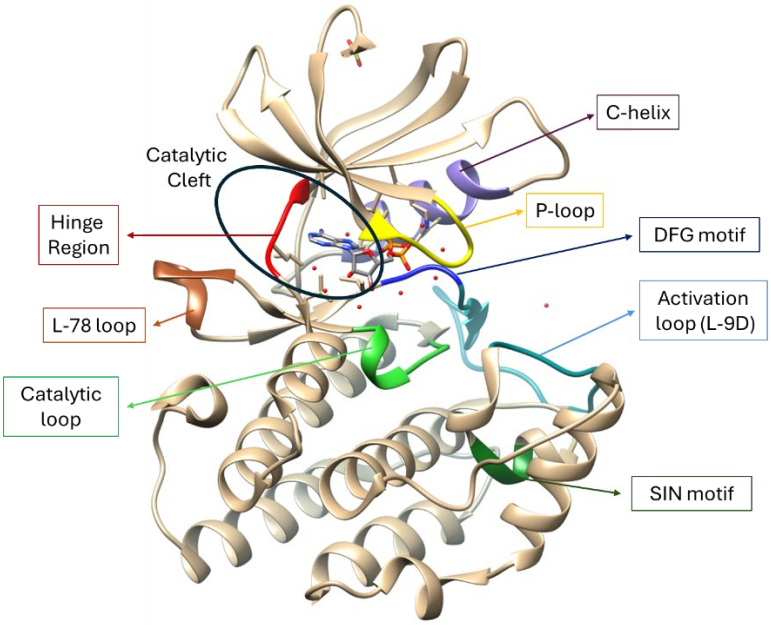

Figure 10: Structure and main motifs of Casein Kinase 1δ (PDB code: 5X17).

Because of its ubiquitous nature and the wide variety of regulated processes by the kinase, it is tightly regulated by multiple mechanisms like phosphorylation states, dimerization and subcellular compartmentalization. Regarding C-terminal domain, autophosphorylation acts as a major inhibitory mechanism, in fact phosphorylation at multiple serine/threonine sites located in the C-term reduces kinase substrate

phosphorylation, while truncation or dephosphorylation of this region increases activity[32,52–54]. Isoform-specific regulation is also observed, since alternative splicing variants display differences in autophosphorylation and subcellular distribution[55]. Moreover, protein–protein interactions play a critical role in modulating CK1δ, as binding partners can either recruit the kinase to specific substrates or influence its localization[29,51]. Subcellular localization itself serves as an additional regulatory layer, with CK1δ shuttling between cytoplasm, nucleus, and other compartments to access to different substrates and mediate context-dependent functions[56]. Finally, CK1δ can be regulated by small-molecule inhibitors, reinforcing its relevance as a promising therapeutic target[57–60].

The C-terminal domain, as already mentioned, can be phosphorylated both by the kinase itself and by other kinases, in this form it acts as a pseudo-substrate[29] interfering with the entrance and interaction with the substrate, preventing the phosphoryl transfer[61]. This regulative mechanism takes place due to the presence of a recognition sequence composed by Ser/Thr-X-X-Y (Y: any aminoacid except serine or threonine)[32]. The phosphorylation at the C-terminal domain downregulates the kinase activity, since it interferes with the entrance and interaction with the substrate, preventing the phosphoryl transfer. It has been demonstrated that CK1δ and the other

isoforms can be phosphorylated by PKA (cAMP-dependent protein kinase), Akt (protein kinase B), CLK2 (CDC-like kinase 2), protein kinase C isoform (PKC), and Chk1 (checkpoint kinase 1)[62,63].

The formation of dimers further acts as a regulative mechanism of CK1δ, this event has been demonstrated by X-ray crystal structures, where dimers of CK1δ were present. This occurs thanks to the presence of dimerization domain capable of interacting with another CK1δ unit, and as a consequence of the homodimer formation, the Arginine13 (Arg13) moves towards the internal part of the enzyme, blocking the ATP that is no longer able to interact in the binding site[29,32,49,64].

1.6. Biological Role and Pathological Implications

1.6.1. Casein Kinase 1δ in Cancer-Related Signaling Pathways

1.6.1.1. p53 signaling pathway

Isoform δ plays a crucial role in tumorigenesis, in particular due to the involvement in the p53 signaling pathway. P53 is a conserved transcriptional factor capable of transactivate various genes involved in the induction of cell cycle arrest and apoptosis. In physiological conditions p53 is expressed at low levels, kept low by the murine double-minute clone 2 protein (MDM2) ligase, that promotes p53 ubiquitination and degradation. When the DNA gets damaged; post-translational

modifications, such as acetylation, induce p53 accumulation and activation in the nucleus. The chemical modification promotes the MDM2 dissociation and p53 is capable of interacting with a specific set of genes that induces cell cycle arrest, to let the cell repair the damaged DNA. If the damage is critical, p53 may induce cell apoptosis to avoid replications of the damaged DNA to daughter's cells, thus avoiding tumorigenesis. For this reason, p53 is called ''the guardian of the genome''[65–67].

It has been observed that CK1δ as other kinases, is able to phosphorylate p53, thus regulating its activation and deactivation. p53 is phosphorylated mainly at serines 6 and 9 following DNA damage[68]. Other phosphorylation concern serine 15, and threonine 18. These modifications weaken the interaction between p53 and MDM2, thereby activating p53 for its function[69,70].

Besides interaction between p53 and CK1δ, the kinase is linked also to the regulation of MDM2, in fact, phosphorylation of MDM2 promotes p53 degradation, thus blocking the apoptosis mechanism induced by p53[71]. Balancing these two effects, involving MDM2 and p53, the role of CK1δ results in modulating the effects of p53 on cell growth and genome integrity. Regarding the antiapoptotic effect of CK1δ, it negatively regulates apoptosis through multiple pathways, including p75-, tumor necrosis factor related apoptosis inducing

ligand (TRAIL), First apoptosis signal receptor (FAS receptor), and Retinoid X Receptor (RXR) mediated mechanisms. CK1δ phosphorylates the p75 tumor necrosis factor, inhibiting p75-mediated apoptosis, and phosphorylates components of the death-inducing signaling complex (DISC), contributing to TRAIL resistance. In FAS-mediated apoptosis, CK1δ prevents caspase-8–dependent mitochondrial apoptosis. Additionally, CK1 modulates the antiapoptotic effects of galectin-3 (Gal-3) through phosphorylation at serine 6, promoting its cytoplasmic localization; mutations at this site increase nuclear Gal-3, which is associated with tumor progression[72,73].

1.6.1.2. Hippo pathway

The Hippo pathway (also known as the Salvador–Warts Hippo pathway) is an evolutionarily conserved regulator of tissue growth and cell fate. It consists in a large network of proteins that control the growth of different tissues during development and regeneration, as well as in pathological states such as cancer. The main actors that regulate the hippo pathway are the following proteins: STE20-like protein kinase 1 (MST1; also known as STK4), and MST2 (also known as STK3), and large tumor suppressor 1 and 2 (LATS1/2), together with the adaptor proteins Salvador homologue 1 (SAV1), Monopolar spindle One Binder kinase activator 1α (MOB1α) and MOB1β. These last three proteins can activate the LATS1/2 kinases which

phosphorylate the transcriptional co-activators YAP and TAZ. This phosphorylation reaction induces their ubiquitination and degradation, thus controlling cell proliferation and tissue development. When the hippo-pathway is ‘’off’’’ YAP and TAZ are pathologically active and move to the nucleus and bind the transcriptional enhancer factor domain (TEAD), activating genes involved in cell proliferation, thus involved in cancer development. CK1δ is a regulative protein of the hippo pathway where interferes by phosphorylating YAP and TAZ, but if its activity is downregulated or altered the degradation is not correct, and it contributes to cancer development[74–76]. The signal cascade is reported in Figure 11.

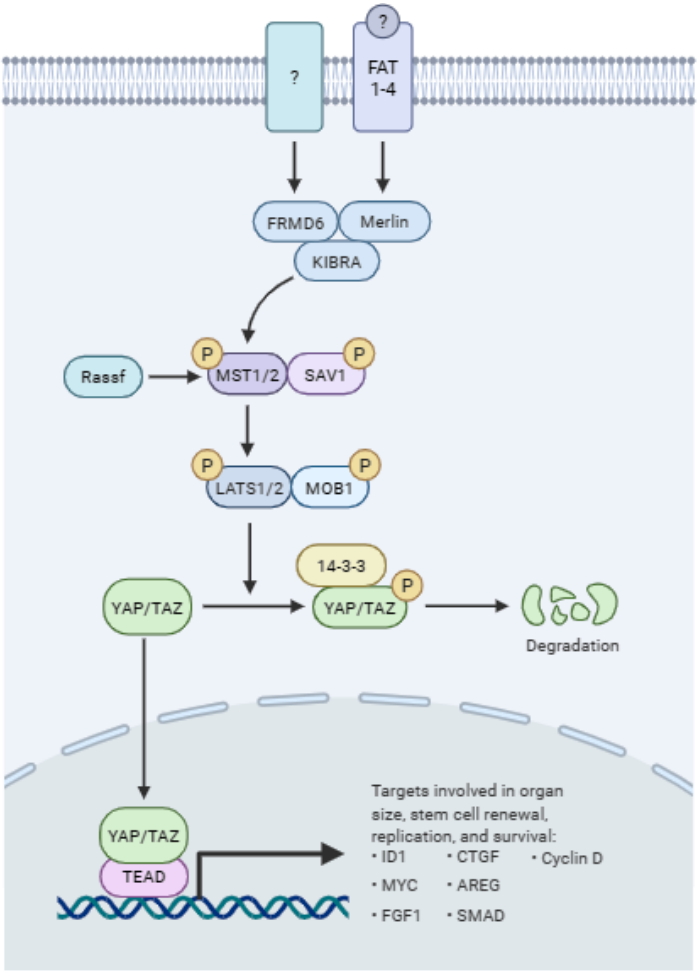

Figure 11: Hyppo signaling Pathway, image created by ***BioRender.com***

1.6.1.3. Hedgehog pathway

The Hedgehog (Hh) signaling pathway plays a fundamental role during embryonic development, where it regulates organogenesis and tissue patterning, while in adults, its activity

is primarily restricted to the maintenance and renewal of epithelial tissues in various internal organs[77]. Dysregulation of this pathway, however, has been strongly linked to tumorigenesis, contributing to the onset of multiple malignancies, including basal cell carcinoma, medulloblastoma, glioma, gastrointestinal tumors, and prostate cancer[78–81].

Basal cell carcinoma and medulloblastoma are cancers with a high unmet need for drug development, the latter being a childhood malignancy often associated with poor prognosis. The principal ligands of this pathway are Sonic Hedgehog (Shh), Indian Hedgehog (Ihh), and Desert Hedgehog (Dhh). In the absence of these ligands, the Patched 1 receptor (PTCH1) suppresses the activity of the seven-pass transmembrane protein Smoothened (SMO), thereby preventing signal transmission to the GLI transcription factors (GLI1, GLI2, GLI3). These GLI proteins are subject to phosphorylation by several kinases, among which the CK1 family has also been shown to play a role. Their phosphorylation is then followed by the ubiquitination and degradation of the GLI proteins, and the genes are not activated[32,81,82].

When one of the ligands is present (Shh, Ihh and Dhh), PTCH is not interacting with SMO, that is able to activate GLI transcription factors that are stabilized and not degraded. Stabilized GLI are able to translocate in the nucleus and activate

the transcription of the target genes, that are responsible for the cell proliferation and differentiation[83]. Another important protein in the pathway, is the protein Suppressor of Fused (SUFU), that contributes to regulate the signal cascade and avoids the GLI factors to enter in the nucleus and activate the target genes[84]. The schematic representation of the hedgehog signaling pathway is reported in Figure 12.

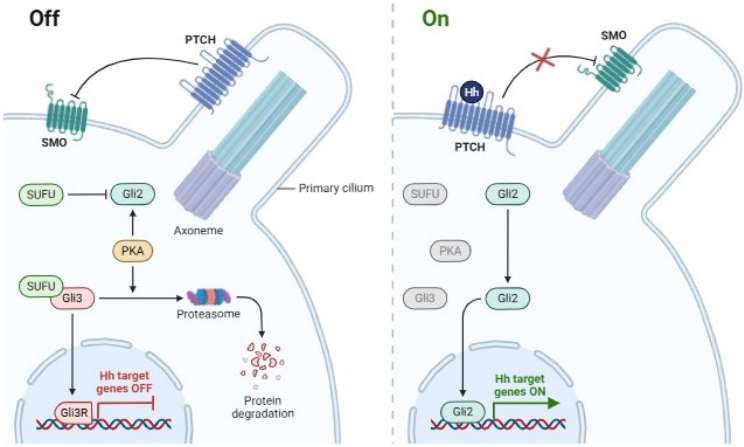

Figure 12: Hedgehog signaling pathway, mode 'off' on the left and mode 'on' iin the right. Image available in ***Biorender.com***

1.6.1.4. Wnt signaling

Wnt signaling pathway is highly conserved in mammals and is strictly connected to embryogenesis, cell homeostasis and tissue regeneration. It has a crucial role in cell differentiation, apoptosis and cell viability as well. Its deregulation may lead to

some pathological conditions such as embryonic deformities, degenerative disease, diabetes and cancer[85].

The Wnt signaling pathway can be divided into two types: the canonical and β-catenin dependent way, and the non-canonical one (β-catenin independent). This last one has two distinct classes including Wnt/planar cell polarity (PCP) and Wnt/calcium (Wnt/Ca^{2+}) pathways. The Wnt/ β-catenin dependent pathway is mainly involved in cell proliferation regulation while the non-canonical one regulates mainly polarity and cell mobility[85].

1.6.1.4.1. Canonical Wnt (β-catenin dependent) pathway

The canonical Wnt pathway is represented in Figure 13. Wnt proteins (Wnts) consist in a group of cysteine-rich glycoproteins. In the absence of a Wnt ligand that binds the receptor complex, β-catenin is sequestered in the cytosol where the destruction complex promotes its degradation. This is composed by Axin, that acts as a scaffold protein for adenomatous polyposis coli (APC), glycogen synthase kinase 3β (GSK-3β) and CK1α CK1α. These two kinases contribute to the sequential phosphorylation of β-catenin, thus promoting its degradation[86,87]. In presence of Wnt ligands, the pathway is activated and the Wnts bind the receptor complex frizzled (Fz) and the low-density lipoprotein receptor-related protein 5/6 (LRP5/6). Thanks to this interaction, the cytoplasmatic protein dishevelled (Dvl) is recruited, phosphorylated and activated.

Active Dvl induces the dissociation of the degradation complex and β-catenin degradation is inhibited. β-catenin is now able to translocate in the nucleus. Active β-catenin binds the T-cell factor and lymphoid-enhancing factor (Tcf/Lef) that controls the target gene expression involved in cell proliferation, cell differentiation and cell polarity[88]. Regarding the involvement of CK1δ, both positive and negative regulatory effects on the Wnt signaling pathway have been reported. In particular, the paralogs CK1δ and CK1ε phosphorylate Axin and Dishevelled (Dvl), inducing conformational changes that weaken the association of the β-catenin destruction complex. This dissociation prevents β-catenin degradation, thereby promoting its stabilization. As a consequence, deregulation of CK1δ activity can lead to the abnormal accumulation of β-catenin, which subsequently translocates into the nucleus and activates the transcription of Wnt target genes involved in cell proliferation. Such aberrant activation ultimately results in uncontrolled cell growth[32].

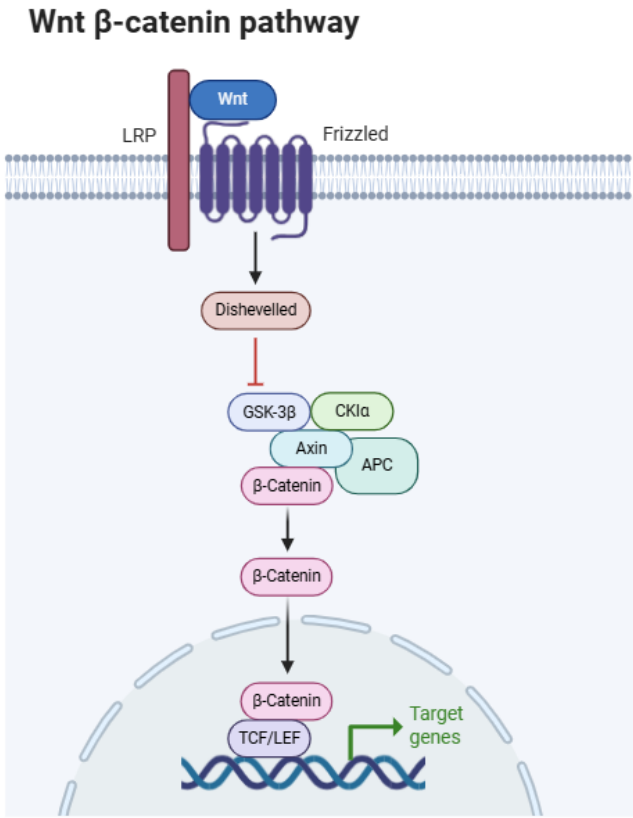

Figure 13: Canonical Wnt signaling pathway (beta-catenin dependent). Image created by ***Biorender.com.***

1.6.1.4.2. Non-Canonical Wnt (β-catenin independent) pathway

The non canonical Wnt signaling pathway starts with some specific Wnt ligands, mainly Wnt5α type (Wnt4, Wnt5α, Wnt5β, Wnt6, Wnt7α and Wnt11). The Wnt5α type ligands may initiate the non-canonical Wnt/planar cell polarity (PCP) or

Wnt/Ca^{2+} pathways and regulate cellular polarization and migration[89].

The typical Wnt ligands, start the non-canonical pathway by interacting with the Fz receptor (Fz 6 and Fz 3) and coreceptors ROR1/2. This interaction activates the Dvl protein that drives the signaling through two different ways, the first one recruits protein Par6 that interacts with Dvl, and Smad ubiquitination regulatory factor (Smurf) is recruited by the phosphorylated Dvl and binds to Par6. Smurf then ubiquitinates Prickle, a protein that normally inhibits Wnt/PCP signaling, targeting it for proteasomal destruction. The breakdown of Prickle enables Dvl to associate with the Dvl-associated activator of morphogenesis (DAAM)[90,91].

This complex can then activate Ras homologue gene-family member A (RhoA). DAAM also activates Profilin. Rac1 activates JNK, which phosphorylates and activates c-Jun to go to the nucleus and initiate gene expression. JNK also activates CapZ interacting protein (CapZIP) via phosphorylation. RhoA activates RHO-associated coiled-coil-containing protein kinase (ROCK) and diaphanous 1 (DIA1). ROCK activates the Myosin II regulatory light chain (MRLC). CapZIP, MRLC, DIA1, and profilin all contribute to actin polymerization, which is vital to cell polarity and migration[90,92,93].

On the other hand, the Wnt/Ca^{2+} pathway operates through G proteins, receptor tyrosine kinases (RTKs), and phospholipase C (PLC). This signaling cascade leads to intracellular calcium release, activation of the serine/threonine protein phosphatase calcineurin, and subsequent accumulation of nuclear factor of activated T cells (NFAT) within the nucleus.

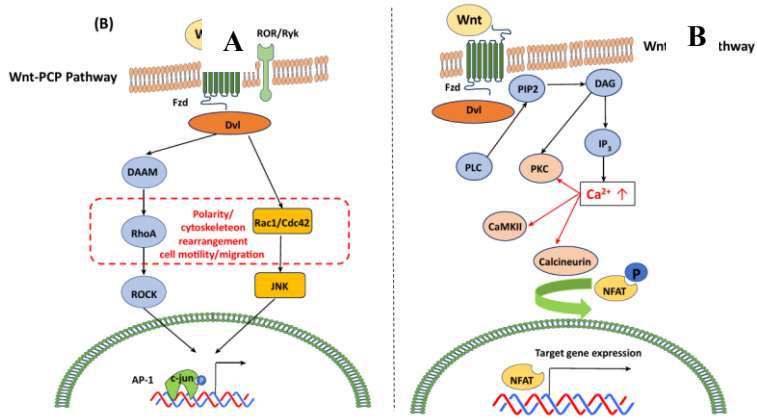

Figure 14: Non canonical and β-catenin independent Wnt signaling pathway, panel A) non canonical Wnt/PCP pathway; panel B) non canonical Wnt/Ca^{2+} pathway [89].

1.6.2. Casein Kinase 1δ in Circadian rhythm disorders

Almost every organism possesses an internal day-night regulative system, called circadian rhythm, allowing the organism to synchronize with light and dark cycles. This internal clock consists in the transduction of specific genes and proteins that are fundamental for a wide pool of functions like the light dependency in falling asleep and weaking up[94], body

temperature[95], blood pressure[96], hormone synthesis[97], digestive secretion[98], immune response[99] and neurological disorders[100]. Whitin this complex regulative system, the principal actors are the so-called period proteins (in particular PER1 and PER2) and cryptochromes CRY (CRY1 and CRY2) whose levels are tightly tuned during the day[101,102].

Another key effector of the circadian rhythm is the Circadian Locomotor Output Cycles Kaput: Brain and Muscle ARNT (Aryl hydrocarbon Receptor Nuclear Translocator)-Like 1, CLOCK:BMAL1 heterodimer, which periodically binds to DNA and activates the transcription of PER and CRY genes. The translated PER and CRY proteins form heterodimers that act as inhibitory complexes capable of translocating into the nucleus, where they interact with and repress CLOCK:BMAL1 activity, thereby inhibiting their own expression[103]. This negative feedback loop is fundamental for maintaining the 24-hour periodicity of the circadian rhythm and it is illustrated in Figure 15[49]. These so-called clock proteins levels are further stabilized and regulated by post-translational modifications like phosphorylation and ubiquitination[104,105]. The phosphoryl transfer acts as a priming event for subsequent ubiquitination and proteasomal degradation, highlighting the crucial role of protein kinases in circadian rhythm regulation[106]. Deregulation of CK1 proteins and in particular isoform δ/ε demonstrated

hyperphosphorylated clock proteins resulting in shortening the circadian rhythm[34,107].

Disruptions in the length of the circadian rhythm have been also linked to neurodegenerative diseases like Alzheimer's one. In particular, patients with late-stage Alzheimer's disease exhibit pronounced circadian disruptions, including increased sleep fragmentation, reduced amplitude of circadian rhythms, and delayed sleep-wake cycles, with both bedtime and wake time shifted later in the day (a phenomenon referred to as "phase delay")[108]. Beyond Alzheimer's pathology, abnormal circadian regulation has also been associated with psychiatric conditions such as depression, anxiety, and bipolar disorder[100].

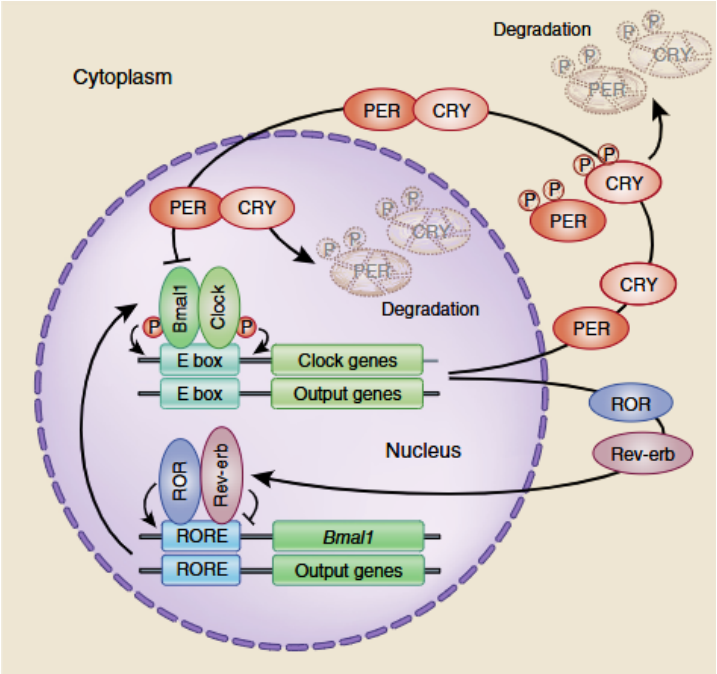

Figure 15: Representation of the circadian rhythm regulation, through clock proteins and CLOCK:BMAL1 complex[109].

1.6.3. Casein Kinase 1δ in Neurodegenerative Disease

Since the age of the global population is progressively increasing and getting older, the appearance of neurodegenerative disorders is growing. These disorders manifest when neuron lose their function and structure, that at the end leads to neuronal death. As a consequence, affected individuals show a gradual decline in cognitive abilities and other mental functions[110].

The most known neurodegenerative disease are Alzheimer's disease (AD), Parkinson's Disease (PD) and Amyotrophic Lateral Sclerosis (ALS), and all are characterized of main molecular events, that's consist in altered protein functions and formation of pathological aggregates which serve as pathological biomarkers.

Many of these proteins are reported to undergo phosphorylation by protein kinases and this deregulation in the expression of CK1δ is found to be present in several neurological disorders[111].

1.6.3.1. Alzheimer's disease (AD)

Alzheimer's disease is a neurological disorder that usually manifests in elderly individuals, and one of the earliest symptoms of the disease is the development of dementia. The pathology is characterized by a particular onset and decline of cognitive functions that progressively worsen. Individuals affected by AD progressively lose their ability to live independently[112]. Thanks to the improvements in diagnosis of neurodegenerative disease, AD can be identified by two main hallmarks that manifest even in the early stage of the disease, β-amyloid and Neurofibrillary Tangles (NFT) formation, consisting in intracellular aggregates of hyperphosphorylated Tau protein that disrupt neuronal function and contribute to cell death. They primarily accumulate in the soma and dendrites of neurons and spread progressively across brain regions[113–115].

Tau protein is encoded on chromosome 17 by the Microtubule-associated protein Tau (MAPT) gene, which is translated into an overall hydrophilic protein with largely unfolded and negatively charged regions enriched in the axons of developing and mature neurons[114]. Tau proteins structures can be divided into two main domains, classified depending on their microtubule interactions and/or their aminoacidic composition[116]. The larger N-terminal domain, is not involved in the interactions with the microtubules and is projected away, for this reason is called ‘’projection domain” and the other is the carboxy-terminal domain; the division of the protein stricture in domain is reported in Figure 16A[114,116,117]. The projection domain can be further divided into two smaller domains, the amino-terminal region with a high proportion of acidic residues and the proline-rich region[117]. The microtubule-binding domain, present in the C-terminal domain can be distinguished into two other sub-groups, the basic, true tubulin-binding region and the acidic carboxy-terminal region [117]. The microtubule binding domain is formed by four repeated motifs, separated by flanking regions, responsible for the interactions between Tau and the microtubules, and contributes their stabilization[118].

The overall composition and distribution of the aminoacids in tau proteins, result in a mainly unfolded structure, that composes a protein with a hydrophilic character. Moreover, the protein has an overall basic character, but the amino terminal, composed of

~120 residues, is acidic, while the carboxy terminal ~40 residues are roughly neutral. This asymmetry of charges is important for interactions with microtubules and other partners, internal folding, and Tau aggregation[119]. Interactions with Tau's protein targets, are also influenced by post-translational modifications, such as phosphorylation, O-glycosylation, methylation, deamidation, acetylation and ubiquitination[120]. Under physiological conditions, the main function of tau is to bind to microtubules and contribute to their stabilization and assembly. Microtubules are essential for maintaining cell shape, enabling motility through cilia or flagella, and forming the mitotic spindle during cell division[120].

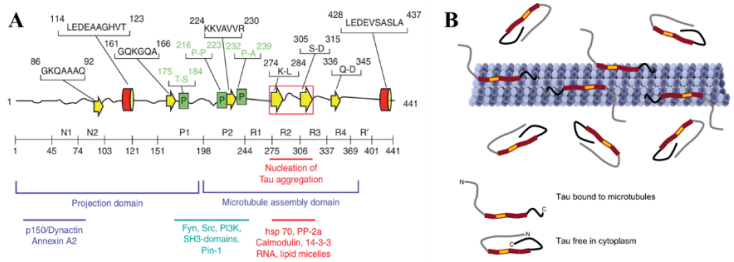

Figure 16: A) Representation of the primary and secondary structure of tau, and its main domains. B) assembly of tau filaments to the microtubules [119,121].

Deregulation of tau proteins—particularly structural alterations that impair their interaction with microtubules and other binding partners—represents one of the major contributors to the development and progression of AD.

Among post translational modifications, hyperphosphorylation has been identified as a central event in AD, and CK1 family is strictly involved in this, in fact it has been demonstrated its capability to phosphorylate Tau in vitro and it is observed its colocalization in neurofibrillary tangles (NFTs) in AD patients. When Tau was first identified as the major component of neurofibrillary tangles (NFTs), it was also found to be abnormally hyperphosphorylated[41,122], this modification was found later to reduce Tau protein's ability to bind tubulin and promote microtubule assembly[123].

In AD, the pattern of Tau phosphorylation evolves with disease progression. Initial phosphorylation events disrupt Tau–microtubule interactions and promote its mislocalization to the somatodendritic compartment. Specific sites, such as Ser199, Ser202/205, Thr231, and Ser262, are associated with the formation of pre-tangles in neuronal processes[124,125]. As pathology progresses, somatic tau levels increase, and additional epitopes, including pSer422, become evident. At these stages, phosphorylation often undergoes cleavage at Asp421, which increases Tau's aggregation propensity; however, phosphorylation at Ser422 can inhibit this cleavage. In later stages of AD, phosphorylation at other sites, such as Ser396, becomes more prominent[125,126].

Adding to the complexity, phosphorylation at certain residues can prime additional phosphorylation events, leading to the generation of multi-site epitopes or promoting conformational changes in Tau[127]. In Figure 17 is represented the comparison between a healthy brain condition and AD affected brain.

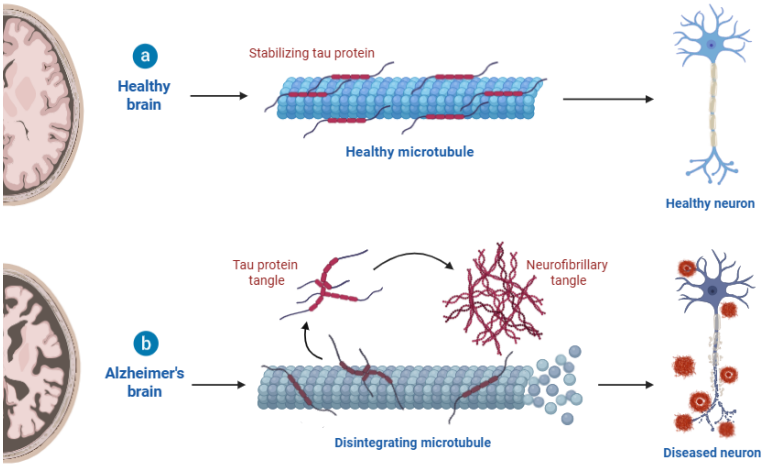

Figure 17: Development of Alzheimer's disease, tau aggregation in NFTs, image created with ***Biorender.com****.*

The second main cause of the AD development is related to aggregation and plaques formation of amyloid β (Aβ), that is also related to the formation of NFT via caspase-3 activation leading to the cleavage of Tau proteins. Furthermore, Aβ-peptide is able to reduce interactions between Tau and microtubules, determining the loss of stabilization. In addition, it has been demonstrated that mutation in the amyloid protein precursor (APP) and presenilin (psen 1 and psen 2) are

responsible for the genetic Alzheimer's disease. Figure 18 illustrates the mechanism of action of β-amyloid aggregates and their role in the onset of pathology[128–130].

Initially, the presence of Aβ in senile plaques led researchers to believe it was an abnormal protein; only later it was discovered that it is normally produced by cleaving the APP during the cell cycle. For this reason, research started to focus on which enzymes trigger the cleavage of APP leading to the accumulation of Aβ[131]. These proteins were pointed out to be β-secretase and γ-secretase.

γ-secretase is an intramembrane protease complex, consisting of four components: presenilin, nicastrin, PEN-2, and APH-1, with presenilin constituting the active site. β-secretase activity originates mainly from an integral membrane aspartyl protease called β-site APP cleaving enzyme 1 (BACE1)[132].

Under physiological conditions, several peptidases contribute to Aβ degradation (insulin-degrading enzyme, neprilysin, and by endothelin-converting enzyme). Aβ levels are balanced by an efflux process, mediated by low-density lipoprotein and influx across the blood–brain barrier[133]. Disease caused by Aβ, comes from an imbalance between the production and clearance of Aβ, leading to its accumulation and consequent neuronal degeneration. When mutations occur at the level of APP, and key enzyme related like Presenilin, the levels of soluble Aβ42,

which has higher β-sheet content, increase. This pathogenic Aβ is still soluble but is more probable to aggregate into oligomers.Unfortunately, these oligomers tend to aggregate as well in insoluble fibrils and then in plaques. In this process, the fibrillogenic Aβ42 isoform, produced by the mutations mentioned above, triggers the misfolding of other Aβ species[131].

Regarding the Aβ several studies highlight a possible correlation between deregulation of CK1 and production of Aβ 42. Furthermore, CK1δ mRNA has been shown to be up-regulated in brain samples from subjects with Alzheimer's disease (AD). Another kinase strictly involved in AD pathological mechanism is GSK3, that can phosphorylate its substrates only if they are pre-phosphorylated by a priming kinase; furthermore, CK1 is one of the few known GSK3-priming kinases, remarking how deep is CK1 family involved in neurodegenerative diseases[134]. Interestingly CK1-specific inhibitors, significantly reduce endogenous Aβ peptide production by selectively interfering with amyloid precursor protein (APP) γ-cleavage. Conversely, overexpression of constitutively active CK1 leads to an increase of Aβ peptide production[134]. The pathogenic formation of Aβ is represented in Figure 18.

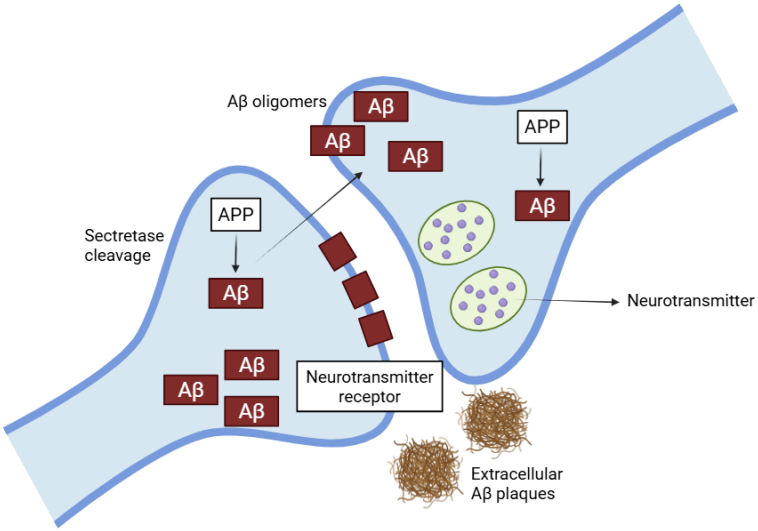

Figure 18: Formation of Aβ fragments and aggregation in extracellular plaques. Image created with ***Biorender.com****.*

1.6.3.2. Parkinson's disease

Parkinson's disease (PD) is a clinical syndrome and degenerative disease, characterized by both motor and non-motor symptoms. Motor manifestations include resting tremors, rigidity, bradykinesia, and postural instability, while non-motor symptoms encompass depression, fatigue, sleep disturbances, and cognitive decline[135,136]. The PD patients, in most cases show characteristic disturbances, these may include vague sensations of numbness or pain without demonstrable sensory loss, as well as descriptions of muscles feeling painful, tender, weak, or stiff[136]. In some cases, early complaints are limited to difficulties with handwriting or an inability to perform repetitive sequential

tasks such as brushing teeth, winding a watch, fastening buttons, or manipulating cutlery. Fatigue is also a frequent symptom, often accompanied by depression and a general sense of slowed activity or weariness. In certain patients, unexplained weight loss may be a prominent early feature[136].

The pathological hallmarks of PD include the degeneration of pigmented brainstem nuclei, particularly the dopaminergic neurons of the *substantia nigra pars compacta*, along with the presence of Lewy bodies (LB), formed by aggregation of α-synuclein, within the remaining neurons. The mechanism of α-synuclein aggregation is represented in Figure 19[137–139].

Misfolded α-synuclein undergoes abnormal phosphorylation, oligomerization, and aggregation, disrupting synaptic function and triggering neuronal death[140]. Among the post-translational modifications, phosphorylation is the most related to pathological implications. In fact, under normal conditions only 4% of α-synuclein is phosphorylated at Ser129, while in patients suffering from synucleinopathies, more than 90% of the protein is phosphorylated[141] . In healthy neurons, phosphorylation of Ser129, is considered important for the physiological uptake of dopamine. Thus, phosphorylation of α-synuclein is a key regulative mechanism of its function[142].

Recent studies have highlighted the role of C K1δ in PD pathogenesis. CK1δ phosphorylates α-synuclein at specific

residues, influencing its aggregation propensity and toxicity. Another key residue is the tyrosine 125, located in close proximity of Ser129, and it has been observed that a priming phosphorylation of Tyr 125, increases the possibility to phosphorylate Ser129[142,143].

Since altered CK1δ activity has been associated with increased α-synuclein pathology, linking this kinase to the molecular cascade underlying PD progression it emerges as a potential therapeutic target. Besides pathological implications of α-synuclein, also Parkin proteins are involved in PD development, and even this key regulator is a CK1δ target[144].

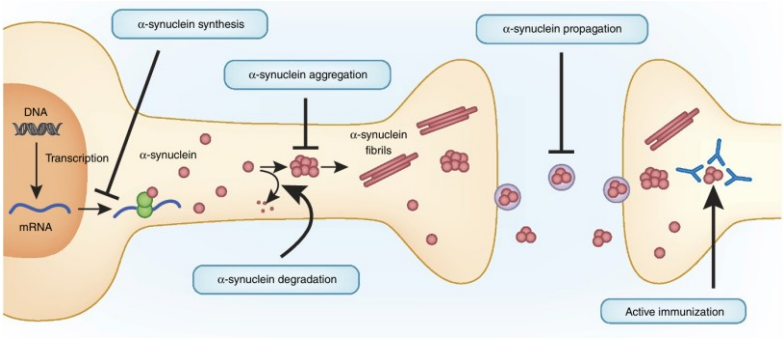

Figure 19:Mechanism of α synuclein aggregation[140].

1.6.3.3. Amyotrophic Lateral Sclerosis

Amyotrophic lateral sclerosis (ALS) is a fatal neurodegenerative disease that involves motor neuron and motility of the affected organism. Initially ALS was classified

as a motor neuronal disease, but now it is considered a complex multisystem disease, that includes both motor and non-motor disturbance. ALS presents as a combination of upper motor neuron (UMN) and lower motor neuron (LMN) dysfunction, affecting the bulbar, cervical, thoracic, or lumbar segments. This dysfunction leads to progressive weakness of voluntary skeletal muscles involved in limb movement, swallowing (dysphagia), speaking (dysarthria), and respiratory function[145,146].

In patients with ALS, frontotemporal dementia (FTD) is observed in approximately 10–15% of cases, though broader cognitive or behavioral impairments are evident in up to 50%, reflecting a clinical continuum between ALS and FTD[147].

Besides genetic causes, several non-genetic factors have been implicated in the pathogenesis of ALS. These include oxidative stress, excitotoxicity, mitochondrial and proteasomal dysfunction, impaired RNA metabolism, altered synaptic activity, disrupted axonal transport, and chronic neuroinflammation[148].

Although the mechanism that led to pathology are not fully understood, one of the major hallmarks of the disease, detectable from the earliest stages, is the abnormal behavior of the transactive response DNA-binding protein 43 kDa (TDP-43). TDP-43 is an RNA- and DNA-binding protein, encoded by TARDBP gene on chromosome 1, and plays a role in multiple

cellular processes, including transcription, pre-mRNA splicing, microRNA maturation, RNA transport, and stress granule formation. Consistent with its diverse nuclear and cytoplasmic roles, TDP-43 is able to shuttle between the nucleus and the cytoplasm, although under physiological conditions its localization is predominantly nuclear[146,149].

Mutations in TDP-43 transcription gene, caused by genetic conditions, is also responsible for familiar ALS, highlighting that TDP-43, is not only a hallmark of the disease but also drives its development[150].

Most of the processes regulated by TDP-43 rely on its ability to bind specific sequences in RNA. This function is mediated by its two highly conserved RNA-recognition motifs (RRM1 and RRM2)**,** which preferentially interact with (UG)n-enriched sequences[151]. The nucleocytoplasmic shuttling of TDP-43, represented also in Figure 20 is controlled by a nuclear localization signal (NLS) located within the N-terminal region and a nuclear export signal (NES) within RRM2[152]. In addition to these domains, the N-terminal and C-terminal regions play essential roles in protein–protein interactions, which are crucial for TDP-43's normal function and are also responsible of the aggregation properties of the protein[149,153].

Since its ubiquitous functions, the protein is tightly regulated, first of all TDP-43 controls its own expression through a

negative feedback loop. TDP-43 binds to the 3′-UTR of its mRNA, leading to nonsense-mediated decay (NMD)-independent mRNA degradation and a decrease in the cellular levels of TDP-43[154]. On the other hand, control of TDP-43, function, localization and levels are influenced by post-translational modifications, and the disruption of its regulation may lead to proteinopathies[154].

The pathological conditions of TDP-43 are a consequence of its hyperphosphorylation, ubiquitination, and fragmentation in portions of ~25 and ~35 KDa (generated through proteolytic cleavage via (Caspases 3 and 7 after Asn89, and Caspase 4 after Asn174) that promote aggregation and toxicity[155,156]. In fact, phosphorylation at multiple sites in the C-terminal domain of TDP43 were identified and they were found to accumulate in brains affected by FTLD-TDP and ALS[156,157]. Besides ALS and FTD, immunohistochemical examination found abnormal accumulation of pTDP-43 also in parkinsonism dementia complex of Guam[158–160], Alzheimer's disease with Lewy bodies (DLB), Pick's disease and hippocampal sclerosis[157,161].

The most common site to be phosphorylated, which an indicator of the disease is at serine 409 and 410 (Ser409/410)[156,162].

In this context, CK1 family, and in particular CK1δ has been observed to directly phosphorylate TDP-43[163].

In the work of Nonaka *et al*, it has been proved that an abnormal activity of CK1δ, in particular its over activity is linked not only to the production of pTDP-43 but also cytoplasmic mislocalization and aggregation of TDP-43 most effectively among the tested kinases. CK1δ 1-317-induced intracellular phosphorylated TDP-43 aggregates were found to serve as seeds for TDP-43 aggregation in cells[163].

Recent findings have demonstrated that TDP-43 exhibits prion-like characteristics, whereby misfolded aggregates can act as seeds to induce conformational changes in native TDP-43 proteins. This seeding process facilitates the propagation of pathological TDP-43 aggregates across interconnected neural systems. In general, prion-like behavior is defined by the capacity of misfolded protein aggregates to serve as templates, converting structurally similar native proteins into pathological

conformations, thereby promoting the spread of proteinopathy within neural networks[164,165].

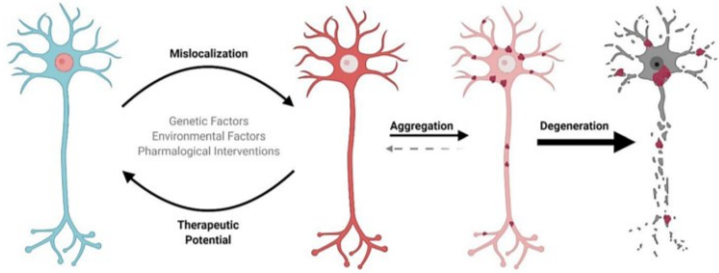

Figure 20: This illustration shows the pathological cascade of TDP-43 toxicity, where cytoplasmic mislocalization and aggregation progressively disrupt neuronal integrity, ultimately leading to neurodegeneration and cell death[156].

1.7. Comparison between selective and pan-kinase inhibitors

Protein kinases represent one of the largest and most versatile druggable families in the human genome, playing fundamental roles in cellular signaling and regulatory networks. Therefore, numerous kinase inhibitors have emerged both as potential therapeutic agents and as valuable molecular probes. Broadly, these compounds can be classified according to their mode of action into selective inhibitors, which target a single kinase or a narrow subset of kinases, and pan-kinase or multi-kinase inhibitors, which modulate multiple kinases simultaneously. Narrow-spectrum inhibitors offer several advantages, including

reduced off-target activity, improved tolerability, and clearer interpretation of the mechanism of action. These features make them particularly valuable during target validation or for elucidating the biological contribution of a specific kinase to a given phenotype[166,167].

Conversely, broad-spectrum inhibitors, despite their inherent lack of selectivity and the increased risk of undesirable off-target effects, may be advantageous in specific therapeutic contexts. Their polypharmacology can enhance efficacy in complex and heterogeneous diseases—such as cancer or inflammatory disorders—where multiple dysregulated pathways contribute to disease progression[168,169]. However, this lack of selectivity often correlates with higher toxicity and complicates the attribution of biological outcomes to individual kinase targets[170].

For these reasons, the design of kinase inhibitors must account for both disease complexity and the desired therapeutic window, aiming for an optimal degree of selectivity that balances efficacy with safety[171].

1.8. Known approved selective inhibitors

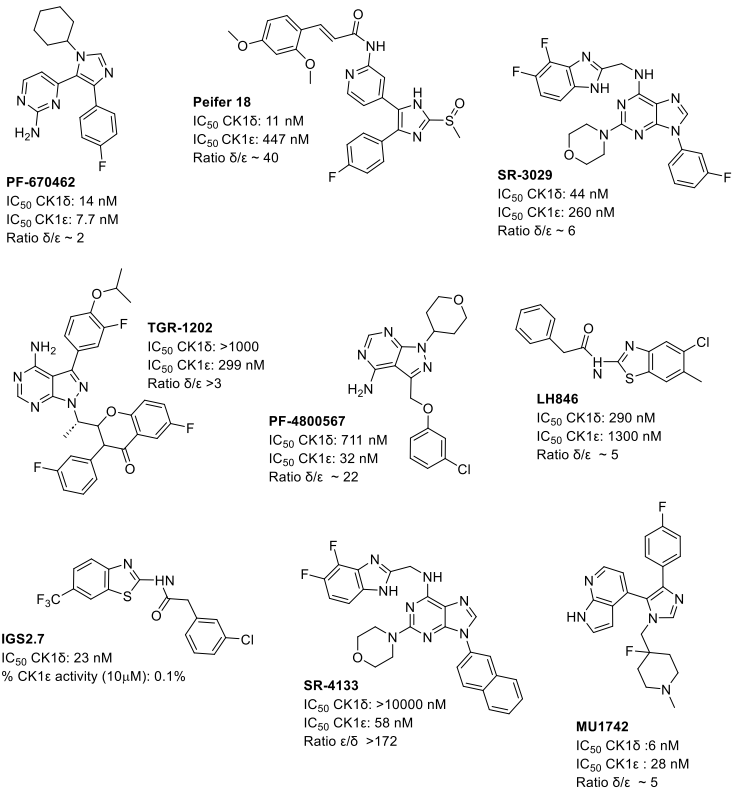

Figure 21: Most potent isoform δ and ε selective inhibitors and the ratio between their activities on δ/ε.

Kinases, and in particular Casein Kinase 1 δ, have emerged as promising therapeutic targets due to their critical roles in diverse cellular processes and their involvement in multiple pathological conditions. Over the past decade, substantial efforts have been directed toward the development of small-

molecule kinase inhibitors. Nevertheless, despite encouraging progress, no approved drugs currently exist that are capable of halting or reversing the progression of neurodegenerative diseases. Therapeutic approaches remain largely palliative, alleviating symptoms without addressing the underlying pathology. Moreover, although several inhibitors have demonstrated high activity against their intended targets, none have successfully advanced to clinical trials, as most have failed during preclinical evaluation[48].

Over the years, several CK1δ inhibitors have been developed; however, many of them suffer from limited selectivity due to the high degree of homology within the kinase domain across CK1 isoforms. This issue is particularly pronounced for CK1δ and CK1ε, which share 98% structural similarity and differ by only seven amino acids. Such minimal variation poses a significant challenge for drug development, as inhibitors designed to target CK1δ often display cross-reactivity with CK1ε, thereby reducing specificity and increasing the risk of off-target effects. Thus, developing selective Casein Kinase 1δ inhibitors is still challenging. Development of isoform selective pharmaceutical tools could also be useful to address specific effects on CK1δ, leading to valuable therapeutic strategies for neurodegenerative disease[25].

Considering the high homology between paralogs δ and ε, in the last years there was an increasing interest in selectively targeting one of the two isoforms. While in literature can be found ε - selective inhibitors, unfortunately it lacks in δ selective ones. In Figure 21 are reported the most active and selective inhibitors developed in the last years. Among them, PF-670462, MU1742 and Peifer 18 are imidazole base inhibitors displaying high potencies towards CK1δ, respectively 14 and , 6 and 11 nM IC_{50} values have been reported, however the first two are as well potent on CK1ε, but Peifer 18 shows great selectivity towards δ and it is the most selective inhibitor reported up to now, reporting a 40-fold selectivity directed to δ[50,59,172]. In spite of its poor selectivity, PF-670462 is still one of the most pharmacological tools used to study CK1δ's role in its different pathological implications, and demonstrated good effects in recovering from circadian rhythm disturbs[173,174].

Regarding the adenine derivatives, SR-3029 exhibits good activity towards CK1δ, and it is slightly selective, with a ratio between the activities of 6 times, in favor of isoform δ respect to ε, on the other hand, TGR-1202 and SR-4133, are potent and epsilon selective inhibitor, with the last one showing 172-fold selectivity towards ε[25,175–177]. Among the benzothiazoles LH846 and IGS2.7 have IC_{50}s in the nanomolar range. The first one, developed as therapeutic tool to treat circadian rhythm disturbs, exhibits a 5-fold selectivity with preference on paralog δ, while

the second one resulted active also on isoform ε when tested at a concentration of 10 μM. IGS2.7 demonstrated also a capability to avoid propagation of the proteinopathy caused by the prion-like behavior of TDP43, and its capability to form, tunneling nanotubes (TNT)-like structures responsible for TDP-43 transport in healthy cells[178–181]. The inhibitors reported in the figure highlight the current lack of isoform-selective inhibitors, thereby underscoring an important knowledge gap and offering the opportunity to develop more targeted therapeutic strategies.

2. AIM OF THE PROJECT

Given the central role of CK1δ in regulating diverse biological processes and its implication in several pathological conditions, including neurodegeneration, there is a growing interest in developing selective inhibitors targeting this kinase. However, as highlighted, the high degree of homology within the CK1 family, particularly between CK1δ and CK1ε, has made the discovery of isoform-selective inhibitors highly challenging. This feature limits the possibility to discriminate CK1δ-specific functions *in vitro* and *in vivo* studies, and also limiting the use of possible therapeutic strategies, due to possible off-target effects. Therefore, the aim of this project is to design and develop small molecules ATP-competitive CK1δ inhibitors with high potency and selectivity within the CK1 family.

The starting point of the project was a screening of in-house compounds (**I-IV**) that resulted in the identification of the hit compound **IV** with an IC_{50} of 1.86 μM toward CK1δ (Figure 22). The initial optimization focused at position 5, some other aromatic moieties have been introduced that led to inactive compounds, except the one with the pyridine ring (**V**), that exhibited a inhibitory potency in the nanomolar range (IC_{50} 110 nM), as reported in Figure 22. Compared to the fluorophenyl group of compound **IV**, the pyridine ring is more suitable, as it can interact strongly with the amino acids in the binding pocket.

In fact, for this compound a co-crystal structure with CK1δ was obtained (Figure 23), thus representing the new starting point for this work.

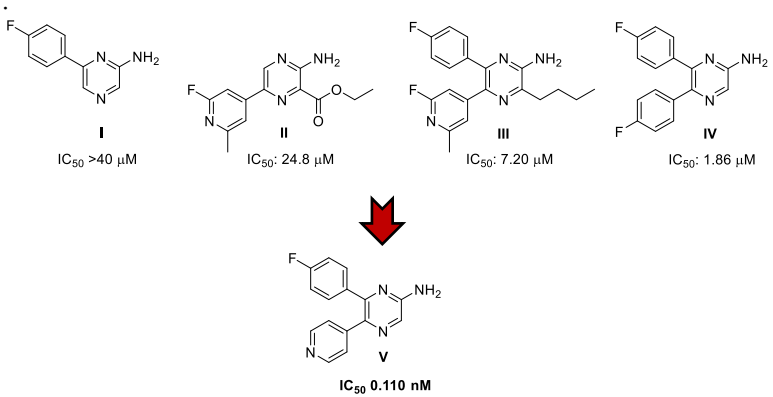

Figure 22: First structure optimization, position 5.

Compound **V** is structurally similar to PF-670462 (Figure 21, IC_{50} = 14 nM). A comparison of their co-crystal structures in Figure 23 reveals that their binding modes are nearly the same: the pyridine ring in compound **V** and the aminopyridine in PF-670462 both interact with Leu85 within the hinge region, while the fluorophenyl moiety in both molecules occupies the hydrophobic pocket. The main structural difference lies in the cyclohexyl group of PF-670462, which protrudes toward the solvent-exposed region of the enzyme in proximity of polar amino acid residues such as aspartates and asparagines. In contrast, compound **V** lacks a substituent in this area, leaving

the corresponding region unoccupied, thus offering the opportunity to target those aminoacids and enhance compounds potencies.

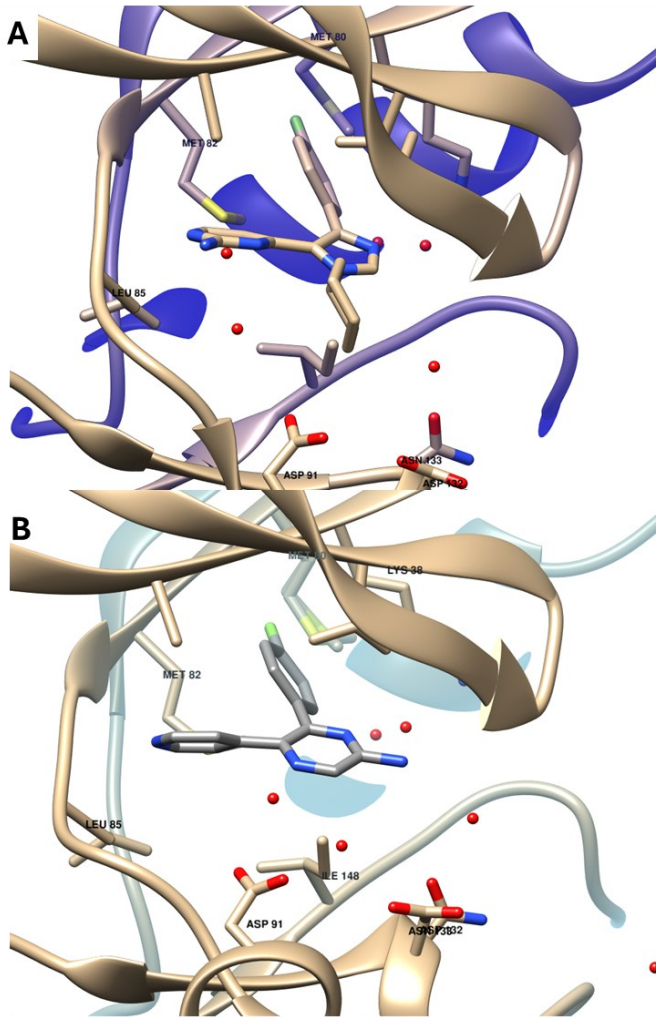

*Figure 23: Comparison between the co-crystal structure of PF-670462 (panel A, PDB:3UZP) and compound **V** (panel B).*

In fact, based on this result, the main aim of this work was to insert a fourth substituent on the pyrazine core at the 3 position, in order to explore the solvent exposed portion of the enzyme, like cyclohexyl moiety in PF-670462. Regarding this, a wide variety of substituents are considered, bearing both polar and hydrophobic groups (Figure 24). Additionally, positions 2 and 6 are also investigated in order to expand the structure-activity but also the structure-selectivity relationship profiles of these compounds (Figure 24). In particular at position 2 to interaction made by the free amino group can be investigated by substituting it with a methylamino or a dimethylamino group. While at position 6, due to the inactivity previously observed with the unsubstituted phenyl ring in compound **VI** (Figure 24), compounds bearing one or more substituents on the phenyl ring are designed, but different in nature or position respect to the parent compound **V**.

Another aim of this PhD thesis is to deeply characterize the resulting most potent inhibitors. Considering biochemical, biophysical validations and also *in vitro* and *in vivo* biological evaluation in models of neurodegeneration.

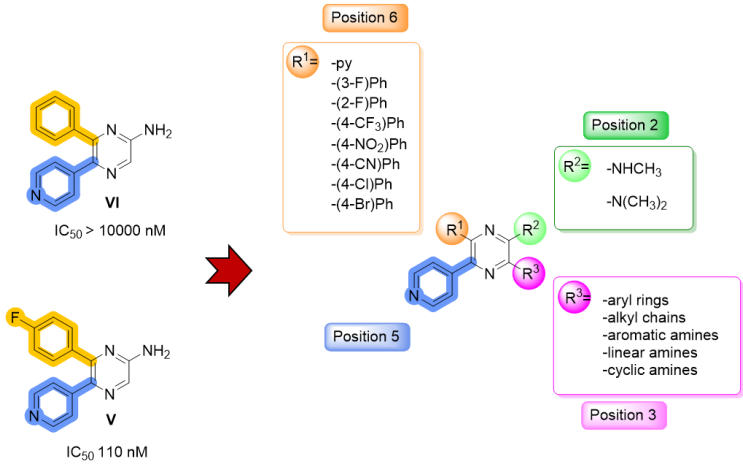

Figure 24: Overview of the designed series to explore the pyrazine scaffold for the developmentCK1δ inhibition.

3. RESULTS AND DISCUSSION

3.1. Chemistry

In order to synthesize the designed compounds, we exploited the versatility of the pyrazine nucleus, that can be easily decorated at position 2,3,5,6 through Suzuki Miyaura Cross coupling reactions, halogenation reactions and nucleophilic aromatic substitution. Pyrazines are highly present in a lot of bioactive molecules, several approved drugs and compounds in advanced clinical trials. This is due to the fact that pyrazine can interact in multiple ways within the binding pockets of different targets, through hydrogen bonding as acceptors, π-interaction with the aromatic ring and coordination bond thanks to the two nitrogen atoms[182].

Starting from compound **V** the idea of the project is to move the investigation from trisubstituted pyrazines to tetrasubstituted ones, in order to explore the chemical space around position 3, keeping the pyridine moiety at position 5, that resulted as promising substituent from previous structure optimization.

To this end, different types of substituents were explored, including both aromatic and polar groups, such as phenyl rings, differently substituted ammines, linear alkyl chains (compounds **1-21,** represented in Figure 25). In this context, we decided to maintain the previously developed synthetic strategy used to obtain the trisubstituted parent compound **V**, then perform

bromination reaction at position 3, to obtain compound **26**, followed by a nucleophilic aromatic substitution to introduce the desired moiety on the same position.

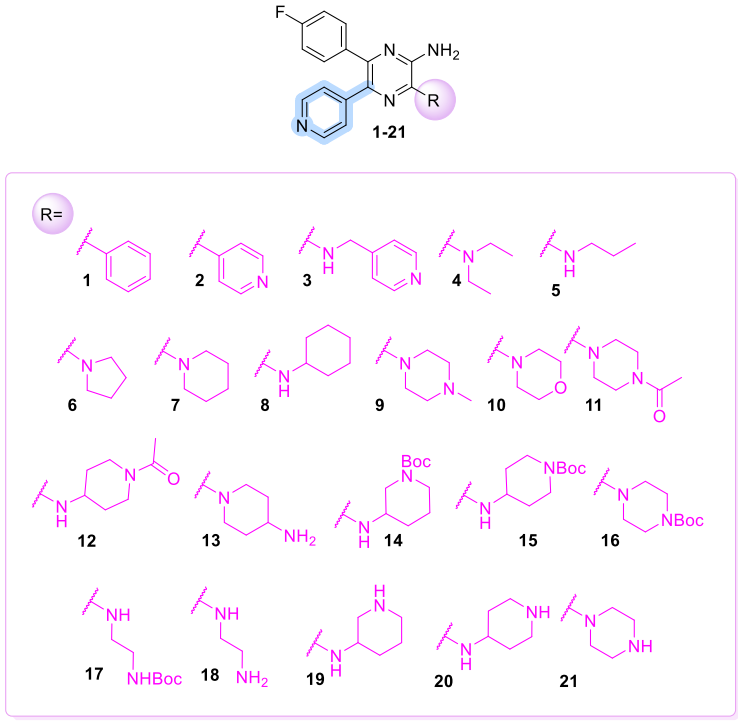

*Figure 25: Synthesized compounds, starting from compound **V**.*

3.1.1.Investigation at position 3

The synthetic strategy adopted for this project, in particular pathway 1, started from the 2-amino-6-chloro pyrazine (**22**), commercially available, on which a first Suzuki Miyaura Cross Coupling reaction was performed to introduce the 4-

fluorophenyl moiety, leading to compound **23**. The reaction occurs in presence of sodium carbonate as base and tetrakis(triphenylphosphine)palladium(0) as the metal-based catalyst.

The Suzuki reaction was followed by a bromination reaction, as represented in Scheme 1. The bromination reaction is not regioselective and leads to the obtaining of multiple products, the two mono-brominated derivatives (**24**, **25**) and a low percentage of the bis-brominated compound. The initial reaction conditions consisted in purging a three necked round bottomed flask with Argon and under vacuum, to introduce then compound **23** and dry dichloroethane (DCM) to obtain a homogeneous solution. The system was then cooled in ice bath and N-bromosuccinimide (NBS) was introduced portionwise to the mixture. Terminated the adding the system was warmed at room temperature for at least one hour. In these conditions the main product resulted in the 3-monobrominated (**25**) derivative with a yield between 53% and 62%.

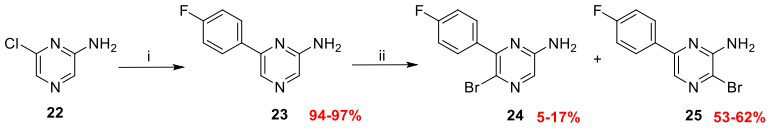

*Scheme 1: reaction scheme for the synthesis of compound **24** and **25**. Reaction conditions: i) 4-fluorophenylboronic acid, Na_2CO_3 (2M), $Pd(PPh_3)_4$, dry Toluene, Ethanol, Water, Ar, Rflx. ii) NBS, DCM, 0 °C→RT.*

Since solubility issues were observed during the reaction setup, and in order to increase the yield of the most interesting and useful isomer (**24**) the reaction has been optimized by changing the solvent, the temperature and the mode of addition of NBS was performed.

Regarding this, using dimethylformamide (DMF) under molecular sieves to solubilize the starting material and adding the NBS as solid, portionwise to the cooled mixture, slightly increased the amount of the 5-monobrominated derivative (**24**), with a yield around 30%, but still leading to the 3-bromoisomer (**25**) as main product (yield 40%). Upon changing the solvent to dry acetonitrile (ACN), the regioselectivity of the reaction was altered, leading predominantly to the formation of the 5-bromoderivative (**24**), the desired compound, as the major product, with a 45% yield. Nevertheless, the overall yield remains relatively low, and further optimization of the reaction parameters will be undertaken to enhance the formation of the desired product. Another approach tried was increasing the temperature and using the microwave reactor to perform the reaction and using ACN as solvent. In this case, the NBS was directly introduced in the microwave reactor tube, and the system heated at 50 °C for 30 minutes. This strategy led basically only to the 3-brominated derivative (**25**), with a yield around 80% and only 6% of the 5-bromoisomer (**24**). Basing the further step of the optimization on what we observed, we

noticed that increasing the temperature leads almost completely to the 3-bromoderivative, while cooling the system until reaction completion and using a more polar and aprotic solvent like ACN drives the regioselectivity to position 5. Basing our consideration on our results, it seems that the 3-bromoderivative (**25**) is the thermodynamically favored product while the isomer with the bromine atom in 5 is the kinetically favored one. We also noticed some solubility issues of the starting materials in ACN so what we decided to do is to solubilize the starting material in dry DCM, and the NBS in dry ACN, cool the system and let the NBS solution drop in the mixture. This approach was the most promising one and led to the desired compound as main product and with a quite good yield around 60%.

In Table 1 are represented the conditions tried and the relative yields of the 5- and 3- brominated compounds (**24, 25**).

Table 1: Optimization of the Bromination reaction, including yields, solvents, Temperature and time conditions.

Solvent	**T(°C), time (hours or min)**	**NBS**	**Cmpd 24**	**Cmpd 25**
Dry DCM	0°C→RT, 1 hour	Solid, portionwise	5-17 %	53-62 %

Dry DMF	0°C, 30 min	Solid, portionwise	29 %	40 %
Dry ACN	0°C→RT, 1 hour	Solid, portionwise	45 %	30 %
Dry ACN	50°C (MW), 2 hours	Directly in the MW tube	6 %	81 %
Dry DCM/ACN*	0°C	Liquid, dropwise	60 %	29 %

Dry DCM was used to solubilize the starting material (23**), while ACN under molecular sieves to solubilize NBS.*

The two isomers were isolated by column chromatography on silica gel, and the products have been characterized using mass (MS) spectrometry and nuclear magnetic resonance (NMR) spectroscopy. In order to identify the two regioisomers, two dimensional (2D) ^{1}H-^{1}H NOESY (Nuclear Overhauser Effect SpectroscopY) experiments were conducted. The experiment is based on the Nuclear Overhauser Effect (NOE) that occurs from dipole–dipole interactions between spatially close nuclei, providing information about through-space proximity and molecular geometry. In panel A, Figure 26, is reported the spectrum of compound **24** and it can be observed the presence of cross-peaks, as result of magnetization transfer between the hydrogen bonded at position 3 of the core and the hydrogens of the amino group. On the other hand, in panel B on the same

figure (Figure 26), reporting the NOESY spectra of the other bromo derivative (**25**) it can be observed only the NOE effect between the hydrogen bonded to the core at the 5-position and the fluorophenyl ring, thus allowing us to distinguish between the two isomers.

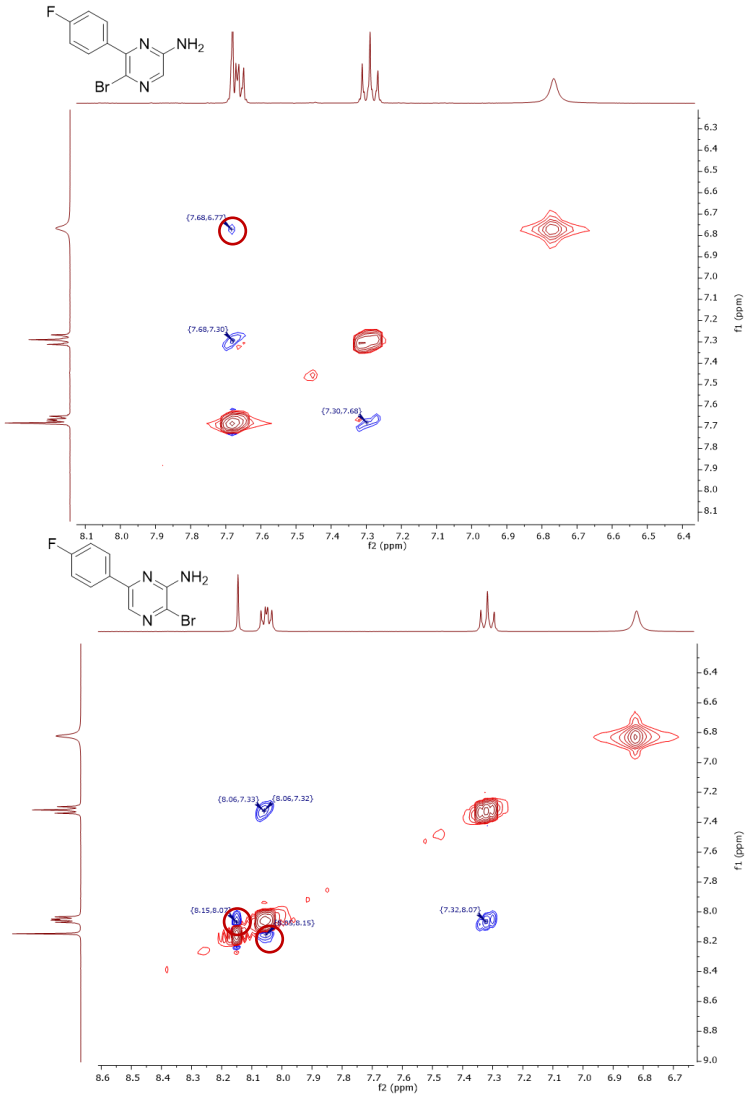

*Figure 26: panel A) 2D-NOESY of the 5-monobrominated compound (**24**). Panel B) 2D-NOESY of the 3-bormoderivative (**25**).*

5-bromo intermediate (**25**), was subsequently used in a cross-coupling reaction to introduce the pyridine moiety, affording compound **V** with a yield of approximately 50%. At this stage, the molecular shape evolved from a tear-drop like scaffold to a cross-shaped inhibitor, through bromination at position 3 to obtain compound **26**.

Starting from this bromoderivative (**26**), a series of substitutions were carried out to explore the chemical space around position 3 and to assess how structural modifications influence biological activity. Specifically, both aromatic and aliphatic substituents were introduced, including simple alkyl chains and more polar amino-containing groups, as illustrated in Scheme 2.

To introduce aromatic moieties, compound **26** was subjected to a Suzuki–Miyaura cross-coupling reaction with phenylboronic acid, yielding compound **1**, and with 4-pyridylboronic acid, leading to compound **2**.

In contrast, to obtain more polar derivatives, nucleophilic aromatic substitution reactions were performed using an excess of the desired amine in ethanol/butanol as solvent. The reactions were carried out in sealed tubes and heated at 110–120 °C for at least 12 hours leading to compounds **3-5** and **7-17**.

For some amines, the reactions afforded the desired products in low yields, likely due to the reduced nucleophilicity of the amine reagents involved. This aspect is particularly relevant for

the introduction of tert-butyl 3-aminopiperidine-1-carboxylate (**14**) tert-butyl 4-aminopiperidine-1-carboxylate (**15**) and tert-butyl (2-aminoethyl)carbamate (**17**), which possess a primary amino group, unlike the other amines used in this study that are secondary and therefore more nucleophilic. To ensure sufficiently basic conditions and maintain the amines in their nucleophilic form, triethylamine was added to the reaction mixture; however, no improvement in product yield was observed. Instead, to obtain compound **13**, we first deprotected the amine and then performed the nucleophilic aromatic substitution to introduce the desired group, considering that the bond with the secondary amino group is favored than the primary one.

Finally, the tert-butyloxycarbonyl (Boc) protected amines (**14-17**), which were initially introduced in their protected form to minimize side reactions and simplify the purification step, were successfully deprotected, restoring the polar amino functionality, using Hydrochloric acid in dioxane (4M) and leading to compounds **18-21** as hydrochloride salts.

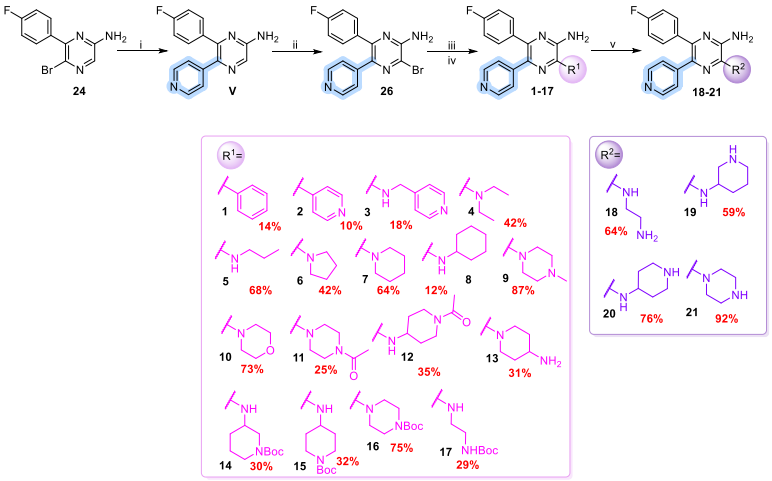

Scheme 2: Synthesis of the pyrazine's based inhibitors, focusing the optimization at position 3. Reaction conditions: i) 4-pyridylboornic acid, Na_2CO_3, $PdCl_2(PPh_3)_2$ 1,4-dioxane, EtOH, H_2O, 120°C; ii) NBS, ACN, DCM; iii) phenylboronic acid/4-pyridylboornic acid, Na_2CO_3, $Pd(PPh_3)_4$ 1,4-dioxane, EtOH, H_2O, 120°C, sealed tube; iv) proper amine, EtOH; iv) HCl (4M) in 1,4-dioxane.

To obtain a comprehensive overview of the substituents introduced at position 3 in terms of physicochemical properties, we decided to incorporate a simple alkyl chain, specifically a butyl group, obtaining compound **31**. For this purpose, the 3-brominated isomer (**25**) was isolated and employed in a cross-coupling reaction based on a modified Kumada coupling, namely the Fürstner variant (Scheme 3)[183].

Prior to the coupling step, the amino group was protected with a Boc group to prevent undesired side reactions. The resulting

Boc-protected bromo intermediate (**27**) was then reacted with a freshly prepared butyl magnesium bromide reagent. The transformation was catalyzed by an iron-based catalyst, following the principles of the Kumada coupling, which allows the formation of C–C bonds between organomagnesium halides and aryl halides under mild conditions. The coupling reaction led to compound **28**, the reaction conditions promoted also one Boc group removal.

The obtained butyl derivative (**28**) was subsequently deprotected under acidic conditions to remove the Boc group, regenerating the free amine (**29**). A new bromination reaction was then performed to form compound **30** and enable the introduction of the pyridine moiety at position 5, through a Suzuki–Miyaura cross-coupling reaction, leading to the desired final compound **31**, as represented in Scheme 3.

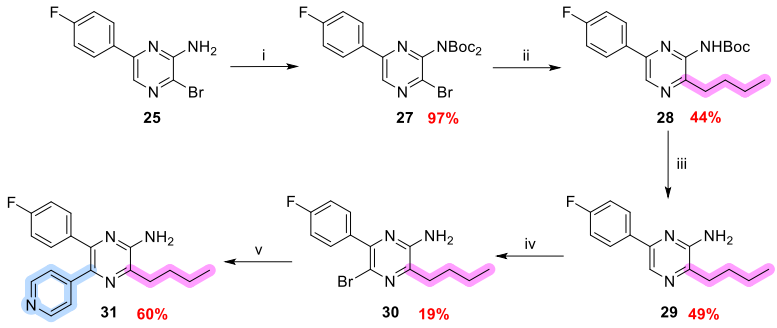

*Scheme 3: Reaction pathway for the synthesis of compound **31.** Reagents and conditions: i) di-tert-butyl-dicarbonate, tetrahydrofuran (THF), 0 °C, 4-(Dimethylamino)pyridine (DMAP), rflx, 2h. ii) ButylBr, Mg, I_2, THF, 60°C, 3-*

4h, Ar/ ButylMgBr, Fe(acac)3, THF, NMP, 0°C-r.t., 4h, Ar; iii) HCl (4M) in 1,4-dioxane; iv) NBS, DCM, 0°C, Ar; v) pyrid-4-yl boronic acid, $Pd(PPh_3)_4$, Na_2CO_3 (2eq), 1,4-dioxane, EtOH, H_2O.

3.1.2. Investigation at position 2

Once we defined a partial structure activity relationship (SAR) profile, exploring the chemical space around position 3, we moved the investigation at position 2, by evaluating the role of that free amino group as donor/acceptor of H-bond interactions. In particular we performed a preliminary investigation, by introducing a simple methyl group and two methylene groups while maintaining the most promising substituents at positions 3 and 5. For this purpose, we started again from the 6-chloro-2-amino pyrazine (**22**) and performed an alkylation reaction to introduce the methyl groups to the amino group. The reaction was performed in presence of sodium hydride as base and methyl iodide as alkylatin agent. The reaction is not selective and it is difficult to be controlled, for this reason we obtained both the monomethyl derivative and the dimethyl derivative. The two products were isolated and used separately to introduce the most promising substituents on the other positions.

Methylated compounds (**32**, **33**) were then used to perform a Suzuki Miyaura cross coupling reaction, to introduce the fluorophenyl group (compounds **34**, **35)**. These last two intermediates were then brominated reaction, leading again to the different regioisomers.

In particular, although the reaction conditions were the same as those described in paragraph 3.1.1, the bisbrominated compound was also obtained as a byproduct. Once again, NMR spectroscopy proved to be a powerful and reliable tool for distinguishing the isolated products. During the purification step, two different fractions were isolated.

From the 1D ^{1}H NMR, of the first fraction reported in Figure 27 it is clearly noticeable the presence of more than one compound. And by the integrals of the peaks, the presence of the bisbrominated compound has emerged as indicated by the absence of an aromatic singlet, and a monobrominated compound.

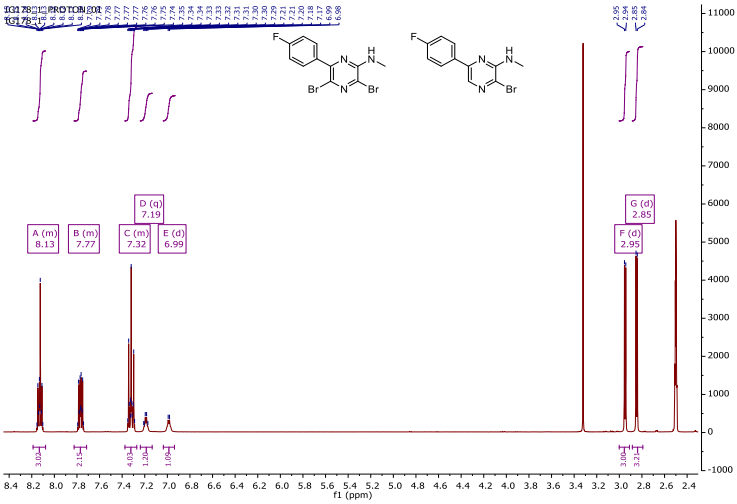

*Figure 27:^{1}H NMR spectra of mixture of compounds obtained from the bromination reaction of compound **34**.*

From the spectra below (Figure 28), it is possible to notice a pattern of signal compatible with the presence of one molecule. The signals, in particular the presence of the singlet at 7.72 ppm, overlapped to the multiplet of the fluorphenyl ring, but still specific of a monobrominated compound.

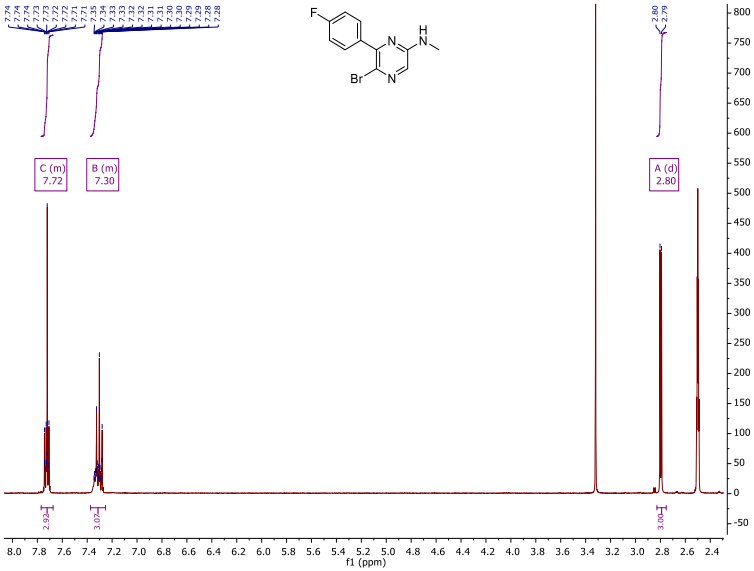

*Figure 28: [1]H NMR spectrum of a monobrominated compound, obtained from the bromination reaction of the methylated compound **34**.*

According to this, this last monobrominated compound was better characterized to assess the position of the bromine atom on the pyrazine core. For this purpose, again the NOESY experiment was performed and confirmed the presence of the 5-brominated regioisomer.

Considering the bis-methyl derivatives, the behavior was slightly different, in fact, from the bromination reaction we isolated only two compounds, which emerged to be a monobromination product and the dibrominated one. NMR helped us again to distinguish the products and identify the regioselectivity of the reaction.

The spectra reported in Figure 29 from one of the products isolated from the reaction, highlights the typical pattern of the fluorophenyl group (signal system A and signal system B), a singlet (C) which integrates for six protons, localized in the aliphatic range and attributed to the two methyl groups on the amine at position 2.At lower magnetic fields, were a singlet belonging to the proton bonded to the pyrazine's core should be, there are only the patterns of the fluorophenyl group. Thus, proving the presences of two bromine atoms in the molecule.

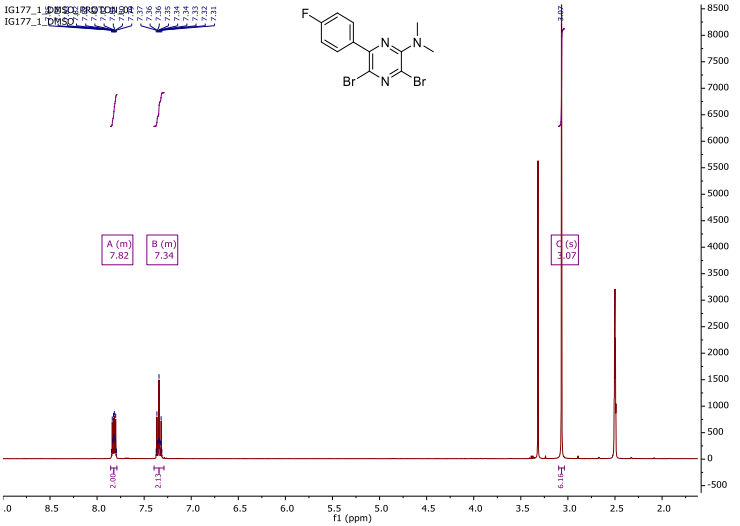

*Figure 29: [1]H NMR spectrum of one product obtained from the bromination of the bis methyl derivative **35**.*

The other fraction isolated from the purification step has been as well characterized using NMR spectroscopy. In this case the presence of a single signal, compatible with the presence of only one bromine atom in the molecule, indicates the isolation of one of the two monobrominated compounds. The spectra is reported in Figure 30.

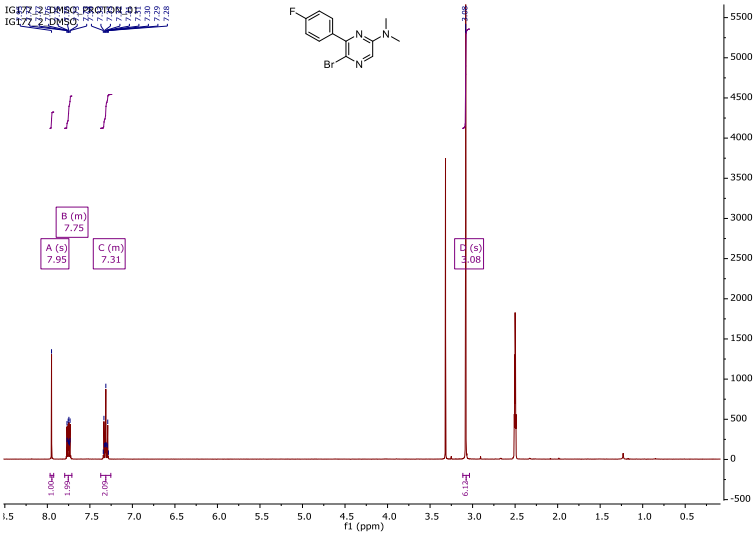

Figure 30: [1]H NMR of the monobrominated isomer, obtained from the bromination reaction for the bismethylated derivative ***35.***

[1]H-[1]H NOESY spectra reported in Figure 31 displays the presence of cross-peaks between the two methyl groups on the nitrogen (3.08 ppm) and the singlet at lower fields (7.95 ppm), confirming the presence of the bromine atom at position 5 on the core. Further proof is the absence of cross-peaks between the singlet and the fluorophenyl system.

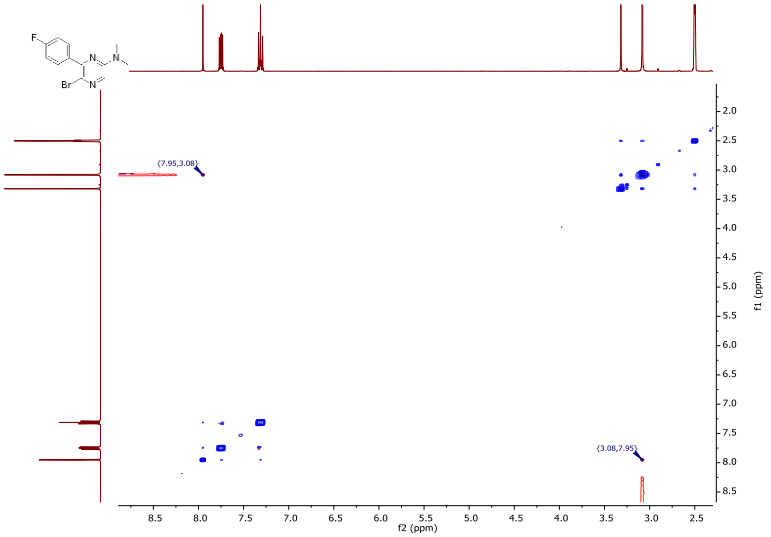

*Figure 31: 2D NOESY of the monobrominated compound obtained from the bromination of compound **37**.*

Moving to the following step, a new Suzuki Miyaura cross coupling reaction on compounds **36** and **37** has been performed leading to the trisubstituted compounds **38**, **39**, with yields of 68% and 63%, respectively. These have been tested as well to compare the activities with the parent compound **V**. Finally, in order to obtain the tetrasubstituted derivatives, a bromination reaction was performed, to introduce the halide at position 3, leading to compounds **40** and **41**. The yields of these reactions are surprisingly high in respect to the reaction performed on the free amino derivatives. At this point a nucleophilic aromatic substitution was performed to introduce the most promising

morpholine moiety (**42**, **43**) and the aminopiperidine at position 3 (**46**, **47**). The synthetic scheme is reported in Scheme 4.

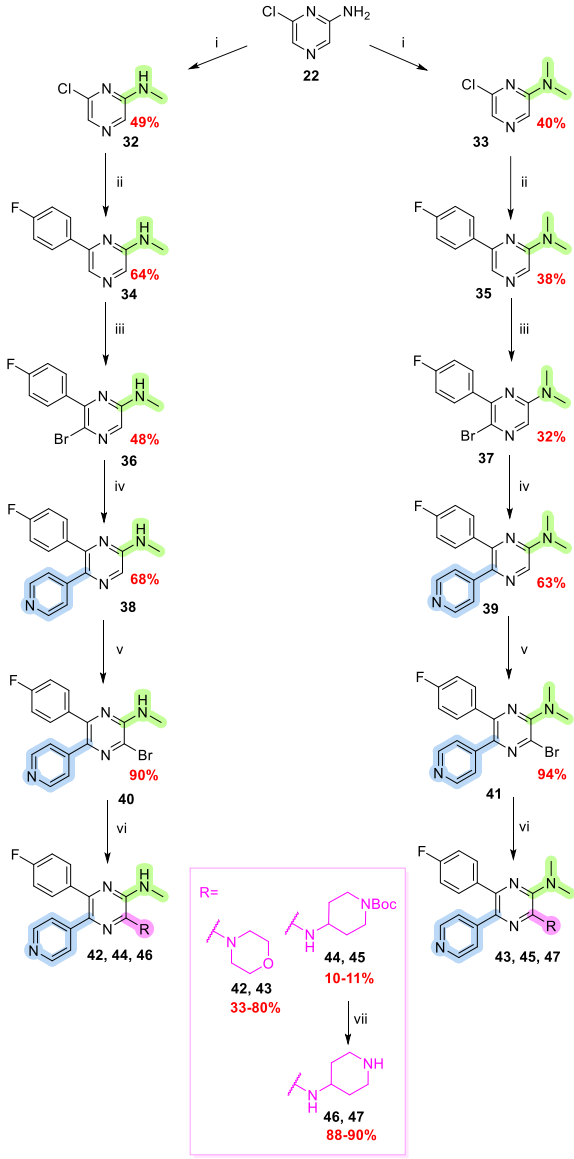

Scheme 4: Synthetic route for the synthesis of compounds ***38, 39, 42-47.*** *Reaction conditions: i)NaH, THF, CH_3I, 0 °C; ii)4-fluorophenylboronic acid, $Pd(PPh_3)_4$, Na_2CO_3 (2M), Toluene, EtOH, 110°C, Ar; iii) NBS, ACN, DCM, 0°C, Ar; iv)4-pyridylboronic acid, Na_2CO_3, $PdCl(PPh_3)_2$, 1,4-dioxane, EtOH, H_2O, 120°C sealed tube; v) NBS, ACN, DCM, 0°C, Ar; vi) amine, EtOH, 120-130°C; vii) HCl in dioxane (4M).*

3.1.3. Investigation at position 6

Based on these findings, the investigation was subsequently extended. At position 6, only the fluorophenyl substituent had been explored thus far, encouraging investigation at this position, in particular studying the role of the fluorine atom on the phenyl group. The fluorine atom has been initially removed leaving a simple phenyl group, but this modification causes the loss of activity of the molecule. Basing the following steps on this result, the fluorine atom has been kept but moved to other positions of the aryl ring, thus synthesizing 3-fluorophenyl derivatives and 2-fluorophenyl derivatives. We then decided to introduce more fluorine atoms, by replacing the fluorophenyl group with the trifluoromethylphenyl substituent, since it is known that the fluorine atom in bioactive compounds may help in improving the pharmacokinetic properties[184]. To further investigate the role of the fluorine atom, different halides have been introduced, in particular *p*-bromophenyl derivatives and *p*-chlorophenyl derivatives were developed, also other groups with increased steric hindrance and different electronic

properties were introduced: nitrophenyl, cyanophenyl, and pyridine groups.

For this purpose, two synthetic pathways have been considered and are reported in Scheme 6, considering two different pathways depending on the substituents that have been introduced. The two ways both started from the 6-chloro-2-aminopyrazine (**22**), the first approach (pathway 1) as already explained in paragraph 3.1.1, proceeds with a Suzuki Miyaura coupling reaction to introduce the functional group at position 6, with this approach the 2- and 3- fluorophenyl substituents were introduced along with the trifluoromethylphenyl derivative (**48-50**). Then a bromination reaction was performed and the two isomers were again separated and isolated (**51-53**), the newly prepared 5-bromoderivatives were used to introduce the pyridine moiety at the same position (**54-56**). This step is followed by a new bromination reaction at position 3 leading to compounds **57-59** and a final nucleophilic aromatic substitution to introduce the most prosing amines (morpholine and aminopiperidine), leading to the final compounds **60-68**.

Instead, Pathway 2 started as well with the commercially available compound **22**, but in this case a bromination reaction was first conducted and the two isomers distinguished through NMR spectroscopy. The first product isolated has been characterized through ^{1}H NMR and it is compatible with a

monobrominated compound, since the presence of a singlet at 7.63 ppm corresponding to a hydrogen bonded to the pyrazine core. The 2D spectrum indicates that probably the compound is the 3-bromo derivative, since there is no NOE effect between the amino group and the proton attached to the core, as shown in the spectrum in Figure 32 (on the top). The other fraction isolated has been as well characterized, and in this case the monodimensional spectrum is again compatible with a monobrominated derivative, but slightly different from the previous one, in particular regarding the resonance of the proton bonded to the core, that results in a singlet at 7.65 ppm and the broad singlet attributed to the amino group at 7.10 ppm. Regarding the bidimensional analysis (Figure 32 on the bottom), the presence of two cross-peaks between the amino group signal and the singlet at lower fields demonstrate the NOE effect between the two systems, thus confirming the positioning of the bromine at position 5 (**69**).

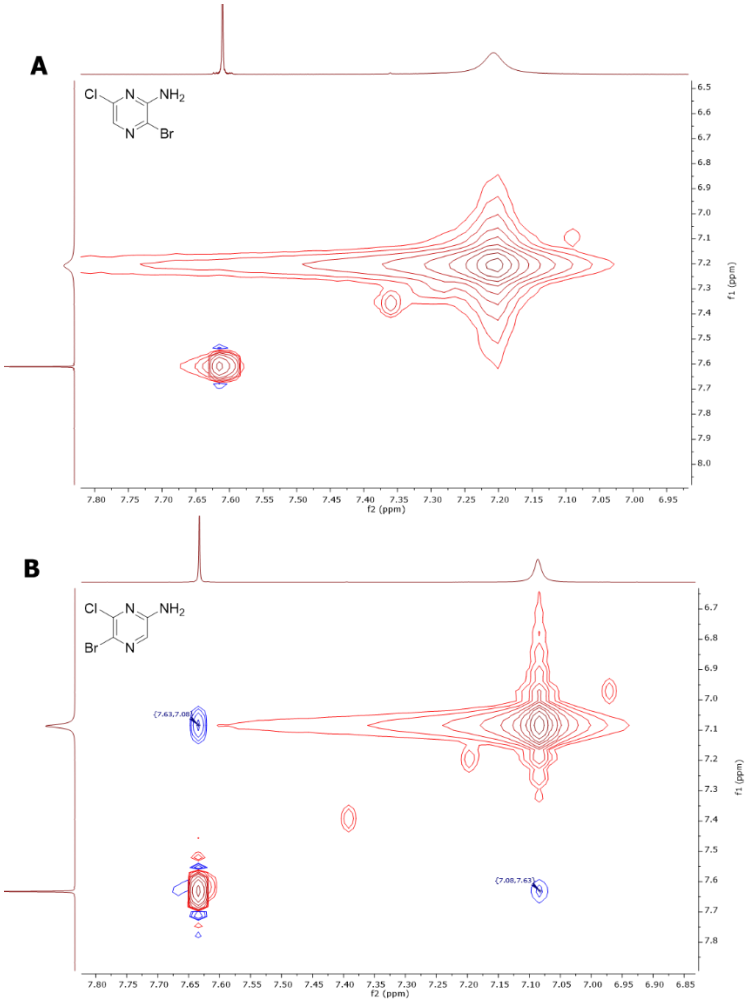

Figure 32: 2D ^{1}H-^{1}H NOESY of the first (on the top, A) and the second product (on the bottom, B) isolated from the bromination of compound ***22****.*

Starting from compound **69**, we exploited the different reactivity of the chlorine and bromine atoms, specifically, the bromine is a better leaving group to perform a first Suzuki–Miyaura cross-coupling reaction with 4-pyridinyl boronic acid under nearly stoichiometric conditions. This enabled the selective introduction of the heteroaromatic ring at position 5 (**70**). After isolating and accumulating the desired intermediate **70**, a second Suzuki–Miyaura coupling was carried out to explore the chemical space around position 6.

This strategy was specifically chosen to introduce bromophenyl and chlorophenyl substituents (**71, 72**) while minimizing possible side reactions. Indeed, following synthetic route 1, at step (iia in Scheme 5) the 4-pyridyl boronic acid could potentially react with both halides in the molecule either two bromine atoms or a bromine and a chlorine, one attached to the pyrazine core and the other on the substituent at position 6. To avoid the formation of undesired side products, we therefore decided to first install the pyridine moiety and subsequently introduce the aryl-halide substituent at position 6. Once compound **70** was obtained, additional groups such as nitrophenyl, cyanophenyl and pyridyl were incorporated, yielding compounds **73**, **74** and **75** respectively. The complete synthetic pathway is shown in Scheme 6.

After obtaining the trisubstituted compounds **71-75** which were subsequently evaluated for their activity on CK1δ, we expanded the synthetic efforts to generate tetrasubstituted derivatives. These were prepared by applying the same sequence of reactions described in paragraph 3.1.1, initially affording the corresponding brominated intermediates (**76-79**), which were then converted into the 3-aminic derivatives (**80-89**).

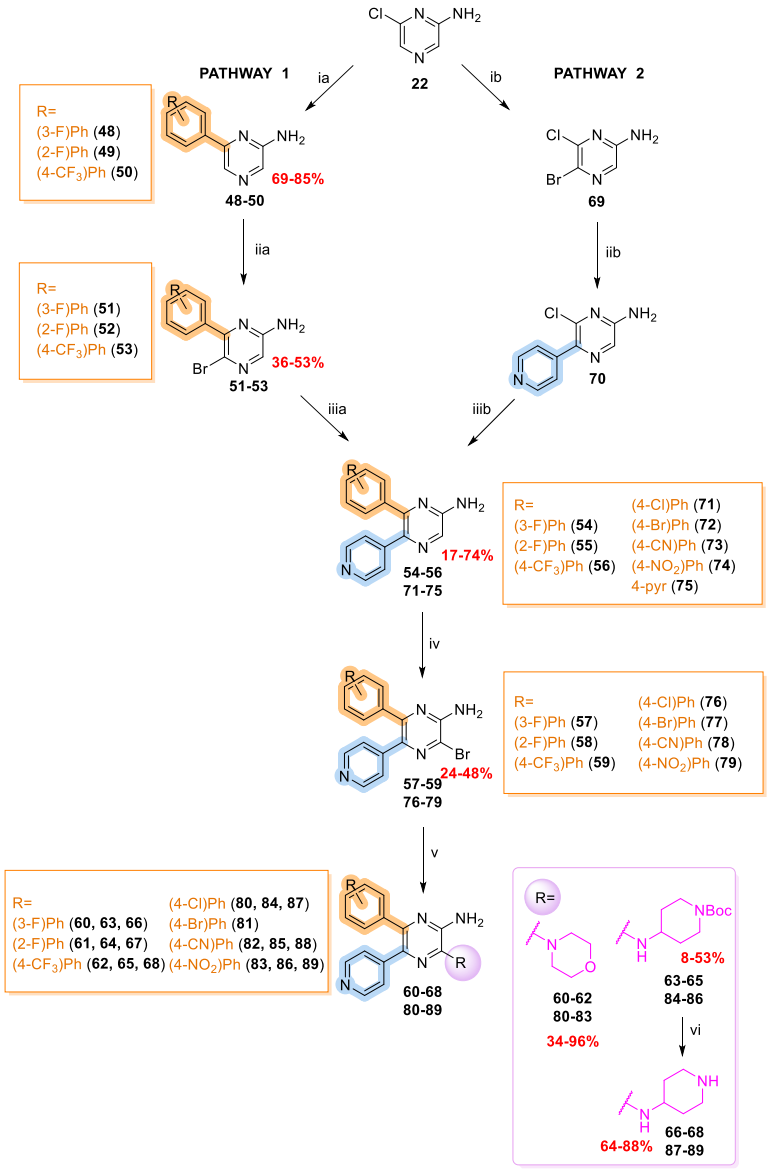

*Scheme 6: Synthetic route for the structure optimization at position 6 (compounds **54-56**, **68-72**, **60-68**, **80-89**). Reaction conditions pathway 1: ia)*

arylboronic acid, $Pd(PPh_3)_4$, Na_3CO_3 (2M), Toluene, EtOH, rflx, Ar; iia) NBS, ACN, DCM, 0°C; iiia) 4-pyridylboronic acid, Na_2CO_3, $Pd(PPh_3)_4$, 1,4-dioxane, EtOH, H_2O, 120°C sealed tube; iv) NBS, ACN, DCM, 0°C, Ar; v)proper amine, EtOH, 120°C, sealed tube; vi)HCl (4M) in 1,4-dioxane; ib) NBS, DCM, 0°C, Ar; iib) 4-pyridylboronic acid, Na_2CO_3, $Pd(PPh_3)_4$, 1,4-dioxane, EtOH, H_2O, 120°C sealed tube; iiib) arylboronic acid, $Pd(PPh_3)_4$, Na_3CO_3 (2M), Toluene, EtOH, rflx, Ar.

3.2. Structure Activity Relationship (SAR)

3.2.1. Enzyme activity assay

All the trisubstituted and tetrasubstituted synthetized compounds (**1-21**, **31**, **38, 39**, **42-45**, **54-56**, **60-68**, **71-75**, **80-89**) obtained from all the multistep optimizations were initially screened on CK1δ, at a concentration of 10 μM, and the % of residual enzymatic activity was measured. Compounds displaying less than 50% of residual enzymatic activity were considered active and their IC_{50}s were also determined. While compounds with a residual activity higher than 50% were considered inactive.

The screening of the compounds was performed using the Kinase-Glo® assay kit (Promega), which is a luminescence-based method relying on a luciferase/luciferin system. After incubation of the plate to allow the enzymatic reaction to occur, the Kinase-Glo reagent was added to stop the reaction. During the kinase reaction, ATP is consumed by the enzyme and ADP is produced. The remaining ATP in each well is then utilized by

luciferase, which oxidizes luciferin to oxyluciferin, resulting in the emission of luminescence. The luminescent signal is proportional to the amount of ATP remaining in the reaction mixture; therefore, a higher signal corresponds to a greater amount of residual ATP, indicating a stronger inhibitory effect of the tested compound on the kinase activity, due to its ability to prevent ATP consumption by the enzyme.

IC_{50} values were instead determined using the ADP-Glo™ Kinase Assay (Promega), which provides a direct measurement of compound activity. Following the kinase reaction, a portion of the ATP is consumed, resulting in the formation of ADP. The assay protocol involves an initial addition of the ADP-Glo Reagent, which depletes any unreacted ATP remaining in the reaction mixture. This step is followed by the addition of the ADP-Glo Detection Reagent, which converts the ADP generated during the enzymatic reaction back into ATP and simultaneously introduces the luciferin/luciferase system. In this way, the measured luminescence signal is directly proportional to the amount of ADP produced, and therefore to the kinase activity, in the presence of the tested compounds. Figure 33 is schematically representing the Kinase Glo and the ADP Glo-based approach.

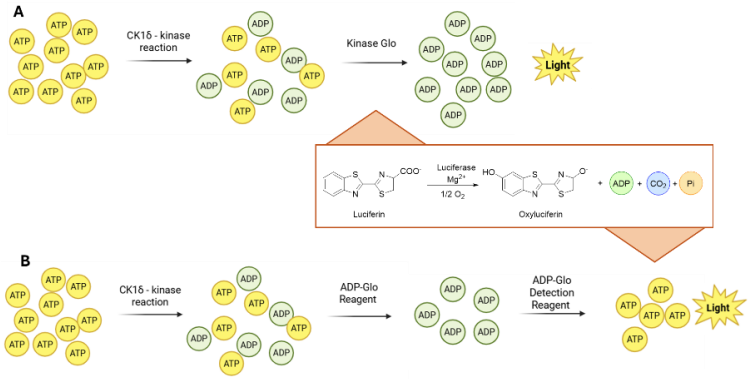

Figure 33: Comparison between Kinase Glo system and ADP Glo system.

Obtained results from the overall structure optimization are reported in Table 2,Table *3* and Table *4*.

3.2.2.Investigation at position 3

Investigation of the substituents at position 3 began with the introduction of a simple phenyl ring (compound **1**), which completely abolished enzymatic inhibition. In contrast, incorporation of a pyridine ring, an heteroaromatic system capable of establishing polar interactions, restored partially the activity, yielding to compound **2**, which is less potent than the parent compound **V**, with an IC_{50} of 318 nM. Extension of the linker between the pyridine moiety and the pyrazine core through the introduction of a 4-(aminomethyl)pyridine (**3**) resulted in a significant enhancement of inhibitory activity, reducing the IC_{50} by half compared with Compound **V**. This observation suggests that increasing the distance of the

heteroaromatic ring can favorably modulate its interaction with the enzyme active site. Obtained results are reported in Table 2.

Table 2: Biochemical results obtained from the investigation at position 3.

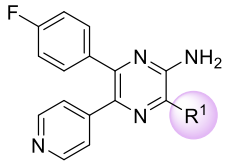

Compound	R^1	Residual Activity %[a] (@10 µM) IC_{50} +/- S.E. (nM)[b]
V		110 ± 24 nM
1		99.6 ± 1.9 %
2		318 ± 102 nM
3	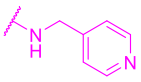	52.7 ± 23.7 nM
4		1180 ± 340 nM
5	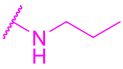	121 ± 47 nM

31		68.9 ± 28.2 nM
18	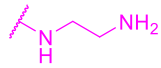	9.03 ± 3.52 nM
6		95.8 ± 46.0 nM
7		51.6 ± 29.3 nM
8	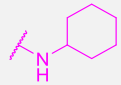	36.7 ± 9.2 nM
21	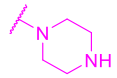	30.0 ± 7.0 nM
9	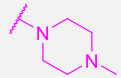	25.0 ± 13.3 nM
11	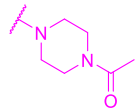	17.5 ± 5.37 nM
10	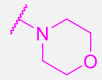	3.15 ± 0.82 nM
19	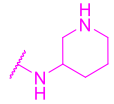	14.9 ± 3.1 nM

20	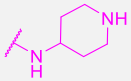	2.62 ± 1.06 nM
13	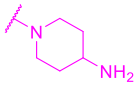	6.43 ± 2.17 nM
12	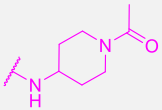	31.1 ± 6.23 nM
17	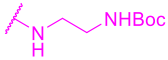	1980 ± 610 nM
14	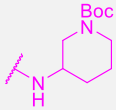	1170 ± 380 nM
15	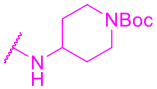	1710 ± 640 nM

[a]Activities are represented as mean +/- Standard deviation and are the result of two independent experiments, each concentration tested in technical duplicate. [b]IC_{50}s are represented as mean +/- standard error and are the result of three independent experiments, each concentration tested in technical duplicate.

Subsequent modifications involving linear substituents mainly focused on amine-containing side chains. The introduction of a diethylamino group (**4**) caused a marked reduction in potency, shifting the IC_{50} into the micromolar range (1.18 µM), exhibiting an activity comparable to the initial hit compound **IV** (1.86 µM). This loss of activity is likely associated with the tertiary nature

of the amine, which prevents efficient hydrogen-bond formation within the binding pocket. To verify this hypothesis, a propylamine was introduced (**5**), affording a secondary amine derivative that regained potency in the high nanomolar range (IC_{50} = 120 nM). Interestingly, replacement with a simple butyl chain (**31**), lacking any polar functional group, still produced an active compound in the high-nanomolar range (IC_{50} = 69 nM). This result indicates that hydrophobic interactions at position 3 can effectively compensate for the absence of polar contacts, highlighting the delicate balance between steric, electronic, and lipophilic factors that govern inhibitor efficiency. Subsequently, we introduced an ethyldiamino linker, bearing two functional groups capable of forming polar interactions with residues within the active site. This modification resulted in a remarkable enhancement of potency, yielding compound **18**, which exhibited an IC_{50} of 9 nM, thus reaching the low-nanomolar range.

Moving to cyclic amines, we introduced for example pyrrolidine and piperidine, leading respectively to compounds **6** and **7**, whose IC_{50}s are 96 nM and 52 nM. Therefore, six membered groups are more favored than five membered ones. In an attempt to confirm the effect of the substituent length on activity; a cyclohexylamine moiety was introduced, which yielded an active compound (**8**) with an IC_{50} of 37 nM, slightly improving the overall potency. Taking example from compound **18** (e.g.

ethylendiamino derivative) we introduced the piperazine ring, mimicking with compound **21** the same distance between the two groups but reducing the flexibility of the pendant. This compound displayed an IC_{50} around 30 nM, surprisingly no strong decrease in the IC_{50} value was observed, probably the increased rigidity of the group fixes the position of the last amino group that is not as efficient as compound **18** to establish polar interactions with the amino acids in the active site. To evaluate the role of the last amino group also the methylpiperazine has been introduced, leading to compound **9**, that basically has the same activity as the demethylated analogue (IC_{50} = 25 nM). Analogously to the effect observed for the methylation of the piperazine ring, we also aimed to evaluate the influence of piperazine acetylation on compound activity, synthesizing compound **11**. The acetylated derivative displayed a lower IC_{50} value (17.5 nM) compared to its non-acetylated counterpart, suggesting that the introduction of the acetyl moiety confers a beneficial effect on binding affinity. This improvement may be attributed to the presence of the carbonyl oxygen of the acetyl group and its correct positioning in terms of distance, which could engage in favorable polar interactions within the kinase active site, potentially acting as a hydrogen bond acceptor and contributing to enhanced stabilization of the ligand-enzyme complex. To further elucidate the role of the terminal amino group, we maintained the cyclic structure of the

substituent while modifying the terminal functionality through the introduction of a morpholine ring. The resulting morpholino derivative (compound **10**) exhibited a marked increase in potency, reaching the low nanomolar range with an IC_{50} value of 3.15 nM, thus ranking among the most active compounds developed in this series. The difference in activity can likely be attributed to the distinct conformation of the morpholine ring, and the unique electronic and steric properties of the oxygen atom in morpholine compared to the terminal secondary amine of piperazine. Considering both the effect of the distance from the pyrazine core and the presence of a terminal polar group, 3-aminopiperidine and 4-aminopiperidine have been also explored, leading to compounds **19** and **20**, respectively. Once again, the positioning of the terminal polar amino group proved to have a significant impact on biological activity. In particular, the 4-aminopiperidine derivative (**20**) emerged as the most potent compound within this first series, exhibiting an IC_{50} value of 2.62 nM, whereas the 3-aminopiperidine analogue (**19**) showed a reduced potency, with an IC_{50} of 14 nM. This difference further supports the importance of the spatial arrangement of the polar group, which likely enables more effective interactions within the kinase active site when located in the 4-position. Regarding this we also decided to introduce the 4-aminopiperidine attaching the group through the secondary amine and leaving the $-NH_2$ in the terminal position

(compound **13**). Compound **13** is still one of the most active compounds included in this series of inhibitors (IC_{50} of 6.43 nM) but is less active than its analogue with the terminal endocyclic NH (**20**, IC_{50} = 2.62 nM).

Again the 4-aminopiperine has been acetylated (**12**) to see if modifying the secondary amine in a tertiary one and placing the carbonyl oxygen further contributes to increasing the potency, as for the acetylated piperazine derivative (**11**). In this case, contrary to the acetylpiperazine derivative (**11**), the modification led to the opposite effect on activity, in fact, compound **12** displayed an IC_{50} of 31 nM. Also Boc-protected amino derivatives (**14-17**) have been tested to evaluate the tolerance of the active site towards more steric hindered group like the *tert*-butyl pendant, and they all displayed potencies in the micromolar range, thus comparable to the first hit compound. The higher IC_{50}s are probably the result of clashes between the residues located in the catalytic pocket and the protective groups. The results are reported in Obtained results from the overall structure optimization are reported in Table 2,Table *3* and Table *4*..

3.2.3.Investigation at position 2

Since compounds **10** and **20** emerged as the most promising derivatives from the optimization at position 3, we next investigated position 2 by introducing one or two methyl

substituents on the free amino group, while preserving the most effective substituents identified in the other positions, the pyridine moiety in 5 and the morpholine or aminopiperidine in position 3. Both trisubstituted and tetrasubstituted analogues were then evaluated against CK1δ.

This modification was designed to evaluate how changes in the steric and electronic properties of the amino group could influence the interaction pattern within the kinase active site, potentially modulating compounds potencies. The obtained results are reported in Table 3.

Looking at the trisubstituted derivatives (**38, 39**) and comparing their activities with those of the parent compound bearing a free amino group (**V,** IC_{50} 110 nM), a clear reduction in potency was observed upon introduction of one or two methyl substituents. Upon methylation, compound **38** displayed and inhibitory activity around 500 nM, probably due to the fact that the amino group is less able to establish strong interactions in the active site, while introducing two methyl groups (compound **39**) the nitrogen becomes tertiary and is therefore no longer able to function as a hydrogen-bond donor, leading to a markedly lower potency (IC_{50} = 983 nM), which approaches the micromolar range, consistent with the reduced capability of the tertiary amine to establish stabilizing interactions within the binding pocket.

Considering now the morpholino tetrasubstituted compounds (**42, 43**), an inverse trend has been observed: the monomethylated compound at position 2 (**42**) is less active than the dimethylated analogue (**43**), displaying respectively IC_{50}s of 843 and 484 nM. This inversion suggests that introduction of the morpholine at position 3 changes the local binding geometry and electronic environment so that increased N-alkylation at position 2 becomes beneficial. Interesting to note that for the tetrasubstituted derivatives bearing the aminopiperidine at position 3, compounds **46** and **47** displayed comparable potency on CK1δ, with IC_{50} values of 68 nM and 69 nM, respectively. These results are better than those displayed by the corresponding trisubstituted derivatives **38** and **39**. These data indicate that the effect of N-methylation is strongly context-dependent and that the substituent at position 3 plays a key role in determining how modifications at position 2 influence the overall binding affinity and inhibitory activity.

Comparing now the activities of the methylated (compounds **42** and **46** with respectively IC_{50}s of 843 nM and 68.5 nM) and dimethylated compounds (compounds **43** and **47** with respectively IC_{50}s of 484 nM and 69.4 nM) with their counterpart with the free amino group (compounds **10** and **20**, 3.15 nM and 2.62 nM), all are less potent than the first series of inhibitors, for this reason it has been decided to maintain the

amino group unsubstituted for the following structure optimization.

Table 3:Activity results from the investigation at position 2.

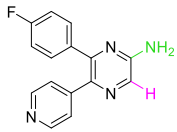

V
IC_{50}: 110 nM

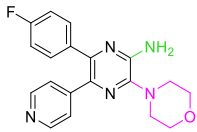

10
IC_{50}: 3.15 nM

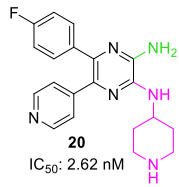

20
IC_{50}: 2.62 nM

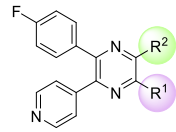

Compound	R^1	R^2	IC_{50} +/- S.E. (nM)
38			517 +/- 149
39			983 +/- 488
42	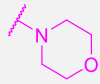		843 +/- 258
43			484 +/- 121
46	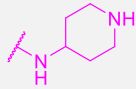		68.5 +/- 13.4
47	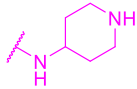		69.4 +/- 16.9

*IC_{50}s of compounds **38, 39, 42, 43, 46, 47**, represented as mean +/- standard error of three independent experiments, each concentration has been tested in technical duplicate.*

3.2.4. Investigation at position 6

Moving the investigation to position 6, and learning from the previous optimization steps, we decided to maintain the amino group at position 2 free, and the most promising substituents at position 3 and 5, thus the pyridine moiety in 5, the morpholine and the aminopiperidine at position 3. As for the previous developed inhibitors, both trisubstituted and tetrasubstituted derivatives were tested on CK1δ (Table 4).

Table 4: biochemical results of the 6-subtituted pyrazine derivatives.

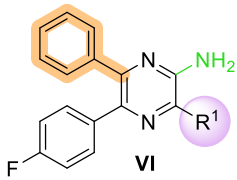

VI

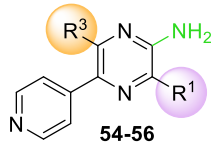

54-56
71-75
60-68
80-89

Cmpd	R^3	R^1	**Residual activity % (@10µM)[a]** **IC_{50} +/- S.E. (nM)[b]**
VI	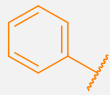		61.5 ± 3 .9 %
75	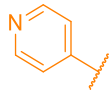		43.8 ± 0.954 %
54	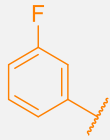		680 ± 169 nM
55	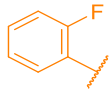		476 ± 76 nM

56	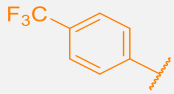		51.7 ± 7.8 %
74	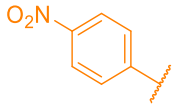		655 ± 236 nM
73	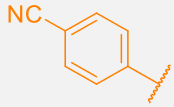		50.5 ± 22.9 nM
71	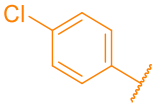		142 ± 48 nM
72	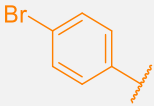		336 ± 68.0 nM
60	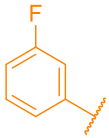	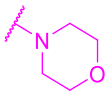	83.4 ± 8.0 nM
61	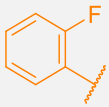	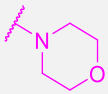	50.9 ± 18.0 nM
62	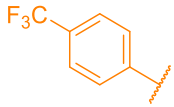	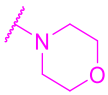	922 ± 281 nM

82	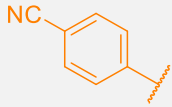	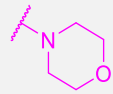	177 ± 44 nM
83	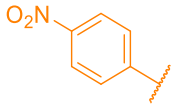	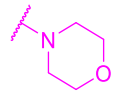	66.5 ± 29.6 nM
80	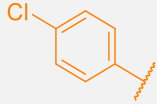	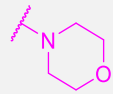	2.03 ± 0.86 nM
81	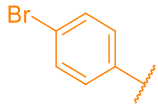	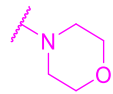	90.5 ± 17.5 nM
66	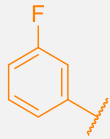	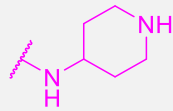	139 ± 45 nM
67	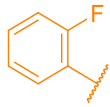	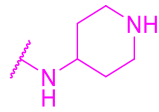	7.13 ± 1.46 nM
68	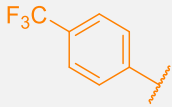	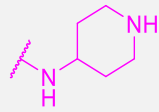	144 ± 58.3 nM
88	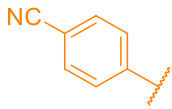	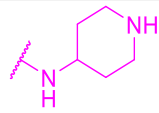	27.9 ± 12.7 nM

89	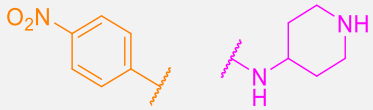	58.7 ± 14.7 nM
87	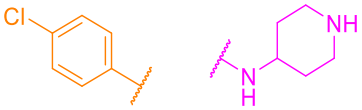	5.60 ± 1.73 nM

[a] Residual enzymatic activities are represented as mean +/- standard deviation and are the result of two independent experiments each one tested in technical duplicate. [b] IC_{50}s are expressed as mean +/- standard error and are the result of three independent experiments each concentration was tested in technical duplicate.

In the trisubstituted series, in a preliminary work, the role of the fluorine atom was evaluated by replacing the fluorophenyl substituent with a simple phenyl ring, but with a *p*-fluorophenyl group at position 5 instead of the pyridine ring. This modification resulted in compound **VI**, which was completely inactive toward CK1δ. While, in this series, introducing a second pyridine moiety slightly improved the activity, affording compound **75**, which retained approximately 44% of residual enzymatic activity. To gain a deeper understanding of the contribution of the fluorine atom, both the position of the substituent on the aromatic ring and its nature were systematically varied. Specifically, 3-fluorophenyl and 2-fluorophenyl derivatives (compounds **54** and **55**) were synthesized. These trisubstituted derivatives exhibited moderate inhibition of CK1δ, with IC_{50} values respectively of 680 nM and

476 nM, thus active in the sub-micromolar range, although significantly less potent than the parent compound **V** (IC_{50} = 110 nM). When more fluorine atoms were introduced, as in the trifluoromethyl derivative (compound **56**), the residual enzymatic activity decreased to approximately 52%, indicating a marked loss of potency. This reduction may be attributed to the bulkier CF_3 group, which likely induces unfavorable steric clashes within the active site, thereby impairing optimal ligand–protein interactions. Based on this hypothesis, we aimed to reduce the steric hindrance of the substituent and to introduce alternative atoms or functional groups that might enhance the overall potency of the compounds.

For this purpose, we introduced nitro and cyan substituents, obtaining compounds **74** and **73**, whose activities differ markedly from each other. The nitrophenyl derivative (**74**) displayed an IC_{50} in the submicromolar range (655 nM), whereas the cyanophenyl analogue (**73**) exhibited significantly higher potency, with an IC_{50} of 50 nM. Comparing these results with those of the parent compound **V** (IC_{50} = 110 nM), it appears that, similar to the trifluoromethylphenyl analogue (**56**), the nitro group, due to its size and rigidity, may introduce steric clashes within the catalytic pocket, thereby preventing the establishment of favorable binding interactions. On the other hand, the cyan group, probably thanks to its smaller size and linear geometry, does not induce the same steric constraints and

enhances the compound's potency even more than the parent molecule (**V**).

To determine whether the observed effect was specific to the fluorine atom or related to halogen substitution in general, we replaced fluorine with other halides, introducing *p*-chlorophenyl and *p*-bromophenyl substituents. Analysis of the corresponding trisubstituted derivatives (**71** and **72**) revealed that both were less active than the *p*-fluorophenyl analogue (**V**). This result suggests that fluorine, due to its small size, fits optimally within the binding pocket. The chlorine atom produced a comparable effect, as reflected by a similar IC_{50} value (142 nM), indicating that its steric dimensions are still compatible with the pocket. In contrast, substitution with bromine resulted in an almost threefold increase in IC_{50}, demonstrating that the larger bromine atom introduces steric hindrance and cannot be accommodated within the pocket as efficiently as the smaller halogens.

From the trisubstituted compounds, we then analyzed tetrasubstituted inhibitors bearing the morpholine ring and the aminopiperidine at position 3.

Considering the morpholino derivatives, the 3-fluoro and 2-fluorophenyl analogues **30** and **61** displayed good activities in the high nanomolar range, with IC_{50} values of 83 nM and 66 nM, respectively. The *p*-nitrophenyl **83** compound also showed comparable potency (IC_{50} = 66 nM), confirming that the *para*

position is optimal for the introduction of substituents on the aromatic ring. Interestingly, the cyan derivative (**82**), which was the most promising among the trisubstituted compounds, exhibited an increased IC_{50} value (177 nM). This observation highlights that substitution in position 3 can strongly influence compounds orientation in the binding site. The trifluorophenyl derivative **62** remained active, even if with an IC_{50} around 1.0 μM. Among all the tested compounds, the *p*-chlorophenyl derivative **80** exhibited the highest potency (IC_{50} = 2.03 nM), confirming that the chlorine atom is well accommodated within the hydrophobic region of the binding pocket. The *p*-bromophenyl analogue **81** retained good activity (IC_{50} = 90.5 nM), but potency is markedly reduced compared to the chloro-derivative (**80**) indicating again that steric constraints may limit the optimal fitting of the larger halogen atom.

Moving to the tetrasubstituted compounds bearing an aminopiperidine moiety at position 3, we observed that the different substitution patterns significantly influence the activity. Among these, the only two compounds lacking a *para*-substituent on the aryl ring at position 6 of the pyrazine core, the 3-fluoro and 2-fluorophenyl derivatives (compounds **66** and **67**), displayed IC_{50} values of 139 nM and 7.1 nM, respectively. The last one represents one of the most active and promising compounds in this series, showing a nanomolar potency comparable to that of the *p*-fluoro analogues **10** and **20**.

In this subset, the introduction of a trifluoromethylphenyl group **68** also resulted in a compound active in the high nanomolar range (IC_{50} = 144 nM), further confirming that position 3 plays a crucial role in driving affinity and activity toward the enzyme.

However, within this series, the introduction of a nitro group **89** resulted in a decrease in potency compared to the corresponding morpholine analogue **83**, while the cyan derivative (**88**) in respect of its counterpart bearing the morpholine displays a decreased IC_{50}, thus proving higher potency (IC_{50} = 27.9 nM). Whereas the chloro-substituted compound **87** showed a slightly increased IC_{50} value relative to its morpholine counterpart **80**.

3.3. Biochemical and biophysical characterization

Based on the results of the structure optimization studies, a few promising compounds have been selected for a more in-depth investigation to better understand their potential pharmacological effects. The compounds chosen for further characterization are **V, 10, 18, 20** and **21**. The following section is focused on the characterization of these compounds, considering biochemical and biophysical approaches.

3.3.1. ATP-competition Assays

To assess the ATP competitive behavior of the compounds ATP competition assays were performed. For this purpose, the experiments were conducted using the ADP Glo system (Promega). First of all, a calibration curve was built up to correlate the amount of ADP to a luminescence signal (ADP was then converted in ATP thanks to the ADP Glo detection reagent system). A linear regression was determined, and the slope was then used to determine the conversion of ADP as result of the kinase activity, data used to calculate 1/v. Compounds **V**, **10**, **18, 20**, and **21** were tested at their IC_{50} value and at a double concentration respect to their IC_{50}, at different and increasing concentrations of ATP. Obtained that information, a Lineweaver Burk plot was built using the reciprocal of the concentration of the ATP used and the reciprocal of the velocity of the reaction. Figure 34 shows the Lineweaver–Burk plots of compounds **V** and **21** from the selected compounds as

representative ones. All compounds exhibited an ATP-competitive inhibition pattern, as evidenced by the nearly identical y-intercepts, indicating no change in the maximal velocity (V_{max}) of the kinase reaction but a variation in the apparent K_m.

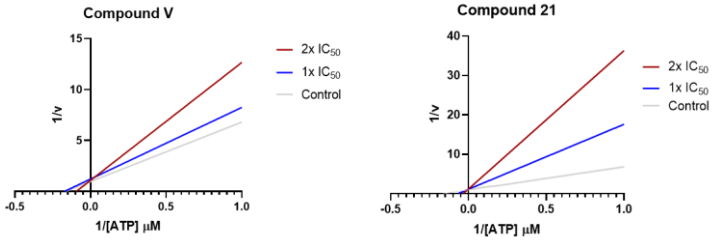

Figure 34: Lineweaver–Burk plots obtained from ATP-competition assays of compounds ***V, 21****. Enzyme kinetics were determined by measuring initial velocities with different concentrations of ATP in the presence of each compound. The experiments were conducted in experimental triplicate, with each concentration point measured in technical duplicate. Data are presented as mean values, and linear regression was used to generate reciprocal plots.*

In Table 5 are reported the y-intercepts of the Lineaweaver Burk plot of each compound. A statistical analysis was performed and none of the linear regressions are significantly different from the control one.

Table 5: y-intercepts of the Lineweaver-Burk plot of every compound

Cmpd	1x IC_{50}	2x IC_{50}	Control
V	1.22 +/- 0.15	1.09 +/- 0.06	0.971 +/- 0.030
21	1.12 +/ 0.08	1.19 +/- 0.09	0.971 +/- 0.030
10	1.16 +/- 0.12	1.08 +/- 0.16	0.971 +/- 0.030
20	0.517+/- 0.054	0.446+/- 0.072	0.342 +/- 0.025
18	0.842+/- 0.115	0.983+/- 0.232	0.971 +/- 0.030

A statical analysis was performed using GraphPad Prism 8.0.2 using One way "Anova" and none of the linear regressions are significantly different from the control one. Y-intercepts are represented as mean +/- standard error.

3.3.2. Thermal Shift Assay (TSA)

Biophysical experiments were conducted by the group of Dr. Paola Storici at Elettra Sincrotrone.

To validate the binding of the synthesized compounds to CK1δ and to assess their effect on protein stability, a thermal shift assay (TSA) was performed by the group of Dr. Paola Storici at Protein Facility at Elettra Sincrotrone. This biophysical technique measures changes in the thermal denaturation profile of a protein upon ligand binding. In the assay, the protein is gradually heated in the presence of a fluorescent dye that specifically binds to exposed hydrophobic regions as the protein unfolds. Ligand binding generally increases the thermal stability

of the protein, shifting the melting temperature (T_m) toward higher values; conversely, destabilizing interactions result in a decrease of T_m. The magnitude of this thermal shift (ΔT_m) is therefore indicative of the strength and nature of the protein–ligand interaction, providing a rapid and reliable method to confirm target engagement under near-physiological conditions[185,186].

Regarding the compounds optimized at position 3, among the tested molecules we also evaluated the parent compound **V** using this technique. The following figure reports the Thermal Shift Assays (TSA) of the most promising derivatives, compared with that of **V**, that displayed a shift in the T_m about 5 °C. It can be observed that the tetrasubstituted derivatives, which are more potent than the parent compound, exhibit a higher shift in the melting temperature of the target enzyme. This behavior reflects their higher binding affinity, resulting in more favorable interactions that stabilize the protein and consequently increase its melting temperature. In Figure 35**Errore. L'origine riferimento non è stata trovata.** is reported the TSA results of compound **V**, while in Figure 36 are reported the corresponding melting curves of compound **21**, **10**, **20** and **18**.

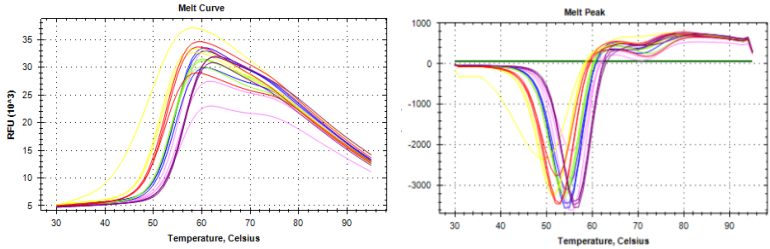

*Figure 35: Thermal shift assay of compound **V**. On the left is reported the denaturation curve of the protein in presence of the compound, on the right is reported the first derivative of the curve, used to determine the melting temperature (T_m). Color code: yellow 0.5x, red 1x, green 3x, blue 5x, pink 10x, purple 15x.*

Compounds **21**, **10**, **20** and **18** displayed a shift in the melting temperature from 7.3 to 9.3 °C, considering that the T_m of the enzyme without compound is 51 °C. To further confirm the correlation between inhibitor potency and the degree of protein stabilization, compound **56** was also evaluated. This compound is inactive against the enzyme, indicating poor affinity for the target, and produced a melting temperature shift of approximately 1 °C, a value too small to be considered significant given the sensitivity limits of the instrument. Melting temperatures of the tested compounds are resumed in Table 6.

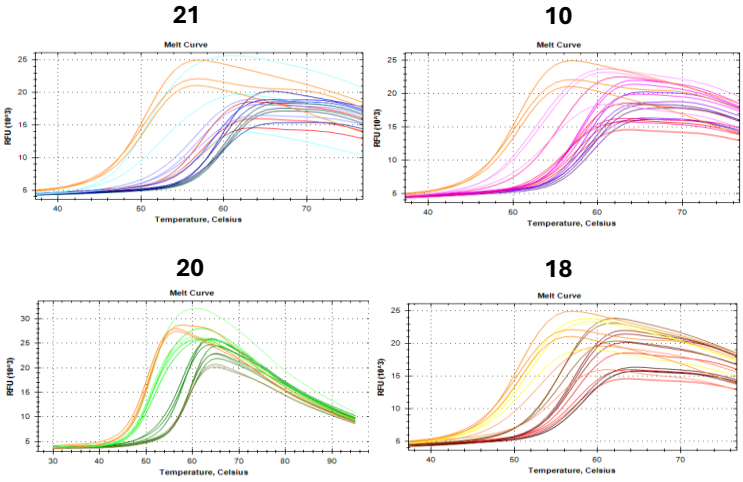

Figure 36: Thermal shift assays of the most promising compounds, only the melting curve is reported.

*Table 6: shifts in the melting Temperature of CK1δ produced by compounds **21**, **10**, **20**, **18**, **56**.*

Compound	ΔT_m (°C)
21	9.3 °C
10	8.3 °C
20	9.0 °C
18	7.3 °C
56	1.0 °C

3.3.3. Co-Crystal structure of the most promising compounds

Thanks to our colleagues in Paola Storici's group, who successfully co-crystallized the most promising compounds with the target protein, we were able to obtain a comprehensive overview of the interactions established within the active site. For this purpose, we compared the co-crystal structures of three inhibitors: PF-670462, a well-known CK1δ/ε inhibitor commonly used as a reference compound to investigate isoform δ behavior, compound **V**, the starting point of this project, and the new compound **20**.

Figure 37 panel B reports the co-crystal structure of compound **V**, which exhibits a binding mode highly similar to that of PF-670462 (panel A), consistent with its relatively high potency. Panel C shows the co-crystal structure of the cross-shaped compound **20** with the protein, one of the most promising compounds synthesized, together with the heat map illustrating the interactions between the ligand and the enzyme (made by Gianluca Novello, University of Padua). A strong polar interaction can be observed between the compound and Asp and Asn polar residues, located in the solvent exposed portion of the ATP binding pocket. These interactions are absent for compound **V**, panel B, while were present in the co-crystal structure of the potent PF-670462 with CK1δ (panel A), where the cyclohexyl group is oriented toward the solvent-exposed

region of the protein, in proximity to polar residues such as Asp91, Asp132, and Asn133.

This polar interaction in compound **20**, combined with the additional contacts established by other substituents of the molecule, is probably responsible for the high potency of the compound toward the enzyme.

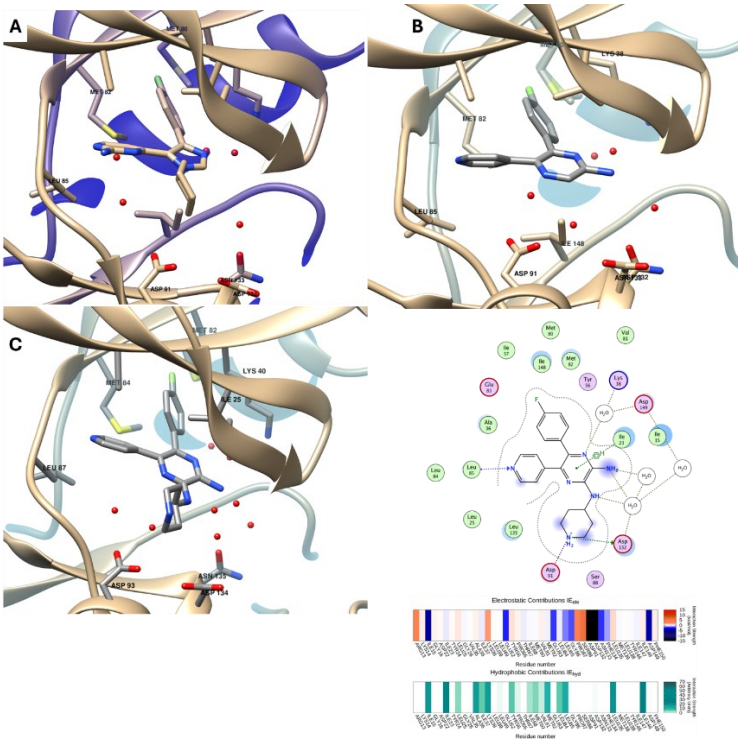

*Figure 37: A) Co-crystal structure of compound PF-670462 PDB:3UZP. B) Co-crystal structure of compound **V** in the catalytic pocket, PDB: 9SJ1. C) co-crystal structure of compound **20** (PDB 9SIZ) and heat map of the interaction within the catalytic pocket.*

Also compounds **10**, **18** and **21** were successfully co-crystallized with the protein and are reported in Figure 38.

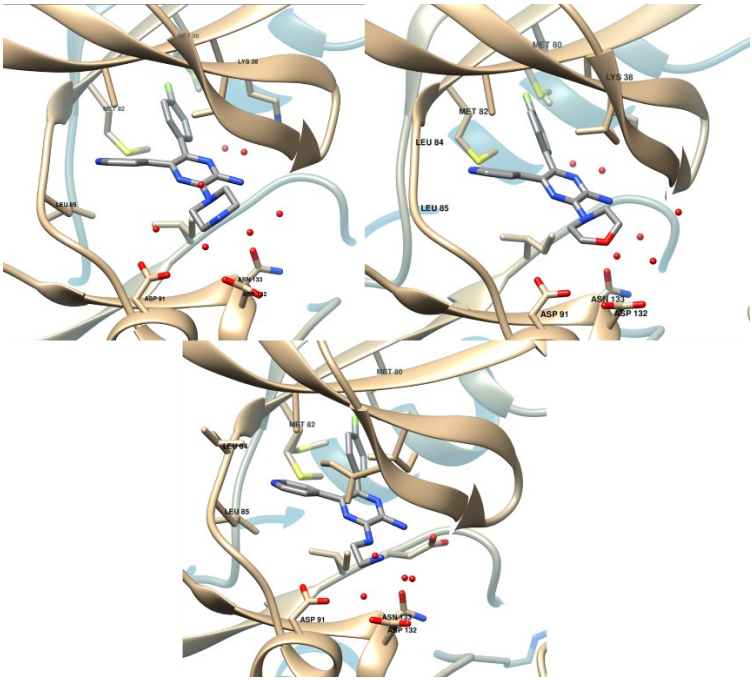

*Figure 38: Co-crystal structure of compounds **21**, **10** and **18**. PDB: 9SIW, 9SIY and 9SJ0.*

3.3.4. Grating Coupled Interferometry (GCI)

Group of Dr. Paola Storici's performed also the kinetic evaluation exploiting the Grating coupled interferometry technique. Grating-Coupled Interferometry (GCI) is a label-free biosensing technique that allows real-time investigation of

molecular interactions. The method is based on the detection of refractive index changes occurring near the sensor surface, where one of the interacting partners, often the protein is immobilized. Light propagates through a diffraction grating, and the wavelength of the light is characterized by a phase. When a ligand interacts with the bonded protein, it induces variations in the refractive index, and in the phase of the refracted light[187]. These phase shifts are measured interferometrically with high sensitivity, providing kinetic parameters such as the association (k_{on}) and dissociation (k_{off}) rate constants, as well as the equilibrium dissociation constant (K_D). The most promising compounds, **V**, **21**, **10**, **20** and **18**, were evaluated using this technique, and their kinetic parameters were determined. Figure 39 shows the corresponding sensorgrams and the calculated kinetic constants. In particular, the sensorgram of compound **20** (panel D) reveals a markedly extended timescale, indicating that the compound dissociates from the enzyme much more slowly than the others, suggesting a high affinity for the target. Consistently, the dissociation rate constant (k_{off}) of compound **20** is significantly lower compared to the other compounds, confirming its very slow off-rate. Based on these observations, compound **20** can be classified as a tight binder of the enzyme.

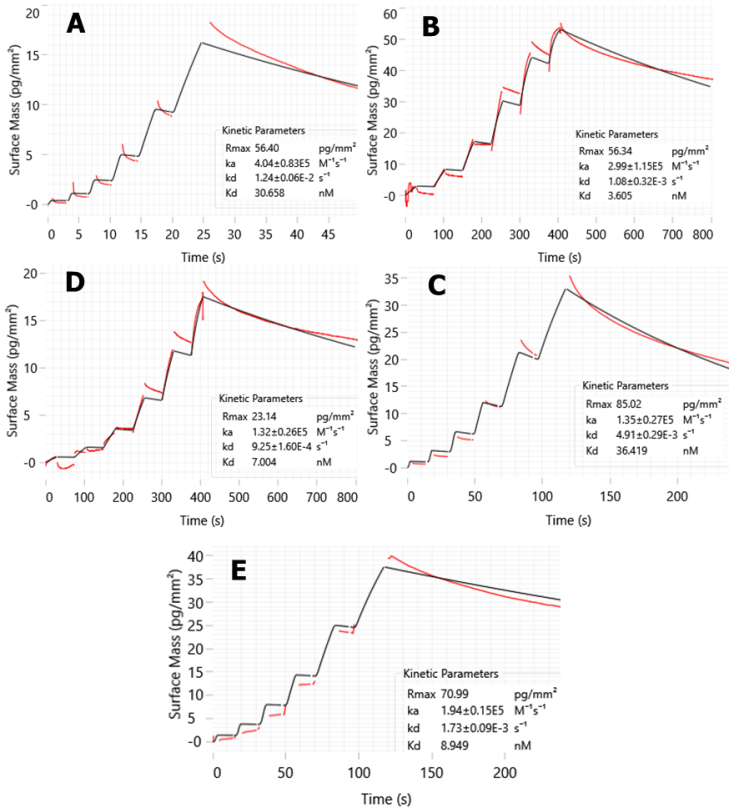

*Figure 39: Quantitative Binding Kinetics Measured by GCI. Representative binding curves are shown for CK1δ interacting with **V** (A), **21** (B), **10** (C), **20** (D), and **18** (E). All sensorgrams were blank-subtracted and double-referenced to correct for nonspecific interactions and bulk refractive index variations. Data analysis and curve fitting were performed using a one-to-one binding model. Quality control metrics, including χ^2 values, parameter errors, and residual distributions, were within acceptable thresholds. The sensorgrams exhibited clear curvature, and the dissociation rate constants (k_{off}) were well within the instrument's measurable range. All derived kinetic parameters fell within the confidence intervals of the model.*

The association and dissociation rate constants, together with the calculated equilibrium dissociation constant (K_D), are summarized in Table 7.

*Table 7: kinetic constants of compound **V**, **21**, **10**, **20** and **18**. In particular the table reports the K_{on} and K_{off} of the compounds and their ratio K_D.*

Compound	K_{on} (M^{-1} s^{-1})	K_{off} (s^{-1})	K_D (nM)
V	3.66 +/- 0.14 E^5	1.39 +/- 0.04 E^{-2}	38.0 +/- 0.4
21	2.63 +/- 0.51 E^5	1.01 +/- 0.10 E^{-3}	3.9 +/- 0.4
10	1.33 +/- 0.19 E^5	4.59 +/- 0.27 E^{-3}	36.4 +/- 2.4
20	1.20 +/- 0.17 E^5	7.63 +/- 2.29 E^{-4}	6.3 +/- 1.0
18	1.95 +/- 0.01 E^5	2.11 +/- 0.53 E^{-3}	10.8 +/- 2.6

3.4. Selectivity

Since kinases catalyze the same type of reaction, they share a highly conserved catalytic domain. This is particularly true for the CK1 family, where CK1δ and CK1ε differ by only seven amino acids. For this reason, among the most promising compounds developed during this project, compounds **10** and **20** were selected for their evaluation of the selectivity across a 100-kinase panel, comprising enzymes from all the major kinase families. The compounds were sent to Eurofins DiscoverX, where a kinase activity profiling assay was performed at a

concentration of 1 μM. Compound **10** was found to be active only against PKA (41% residual activity), CK1α (21%), CK1ε (8%), and SAPK2a (9%), while compound **20** , showed activity on the same targets, except PKA, with respectively the following percentages, 28% for CK1α, 8% for CK1ε and 21% for SAPK2a. In Table 8 is reported the panel on which the compounds were tested and the relative % of residual activity.

Table 8: selectivity panel used by Eurofins DiscoverX.

	Catalogue Number	**Compound 16 @ 1 μM**	**Compound 14 @ 1 μM**
Abl(h)	14-529KP	100	108
ALK(h)	14-555KP	91	98
AMPKα1(h)	14-840KP	106	104
A-Raf(h)	14-956KP	105	107
ASK1(h)	14-606KP	81	91
Aurora-A(h)	14-511KP	96	105
CaMKI(h)	14-663KP	113	97
Cdc7/cyclinB1(h)	16-025KP	85	93
CDK1/cyclinB(h)	14-450KP	101	103

CDK2/cyclinA(h)	14-448KP	109	108
CDK2/cyclinE(h)	14-475KP	126	90
CDK3/cyclinE(h)	14-487KP	96	94
CDK5/p25(h)	14-516KP	101	87
CDK6/cyclinD3(h)	14-519KP	109	105
CDK7/cyclinH/MAT1(h)	14-476KP	100	109
CDK9/cyclin T1(h)	14-685KP	108	108
CDK14/cyclinY(h)	15-034KP	93	89
CDK16/cyclinY(h)	16-041KP	109	104
CDK17/cyclinY(h)	16-042KP	110	99
CDK18/cyclinY(h)	15-031KP	116	119
CDKL4(h)	16-031KP	106	107

ChaK1(h)	14-961KP	105	107
CHK1(h)	14-346KP	90	96
CK1α(h)	16-050KP	28	21
CK1ε(h)	16-045KP	8	8
CK1γ1(h)	14-711KP	84	87
CK1γ2(h)	14-712KP	93	90
CK1γ3(h)	14-713KP	96	99
CK1δ(h)	14-520KP	1	-1
CK2α2(h)	14-689KP	100	85
c-RAF(h)	14-352KP	94	94
DRAK1(h)	14-668KP	99	108
DYRK3(h)	15-002KP	97	106
eEF-2K(h)	14-654KP	98	99
EGFR(h)	14-531KP	100	96
EphA5(h)	14-639KP	97	90
EphB4(h)	14-554KP	96	81
Fyn(h)	14-441KP	90	92
GRK5(h)	14-714KP	104	106
GRK6(h)	14-715KP	93	100

GSK3β(h)	14-306KP	95	87
IGF-1R(h)	14-465KP	98	83
IKKα(h)	14-461KP	102	108
IRAK4(h)	14-599KP	111	120
JAK2(h)	14-640KP	94	92
KDR(h)	14-630KP	95	66
LOK(h)	14-686KP	83	78
Lyn(h)	14-510KP	93	88
MAPKAP-K2(h)	14-337KP	110	101
MAPKAP-K3(h)	14-585KP	95	98
MEK1(h)	14-429KP	93	94
MLK1(h)	14-690KP	109	97
MLK4(h)	16-051KP	92	87
Mnk2(h)	14-664KP	97	95
MOK(h)	14-960KP	98	95
MSK2(h)	14-616KP	98	103
MST1(h)	14-624KP	97	110

mTOR(h)	14-769KP	92	98
NEK2(h)	14-545KP	98	93
p70S6K(h)	14-486KP	104	105
PAK2(h)	14-481KP	108	106
PASK(h)	14-701KP	108	110
PEK(h)	14-916KP	91	101
PDGFRβ(h)	14-463KP	92	95
PDHK2(h)	16-038KP	110	119
PDHK4(h)	15-024KP	93	91
Pim-1(h)	14-573KP	94	92
PKA(h)	14-440KP	61	41
PKBα(h)	14-276KP	86	96
PKCα(h)	14-484KP	98	93
PKCβI(h)	14-503KP	94	69
PKCγ(h)	14-483KP	97	97
PKCθ(h)	14-444KP	94	91
PKCζ(h)	14-525KP	118	117
PKG1α(h)	14-688KP	98	103
Plk3(h)	14-572KP	103	94

PRAK(h)	14-334KP	110	113
ROCK-I(h)	14-601KP	94	107
Rse(h)	14-535KP	109	98
Rsk1(h)	14-509KP	88	103
SAPK2a(h)	14-251KP	21	9
RPK1(h)	14-564KP	95	87
TAF1L(h)	16-024KP	98	96
TAK1(h)	14-600KP	95	100
TRB2(h)	16-016KP	87	90
TSSK2(h)	14-632KP	85	89
TSSK3(h)	15-021KP	107	106
TTBK1(h)	15-018KP	105	99
TTBK2(h)	15-019KP	112	104
VRK1(h)	16-033KP	112	97
ATM(h)	14-933KP	99	102
ATR/ATRIP(h)	14-953KP	105	101
DNA-PK(h)	14-950KP	102	87
PI3 Kinase (p110b/p85a)(h)	14-603KP	103	92

PI3 Kinase (p120g)(h)	14-558KP	95	92
PI3 Kinase (p110d/p85a)(h)	14-604KP	86	110
PI3 Kinase (p110a/p85a)(h)	14-602KP	102	108
PI3KC2a(h)	14-906KP	102	98
PIP4K2a(h)	14-901KP	108	107

In the laboratory of Professor Ana Martinez at CSIC-CIB in Madrid, during the Erasmus^{+} mobility period of the doctoral program, the most promising compounds were tested against a small kinase panel comprising GSK3β, SGK1, and CK1. The assays were performed using the Kinase-Glo system. Compounds were initially tested at a fixed concentration of 10 μM, and the percentage of residual enzymatic activity was measured. For those displaying less than 50% residual activity, IC_{50} values were subsequently determined. Table 9 summarizes the results of this selectivity profile and the corresponding IC_{50} values. All compounds showed activity toward the CK1ε isoform; however, a particularly finding was obtained for compound **20**, which demonstrated remarkable selectivity for the CK1δ isoform. To the best of our knowledge, no inhibitors exhibiting such pronounced selectivity for CK1δ over CK1ε

have been previously reported. This unprecedented selectivity makes compound **20** a valuable chemical probe to specifically investigate the biological functions regulated by CK1δ, independently of those mediated by the closely related CK1ε isoform. Such a tool could greatly facilitate the dissection of isoform-specific signaling pathways and deepen our understanding of the distinct physiological and pathological roles of CK1δ.

*Table 9: selectivity profile of compounds **V, 21, 10**, **20** and **18** on a small kinase panel.*

Cmpd	SGK1	GSK3β	CK1ε	CK1δ	Ratio δ/ε
V	>10 µM	>10 µM	**179 nM**	**110 nM**	**1.6**
21	>10 µM	>10 µM	**39.9 nM**	**30.0 nM**	**1.3**
10	>10 µM	6.26 µM	**77.3 nM**	**3.15 nM**	**25**
20	8.51 µM	>10 µM	**260 nM**	**2.62 nM**	**100**
18	>10 µM	>10 µM	**206 nM**	**9.03 nM**	**23**

3.5. Preliminary Pharmacokinetic Evaluation

3.5.1. Parallel Artificial Membrane Permeability Assay – Blood Brain Barrier (PAMPA – BBB)

When studying neurodegenerative disorders, it is crucial that the developed pharmacological tools are able to reach the central nervous system (CNS). For this reason, we evaluated the ability of our compounds to passively pass the blood brain barrier (BBB) by performing Parallel Artificial Membrane Permeability Assay (PAMPA-BBB) experiments. The PAMPA assay is an *in vitro* technique used to evaluate the passive permeability of compounds across biological membranes. In this variant (PAMPA - BBB), the assay exploits a BBB mimicking membrane composed of mammal brain phospholipid, allowing the estimation of a compound's ability to reach the central nervous system through passive permeability. The method consists of two 96-well plates, one is acting as a donor plate and the second one, the acceptor plate is separated by the artificial membrane from the first one. Compound concentration was determined using a UV visible spectroscopy, and after the incubation acceptor wells have been analyzed in order to determine the apparent permeability, P_e. To validate the assay, ten commercial drugs with well-known CNS permeabilities were first tested, and their experimentally apparent P_e values were correlated with literature P_e values. This correlation was used to build a linear regression model, used to

define cut-off values that classify compounds as CNS permeable (CNS+), non-permeable (CNS−), or borderline (CNS+/−). Once the calibration curve was established, the absorbance of the test compounds was measured, and their concentrations were adjusted to ensure values remained within the linear range of the Lambert - Beer law[188,189].

In Figure 40 are reported the passive permeability values of compounds **V**, **VI**, **1-3, 6-10, 18-21, 31, 54-56, 60-62, 66, 67, 71, 72, 80** and **81.** It is possible to notice that most of the compounds succeeded in passively permeating the membrane thus resulting in CNS+ compounds. Among them most have as substituent in position 3 the morpholine group, suggesting that this is a promising substituent capable of favorably modulating the physical-chemical properties of the compounds. The most promising compounds that have been selected for all the characterization process (**V**, **21**, **10**, **20** and **18**) all demonstrate from moderate to good behavior in crossing the BBB, as represented in Figure 40, in particular compounds **10** and **20** were two of the most permeable compounds, while compound **V**, **21** and **18** have a borderline behavior. But in general, the compounds can be considered capable of targeting the CNS, thus fulfilling a crucial criteria when developing CNS drugs.

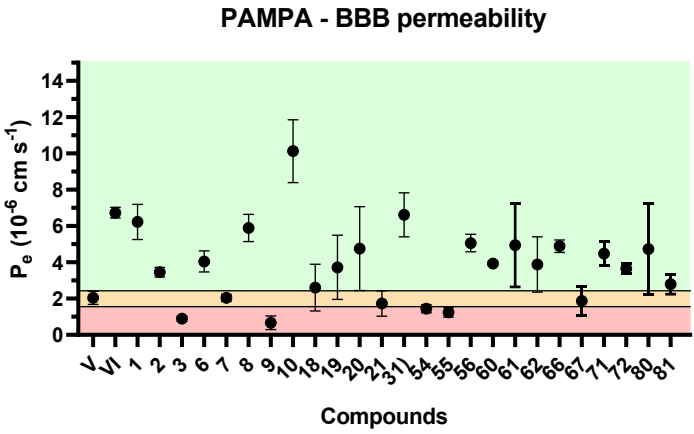

Figure 40: PAMPA–BBB permeability results. Data reported are means of apparent Pe values ± SD from two independent experiments.

3.5.2.Microsomal stability assay

Understanding the pharmacokinetic properties of new compounds is essential to predict their *in vivo* behavior, including absorption, distribution, metabolism, and excretion (ADME). Among these parameters, metabolic stability plays a crucial role in determining a compound's half-life and overall bioavailability. To evaluate this aspect, *in vitro* microsomal stability assays are commonly employed, providing an estimate of the rate at which a compound is metabolized by liver enzymes. In this study, the metabolic stability of the synthesized compounds was assessed using mouse liver microsomes, which contain phase I metabolic enzymes such as cytochrome P450s. Mouse species was chosen due to the fact that it represents the

most common used in animal models. By monitoring the percentage of the tested compound remaining over time, it is possible to estimate its intrinsic clearance and predict its metabolic stability *in vivo.* For this purpose, we sent the compound to Nuvisan company, that performed the experiments and the following table (Table 10) resumes the data obtained from the *in vitro* pharmacokinetic experiments. Among the tested compounds, **21** exhibited the most favorable metabolic profile, showing a low intrinsic clearance (0.69 L/h/kg) and a long half-life of approximately 208 minutes, corresponding to roughly three hours of stability in mouse liver microsomes. This suggests a reduced susceptibility to metabolic degradation and promising pharmacokinetic behavior. In contrast, compound **10** showed a very high clearance rate (18 L/h/kg) and a short half-life of only 8 minutes, indicating that it is rapidly metabolized and therefore less suitable in its current form. This property should be further optimized to improve its stability while maintaining CNS permeability. In Table 10 are reported the results of the *in vitro* microsomal stability.

Table 10: Summary of in vitro pharmacokinetic parameters for the tested compounds. Microsomal stability was assessed in mouse liver microsomes to determine the apparent intrinsic clearance (CLint,app) and half-life ($t_{1/2}$).

Compound	$CL_{intr\ app}$[a] (L/h/kg)	$t_{1/2}$[b] (min)
V	5.1	28
21	0.69	208
10	18	8
20	2.2	66
18	3.0	48

[a]*Intrinsic Clearance of the tested compounds (CL intr app expressed in L/h/kg) obtained from mouse liver microsomal stability assay, performed by Nouvisan.*
[b] *half-life (t1/2) calculated from the disappearance rate of the tested compound in the microsomal assay.*

3.6. Biological evaluation

3.6.1. In vitro cell based assays (SH-SY5Y neuroblastoma cell line)

Experiments were performed during the Erasmus+ program at the lab. Professor Ana Martinez (CSIC-CIB) in Madrid. Most promising compounds have been tested on the SH-SY5Y neuroblastoma cell line. These cells possess neuronal characteristics and can be differentiated into mature neuron-like phenotypes using agents such as retinoic acid or brain-derived neurotrophic factor (BDNF). Once differentiated, SH-SY5Y cells exhibit morphological and biochemical properties typical of neurons, including neurite outgrowth and expression of neuronal markers. Because they are easy to culture, genetically manipulate, and highly reproducible, SH-SY5Y cells represent a valuable in vitro model to study molecular mechanisms involved in neurodegeneration, neurotoxicity, and neuroprotection. Their sensitivity to oxidative and mitochondrial stress makes them particularly suitable for modeling neurodegenerative diseases such as Parkinson's disease, Alzheimer's disease, and amyotrophic lateral sclerosis (ALS)[190].

For this reason, the compounds were tested initially to evaluate their toxicity on the cell line, and then on an ALS model to investigate their neuroprotective behavior.

3.6.2. MTT assay – cytotoxicity experiments

Regarding the cytotoxicity experiments, compounds **V**, **21**, **10**, **20**, **18** and **67** have been tested at a final concentration of 1, 3 and 10 μM. For this purpose, 60000 cell/well have been seeded in a transparent 96-well plate and incubated for 24 hours. After that time cells were treated with the compounds at the desired concentration and incubated again for 24 hours. Last MTT -(4,5-dimethylthiazol-2-yl)-2,5-diphenyltetrazolium bromide) was introduced in the wells and after 3 hours the absorbance of the plate was recorded. Viable cells convert the yellow tetrazolium compound MTT into insoluble purple formazan crystals through mitochondrial enzymes. Once these crystals are solubilized, the resulting color intensity is directly proportional to the number of living cells present. In the plate was introduced also a control represented by the untreated cells, that produce 100% of cell viability. The results are related to the control wells.

In Figure 41 is reported cell viability % resulted from the cell treatment with the test compounds. It is appreciable to notice that none of the compounds resulted in being toxic on the cell line, neither at the highest concentration (10 μM). Only compound **21** produced a slight decrease in cell survival when tested at 10 μM, around 80 % which is the cut-off value to assess if a compound is toxic or not on the cell line. For this reason, it has been excluded from the neuroprotection experiment.

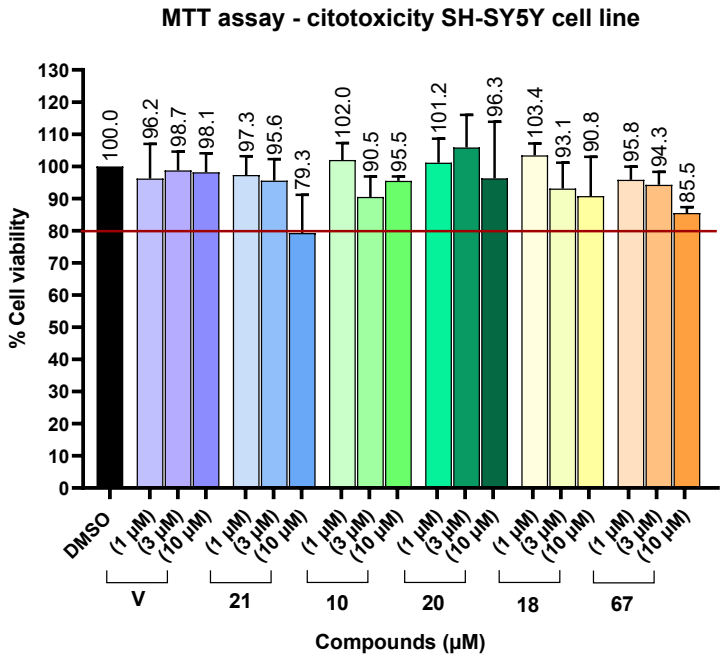

*Figure 41: MTT assay of compounds **V, 21, 10, 20, 18, 67** at the concentration of 1, 3 and 10 µM. In y axis the cell viability percentage is reported. The elaboration performed with GraphPad Prism 8.0 in "Anova" mode is the result of three independent experiments and each experiment is conducted using the mean of six wells per compound Results are expressed as the mean of three data ± standard error (error bars); ***p<0.0005 significantly different from the control, **p<0.005 significantly different from the control, *p<0.05 significantly different from the control.*

3.6.3. Neuroprotection experiments – immunoblotting assay

Compounds **V**, **10, 20, 18, 67**, that displayed no toxicity on the cell line were investigated for their potentially neuroprotective behavior on a disease model. For this purpose, cells were treated with Ethacrynic Acid (EA), diuretic known to act as a potent oxidative agent, mainly because of the depletion of intracellular glutathione (GSH) and the consequent accumulation of reactive oxygen species (ROS)**.** Increased oxidative stress levels has been linked with the pathogenesis of amyotrophic lateral sclerosis (ALS) in particular with the phosphorylation, solubility, and aggregation of TDP-43, main pathological hallmark of the disease[191].

The experiment consisted of harvesting and seeding 2000000 cell/well in a 6-well plate, and after 24 hours of incubation cells were treated first with the compound at a concentration of 5 μM and after another hour of incubation with EA (70 μM). After 24 hours of incubation cells were collected and extracted with a lysis buffer.

To set up the Western Blot analysis in optimal conditions, a calibration curve was performed measuring the absorbance with increasing concentrations of albumin, in order to correlate an absorbance value to a concentration of protein. This step is needed to quantify the total protein concentration from the

lysate in order to load equal amounts of protein to the electrophoresis gel, the calibration curve is reported in Figure 42.

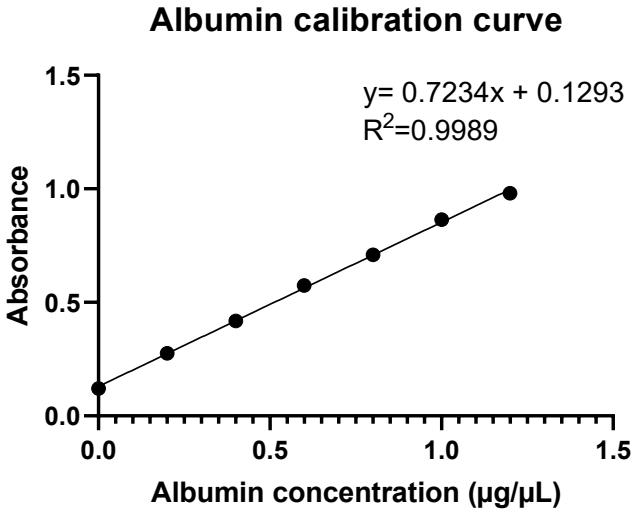

Figure 42: Albumin calibration curve and protein quantification.

Once the samples were loaded onto the gel and electrophoresis was completed, the separated proteins were transferred onto membranes pre-activated with methanol. The membranes were then incubated with specific primary antibodies targeting total TDP-43 (mouse, Proteintech, 67345-1-Ig; dilution 1:1000 in TBST) and phosphorylated TDP-43 at Ser409/410 (rabbit, Proteintech, 22309-1-AP; dilution 1:1000 in TBST). Following 24 hours of incubation at 4 °C, the membranes were washed and then incubated for 1 hour at room temperature with HRP-

conjugated secondary antibodies (goat anti-mouse IgG–HRP, Bio-Rad, and goat anti-rabbit IgG–HRP; dilution 1:5000 in TBST). After additional washes, luminol and hydrogen peroxide were added to the membranes, and the chemiluminescent signal was detected; band intensities were then quantified using ImageLab software (Bio-Rad). GAPDH was used as a loading control and ‘’*housekeeping’’* protein to verify that the amount of total protein charged is equal in all the lines and to assess that variation in the target protein bands are not due to uneven loading. Levels of phosphorylated TDP-43 (pTDP-43) were normalized to total TDP-43, and total TDP-43 was further normalized to GAPDH.

In Figure 43, the results of the Western blot analysis are shown. All tested compounds demonstrated a clear reduction in pTDP-43 levels compared with the negative control (cells treated only with ethacrynic acid). An additional compound, the well-known CK1δ inhibitor IGS2.7, was included as an internal control to confirm the reliability of the experimental setup.

Importantly, the observed decrease in phosphorylated TDP-43 indicates that the compounds are able to counteract the oxidative-stress–induced dysregulation of TDP-43, suggesting a neuroprotective effect. Since abnormal phosphorylation and aggregation of TDP-43 are key molecular events in the pathogenesis of amyotrophic lateral sclerosis (ALS), these

findings highlight the potential of the tested molecules as promising therapeutic candidates for the treatment or modulation of ALS-related neurodegeneration

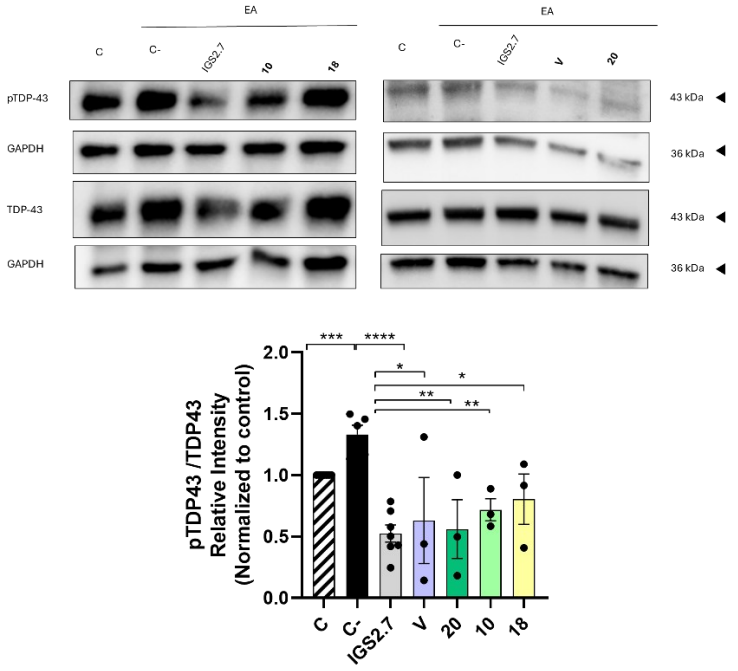

*Figure 43: Western blot analysis of phosphorylated TDP-43 levels in SH-SY5Y cells for compounds **V**, **10**, **20** and **18**. Representative immunoblots (on the top) show phosphorylated TDP-43 (pTDP-43), total TDP-43, and GAPDH (loading control). The bar graph (on the bottom) reports the quantification of pTDP-43 normalized to total TDP-43 levels and further normalized to GAPDH. Data represent mean ± SD of independent experiments. ****p<0.0001 significantly different from the control, ***p<0.0005*

*significantly different from the control, **p<0.005 significantly different from the control, *p<0.05 significantly different from the control.*

3.6.4.In vivo experiments – Drosophila model

Given the promising results obtained in vitro on cultured cells, particularly for two of the tested compounds, we decided to further investigate their effects in vivo using Drosophila melanogaster models overexpressing TDP-43, these models reproduce several pathological and functional alterations associated with amyotrophic lateral sclerosis (ALS). In these models, human TDP-43 can be selectively overexpressed in different tissues, including eyes and motor neurons, leading to distinct phenotypic outcomes that mimic ALS-related pathology. Overexpression in the eye induces a progressive neurodegenerative phenotype that can be easily visualized and quantified by assessing structural degeneration, while neuronal overexpression results in motor impairment and reduced lifespan, reflecting the loss of motor function and vitality typically observed in ALS patients. Regarding this project another advantage in using drosophilae as a model is the fact that expresses a homologue of CK1δ/ε called Doubletime (DBT). This kinase, as for the human one, is strictly involved in several processes, one of the most important is regulation of circadian rhythm. Thanks to the high homology between DBT and CK1δ/ε, it is commonly used as a model to the *in vivo* assessment of the effects of CK1δ/ε inhibitors[192]. Furthermore,

DBT is responsible for the phosphorylation and aggregation of TDP-43[193]. For all these reasons this experimental setup provides a versatile and well-established system to evaluate the neuroprotective potential of the tested compounds across multiple ALS-relevant endpoints, such as neurodegeneration, motility, and survival[193].

These experiments were conducted by the group of Professor Marco Bisaglia at the University of Padua, Biology Department.

3.6.5. Immunoblotting experiments

We first assessed by Western blot whether the CK1δ inhibitors were able to reduce the accumulation of the phosphorylated form of TDP-43, also *in vivo*. For this purpose, flies were incubated with the 5 selected compounds **V**, **21**, **10**, **20**, **18** at a final concentration of 100 μM (Figure 44). Each molecule resulted in being able to reduce pTDP-43 levels in comparison to untreated animals. In particular compound **10** resulted in being the most neuroprotective compound, capable of significantly reducing pTDP-43 levels. The results from the western blots are reported in Figure 44.

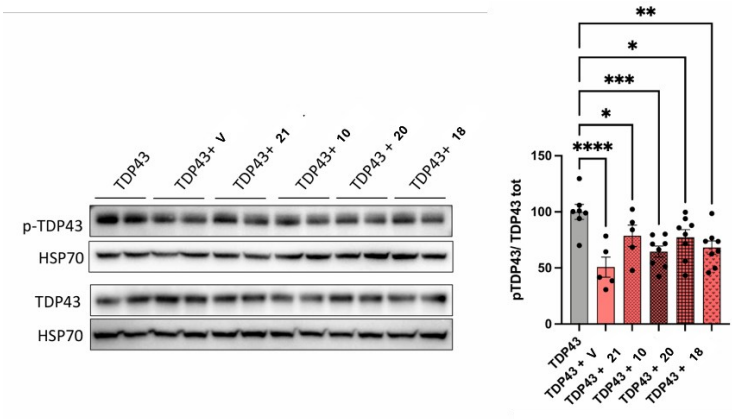

*Figure 44:immunoblotting experiments for compounds **V**, **21**, **10**, **20** and **18** tested at a final concentration of 100 μM for the quantification of phosphorylated TDP-43 on drosophilae. Representative immunoblots (left) show phosphorylated TDP-43 (p-TDP-43), total TDP-43, and HSP70 (loading control). Data represent mean ± SD of independent experiments. ****p<0.0005 significantly different from the control, ***p<0.005 significantly different from the control, **p<0.05 significantly different from the control, *p<0.5 significantly different from the control.*

3.6.6.Lifespan experiments

After confirming that our compounds effectively inhibit the Drosophila CK1δ ortholog, we next evaluated their potential neuroprotective effects in our ALS model. Initially, we selected compounds **V** and **21** to assess their impact on fly longevity. Flies overexpressing TDP-43 were grown with 100 μM of the CK1δ inhibitor, and in parallel untreated flies to use as control. In normal conditions, flies survive for 2/3 months while overexpressing TDP-43 levels significantly reduced flies'

lifespan, however treatment with compounds **V**, **21**,**10** produced a mild but still statistically significant enhancement of flies surviving. On the other hand, despite the potency of compounds **20** and **18**, that were subsequently tested, no effect was observed on the animals treated with those compounds. Surprisingly, **20** and **10** gave a neuroprotective effect at a lower dose (10 μM), resulting in an increase in lifetime of the treated animals.

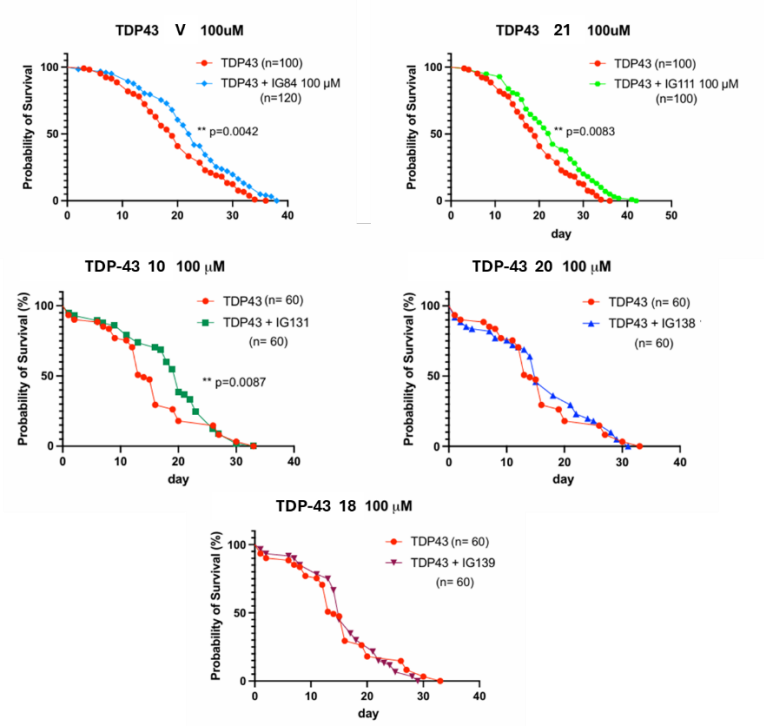

*Figure 45: lifespan experiments conducted on compounds **V**, **21**, **20**, **10** and **18**. The experiments were performed on a cluster of 120, 100 and 60 animals. ****p<0.0005 significantly different from the control. ***p<0.005*

*significantly different from the control. **p<0.05 significantly different from the control. *p<0.5 significantly different from the control.*

3.6.7. Climbing experiments

The neuroprotective effects observed during lifespan experiments have been supported also by the results observed during the climbing assay.

Since the impairment of motor capability is one of the phenotypes associated with ALS, we then compared the locomotor behavior of flies through a negative geotaxis-based climbing assay. The analysis was carried out at different times, starting from newly enclosed flies (0-2 day-old) up to 2 weeks. Although in general the presence of 100 μM compounds **V**, **21**, **20** and **18** did not affect fly locomotion compared to untreated flies, after two weeks of treatment compound **21** gave a protective effect, improving motility of the treated animals. On the other hand, compound **10,** when administered at a concentration of 100 μM significantly improved the climbing index of 1 week old flies overexpressing TDP-43. The quantification of the locomotion activity is reported in Figure 46.

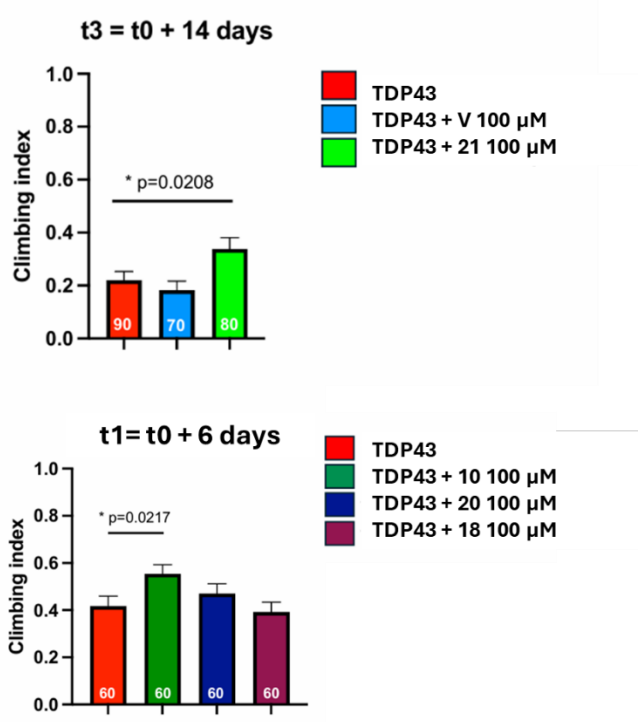

*Figure 46: Climbing experiments conducted on compounds **V**, **21**, **20**, **10** and **18**. *p<0.5 significantly different from the control.*

3.6.8. Eyes degeneration

Drosophilae represent a good and widely used model to study neurodegeneration thanks to the fact that TDP-43 can be overexpressed in the eyes, and *D. melanogaster* eyes have highly organized patterns that could show degenerative phenotypes. With this aim TDP-43 was selectively over expressed at eyes level. Flies overexpressing TDP-43 showed

some degree of eye degeneration already after 2 weeks, flies were treated with compounds and eyes analyzed at different times. Treatment with either compound **V** or **21** resulted in eye protection with the effects that became statistically significant after 4 weeks of treatment (Figure 47).

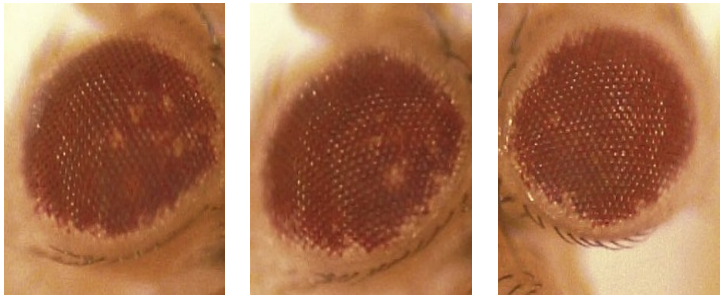

Control **V** 100 µM **21** 100 µM

Figure 47: *Neuroprotection effect observed in 4 weeks old flies' eyes.*

Summarizing the in vivo experiments performed on Drosophila models, compound **10** demonstrated the strongest effects in the western blot analysis, showing a significant reduction in pTDP-43 levels compared with untreated controls, and then demonstrated a neuroprotective effect in both lifespan and climbing assays. Also compound **V** gave good results both in pTDP-43 levels reduction, lifespan increase and in contrasting eye degeneration. Finally, compound **21**, showed the most promising results, even if reduced pTDP43 levels with a p value in the range 0.05-0.005, it displayed a neuroprotective

behaviour in all the other experiments, with a higher statistical significance for the lifespan assay.

4. EXPERIMENTAL SECTION

4.1. Chemistry

4.1.1. General chemistry

Reagents were obtained from commercial suppliers and used without further purification. Reactions were monitored by Thin Layer Chromatography (TLC), on precoated silica gel plates (Macherey-Nagel, 60FUV254). Final compounds and intermediates were purified by flash chromatography using as stationary phases silica gel (Macherey-Nagel, silica 60, 240-400 mesh). When used, light petroleum ether refers to the fractions boiling at 40-60°C. Melting points were determined with a Stuart SMP10 melting point apparatus, and they were not corrected. The ^{1}H NMR and ^{13}C NMR were determined in DMSO-d_6 and recorded on Varian 400 MHz spectrometers; chemical shifts (δ scale) are reported in parts per million (ppm) and referenced to residual solvent peak, with splitting patterns abbreviated to: s (singlet), d (doublet), dd (doublet of doublets), dt (doublet of triplets), t (triplet), m (multiplet) and bs (broad signal). Coupling constants (*J*) are given in Hz. MS-ESI analysis were performed using ESI Bruker 4000 Esquire spectrometer, LTQ-XL, while High Resolution Mass Spectrometry (HRMS) with microTOF-Q (Bruker) Compound purities were determined by HPLC using the instrument SHIMADZU CBM-20A, column Gemini® 5 µm NX-C18 (Phenomenex®). Elution gradient was performed for 20 min at the flow of 1 ml/min from

water-acetonitrile 80:20 to 10:90. The detector was set at 254 nm. "Flash chromatography was performed on a Biotage Isolera system using water and acetonitrile in the appropriate proportions, employing a 6 g Sfär DUO C_{18} cartridge.

4.1.1.1. Investigation at position 3

*Synthesis of 6-(4-fluorophenyl)pyrazin-2-amine (**23**):*

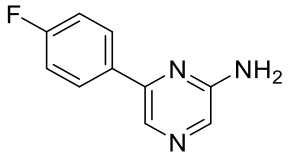

Under argon atmosphere, 3.0 g (1 eq, 15.8 mmol) of commercially available 2-amino-6-chloropyrazine (**22**) were dissolved in 93 mL of toluene under molecular sieves, 9.5 ml of ethanol and 15 mL of a 2M solution of sodium carbonate. To the mixture, 3.88 g of 4-flurophenylboronic acid (1.2 eq, 27.8 mmol) were introduced, followed by the tetrakis(triphenylposphine) palladium ($Pd(PPh_3)_4$), (0.04 eq, 0.63 mmol). The system was refluxed at 110°C for 4 hours, under Ar atmosphere. Once completed, the solvent was removed under reduced pressure. The crude was dissolved in dichloromethane (300 ml), then washed with water (3x100 mL). The organic phases were collected and dried under anhydrous sodium sulphate. The solvent was removed under reduced pressure and the obtained solid was purified by chromatographic

column using a mixture of petroleum ether and ethyl acetate (7:3) as elution phase. The obtained compound was precipitated using a mixture of ethyl acetate and petroleum ether. Pale yellow solid, yield 94-97 %. ^{1}H NMR (400 MHz, DMSO-d_6) δ 8.27 (s, 1H), 8.13 – 7.97 (m, 2H), 7.85 (s, 1H), 7.39 – 7.21 (m, 2H), 6.52 (s, 2H). ^{13}C NMR (101 MHz, DMSO-d_6) δ 162.81 (d, $^{1}J_{CF}$ = 246.2 Hz), 155.19, 147.55, 133.29 (d, $^{4}J_{CF}$ = 3.0 Hz), 131.05, 128.53 (d, $^{3}J_{CF}$ = 8.4 Hz), 128.14, 115.55 (d, $^{2}J_{CF}$= 21.5 Hz). Calculated mass for $C_{10}H_8FN_3$: 190.0775 $[M+H]^+$. ES-MS (methanol) *m/z*: 189.9 $[M+H]^+$. Purity HPLC 97%.

*Synthesis of 5-bromo-6-(4-fluorophenyl)pyrazin-2-amine (**24**):*

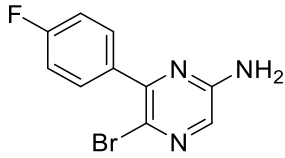

Method A: the 6-(4-fluorophenyl)pyrazin-2-amine (**23**) was dissolved in dry DCM, and the system was put at 0°C, then 1.1 eq. of NBS were added to the system. The system was cooled for 2 hours in the ice bath under argon atmosphere and once the reaction was completed, the solvent was evaporated *in vacuo* and the crude was dissolved in dichloromethane (3x120 mL) and washed with water, brine solution and a saturated solution of $NaHCO_3$ (3x40 mL). The organic phases were collected and dried over sodium sulphate, the solvent removed under reduced

pressure and the crude purified by chromatographic column, using an elution mixture composed of petroleum ether and ethyl acetate (7:3). Yield 5-17%.

Method B: the 6-(4-fluorophenyl)pyrazin-2-amine (**23**) was dissolved in dry DMF, and the system was put at 0°C, then 1.1 eq. of NBS were added to the system. The system was left 30 minutes in the ice bath under argon atmosphere and once the reaction was completed, the solvent was evaporated *in vacuo* and the crude was dissolved in dichloromethane (3x75 mL) and washed with water, brine solution and a saturated solution of $NaHCO_3$ (3x25 mL). The organic phases were collected and dried over sodium sulphate, the solvent removed under reduced pressure and the crude purified by chromatographic column, using an elution mixture composed of petroleum ether and ethyl acetate (7:3). Yield 29%.

Method C: the 6-(4-fluorophenyl)pyrazin-2-amine (**23**) was dissolved in acetonitrile under molecular sieves, and the system was cooled at 0°C, then 1.1 eq. of NBS were added to the system, and it was left in ice bath and under argon atmosphere until reaction completion. Then the solvent was evaporated *in vacuo* and the crude was dissolved in dichloromethane (3x150 mL) and washed with water, brine solution and a saturated solution of $NaHCO_3$ (3x50 mL). The organic phases were collected and dried over sodium sulphate, the solvent removed

under reduced pressure and the crude purified by chromatographic column, using an elution mixture composed of petroleum ether and ethyl acetate (7:3). Yield 45%.

Method D: 1 equivalent of compound **23** and 1.1 eq of NBS were introduced in a microwave reactor vessel and dissolved in ACN. The instrument parameters were set to 50°C, 1200 r.p.m. and the reaction was left in the microwave for 2 hours. The solvent was removed under reduced pressure and the crude was dissolved in DCM (3x45 mL) and washed with water, brine solution and a saturated solution of $NaHCO_3$. The organic phase was dried over Na_2SO_4 and the solvent removed *in vacuo*. The crude purified by chromatographic column, using an elution mixture composed of petroleum ether and ethyl acetate (7:3). Yield 6%.

Method E: In a three necked round bottomed flask under argon atmosphere were introduced 2 g (1 eq, 10.6 mmol) of the 6-(4-fluorophenyl)pyrazin-2-amine (**23**). The compound was dissolved in dry dichloromethane (5 mL/mmol), the system was left at 0°C, then 2.08 grams (1.1 eq, 11.7 mmol) were dissolved in dry acetonitrile and added dropwise to the reaction mixture. After the addition was complete, the reaction mixture was stirred at 0 °C for at least one hour. Upon completion of the reaction, the solvent was removed under reduced pressure. The resulting crude residue was dissolved in fresh dichloromethane

(100 mL) and washed with water, a saturated sodium bicarbonate solution, and brine. Combined organic phases were dried over anhydrous Na_2SO_4. The salt was then filtered and the solvent removed under reduced pressure. The crude was then purified by chromatographic column using an elution mixture composed of petroleum ether and ethyl acetate (7:3). Yellow/orange solid, yield 57-60%.

^{1}H NMR (400 MHz, DMSO-d_6) δ 7.72 – 7.63 (m, 3H), 7.35 – 7.24 (m, 2H), 6.77 (s, 2H). ^{13}C NMR (101 MHz, DMSO-d_6) δ 162.26 (d, $^1J_{CF}$ = 246.2 Hz), 154.68, 149.86, 134.31 (d, $^4J_{CF}$ = 3.2 Hz), 131.43 (d, $^3J_{CF}$= 8.5 Hz), 130.75, 122.14, 114.82 (d, $^2J_{CF}$ = 21.6 Hz). Calculated mass for $C_{10}H_7BrFN_3$ 267.988 g/mol ^{79}Br[M+H]$^+$, 269.986 g/mol ^{81}Br[M+H]$^+$. ESI-MS (methanol) *m/z*: 268.08 ^{79}Br[M+H]$^+$, 270.08 ^{81}Br[M+H]$^+$.

The reaction leads also to the *3-bromo-6-(4-fluorophenyl)pyrazin-2-amine* ***(25)****;*

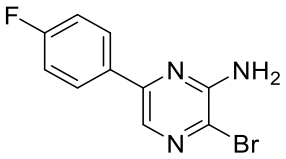

Method A: yellow solid, yield 53-62 %.

Methos B: yield 40%.

Method C: yield 30%.

Method D: yield 81%.

Method E: yield 29%.

^{1}H NMR (400 MHz, DMSO-d_6) δ 8.14 (s, 1H), 8.09 – 8.00 (m, 2H), 7.40 – 7.24 (m, 2H), 6.82 (s, 2H). ^{13}C NMR (101 MHz, DMSO-d_6) δ 163.07 (d, $^{1}J_{CF}$ = 246.9 Hz), 152.77, 147.66, 132.06, 128.77 (d, $^{3}J_{CF}$ = 8.5 Hz), 128.23, 123.93, 115.73 (d, $^{2}J_{CF}$ = 21.6 Hz). Calculated mass for $C_{10}H_7BrFN_3$ 267.988 g/mol ^{79}Br[M+H]$^+$, 269.986 g/mol ^{81}Br[M+H]$^+$. ESI-MS (methanol) *m/z*: 267.9 ^{79}Br[M+H]$^+$, 269.9 ^{81}Br[M+H]$^+$.

*Synthesis 5-(pyridin-4-yl)-6-(4-fluorophenyl)pyrazin-2-amine (**V**):*

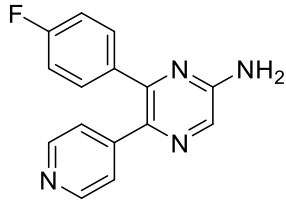

In a dry, argon-purged sealed reaction tube equipped with a magnetic stir bar, 1.0 gram of compound **24** (1 eq, 3.8 mmol), the appropriate boronic acid (1.2 eq, 4.5 mmol), and Na_2CO_3 (2.0 eq. 7.6 mmol) were added, followed by $PdCl_2(PPh_3)_2$ (0.05 eq, 0.19 mmol) a mixture of dry 1,4-dioxane, ethanol, and water was added under inert atmosphere. The tube was sealed, and the reaction mixture was heated to 120-130 °C under stirring for 12 hours. Once the reaction was completed, the solvent was

removed under reduced pressure, the solid was then dissolved in DCM (150 mL) and washed with water (3x50 mL). The organic phases were then combined and dried over anhydrous sodium sulphate. The solvent was removed and the crude purified by chromatographic column using an elution mixture composed of light petroleum and ethyl acetate (7:3). Yellow solid, yield 54%. ^{1}H NMR (400 MHz, DMSO-d_6) δ 8.42 (d, J = 6.1 Hz, 2H), 7.99 (s, 1H), 7.40 – 7.33 (m, 2H), 7.23 – 7.14 (m, 4H), 6.88 (s, 2H). ^{13}C NMR (101 MHz, DMSO-d_6) δ 166.75 (d, $^{1}J_{CF}$ = 247.2 Hz), 155.51, 148.96, 148.06, 133.47 (d, $^{4}J_{CF}$ = 2.4 Hz), 131.29, 128.92 (d, $^{3}J_{CF}$ = 8.5 Hz), 128.42, 121.39, 115.96 (d, $^{2}J_{CF}$ = 21.5 Hz), 109.91. ESI-MS (methanol) *m/z*: 267.0 $[M+H]^+$. HRMS-ESI $C_{15}H_{11}FN_4$: experimental *m/z* 267.1041 $[M+H]^+$, theoretical *m/z* 267.1041 $[M+H]^+$, Δ = 0.0000. Purity HPLC 100%.

*Synthesis 5-(pyridin-4-yl)-3-bromo-6-(4-fluorophenyl)pyrazin-2-amine (**26**):*

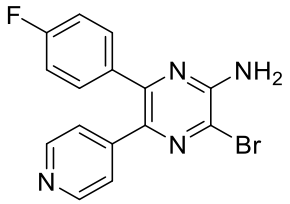

Under argon atmosphere, 1 eq. of **V** (800 mg, 3 mmol) was dissolved in DCM and 1.1 eq of NBS (3.3 mmol, 587 mg) were added to the mixture portioned. Once the adding was

terminated, the system was left at 0°C for 2 hours. Once the reaction was completed, the mixture was washed with water, brine and a saturated solution of $NaHCO_3$ (3x50 mL). The organic phase was dried under anhydrous sodium sulphate and the solvent removed under reduced pressure. The crude was purified by flash chromatography using an elution mixture of ethyl acetate and petroleum ether (6:4). Yellow solid, yield 54%. ^{1}H NMR (400 MHz, DMSO-d_6) δ 8.48 – 8.42 (m, 2H), 7.41 – 7.35 (m, 2H), 7.24 – 7.12 (m, 6H). Calculated mass for $C_{15}H_{10}BrFN_4$: 345.0146 g/mol ^{79}Br[M+H]$^+$; 347.0125 ^{81}Br[M+H]$^+$. ESI-MS (methanol) *m/z*: 345.15 ^{79}Br[M+H]$^+$; 347.13 ^{81}Br[M+H]$^+$.

*General procedure for the synthesis of 3-subtìstituted-6-(4-fluorophenyl)-5-(pyridin-4-yl)pyrazin-2-amine (**1, 2**)*:

In a sealed tube 179 mg (0.52 mmol) of compound **26** were dissolved in 1 mL of ethanol. 1 mL of 1,4-dioxane and 1.5 mL of water. In the reaction mixture were then introduced mg of Na_2CO_3 (2 eq, 1.04 mmol), and $Pd(PPh_3)_4$ in catalytic amounts (0.05 eq, 0.026 mmol) and the system heated at 120-130°C for 10 hours. Once the reaction was completed the solvent was removed under reduced pressure and then the crude dissolved in ethyl acetate (30 mL) and the organic phase washed with water (3x10 mL). The organic phases were collected and dried over anhydrous Na_2SO_4. The crude was then purified by flash

chromatography using a mixture of ethyl acetate and petroleum ether (8:2) as elution mixture.

*6-(4-fluorophenyl)-3-phenyl-5-(pyridin-4-yl)pyrazin-2-amine (**1**):*

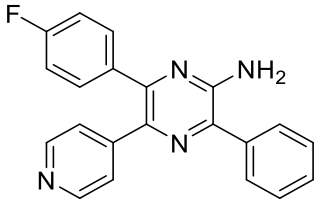

Yellow solid, yield 14%. ^{1}H NMR (400 MHz, DMSO-d_6) δ 8.47 – 8.41 (m, 2H), 7.84 – 7.79 (m, 2H), 7.56 – 7.41 (m, 5H), 7.32 – 7.26 (m, 2H), 7.26 – 7.16 (m, 2H), 6.65 (s, 2H). ^{13}C NMR (101 MHz, DMSO-d_6) δ 162.26 (d, $^{1}J_{CF}$ = 246.3 Hz), 151.42, 149.33, 147.84, 146.39, 137.26, 136.77, 136.40, 134.73, 131.65 (d, $^{3}J_{CF}$ = 8.3 Hz), 128.81, 128.75, 128.20, 123.63, 115.22 (d, $^{2}J_{CF}$ = 21.7 Hz). ESI-MS (methanol) *m/z*: 343.14 $[M+H]^{+\cdot}$ HRMS-ESI: $C_{21}H_{15}FN_4$ experimental *m/z* 343.1354 $[M+H]^{+}$; theoretical *m/z* 343.1354 $[M+H]^{+}$. Δ = 0.0000. Purity HPLC 98 %.

*6-(4-fluorophenyl)-3,5-di(pyridin-4-yl)pyrazin-2-amine (**2**):*

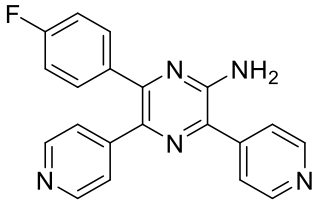

Orange solid, yield 10%. ^{1}H NMR (400 MHz, DMSO-d_6) δ 8.77 – 8.66 (m, 2H), 8.50 – 8.42 (m, 2H), 7.86 – 7.78 (m, 2H), 7.49 – 7.40 (m, 2H), 7.33 – 7.26 (m, 2H), 7.26 – 7.18 (m, 2H), 6.89 (s, 2H). ^{13}C NMR (101 MHz, DMSO-d_6) δ 160.53 (d, $^{1}J_{CF}$ = 214.4 Hz), 151.95, 151.02, 150.54, 149.84, 146.49, 144.55, 144.42, 134.86, 134.44, 132.14 (d, $^{3}J_{CF}$ = 8.6 Hz), 124.02, 123.07, 115.71 (d, $^{2}J_{CF}$ = 21.6 Hz). ESI-MS (methanol) *m/z*: 344.13 $[M+H]^+$. HRMS-ESI $C_{20}H_{14}FN_5$: experimental *m/z* 344.1305 $[M+H]^+$; theoretical *m/z* 344.1306 $[M+H]^+$. Δ = 0.0001. Purity HPLC 98%.

*General procedure for the synthesis of 3-substituted-6-(4-fluorophenyl)-5-(pyridin-4-yl)pyrazin-2-amine (**3-17**):*

The brominated derivative **26** was used to perform a nucleophilic aromatic substitution to introduce the different amino portions. In a sealed tube 150 mg (1 eq, 0.44 mmol) of **26** were dissolved in ethanol, then 3 eq (1.3 mmol) of the proper amine were introduced in the mixture. The system was left at 120-130 °C for 2-5 nights. Once the reaction was completed, the solvent was removed under reduced pressure and the obtained crude purified by flash chromatography, using an elution mixture of ethyl acetate and petroleum ether (8:2).

*5-(4-fluorophenyl)-6-(pyridin-4-yl)-N^2-(pyridin-4-ylmethyl)pyrazine-2,3-diamine (**3**):*

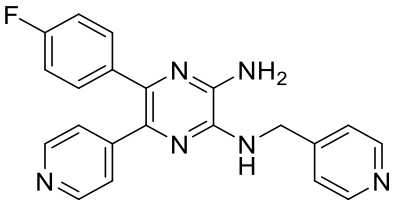

Yellow/orange solid. Yield 18 %. ^{1}H NMR (400 MHz, DMSO-d_6) δ 8.52 – 8.50 (m, 2H), 8.34 – 8.31 (m, 2H), 7.39 – 7.35 (m, 2H), 7.28 – 7.23 (m, 2H), 7.21 – 7.16 (m, 1H), 7.13 – 7.08 (m, 2H), 7.07 – 7.04 (m, 2H), 6.55 (s, 2H), 4.67 (d, J = 5.5 Hz, 2H). ESI-MS (methanol) *m/z*: 373.27 $[M+H]^+$. HRMS-ESI $C_{21}H_{17}FN_6$: experimental *m/z* 373.1570 $[M+H]^+$; theoretical *m/z* 373.1572 $[M+H]^+$. Δ = 0.0002. Purity HPLC 84%.

*N^2,N^2-diethyl-5-(4-fluorophenyl)-6-(pyridin-4-yl)pyrazine-2,3-diamine (**4**):*

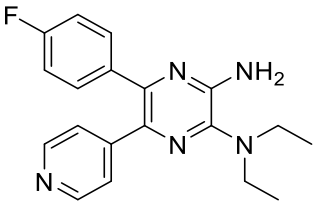

Ochre solid yield 42 %.^{1}H NMR (400 MHz, DMSO-d_6) δ 8.43 – 8.38 (m, 2H), 7.38 – 7.32 (m, 2H), 7.24 – 7.21 (m, 2H), 7.18 – 7.12 (m, 2H), 6.28 (s, 2H), 3.27 (q, J = 7.1 Hz, 5H), 1.08 (t, J = 7.0 Hz, 6H). ^{13}C NMR (101 MHz, DMSO-d_6) δ 161.66 (d, $^{1}J_{CF}$ = 211.3 Hz), 156.84, 151.26, 149.26, 147.82, 146.86, 143.33, 131.50 (d, $^{3}J_{CF}$ = 8.1 Hz), 123.64, 123.54, 119.00, 115.08 (d,

$^{2}J_{CF}$ = 21.1 Hz), 42.79, 12.64 ESI-MS (methanol) *m/z*: 338.22 $[M+H]^+$. HRMS-ESI $C_{19}H_{20}FN_5$*:* experimental *m/z* 338.1772 $[M+H]^+$; theoretical *m/z* 338.1776 $[M+H]^+$. Δ = 0.0004. Purity HPLC 96%**.**

*5-(4-fluorophenyl)-N²-propyl-6-(pyridin-4-yl)pyrazine-2,3-diamine (**5**):*

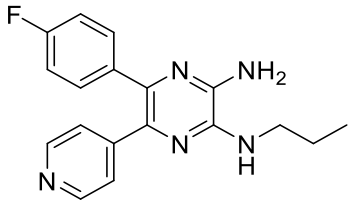

Brown solid, yield 68 %. ^{1}H NMR (400 MHz, DMSO-d_6) δ 8.40 – 8.34 (m, 2H), 7.30 – 7.23 (m, 2H), 7.23 – 7.18 (m, 2H), 7.13 – 7.05 (m, 2H), 6.51 – 6.39 (m, 3H), 3.42 – 3.35 (m, 2H), 1.65 (h, *J* = 7.4 Hz, 2H), 0.96 (t, *J* = 7.4 Hz, 3H). ^{13}C NMR (101 MHz, DMSO-d_6) δ 161.38 (d, $^{1}J_{CF}$ = 244.0 Hz), 149.07, 147.66, 143.05, 141.48, 136.27, 135.90, 132.61, 131.39 (d, $^{3}J_{CF}$ = 8.2 Hz), 123.71, 114.86 (d, $^{2}J_{CF}$ = 21.4 Hz), 42.66, 21.92, 11.78. ESI-MS (methanol) *m/z*: 324.18 $[M+H]^+$. HRMS-ESI $C_{18}H_{18}FN_5$*:* experimental *m/z* 324.1617 $[M+H]^+$; theoretical *m/z* 324.1619 $[M+H]^+$. Δ = 0.0002. Purity HPLC 95 %.

*6-(4-fluorophenyl)-5-(pyridin-4-yl)-3-(pyrrolidin-1-yl)pyrazin-2-amine (**6**):*

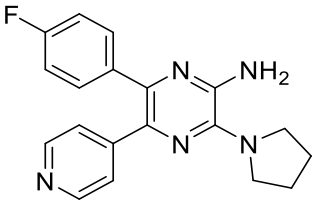

Pale yellow solid, yield 42%. ^{1}H NMR (400 MHz, DMSO-d_6) δ 8.42 – 8.35 (m, 2H), 7.37 – 7.30 (m, 2H), 7.28 – 7.23 (m, 2H), 7.18 – 7.09 (m, 2H), 6.21 (s, 2H), 3.39 (t, J = 6.8 Hz, 2H), 3.25 (t, J = 6.8 Hz, 2H), 1.88 – 1.80 (m, 3H), 1.80 – 1.67 (m, 1H). HRMS-ESI $C_{19}H_{18}FN_5$: experimental *m/z* 336.1617 $[M+H]^+$; theoretical *m/z* 336.1619 $[M+H]^+$. Δ = 0.0002. Purity HPLC 98 %.

6-(4-fluorophenyl)-3-(piperidin-1-yl)-5-(pyridin-4-yl)pyrazin-2-amine (**7**):

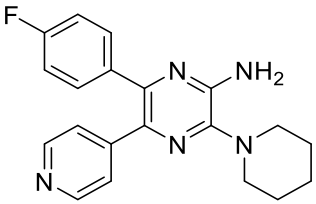

Orange solid. Yield 64%. ^{1}H NMR (400 MHz, DMSO-d_6) δ 8.46 – 8.36 (m, 2H), 7.41 – 7.29 (m, 2H), 7.28 – 7.18 (m, 2H), 7.18 – 7.08 (m, 1H), 6.36 (s, 2H), 3.17 – 3.10 (m, 2H), 3.04 – 2.98 (m, 2H), 1.74 – 1.53 (m, 8H). ^{13}C NMR (101 MHz, DMSO-d_6) δ 189.91 (d, $^{1}J_{CF}$ = 203.7 Hz), 174.29, 173.67, 149.20, 147.38, 147.18, 135.30 (d, $^{2}J_{CF}$ = 25.0 Hz), 131.41, 123.50, 48.85, 44.02,

25.13, 22.60. HRMS-ESI $C_{20}H_{20}FN_5$*:* experimental *m/z* 350.1774 $[M+H]^+$; theoretical *m/z* 350.1776 $[M+H]^+$. Δ = 0.0002. Purity HPLC 97 %.

N^2-cyclohexyl-5-(4-fluorophenyl)-6-(pyridin-4-yl)pyrazine-2,3-diamine (**8**):

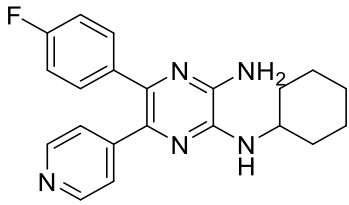

White solid, yield 12%. ^{1}H NMR (400 MHz, DMSO-d_6) δ 8.41 (d, *J* = 31.2 Hz, 2H), 7.29 – 7.22 (m, 2H), 7.22 – 7.14 (m, 3H), 7.14 – 7.06 (m, 2H), 6.47 (s, 2H), 6.19 (d, *J* = 6.8 Hz, 1H), 3.97 – 3.84 (m, 1H), 2.03 (d, *J* = 12.2 Hz, 2H), 1.81 – 1.71 (m, 2H), 1.69 – 1.51 (m, 2H), 1.38 – 1.21 (m, 4H). ^{13}C NMR (101 MHz, DMSO-d_6) δ 150.92 (d, $^1J_{CF}$ = 283.2 Hz), 149.12, 147.75, 143.02, 140.65, 135.86, 132.58, 131.42 (d, $^3J_{CF}$ = 8.0 Hz), 123.72, 123.53, 114.93 (d, $^2J_{CF}$ = 21.1 Hz), 49.35, 32.54, 29.60, 25.65, 24.85. ESI-MS (methanol) *m/z*: 364.19 $[M+H]^+$. HRMS-ESI $C_{21}H_{22}FN_5$: experimental *m/z* 364.1933 $[M+H]^+$; theoretical *m/z* 364.1932 $[M+H]^+$. Δ = 0.0001. Purity HPLC 100 %.

6-(4-fluorophenyl)-3-(4-methylpiperazin-1-yl)-5-(pyridin-4-yl)pyrazin-2-amine (**9**):

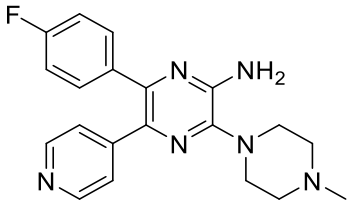

White solid, yield 87%. ^{1}H NMR (400 MHz, DMSO-d_6) δ 8.44 – 8.37 (m, 2H), 7.38 – 7.31 (m, 2H), 7.26 – 7.20 (m, 2H), 7.19 – 7.12 (m, 2H), 6.41 (s, 2H), 3.20 (s, 4H), 2.56 (s, 4H), 2.26 (s, 3H). ^{13}C NMR (101 MHz, DMSO-d_6) δ 155.56 (d, $^{1}J_{CF}$ = 254.8 Hz), 149.22, 147.34 (d, $^{4}J_{CF}$ = 3.4 Hz), 146.92, 146.64, 143.79, 142.39, 135.31, 132.89, 131.45 (d, $^{3}J_{CF}$ = 8.2 Hz), 123.49, 115.06 (d, $^{2}J_{CF}$ = 21.3 Hz), 109.55, 54.24, 47.42, 45.88. ESI-MS (methanol) *m/z*: 365.33 $[M+H]^+$. HRMS-ESI $C_{20}H_{21}FN_6$: experimental *m/z* 365.1886 $[M+H]^+$; theoretical *m/z* 365.1885 $[M+H]^+$. Δ = 0.0001. Purity HPLC 95 %.

*6-(4-fluorophenyl)-3-morpholino-5-(pyridin-4-yl)pyrazin-2-amine (**10**):*

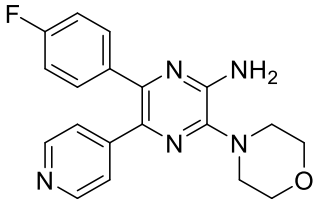

Pale yellow solid, yield 73%. ^{1}H NMR (400 MHz, DMSO-d_6) δ 8.41 (s, 2H), 7.35 (s, 2H), 7.25 (s, 2H), 7.16 (s, 2H), 6.54 (s, 2H), 3.80 (s, 4H), 3.16 (t, J = 4.6 Hz, 4H). ^{13}C NMR (101 MHz,

DMSO-d_6) δ 161.97 (d, $^1J_{CF}$ = 244.9 Hz), 149.30, 147.11, 146.75, 143.66, 142.87, 133.01, 131.57 (d, $^3J_{CF}$ = 8.2 Hz), 123.64, 115.20 (d, $^2J_{CF}$ = 21.6 Hz), 109.66, 65.97, 48.23. ESI-MS (methanol) *m/z*: 352.25 $[M+H]^+$. HRMS-ESI $C_{19}H_{19}FN_5O$: experimental *m/z* 352.1566 $[M+H]^+$; theoretical *m/z* 352.1568 $[M+H]^+$. Δ = 0.0002. Purity HPLC 100 %.

*1-(4-(3-amino-5-(4-fluorophenyl)-6-(pyridin-4-yl)pyrazin-2-yl)piperazin-1-yl)ethan-1-one (**11**):*

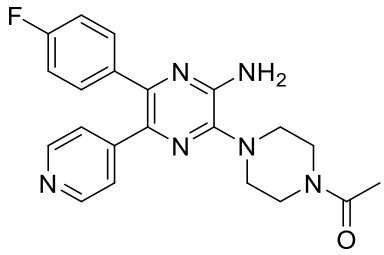

Ochre powder, yield 25 %. ^{1}H NMR (400 MHz, DMSO-d_6) δ 8.46 – 8.35 (m, 2H), 7.41 – 7.31 (m, 2H), 7.28 – 7.20 (m, 2H), 7.21 – 7.09 (m, 2H), 6.58 (s, 2H), 3.73 – 3.60 (m, 4H), 3.24 – 3.14 (m, 2H), 3.18 – 3.03 (m, 3H), 2.05 (s, 3H). ^{13}C NMR (101 MHz, DMSO-d_6) δ 170.06 (d, $^1J_{CF}$ = 248.1 Hz), 169.32, 161.08, 149.45, 147.53, 147.15, 143.91, 143.45, 135.47 (d, $^4J_{CF}$ = 3.2 Hz), 131.87 (d, $^3J_{CF}$ = 8.0 Hz), 124.06, 115.53 (d, $^2J_{CF}$ = 21.4 Hz), 48.35, 47.92, 45.78, 40.98, 21.50. HRMS-ESI $C_{21}H_{21}FN_6O$: calculated *m/z* 393.1834 $[M+H]^+$, experimental *m/z* 393.1830 $[M+H]^+$, Δ= 0.0004. Purity HPLC 98 %.

*1-(4-((3-amino-5-(4-fluorophenyl)-6-(pyridin-4-yl)pyrazin-2-yl)amino)piperidin-1-yl)ethan-1-one (**12**):*

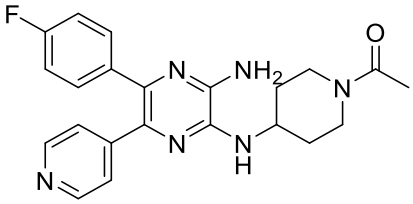

Yellow solid, yield 35%. ^{1}H NMR (400 MHz, DMSO-d6) δ 8.46 – 8.35 (m, 2H), 7.87 (d, J = 7.5 Hz, 1H), 7.39 – 7.30 (m, 2H), 7.27 – 7.22 (m, 2H), 7.19 – 7.12 (m, 2H), 6.42 (s, 2H), 3.79 – 3.68 (m, 1H), 3.61 (d, J = 12.7 Hz, 2H), 2.86 (t, J = 11.9 Hz, 2H), 2.11 – 1.93 (m, 1H), 1.85 – 1.78 (m, 3H), 1.70 – 1.56 (m, 2H). ^{13}C NMR (101 MHz, DMSO-d_6) δ 169.46, 162.19 (d, $^{1}J_{CF}$ = 245.2 Hz), 149.42, 147.31, 147.20, 144.48, 142.69, 135.54 (d, $^{4}J_{CF}$ = 3.1 Hz), 133.36, 131.79 (d, $^{3}J_{CF}$ = 8.3 Hz), 123.98, 115.45 (d, $^{2}J_{CF}$ = 21.4 Hz), 47.00, 46.34, 31.29, 22.98. Calculated mass for $C_{22}H_{23}FN_6O$: 407.199 $[M+H]^+$. ESI-MS (methanol) 407.30 $[M+H]^+$. HRMS – ESI $C_{22}H_{23}FN_6O$: calculated *m/z* 407.1990 $[M+H]^+$, experimental *m/z* 407.1991 $[M+H]^+$. Δ = 0.0001. Purity HPLC 99 %.

*3-(4-aminopiperidin-1-yl)-6-(4-fluorophenyl)-5-(pyridin-4-yl)pyrazin-2-amine (**13**):*

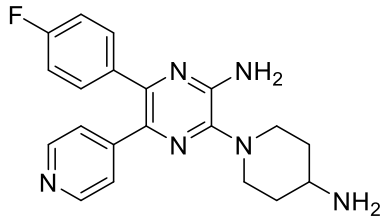

Yellow/orange solid, yield 31%. ^{1}H NMR (400 MHz, DMSO-d_6) δ 8.47 (s, 2H), 8.13 (s, 2H), 7.37 (m, , 2H), 7.18 (m, 2H), 6.64 (s, 2H), 3.71 (m, 2H), 3.07 (m, 4H), 2.04 – 1.97 (m, 3H), 1.79 (m, 3H), ESI-MS (methanol) 365.28 $[M+H]^+$. HRMS-ESI $C_{20}H_{21}FN_6$: calculated *m/z* 365.1884 $[M+H]^+$, experimental *m/z* 365.1884 $[M+H]^+$. Δ = 0.0000. Purity HPLC 96 %.

*tert-butyl 3-((3-amino-5-(4-fluorophenyl)-6-(pyridin-4-yl)pyrazin-2-yl)amino)piperidine-1-carboxylate (**14**):*

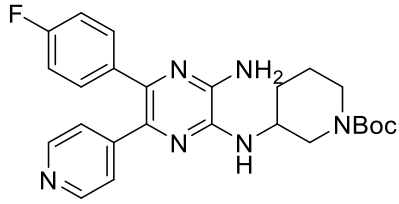

Yellow/orange solid, yield 30%. ^{1}H NMR (400 MHz, DMSO-d_6) δ 8.40 – 8.33 (m, 2H), 7.33 – 7.27 (m, 2H), 7.23 – 7.15 (m, 2H), 7.15 – 7.09 (m, 2H), 6.77 (s, 1H), 6.55 (s, 2H), 3.95 – 3.87 (m, 1H), 3.76 – 3.60 (m, 2H), 3.49 – 3.34 (m, 2H), 1.95 – 1.71 (m, 3H), 1.71 – 1.59 (m, 2H), 1.38 (s, 8H). Calculated mass for

$C_{25}H_{29}FN_6O_2$: 465.24 g/mol $[M+H]^+$. ESI-MS (methanol) *m/z*: 465.36 $[M+H]^+$.

tert-butyl 4-((3-amino-5-(4-fluorophenyl)-6-(pyridin-4-yl)pyrazin-2-yl)amino)piperidine-1-carboxylate (**15**):

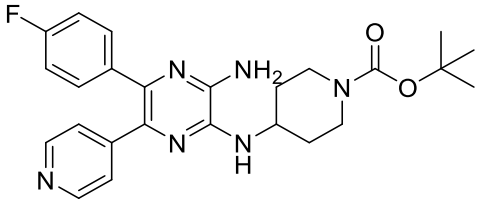

Yellow/orange solid, yield 32%. ^{1}H NMR (400 MHz, DMSO-d_6) δ 8.38 (d, J = 5.9 Hz, 2H), 7.26 (dd, J = 8.7, 5.7 Hz, 2H), 7.22 – 7.17 (m, 2H), 7.10 (t, J = 8.9 Hz, 2H), 6.47 (s, 2H), 6.26 (d, J = 6.7 Hz, 1H), 4.16 – 4.04 (m, 1H), 3.90 (d, J = 14.0 Hz, 2H), 2.97 (s, 3H), 2.07 – 1.98 (m, 2H), 1.41 (s, 9H). Calculated mass for $C_{25}H_{29}FN_6O_2$: 465.24 g/mol $[M+H]^+$. ESI-MS (methanol) *m/z*: 465.33 $[M+H]^+$.

*tert-butyl 4-(3-amino-5-(4-fluorophenyl)-6-(pyridin-4-yl)pyrazin-2-yl)piperazine-1-carboxylate (**16**):*

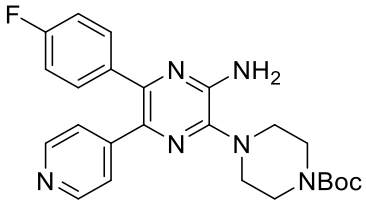

Yellow solid, yield 75%. ^{1}H NMR (400 MHz, DMSO-d_6) δ 8.42 – 8.39 (m, 2H), 7.38 – 7.33 (m, 2H), 7.25 – 7.22 (m, 2H), 7.19 – 7.14 (m, 2H), 6.55 (s, 2H), 3.58 – 3.51 (m, 4H), 3.15 – 3.09 (m, 4H), 1.43 (s, 9H). Calculated mass for $C_{24}H_{27}FN_6O_2$: 451.2252 g/mol M+H]$^+$. ESI-MS (methanol) *m/z*: 451.22 M+H]$^+$.

*tert-butyl (2-((3-amino-5-(4-fluorophenyl)-6-(pyridin-4-yl)pyrazin-2-yl)amino)ethyl)carbamate (**17**):*

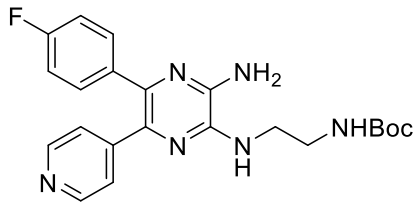

Orange solid, yield 29 %. ^{1}H NMR (400 MHz, DMSO-d_6) δ 8.40 – 8.35 (m, 2H), 7.31 – 7.21 (m, 4H), 7.14 – 7.08 (m, 2H), 6.94 – 6.88 (m, 1H), 6.58 – 6.53 (m, 1H), 6.42 (s, 2H), 3.50 – 3.43 (m, 2H), 3.25 – 3.17 (m, 2H), 1.37 (s, 9H). Calculated mass for $C_{22}H_{25}FN_6O_2$: 425.21 g/mol [M+H]$^+$. ESI-MS (methanol) *m/z*: 425.30 [M+H]$^+$. Purity HPLC 97 %.

*General procedure **for** Boc (tert-butoxycarbonyl) group removal (**18-21**).*

1 eq of the Boc-protected derivatives (**14-17**) was introduced in a round bottomed flask, and 2 mL of HCl in dioxane (4M), were introduced using a syringe and covering the flask with a flip-

flop cap. The reaction was left at room temperature for 12 hours under stirring.

*N^2-(2-aminoethyl)-5-(4-fluorophenyl)-6-(pyridin-4-yl)pyrazine-2,3-diamine (**18**):*

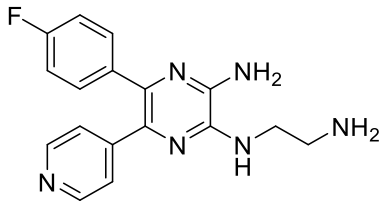

Orange/brown solid, yield 64 %. ^{1}H NMR (400 MHz, DMSO-d_6) δ 8.69 – 8.56 (m, 2H), 8.42 – 8.14 (m, 4H), 7.87 – 7.80 (m, 2H), 7.45 – 7.36 (m, 2H), 7.28 – 7.17 (m, 2H), 3.80 – 3.67 (m, 2H), 3.24 – 3.03 (m, 3H). ^{13}C NMR (101 MHz, DMSO-d_6) δ 163.89 (d, $^1J_{CF}$ = 189.1 Hz), 149.11, 149.10, 143.70, 141.23, 136.89, 131.37 (d, $^3J_{CF}$ = 8.7 Hz), 127.51, 123.69, 121.45, 114.93 (d, $^2J_{CF}$ = 21.5 Hz), 48.29, 44.19. ESI-MS (methanol) *m/z*: 325.25 $[M+H]^+$. HRMS-ESI $C_{17}H_{17}FN_6$: experimental *m/z* 325.1570 $[M+H]^+$; theoretical *m/z* 325.1572 $[M+H]^+$. Δ = 0.0002. Purity HPLC 96%.

*5-(4-fluorophenyl)-N2-(piperidin-3-yl)-6-(pyridin-4-yl)pyrazine-2,3-diamine (**19**):*

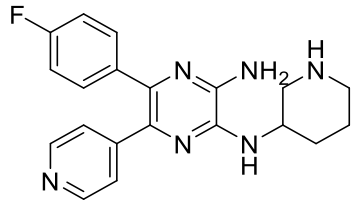

Brown solid, yield 59%. ^{1}H NMR (400 MHz, DMSO-d_6) δ 9.47 (s, 2H), 8.98 (s, 2H), 8.63 – 8.56 (m, 2H), 7.88 – 7.81 (m, 2H), 7.43 – 7.36 (m, 2H), 7.26 – 7.19 (m, 2H), 4.50 – 4.39 (m, 2H), 3.06 – 2.94 (m, 2H), 2.94 – 2.83 (m, 2H), 2.05 – 1.95 (m, 2H), 1.89 – 1.69 (m, 4H). ^{13}C NMR (101 MHz, DMSO-d_6) δ 173.70, 162.36 (d, J = 246.0 Hz), 155.46, 144.30, 141.37, 140.42, 134.24, 131.80 (d, J = 8.1 Hz), 128.63, 125.47, 115.86 (d, J = 21.7 Hz), 46.22, 44.77, 44.32, 27.53, 20.45. HRMS-ESI $C_{20}H_{21}FN_6$: experimental *m/z* 365.1884 $[M+H]^+$; theoretical *m/z* 365.1885 $[M+H]^+$. Δ = 0.0001. Purity HPLC 94%.

5-(4-fluorophenyl)-N^2-(piperidin-4-yl)-6-(pyridin-4-yl)pyrazine-2,3-diamine (**20**):

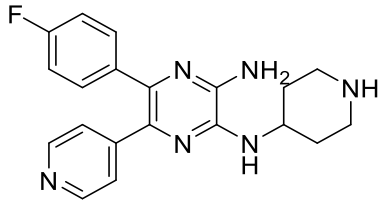

Brown solid, yield 76%. ^{1}H NMR (400 MHz, DMSO-d_6) δ 9.03 (d, J = 41.3 Hz, 2H), 8.61 (d, J = 6.0 Hz, 2H), 7.78 (d, J = 6.0 Hz, 2H), 7.42 – 7.19 (m, 6H), 4.29 – 4.22 (m, 2H), 3.44 – 3.31

(m, 3H), 3.13 – 2.97 (m, 3H), 2.22 – 2.11 (m, 2H), 1.94 – 1.79 (m, 3H). ^{13}C NMR (101 MHz, DMSO-d_6) δ 160.60 (d, $^{1}J_{CF}$ = 171.1 Hz), 144.28, 140.58, 134.74, 131.70 (d, $^{3}J_{CF}$ = 8.2 Hz), 128.74, 125.20, 115.69 (d, $^{2}J_{CF}$ = 23.0 Hz), 109.57, 48.60, 41.90, 27.70. ESI-MS (methanol) *m/z*: 365.33 $[M+H]^+$. HRMS-ESI $C_{20}H_{21}FN_6$: experimental *m/z* 365.1884 $[M+H]^+$; theoretical *m/z* 365.1885 $[M+H]^+$. Δ = 0.0001. Purity HPLC 99 %.

*6-(4-fluorophenyl)-3-(piperazin-1-yl)-5-(pyridin-4-yl)pyrazin-2-amine (**21**):*

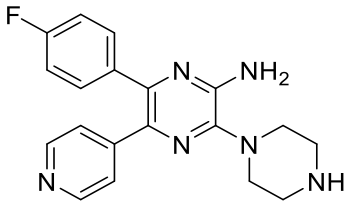

Yellow solid. Yield 92 %. ^{1}H NMR (400 MHz, DMSO-d_6) δ 9.57 (s, 2H), 8.73 – 8.64 (m, 2H), 7.84 – 7.76 (m, 2H), 7.50 – 7.43 (m, 2H), 7.28 – 7.22 (m, 3H), 3.49 – 3.38 (m, 4H), 3.36 – 3.26 (m, 4H). ^{13}C NMR (101 MHz, DMSO-d_6) δ 162.51 (d, $^{1}J_{CF}$ = 246.6 Hz), 155.13, 148.06, 146.82, 142.89, 140.69, 134.33 (d, $^{4}J_{CF}$ = 3.0 Hz), 131.72 (d, $^{3}J_{CF}$ = 8.2 Hz), 129.22, 125.21, 115.75 (d, $^{2}J_{CF}$ = 21.6 Hz), 44.52, 42.34. ESI-MS (methanol) *m/z*: 351.17 $[M+H]^+$. HRMS-ESI $C_{19}H_{19}FN_6$: experimental *m/z* 351.1727 $[M+H]^+$; theoretical *m/z* 351.1728 $[M+H]^+$. Δ = 0.0001. Purity HPLC 96%.

*Synthesis of tert-butyl (3-bromo-6-(4-fluorophenyl)pyrazin-2-yl)(tert-butoxycarbonyl)carbamate (**27**):*

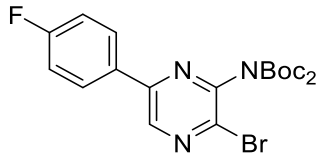

Toto 4.3 g (1 eq, 16.2 mmol) of compound **25** were used to protect the amino group in presence of ditertbutyldicarbonate in anhydrous THF (173 mL) the system was left at 0°C and then 390 mg (0.2 eq, 3.24 mmol) of DMAP were introduced portioned. The system was left under stirring for 2 hours. The solvent was removed and the crude solubilized in 100 mL of ethyl acetate, and the solution washed with water and brine (30 mL x3). The organic phases were collected and dried over anhydrous Na_2SO_4. Once the solvent was removed under reduced pressure, the crude was purified with chromatographic column using an elution mixture of 9:1 petroleum ether and ethyl acetate. The product was precipitated from ethyl acetate and petroleum ether. Pale yellow solid, yield 97%. ^{1}H NMR (400 MHz, DMSO-d_6) δ 9.15 (s, 1H), 8.29 – 8.11 (m, 2H), 7.46 – 7.36 (m, 3H), 1.37 (s, 18H). ^{13}C NMR (101 MHz, dmso) δ 164.06 (d, $^1J_{CF}$ = 249.1 Hz), 149.31, 149.24, 146.95, 141.34 (CH), 137.91, 130.44 (d,$^4J_{CF}$ = 3.1 Hz), 129.67 (CH, d, $^3J_{CF}$ = 8.8 Hz), 116.71 (CH, d, $^2J_{CF}$ = 23.6 Hz), 84.24, 27.65 (CH_3).

ESI-MS (methanol): *m/z* 490.1 $^{79}Br[M+Na]^+$, 492.1 $^{81}Br[M+Na]^+$, *m/z* 390.0 $[M\text{-}Boc+Na]^+$.

*Synthesis of tert-butyl (3-butyl-6-(4-fluorophenyl)pyrazin-2-yl)carbamate (**28**):*

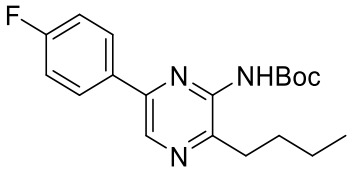

Under argon atmosphere, in 33 mL of anhydrous THF, were introduced 593 mg of magnesium (9 eq, 24.4 mmol) and a catalytic amount of iodine. To the mixture 1.87 mL (6 eq, 16 mmol) of bromobutane were added slowly. The system was left at 70 °C for 2 hours. The resulting product was directly utilized in the next synthetic step without further purification. Separately, 1.0 grams of compound **27** (1 eq, 2.71 mmol) was solubilized in 30 mL of anhydrous THF then 8.6 mg $Fe(acac)_3$ (0.03 eq, 0.024 mmol) and 27 ml of NMP were added to the reaction mixture. The system was left in ice bath and the Grignard Reagent freshly prepared was introduced slowly. The system was left at 0 °C for 3 hours. Once completed the reaction, the solvent was removed under reduced pressure, the crude was then solved in diethylether (60 mL) and washed with water and brine (3x20 mL). The organic phases were then collected and dried over anhydrous Na_2SO_4. The crude was then purified by

chromatographic column using an elution mixture composed by petroleum ether and ethyl acetate 9:1. The product (**28**) was then precipitated using ethyl acetate and petroleum ether. White powder, yield 44%. ^{1}H NMR (400 MHz, DMSO-d_6) δ 9.49 (s, 4H), 8.96 (s, 5H), 8.17 – 8.09 (m, 10H), 7.39 – 7.31 (m, 10H), 2.78 (t, J = 8.0 Hz, 9H), 1.66 (p, J = 7.5 Hz, 14H), 1.46 (s, 38H), 1.39 – 1.25 (m, 14H), 0.89 (t, J = 7.3 Hz, 13H). ESI-MS (methanol) *m/z*: 368.1 $[M\text{-}Boc+Na]^{+}$.

*Synthesis of 3-butyl-6-(4-florophenyl)pyrazin-2-amine (**29**):*

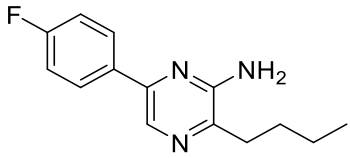

60 mg (1 eq, 0.18 mmol) of **28** were introduced in a round bottomed flask, and 4 ml of hydrochloric acid in 1,4-dioxane (4M) were introduced in the flask. The system was left at room temperature under stirring overnight. When the reaction was terminated, the solvent was removed and the product precipitated using methanol and ethyl acetate. Yellow powder, yield 49%. ^{1}H NMR (400 MHz, DMSO-d_6) δ 8.23 (s, 1H), 8.08 – 7.97 (m, 2H), 7.32 – 7.24 (m, 2H), 6.28 (s, 2H), 2.73 – 2.59 (m, 2H), 1.74 – 1.58 (m, 2H), 1.45 – 1.29 (m, 2H), 1.02 – 0.82 (m, 3H). ^{13}C NMR (101 MHz, DMSO-d_6) δ 162.99 (d, $^{1}J_{CF}$ = 245.7 Hz), 153.31, 145.76, 141.71, 133.92 (d, $^{3}J_{CF}$ = 3.0 Hz),

128.67, 128.63, 127.98, 115.91 (d, $^2J_{CF}$ = 21.5 Hz), 32.26, 28.72, 22.39, 14.37. Calculated mass for $C_{14}H_{16}FN_3$: 246.140 g/mol $[M+H]^+$. ESI-MS (methanol): *m/z* 246.0 $[M+H]^+$.

*Synthesis of 5-bromo-3-butyl-6-(4-fluorophenyl)pyrazin-2-amine (**30**):*

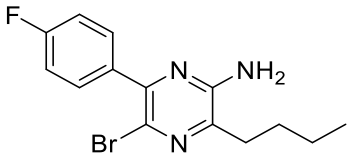

115 mg (1 eq, 0.47 mmol) of compound **29** were introduced in a three necked round bottomed flask, after argon atmosphere. 5 mL of dry dichloromethane were introduced in the same flask keeping the Ar atmosphere. The system was left a 0°C and 99.5 mg (1.2 eq, 0.56 mmol) of NBS were added portioned to the mixture. After the addition of NBS was complete, the reaction mixture was stirred at 0 °C for 1 hour. The progress of the reaction was monitored by TLC using a petroleum ether/ethyl acetate (7:3) mixture as elution system. Once completed the solvent was removed under reduced pressure and the crude solved in dichloromethane (100 ml) and washed with water, brine solution and a saturated solution of $NaHCO_3$ (3x 30 mL). The organic phases collected and dried over anhydrous Na_2SO_4. The salt was filtered the solvent removed under reduced pressure and the solid purified by chromatography column using an elution mixture composed by petroleum ether and ethyl

acetate (7:3). White powder, yield 19%. ^{1}H NMR (400 MHz, DMSO-d_6) δ 7.69 – 7.62 (m, 2H), 7.32 – 7.22 (m, 2H), 6.55 (s, 2H), 2.66 – 2.57 (m, 2H), 1.62 (p, J = 7.5 Hz, 2H), 1.46 – 1.33 (m, 2H), 0.93 (t, J = 7.3 Hz, 3H). Calculated mass for $C_{14}H_{15}BrFN_3$: 324.05 g/mol ^{79}Br[M+H]$^+$; 326.1 g/mol ^{81}Br[M+H]$^+$. ESI-MS (methanol) *m/z*: 324.1 ^{79}Br[M+H]$^+$; 326.1 ^{81}Br[M+H]$^+$.

*Synthesis 3-butyl-6-(4-fluorophenyl)-5-(pyridin-4-yl)pyrazin-2-amine (**31**):*

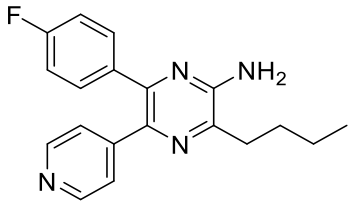

Under argon atmosphere the bromo derivative **30** was dissolved in dry 1,4-dioxane, ethanol and water. In the reaction mixture were introduced tot mg of 4-pyridinylboronic acid, x grams of Na_2CO_3 (2 eq, mmol) and $PdCl_2(PPh_3)_2$ as catalyst (0.04 eq, mmol). The reaction system was heated at 120 °C overnight. When the reaction completed the solvent was removed under reduced pressure, and the solid dissolved in ethyl acetate. The organic phase was washed with water. The organic phases were collected and dried over dry Na_2SO_4. and the solvent was removed under reduced pressure. The crude was purified through chromatographic column using an elution mixture

composed by ethyl acetate and petroleum ether (8:2). The purified solid has been precipitated with ethyl acetate and diethyl ether. White solid, yield 60%. ^{1}H NMR (400 MHz, DMSO-d_6) δ 8.41 (d, J = 5.4 Hz, 2H), 7.39 – 7.31 (m, 2H), 7.25 – 7.19 (m, 2H), 7.19 – 7.12 (m, 2H), 6.66 (s, 2H), 2.71 (t, J = 7.6 Hz, 2H), 1.71 (p, J = 7.6 Hz, 2H), 1.42 (h, J = 7.6 Hz, 2H), 0.94 (t, J = 7.3 Hz, 3H). ^{13}C NMR (101 MHz, DMSO-d_6) δ 160.79, 152.29, 149.22, 146.72 (d, $^{3}J_{CF}$ = 8.4 Hz), 140.85, 135.28, 134.99, 131.51 (d, $^{3}J_{CF}$ = 8.5 Hz), 123.53, 115.09 (d, $^{2}J_{CF}$ = 21.5 Hz), 31.66, 28.25, 22.01, 13.96. ESI-MS (methanol) *m/z* $C_{19}H_{19}FN_4$: 323.16 $[M+H]^+$. HRMS-ESI $C_{19}H_{19}FN_4$: experimental *m/z* 323.1664 $[M+H]^+$, theoretical *m/z* 323.1667 $[M+H]^+$, Δ = 0.0003. Purity HPLC 100%.

4.1.1.2. Investigation at position 2

General procedure for the Synthesis of 6-chloro-N-substitutedpyrazin-2-amine

A three-neck round-bottom flask was dried under vacuum and subsequently flushed with argon. To the flask were added sodium hydride (3.0 eq, 60% purity) and dry THF to afford a 0.16 M suspension of NaH in THF. 6-Chloro-2-aminopyrazine **22** (1.0 eq) was then introduced, and the reaction mixture was cooled in an ice bath for approximately 30 minutes. Subsequently, methyl iodide (1.2 eq) was added dropwise. The mixture was maintained at 0 °C for several hours. Upon completion of the reaction, the solvent was removed under reduced pressure. The crude residue was purified by flash column chromatography using a 9:1 mixture of petroleum ether/ethyl acetate as the eluent to afford the desired product.

*Synthesis of 6-chloro-N-methylpyrazin-2-amine (**32**):*

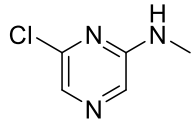

Pale yellow solid, yield 49%. ^{1}H NMR (400 MHz, DMSO-d_6) δ 7.85 (s, 1H), 7.67 (s, 1H), 7.50 (s, 1H), 2.78 (d, J = 4.8 Hz, 3H). Calculated mass for $C_5H_6ClN_3$: 144.03 g/mol ^{35}Cl[M+H]$^{+}$,

146.03 g/mol $^{37}Cl[M+H]^+$. ESI-MS (methanol) *m/z*: 143.95 $^{35}Cl[M+H]^+$, *m/z* 145.98 $^{37}Cl[M+H]^+$.

The reaction leads also to 6-*chloro-N,N-dimethylpyrazin-2-amine* (**33**) as a yellow solid.

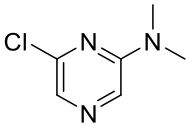

Yield 40 %. ^1H NMR (400 MHz, DMSO-d_6) δ 8.10 (s, 1H), 7.79 (s, 1H), 3.07 (s, 6H). Calculated mass for $C_6H_8ClN_3$: 158.048 g/mol $^{35}Cl[M+H]^+$, 160.48 g/mol $^{37}Cl[M+H]^+$. ESI-MS (methanol) m/z: 157.99 $^{35}Cl[M+H]^+$, 159.96 $^{37}Cl[M+H]^+$.

The two compounds were isolated and used to perform the following reaction separately.

*General synthesis of the 6-(4-fluorophenyl)-N-substitutedpyrazin-2-amine (**34**,**35**).*

The methylated compounds obtained from the previous steps, were solubilized using 1,4-dioxane, ethanol and water in a sealed tube (1eq). The 4-fluorophenyl boronic acid (1.2 eq), the catalyst $Pd(PPh_3)_4$ (0.05 eq) and Na_2CO_3 (2eq) were then added to the system. The reaction mixture was heated at 120°C for 5 hours. At reaction completion, the solvent was removed under reduced pressure, the crude redissolved in dichloromethane (70 mL) and washed with water (3x20 mL). The organics phases

were collected and dried under anhydrous Na_2SO_4. The salt was then filtered and the solvent evaporated in vacuo. The crude was then purified by precipitation using ethyl acetate and petroleum ether.

*6-(4-fluorophenyl)-N-methylpyrazin-2-amine (**34**)*:

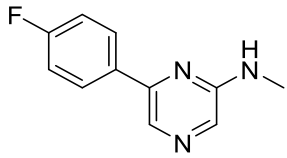

Pale yellow solid, yield 45%. ^{1}H NMR (400 MHz, DMSO-d_6) δ 8.25 (s, 1H), 8.14 – 8.06 (m, 3H), 7.87 (s, 1H), 7.34 – 7.27 (m, 2H), 7.18 – 7.07 (m, 2H), 2.88 (d, J = 4.8 Hz, 3H).

*6-(4-fluorophenyl)-N,N-dimethylpyrazin-2-amine (**35**)*:

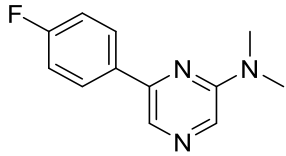

Yellow solid, yield 35%. ^{1}H NMR (400 MHz, DMSO-d_6) δ 8.38 (s, 1H), 8.17 – 8.10 (m, 3H), 7.36 – 7.26 (m, 2H), 3.14 (s, 6H).

*General procedure for the bromination reaction of the 6-(4-fluorophenyl)-N-substitutedpyrazin-2-amine (**36**, **37**):*

Under argon atmosphere compounds **34**, **35** were solubilized in dry dichloromethane, NBS (1.1eq) was solubilized in ACN and

added dropwise to the mixture while keeping the overall system in ice bath. Once the reaction was completed, the solvent was removed under reduced pressure, the crude was solubilized in DCM (50 mL) and washed with water, brine solution and a saturated solution of $NaHCO_3$ (3x15 mL). The organic phases were dried over Na_2SO_4, and the solved removed at reduced pressure. The crude was then purified by chromatographic column using an elution mixture composed by ethyl acetate/ petroleum ether in proportion 6:4. The separation was done by gradient reaching the ration 1:0.

*5-bromo-6-(4-fluorophenyl)-N-methylpyrazin-2-amine (**36**)*:

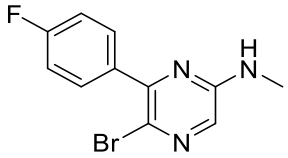

yellow/orange solid, yield%. ^{1}H NMR (400 MHz, DMSO-d_6) δ 7.76 – 7.69 (m, 3H), 7.38 – 7.26 (m, 3H), 2.80 (d, J = 4.8 Hz, 3H).

*5-bromo-6-(4-fluorophenyl)-N,N-dimethylpyrazin-2-amine (**37**)*:

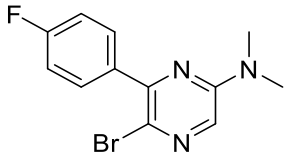

Yellow product, yield 63%. ^{1}H NMR (400 MHz, DMSO-d_6) δ 7.95 (s, 1H), 7.80 – 7.71 (m, 2H), 7.37 – 7.25 (m, 2H), 3.08 (s, 6H).

*General procedure for the synthesis of 6-(4-fluorophenyl)-N-substituted-5-(pyridin-4-yl)pyrazin-2-amine (**38**, **39**):*

After purging a sealed tube with argon, the brominated derivatives (**36**, **37**), $PdCl_2(PPh_3)_2$ (0.05 eq), Na_2CO_3 (2eq) and the 4-pyridyl boronic acid (1.1eq) were introduced in the tube and solubilized in 1,4-diozane, ethanol and water. The reaction was left at 120°C overnight. The following day, the solvent was removed under reduced pressure and the crude dissolved in ethyl acetate (50 mL) ad washed with water, (3x15 mL). the organic phases were collected, dried over anhydrous sodium sulphate and the solvent removed. The crude purified by chromatographic column using an elution mixture composed of light petroleum and ethyl acetate (7:3).

*6-(4-fluorophenyl)-N-methyl-5-(pyridin-4-yl)pyrazin-2-amine (**38**):*

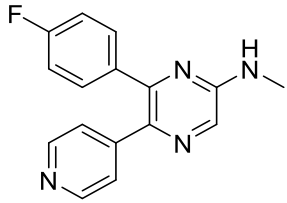

Yellow solid, yield 68 %. ^{1}H NMR (400 MHz, DMSO-d_6) δ 8.45 – 8.38 (m, 2H), 8.02 (s, 1H), 7.52 – 7.38 (m, 3H), 7.23 –

7.13 (m, 4H), 2.89 (d, J = 4.8 Hz, 3H). HRMS-ESI $C_{16}H_{13}FN_4$: calculated *m/z* 281.1197 $[M+H]^+$, experimental *m/z* 281.1196 $[M+H]^+$, Δ= 0.0001. Purity HPLC 99 %.

*6-(4-fluorophenyl)-N,N-dimethyl-5-(pyridin-4-yl)pyrazin-2-amine (**39**):*

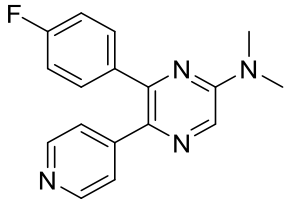

Yellow solid, yield 62%: ^{1}H NMR (400 MHz, DMSO-d_6) δ 8.44 (d, J = 5.6 Hz, 2H), 8.26 (s, 1H), 7.48 – 7.38 (m, 2H), 7.27 – 7.14 (m, 4H), 3.18 (s, 6H). HRMS-ESI $C_{17}H_{16}FN_4$: calculated *m/z* 295.1353 $[M+H]^+$, experimental *m/z* 295.1351 $[M+H]^+$. Δ= 0.0002. Purity 100%.

*General procedure for the synthesis of 3-Bromo-6-(4-fluorophenyl)-N-substituted-5-(pyridin-4-yl)pyrazin-2-amine (**40**, **41**):*

After drying under vacuum and purging with argon a multi necked round bottomed flask, the 5-pyridil derivatives **37** and **38** were introduced in the flask, solubilized in DCM and the system cooled in ice bath. NBS (1.1 eq) was then solubilized in dry ACN and added dropwise to the system. One the reaction completion, the solvent was removed under reduced pressure and the crude solubilized in DCM (40 mL) and washed with water, brine solution and a saturated solution of $NaHCO_3$ (3x20

mL). The organic phases were collected and dried over sodium sulphate, the solid was filtered and the solvent evaporated under *vacuum*. The product was purified by precipitation using ethyl acetate and diethyl ether.

*3-Bromo-6-(4-fluorophenyl)-N-methyl-5-(pyridin-4-yl)pyrazin-2-amine (**40**)*:

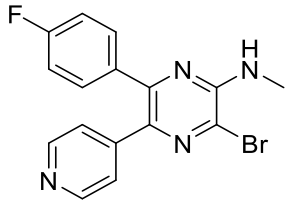

Orange solid, yield 90%. ^{1}H NMR (400 MHz, DMSO-d_6) δ 8.53 – 8.38 (m, 2H), 7.48 – 7.40 (m, 2H), 7.31 (q, J = 4.5 Hz, 1H), 7.24 – 7.17 (m, 4H), 2.94 (d, J = 4.6 Hz, 3H). Calculated mass for $C_{16}H_{12}BrFN_4$: 359.0302 ^{79}Br[M+H]$^+$, 361.03 ^{81}Br[M+H]$^+$. ESI-MS (methanol) *m/z*: 359.08 ^{79}Br[M+H]$^+$, 361.07 ^{81}Br[M+H]$^+$.

*3-Bromo-6-(4-fluorophenyl)-N,N-dimethyl-5-(pyridin-4-yl)pyrazin-2-amine (**41**)*:

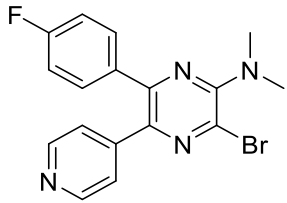

Yellow/orange powder, yield 94%.^{1}H NMR (400 MHz, DMSO-d_6) δ 8.51 – 8.48 (m, 2H), 7.53 – 7.47 (m, 2H), 7.31 – 7.27 (m, 2H), 7.24 – 7.18 (m, 2H), 3.17 (s, 6H). Calculated mass for $C_{17}H_{14}BrFN_4$: 373.0459 g/mol $^{79}Br[M+H]^+$, 375.04 $^{81}Br[M+H]^+$. ESI-MS (methanol) m/z 373.13 $^{79}Br[M+H]^+$, 375.13 $^{81}Br[M+H]^+$.

*General synthesis of compounds **42-45**:*

A solution of the previously synthesizes brominated compounds **40**, **41** (1.0 eq.) and 3 equivalents of the proper amine (morpholine or tert-butyl 4-aminopiperidine-1-carboxylate) in ethanol (7.5 mL per mmol of substrate) was heated at 120 °C for 4 days. Upon completion, the solvent was removed under reduced pressure. The crude solid was purified by column chromatography**,** eluting with a 6:4 mixture of ethyl acetate/petroleum ether and gradually increasing the polarity to an 8:2 ratio**.** Fractions containing the desired product were combined, and the solvent was removed under reduced pressure. The residue was further purified by precipitation from petroleum ether and ethyl acetate**,** affording the final product.

*6-(4-fluorophenyl)-N-methyl-3-morpholino-5-(pyridin-4-yl)pyrazin-2-amine (**42**):*

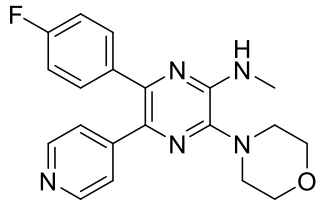

Pale yellow solid, yield 75%. ^{1}H NMR (400 MHz, DMSO-d_6) δ 8.90 – 8.63 (m, 3H), 8.44 – 8.36 (m, 2H), 7.46 – 7.38 (m, 2H), 7.28 – 7.22 (m, 2H), 7.21 – 7.12 (m, 2H), 6.66 (q, J = 4.6 Hz, 1H), 3.85 – 3.79 (m, 4H), 3.14 (t, J = 4.6 Hz, 4H), 2.93 (d, J = 4.6 Hz, 3H). ^{13}C NMR (101 MHz, DMSO-d_6) δ 161.93 (d, $^{1}J_{CF}$ = 245.1 Hz), 149.23, 146.72, 146.20, 143.95, 142.44, 135.53, 131.49 (d, $^{3}J_{CF}$ = 8.3 Hz), 131.49, 123.50, 115.13 (d, $^{2}J_{CF}$ = 21.5 Hz), 65.87, 48.40, 27.99. HRMS-ESI $C_{20}H_{20}FN_5O$: calculated *m/z* 366.1724 $[M+H]^+$, experimental *m/z* 366.1725 $[M+H]^+$. Δ= 0.0001. Purity HPLC 98%.

6-(4-fluorophenyl)-N,N-dimethyl-3-morpholino-5-(pyridin-4-yl)pyrazin-2-amine ***(43):***

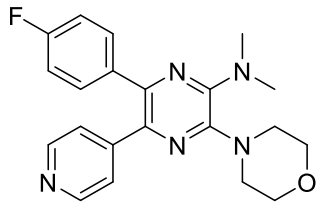

Ochre powder, yield 33%. ^{1}H NMR (400 MHz, DMSO-d_6) δ 8.54 – 8.39 (m, 2H), 7.53 – 7.42 (m, 2H), 7.40 – 7.31 (m, 2H), 7.24 – 7.09 (m, 2H), 3.81 (d, J = 4.6 Hz, 4H), 3.40 – 3.26 (m, 6H), 3.02 (s, 6H). ^{13}C NMR (101 MHz, DMSO-d_6) δ 161.96 (d, $^{1}J_{CF}$ = 245.5 Hz), 149.44, 146.15, 145.51, 143.28, 134.81 (d, $^{4}J_{CF}$ = 3.1 Hz), 134.55, 131.43 (d, $^{3}J_{CF}$ = 8.3 Hz), 123.46, 115.21 (d, $^{2}J_{CF}$ = 21.5 Hz), 65.93, 46.78, 38.22. HRMS (ESI-TOF) $C_{20}H_{20}FN_5O$: calculated *m/z* 380.1881 $[M+H]^+$, experimental *m/z* 380.1880 $[M+H]^+$, Δ= 0.0001. Purity HPLC 95%.

*tert-butyl 4-((5-(4-fluorophenyl)-3-(methylamino)-6-(pyridin-4-yl)pyrazin-2-yl)amino)piperidine-1-carboxylate (**44**):*

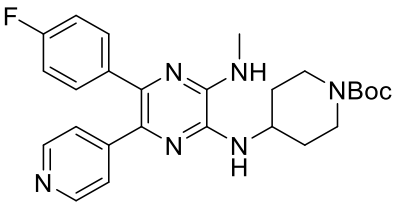

Orange solid, yield 10%. ^{1}H NMR (400 MHz, DMSO-d_6) δ 8.38 (d, J = 5.1 Hz, 2H), 7.41 – 7.26 (m, 2H), 7.21 (d, J = 5.2 Hz, 2H), 7.11 (t, J = 8.8 Hz, 2H), 6.75 (s, 1H), 6.27 (d, J = 6.5 Hz, 1H), 4.10 (s, 1H), 3.98 – 3.78 (m, 2H), 3.09 – 2.82 (m, 4H), 2.10 – 1.91 (m, 2H), 1.41 (s, 9H).

*tert-butyl 4-((3-(dimethylamino)-5-(4-fluorophenyl)-6-(pyridin-4-yl)pyrazin-2-yl)amino)piperidine-1-carboxylate (**45**):*

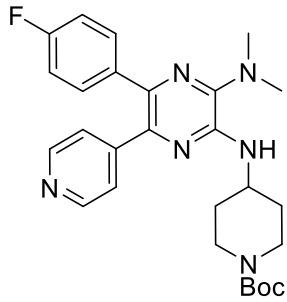

Yellow solid, yield 11%. ^{1}H NMR (400 MHz, DMSO-d_6) δ 8.48 – 8.41 (m, 2H), 7.38 – 7.32 (m, 2H), 7.31 – 7.27 (m, 2H), 7.12 (t, J = 8.9 Hz, 2H), 6.33 (d, J = 7.5 Hz, 1H), 4.16 – 4.07 (m, 1H), 3.92 (d, J = 13.2 Hz, 2H), 2.84 (s, 6H), 1.96 – 1.86 (m, 2H), 1.59 – 1.48 (m, 2H), 1.41 (s, 9H).

*General procedure for the Boc-protecting group removal (**46**, **47**)*

Tot grams of the Boc-protected derivatives (**44**, **45**) were introduced in a round bottomed flask, and 2 ml of HCl in 1,4-dioxane (4M), were introduced using a syringe and covering the flask with a cap. The reaction was left at room temperature for 12 hours under stirring.

*5-(4-fluorophenyl)-N^3-methyl-N^2-(piperidin-4-yl)-6-(pyridin-4-yl)pyrazine-2,3-diamine (**46**):*

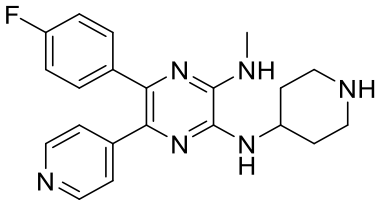

Orange solid, yield 90%. ^{1}H NMR (400 MHz, DMSO-d_6) δ 9.31 (d, J = 13.8 Hz, 1H), 9.02 (s, 1H), 8.73 – 8.63 (m, 2H), 8.01 – 7.86 (m, 2H), 7.54 – 7.43 (m, 2H), 7.26 – 7.15 (m, 2H), 6.79 (d, J = 6.5 Hz, 1H), 4.23 – 4.15 (m, 2H), 3.31 (d, J = 13.2 Hz, 2H), 3.12 – 3.00 (m, 2H), 2.98 (s, 5H), 2.12 (dd, J = 13.1, 2.4 Hz, 2H), 1.97 – 1.83 (m, 2H). ^{13}C NMR (101 MHz, DMSO-d_6) δ 155.42 (d, J = 227.3 Hz), 152.97, 149.74, 143.99, 140.69, 140.48, 135.67, 131.90 (d, J = 8.1 Hz), 125.41, 115.89 (d, J = 21.3 Hz), 45.46, 42.24, 41.87, 28.01, 27.83. HRMS-ESI $C_{21}H_{23}FN_6$: calculated *m/z* 379.2041 $[M+H]^+$, experimental *m/z* 379.2036 $[M+H]^+$, Δ= 0.0005. Purity HPLC 95%.

*5-(4-fluorophenyl)-N^3,N^3-dimethyl-N^2-(piperidin-4-yl)-6-(pyridin-4-yl)pyrazine-2,3-diamine (**47**):*

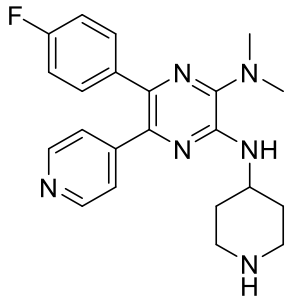

Orange/brown solid, yield 88 %. ^{1}H NMR (400 MHz, DMSO-d_6) δ 9.19 (s, 1H), 8.99 (d, J = 9.8 Hz, 1H), 8.64 – 8.54 (m, 2H), 7.84 – 7.76 (m, 2H), 7.49 – 7.41 (m, 2H), 7.26 – 7.17 (m, 2H), 4.32 – 4.23 (m, 1H), 3.44 – 3.34 (m, 2H), 3.05 (q, J = 9.8 Hz, 2H), 2.94 (s, 3H), 2.20 – 2.11 (m, 2H), 1.88 (tdd, J = 13.6, 9.0, 3.8 Hz, 2H). ^{13}C NMR (101 MHz, DMSO-d_6) δ 162.60 (d, J = 246.1 Hz), 149.71, 146.85, 142.78, 141.64, 139.06, 134.92 (d, J = 3.1 Hz), 132.15 (d, J = 8.6 Hz), 126.15, 125.62, 116.29 (d, J = 19.5 Hz). HRMS (ESI-TOF) $C_{22}H_{25}FN_6$: calculated *m/z* 393.2197 $[M+H]^+$, experimental *m/z* 393.2197 $[M+H]^+$ Δ= 0.0000. Purity HPLC 85 %.

4.1.1.3. Investigation at position 6

4.1.1.3.1. ***Pathway 1***

*General procedure for the synthesis of 6-substituted-2-aminopyrazines (**54-56, 71-75, 60-68, 80-89**):*

After drying and purging with argon a multi-necked round bottomed flask, 1 equivalent of 6-chloropyrazin-2-amine (**22**) and 1.2 equivalents of the corresponding arylboronic acid were introduced under an argon atmosphere. The reaction was carried out in a solvent system consisting of toluene (5.9 mL/mmol), ethanol (0.6 mL/mmol), and an aqueous solution of sodium carbonate 2M (1.0 mL/mmol) 0.03 eq of $Pd(PPh_3)_4$ were used as catalyst and the system was heated in reflux conditions for 4 hours, the progress monitored by TLC, using a eluent mixture composed by petroleum ether and ethyl acetate. After completion, the solvent was removed under reduced pressure. The crude was then solubilized in 150 mL of DCM and washed with water (3x 50 mL). The aqueous phases were extracted with new DCM, the organic phases combined and dried over anhydrous sodium sulphate. The solvent was then removed and the crude purified by chromatographic column. The purification stage was performed using an elution mixture composed by petroleum ether/ethyl acetate mixture (7:3) and gradually shifting to ethyl acetate/petroleum ether (7:3).

*6-(3-fluorophenyl)pyrazin-2-amine (**48**):*

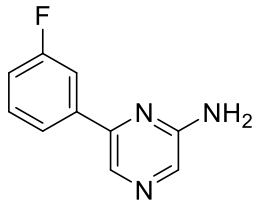

White-yellow solid, yield 98%. ^{1}H NMR (400 MHz, DMSO-d_6) δ 8.33 (s, 1H), 7.88 (s, 1H), 7.87 – 7.83 (m, 1H), 7.83 – 7.77 (m, 1H), 7.55 – 7.47 (m, 1H), 7.30 – 7.21 (m, 1H), 6.57 (s, 2H). Calculated mass for $C_{10}H_8FN_3$: 190.0775 g/mol $[M+H]^+$. ESI-MS (methanol) *m/z* 190.00 $[M+H]^+$.

*6-(2-fluorophenyl)pyrazin-2-amine (**49**):*

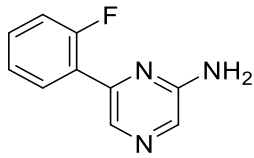

Pale yellow solid, yield 69%. ^{1}H NMR (400 MHz, DMSO-d_6) δ 8.09 (d, J = 2.8 Hz, 1H), 7.90 – 7.82 (m, 2H), 7.52 – 7.44 (m, 1H), 7.35 – 7.28 (m, 2H), 6.58 (s, 2H). Calculated mass for $C_{10}H_8FN_3$: 190.0775 g/mol $[M+H]^+$. ESI-MS (methanol) *m/z*: 190.08 $[M+H]^+$.

*6-(4-(trifluoromethyl)phenyl)pyrazin-2-amine (**50**):*

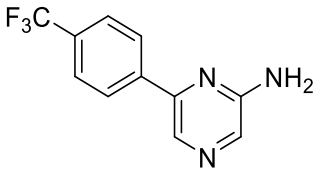

White-yellow solid, yield 85 %. ^{1}H NMR (400 MHz, DMSO-d6) δ 8.37 (s, 1H), 8.21 (d, J = 8.2 Hz, 2H), 7.92 (s, 1H), 7.83 (d, J = 8.2 Hz, 2H), 6.64 (s, 2H). Calculated mass for $C_{11}H_8F_3N_3$: 240.0743 g/mol $[M+H]^+$. ESI-MS (methanol) *m/z*: 240.17 $[M+H]^+$.

*General procedure for the synthesis of the 5-bromo-6-substituted-2-aminopyrazines (**51-53**):*

A solution of 6-aryl-pyrazin-2-amine **48-50** (1 eq), obtained from the previous synthetic step, was dissolved in acetonitrile (5 mL/mmol) under an argon atmosphere and cooled in an ice bath. In parallel, N-bromosuccinimide (1.1 eq.) was dissolved in acetonitrile (5 mL/mmol) and then added dropwise to the reaction mixture. After the addition was complete, the mixture was kept in the ice bath for 3 hours. The reaction progress was monitored by TLC using petroleum ether/ethyl acetate (7:3) as the eluent. The solvent was removed under reduced pressure, and the crude residue was suspended in dichloromethane (150

mL). The suspension was successively washed with water (3 x 30 mL), brine (3 x 10 mL), and saturated sodium bicarbonate solution (3 x 10 mL). The product was then completely collected by extracting the aqueous phase with dichloromethane (30 mL), and the combined organic phases were dried over anhydrous Na_2SO_4. The crude was obtained after filtration of the salt and solvent removal under reduced pressure. Purification was carried out by column chromatography, starting with a petroleum ether/ethyl acetate (7:3) as elution mixture and gradually moving to a 4:6 ratio. The purification step led to two different portions, one containing the 3,5-bisbromoderivative and the 3-monobromurated one and the second fraction with the desired product.

5-bromo-6-(3-fluorophenyl)pyrazin-2-amine ***(51)****:*

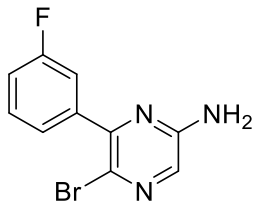

Orange powder, yield 53 %. ^{1}H NMR (400 MHz, DMSO-d_6) δ 7.71 (s, 1H), 7.55 – 7.48 (m, 1H), 7.48 – 7.44 (m, 1H), 7.44 – 7.40 (m, 1H), 7.32 – 7.25 (m, 1H), 6.80 (s, 2H). Calculated mass for $C_{10}H_7BrFN_3$: 267.988 g/mol ^{79}Br[M+H]$^+$ e 269.986 g/mol

^{81}Br[M+H]$^{+}$. ESI-MS (methanol): *m/z* 267.9879 ^{79}Br[M+H]$^{+}$, *m/z* 269.9858 ^{81}Br[M+H]$^{+}$.

*5-bromo-6-(2-fluorophenyl)pyrazin-2-amine (**52**):*

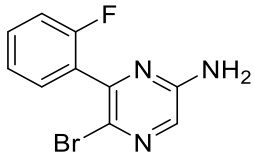

Yellow solid, yield 51%. ^{1}H NMR (400 MHz, DMSO- d_6) δ 7.73 (s, 1H), 7.55 – 7.48 (m, 1H), 7.46 – 7.40 (m, 1H), 7.34 – 7.28 (m, 2H), 6.81 (s, 2H). Calculated mass for $C_{10}H_7BrFN_3$: 267.988 g/mol ^{79}Br[M+H]$^{+}$, 269.986 g/mol ^{81}Br[M+H]$^{+}$. ESI-MS (methanol) *m/z*: 268.00 ^{79}Br[M+H]$^{+}$ *m/z* 270.00 ^{81}Br[M+H]$^{+}$.

*5-bromo-6-(4-(trifluoromethyl)phenyl)pyrazin-2-amine (**53**):*

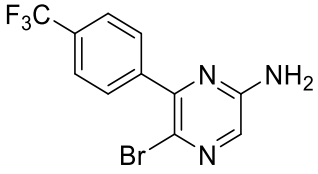

Yellow solid, yield 36 %. ^{1}H NMR (400 MHz, DMSO- d_6) δ 7.88 – 7.79 (m, 4H), 7.73 (s, 1H), 6.85 (s, 2H). calculated mass for $C_{11}H_7BrF_3N_3$: 317.9848 g/mol ^{79}Br[M+H]$^{+}$ 319.9827g/mol

$^{81}Br[M+H]^+$. ESI-MS (methanol): *m/z* 318.08 $^{79}Br[M+H]^+$; *m/z* 320.08 $^{81}Br[M+H]^+$.

*General procedure for the synthesis of 6-subtituted-5-pyridinyl-pyrazin-2-amines (**54-56**):*

In a sealed tube, 1 eq of 6-subtituted-5-bromo-pyrazin-2-amine (**51-53**) were dissolved in a mixture of water, 1,4-dioxane and ethanol. 1.2 eq of 4-pyridinylboronic acid were then added to the mixture, along with $Pd(PPh_3)_4$ (0.03 eq.), and 2 equivalents of Sodium carbonate. The system was heated at 120°C for 12 hours. The reaction progress was monitored by TLC using petroleum ether/ethyl acetate (6:4) as the eluent. After completion, the solvent was removed under reduced pressure. The crude residue was solubilized in ethyl acetate (150 mL) and washed with water (3x50 mL). The aqueous layers were extracted again with ethyl acetate (50 mL), and the combined organic phases were dried over anhydrous Na_2SO_4, followed by its filtration. Solvent removal under reduced pressure afforded the crude product. Purification was performed by column chromatography, starting with an elution mixture composed by petroleum ether/ethyl acetate (6:4) and gradually increasing the polarity to a 2:8 ratio. The isolated product was further purified by precipitation from a mixture of ethyl acetate and petroleum ether.

*5-(pyridin-4-yl)-6-(3-fluorophenyl)pyrazin-2-amine (**54**)*

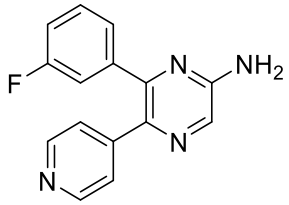

Yellow solid, yield 41%, melting point 235 °C. ^{1}H NMR (400 MHz, DMSO-d_6) δ 8.45 – 8.40 (m, 2H), 8.01 (s, 1H), 7.40 – 7.31 (m, 1H), 7.24 – 7.15 (m, 4H), 7.12 – 7.07 (m, 1H), 6.92 (s, 2H). ^{13}C NMR (101 MHz, DMSO-d_6) δ 161.82 (d, $1J_{CF}$ = 243.7 Hz), 154.44, 149.25, 148.69, 146.35, 141.17 (d, $^{3}J_{CF}$ = 7.5 Hz), 136.07, 131.01, 130.17 (d, $^{3}J_{CF}$ = 8.3 Hz), 125.61, 123.55, 116.08 (d, $^{2}J_{CF}$= 22.4 Hz), 115.35 (d, $^{2}J_{CF}$ = 20.9 Hz). HRMS-ESI (methanol) $C_{15}H_{11}FN_4$: calculated *m/z* 267.1041 $[M+H]^+$, experimental *m/z* 267.1040 $[M+H]^+$. Δ = 0.0001. Purity HPLC 99 %.

*5-(pyridin-4-yl)-6-(2-fluorophenyl)pyrazin-2-amine (**55**):*

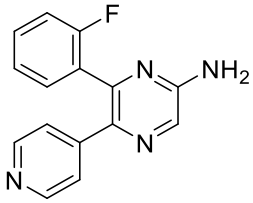

Yellow solid, yield 59%. Melting point 249 °C. ^{1}H NMR (400 MHz, DMSO-d_6) δ 8.39 (dd, J = 4.3, 1.7 Hz, 2H), 8.05 (s, 1H), 7.52 – 7.42 (m, 2H), 7.32 – 7.26 (m, 1H), 7.17 (dd, J = 4.3, 1.6 Hz, 2H), 7.16 – 7.09 (m, 1H), 6.94 (s, 2H). ^{13}C NMR (101 MHz, DMSO-d_6) δ 158.69 (d, $^{1}J_{CF}$ = 246.1 Hz), 154.72, 149.25, 146.18, 145.09, 137.05, 131.71 (d, $^{4}J_{CF}$ = 3.1 Hz), 131.46, 131.05 (d, $^{3}J_{CF}$ = 8.2 Hz), 126.83 (d, $^{2}J_{CF}$ = 15.1 Hz), 124.73, 122.40, 115.69 (d, $^{2}J_{CF}$ = 21.7 Hz). HRMS (methanol) $C_{15}H_{11}FN_4$: calculated *m/z* 267.1042 $[M+H]^+$, experimental *m/z* 267.1042 $[M+H]^+$. Δ = 0.0001. Purity HPLC 100%.

*5-(pyridin-4-yl)-6-(4-(trifluoromethyl)phenyl)pyrazin-2-amine (**56**):*

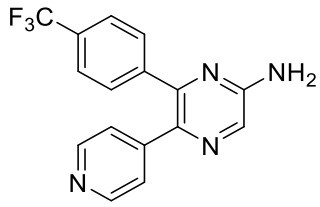

Yellow solid, yield 52 %, melting point 195 °C. ^{1}H NMR (400 MHz, DMSO-d_6) δ 8.43 (d, J = 4.5 Hz, 2H), 8.04 (s, 1H), 7.71 (d, J = 7.9 Hz, 2H), 7.55 (d, J = 7.7 Hz, 2H), 7.21 (d, J = 4.5 Hz, 2H), 6.96 (s, 2H). ^{13}C NMR (101 MHz, DMSO-d_6) δ 154.91, 149.76, 149.01, 146.65, 143.25, 136.71, 131.72, 130.70, 129.17 (q, $^{2}J_{CF}$ = 30.9 Hz), 125.82 (d, $^{2}J_{CF}$ = 18.2 Hz), 125.53, 124.06. HRMS-ESI (methanol) $C_{16}H_{11}F_3N_4$: calculated *m/z* 317.1009

$[M+H]^+$, experimental *m/z* 317.1007 $[M+H]^+$. Δ = 0.0002. Purity HPLC 93 %.

4.1.1.3.2. ***Pathway 2***

*Synthesis of 3-bromo-6-chloropyrazin-2-amine (**69**):*

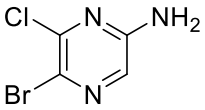

6-chloropyrazin-2-amine (compound **22**) (1.0 eq) was solubilized in dichloromethane (5 mL/mmol), the system was kept under an argon atmosphere and cooled in an ice bath. Separately, NBS (1.1 eq) was dissolved in acetonitrile (5 mL/mmol) and added dropwise to the reaction mixture. After the addition was complete, the mixture was stirred at 0 °C for 5 h. once reaction completion, the solvent was removed under reduced pressure, and the resulting solid was dissolved in dichloromethane (150 mL) and washed with water (3x50 mL), brine (3x10 mL), and saturated $NaHCO_3$ solution (3x10 mL). The aqueous layers were further extracted with dichloromethane (50 mL). The combined organic phases were dried over anhydrous Na_2SO_4, filtered, and concentrated under reduced pressure. The crude residue was purified by column chromatography, using an elution mixture composed by petroleum ether/ ethyl acetate 7:3, with gradient until reaching

a 6:4 proportion, yielding a yellow solid (59% yield). ^{1}H NMR (400 MHz, DMSO-d_6): δ 7.65 (s, 1H), 7.10 (s, 2H). Calculated mass for $C_4H_3BrClN_3$: 207.93 g/mol $^{79}Br^{35}Cl[M+H]^+$, 209.91 g/mol $^{81}Br^{35}Cl[M+H]^+$ /$^{79}Br^{37}Cl[M+H]^+$, 211.89 g/mol $^{81}Br^{37}Cl[M+H]^+$. ESI-MS (methanol): *m/z* 207.87 $^{79}Br^{35}Cl[M+H]^+$, *m/z* 209.91 $^{81}Br^{35}Cl[M+H]^+$/$^{79}Br^{37}Cl[M+H]^+$, *m/z* 211.89 $^{81}Br^{37}Cl[M+H]^+$.

Synthesis of 6-chloro-5-(pyridin-4-yl)pyrazin-2-amine (**70**)

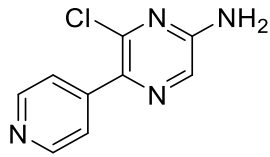

Compound 5-Bromo-6-chloropyrazin-2-amine **69** (1.0 eq), 4-pyridylboronic acid (1.2 eq), Na_2CO_3 (2.0 eq), and $Pd(PPh_3)_4$ (0.03 equiv) were combined in a sealed tube. The solids were dissolved in a solvent mixture consisting of H_2O (3 mL/mmol), dry 1,4-dioxane (1.94 mL/mmol), and ethanol (1.94 mL/mmol). The resulting solution was heated at 110-120 °C overnight. After completion, the reaction mixture was cooled to room temperature, and the solvent was removed under reduced pressure. The residue was dissolved in ethyl acetate (150 mL) and washed with water (3x50 mL). The aqueous layers were extracted with ethyl acetate (50 mL), and the combined organic phases were dried over anhydrous Na_2SO_4, filtered, and

concentrated under reduced pressure. The crude product was purified by column chromatography, starting with a petroleum ether/ethyl acetate mixture (6:4) and gradually increasing to pure ethyl acetate, yielding the desired compound as a pale-yellow solid. Yield 54%. ^{1}H NMR (400 MHz, DMSO-d_6) δ 8.66 – 8.57 (m, 2H), 7.97 (s, 1H), 7.73 – 7.64 (m, 2H), 7.26 (s, 2H). Calculated mass for $C_9H_7ClN_4$: 207.04 g/mol $^{35}Cl[M+H]^+$, 209.04 g/mol $^{37}Cl[M+H]^+$. ESI-MS (methanol) *m/z*: 207.00 $^{35}Cl[M+H]^+$; 209.00 $^{37}Cl[M+H]^+$.

*General Procedure for the Synthesis of 6-Aryl-5-Pyridin-Piperazin-2-Amine Derivatives (**71-75**):*

Method A: 5-(Pyridin-4-yl)-6-chloropyrazin-2-amine **70** (1.0 eq) was reacted with the desired arylboronic acid (1.2 eq) under an argon atmosphere. The reagents were dissolved in dry toluene (5.9 mL/mmol), ethanol (0.6 mL/mmol), and a 2M aqueous solution of Na_2CO_3 (1.0 mL/mmol). $Pd(PPh_3)_4$ (0.03 eq) was added, and the reaction mixture was heated under reflux for 3 h. After completion, the solvents were removed under reduced pressure. The residue was suspended in ethyl acetate (150 mL) and washed with water (3×50 mL). The aqueous layers were extracted with ethyl acetate (50 mL). The combined organic phases were dried over anhydrous Na_2SO_4, filtered, and concentrated under reduced pressure. The crude product was

purified by column chromatography, starting with ethyl acetate/petroleum ether (1:1) and gradually increasing to 9:1.

Method B: in a sealed tube, 5-(pyridin-4-yl)-6-chloropyrazin-2-amine **70** (1.0 eq) and the proper arylboornic acid (1.1 eq) were introduced under an argon atmosphere. Na_2CO_3 (2.0 eq) and $Pd(PPh_3)_4$ (0.04 eq) were added as well. The reagents were dissolved in a mixture of H_2O (15 mL), dry dioxane (10 mL), and ethanol (10 mL). The system was left at 130 °C overnight. After completion, the solvents were removed under reduced pressure. The crude residue was dissolved in ethyl acetate (150 mL) and washed with H_2O (3x50 mL). The aqueous phases were extracted with ethyl acetate (50 mL), and the combined organic layers were dried over anhydrous Na_2SO_4, filtered, and concentrated under reduced pressure. The crude product was purified by column chromatography, starting with ethyl acetate/petroleum ether (1:1) and gradually increasing to 9:1.

*5-(Pyridin-4-yl)-6-(4-chlorophenyl)pyrazin-2-amine (**71**):*

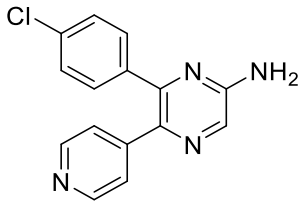

Method A. Pale yellow solid, yield 41 - 74%. Melting point 227 °C. ^{1}H NMR (400 MHz, DMSO-d_6) δ 8.43 (dd, J = 4.3, 1.7 Hz, 2H), 8.00 (s, 1H), 7.43 – 7.38 (m, 2H), 7.36 – 7.32 (m, 2H), 7.21 (dd, J = 4.3, 1.7 Hz, 2H), 6.91 (s, 2H). ^{13}C NMR (101 MHz, DMSO-d_6) δ 154.45, 149.31, 148.82, 146.45, 137.56, 136.03, 133.31, 131.24, 130.84, 128.26, 123.56. HRMS-ESI (methanol) $C_{15}H_{11}ClN_4$: calculated *m/z* 283.0745 ^{35}Cl[M+H]$^+$, *m/z* 285.0715 ^{37}Cl[M+H]$^+$, experimental *m/z* 283.0744 ^{35}Cl[M+H]$^+$, Δ = 0.0001; *m/z* 285.0714 ^{37}Cl[M+H]$^+$, Δ = 0.0001. Purity HPLC 100%.

*5-(pyridin-4-yl)-6-(4-bromophenyl)pyrazin-2-amine (**72**)*:

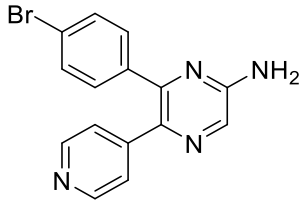

Method A. Pale yellow solid, yield 17-24%. Melting point 202 °C. Crude purified through HPLC using methanol and water from 20:80 to 60:40. ^{1}H NMR (400 MHz, DMSO-d_6) δ 8.46 – 8.40 (m, 2H), 8.00 (s, 1H), 7.44 – 7.30 (m, 4H), 7.25 – 7.15 (m, 2H), 6.91 (s, 2H). HRMS-ESI (methanol) $C_{15}H_{11}BrN_4$: calculated *m/z* 327.0239 ^{79}Br[M+H]$^+$, *m/z* 329.0219 ^{81}Br[M+H]$^+$, experimental *m/z* 327.0240 ^{79}Br[M+H]$^+$, Δ = 0.0001; *m/z* 329.0219 ^{81}Br[M+H]$^+$ Δ = 0.0000. Purity HPLC 95%.

*4-(6-amino-3-(pyridin-4-yl)pyrazin-2-yl)benzonitrile (**73**):*

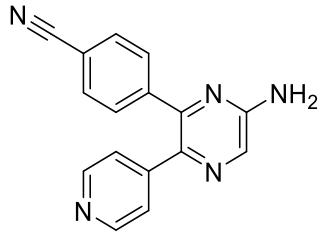

Method B. White solid, yield 27%. ^{1}H NMR (400 MHz, DMSO-d_6) δ 8.55 – 8.31 (m, 1H), 8.04 (s, 0H), 7.89 – 7.68 (m, 1H), 7.56 – 7.41 (m, 1H), 7.28 – 7.09 (m, 1H), 6.98 (s, 1H). ^{13}C NMR (101 MHz, DMSO-d_6) δ 154.54, 149.42, 148.45, 146.12, 143.45, 136.37, 132.22, 131.53, 130.45, 123.71, 118.69, 111.13. HRMS-ESI (methanol) $C_{16}H_{11}N_5$: calculated *m/z* 274.1087 $[M+H]^+$; experimental *m/z* 274.1088 $[M+H]^+$. Δ= 0.0001. Purity HPLC 100 %.

*6-(4-nitrophenyl)-5-(pyridin-4-yl)pyrazin-2-amine (**74**):*

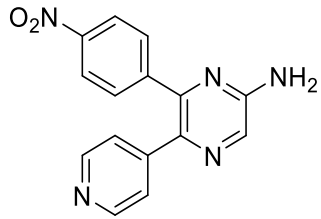

Method B: pale yellow-white solid, yield 35 %. ^{1}H NMR (400 MHz, DMSO-d_6) δ 8.46 – 8.41 (m, 2H), 8.24 – 8.17 (m, 2H), 8.06 (s, 1H), 7.65 – 7.57 (m, 2H), 7.24 – 7.19 (m, 2H), 7.01 (s,

2H). Calculated ass for: 294.0986 g/mol $[M+H]^+$. HRMS-ESI (methanol) $C_{15}H_{11}N_5O_2$: calculated *m/z* 294.0986 $[M+H]^+$; experimental *m/z* 294.0981 $[M+H]^+$. Δ= 0.0005. Purity HPLC 90 %.

*5,6-di(pyridin-4-yl)pyrazin-2-amine (**75**):*

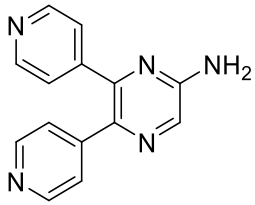

Method B: white solid, yield 26-32%. ^{1}H NMR (400 MHz, DMSO-d_6) δ 8.58 – 8.52 (m, 2H), 8.47 – 8.42 (m, 2H), 8.05 (s, 1H), 7.35 – 7.28 (m, 2H), 7.25 – 7.18 (m, 2H), 6.99 (s, 2H). ESI-MS (methanol) *m/z*: 250.13 $[M+H]^+$. HRMS-ESI (methanol) $C_{14}H_{11}N_5$: calculated *m/z* 250.1087 $[M+H]^+$, experimental *m/z* 250.1087 $[M+H]^+$. Δ= 0.0000. Purity HPLC 92%.

*General Procedure for the Synthesis of 6-Aryl-3-Bromo-5-Pyridin-Pyrazin-2-Amines (**57-59**, **76-79**):*

6-Aryl-5-(pyridin-4-yl)pyrazin-2-amine (**32–36**, 1.0 eq) was dissolved in dichloromethane (5 mL/mmol) under an argon atmosphere and cooled in an ice bath. NBS (1.2 eq), dissolved in acetonitrile (5 mL/mmol), was added dropwise to the reaction mixture. After completion of the addition, the mixture was kept in the ice bath for 4 h. The solvent was removed under reduced

pressure, the crude dissolved in DCM (150 mL) and washed successively with water (3x30 mL), brine (3x10 mL), and saturated aqueous $NaHCO_3$ (3x10 mL). The combined organic phases were dried over anhydrous Na_2SO_4, filtered, and concentrated under reduced pressure. The crude residue was purified by column chromatography, starting with ethyl acetate/petroleum ether (6:4) and gradually increasing to 8:2. The obtained solid was then precipitated using ethyl acetate and petroleum ether yielding the desired product.

*3-Bromo-5-(pyridin-4-yl)-6-(3-fluorophenyl)pyrazin-2-amine (**57**)*:

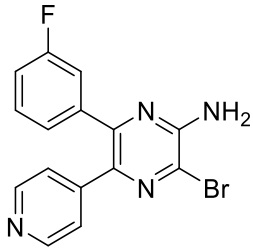

Yellow solid, yield 34 %. ^{1}H NMR (400 MHz, DMSO-d_6) δ 88.48 – 8.42 (m, 2H), 7.42 – 7.35 (m, 1H), 7.28 – 7.14 (m, 6H), 7.14 – 7.09 (m, 1H). Calculated mass for $C_{15}H_{10}BrFN_4$: 345.01 g/mol ^{79}Br[M+H]$^+$, 347.01 g/mol ^{81}Br[M+H]$^+$. ESI-MS (methanol) m/z 345.08 ^{79}Br[M+H]$^+$, m/z 347.08 ^{81}Br[M+H]$^+$.

*3-Bromo-5-(pyridin-4-yl)-6-(2-fluorophenyl)pyrazin-2-amine (**58**)*:

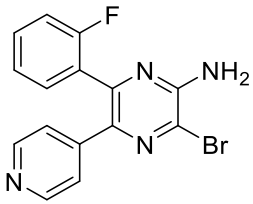

Yellow solid, yield 44 %. ^{1}H NMR (400 MHz, DMSO-d_6) δ 8.44 – 8.41 (m, 2H), 7.55 – 7.46 (m, 2H), 7.33 – 7.28 (m, 1H), 7.25 (s, 2H), 7.19 – 7.13 (m, 3H). Calcd for $C_{15}H_{10}BrFN_4$: 344.01 g/mol ^{79}Br[M+H]$^+$, 346.01 g/mol ^{81}Br[M+H]$^+$. ESI-MS (methanol) *m/z* 345.08 ^{79}Br[M+H]$^+$, *m/z* 347.08 ^{81}Br[M+H]$^+$.

*3-bromo-5-(pyridin-4-yl)-6-[4-(trifluoromethyl)phenyl]pyrazin-2-amine (**59**)*:

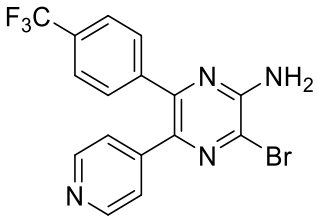

Yellow solid, yield 30 %. ^{1}H NMR (400 MHz, DMSO-d_6) δ 8.46 (dd, J = 4.0, 1.7 Hz, 2H), 7.73 (d, J = 8.1 Hz, 2H), 7.57 (d, J = 8.0 Hz, 2H), 7.25 (s, 2H), 7.20 (dd, J = 4.0, 1.7 Hz, 2H).

Calculated mass for $C_{16}H_{10}BrF_3N_4$: 395.01 g/mol $^{79}Br[M+H]^+$, 397.01 g/mol $^{81}Br[M+H]^+$. ESI-MS (methanol) *m/z* 395.17 $^{79}Br[M+H]^+$, *m/z* 397.17 $^{81}Br[M+H]^+$.

*3-Bromo-5-(pyridin-4-yl)-6-(4-chlorophenyl)pyrazin-2-amine (**76**)*:

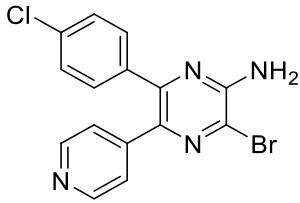

Yellow solid, yield 35 %. ^1H NMR (400 MHz, DMSO-d_6) δ 8.48 – 8.44 (m, 2H), 7.45 – 7.41 (m, 2H), 7.38 – 7.34 (m, 2H), 7.23 – 7.15 (m, 4H). Calculated for $C_{15}H_{10}BrClN_4$: 360.98 g/mol $^{35}Cl[M+H]^+$, 362.98 g/mol $^{35}Cl[M+H]^+$. ESI-MS (methanol) *m/z* 361.08 $^{35}Cl^{79}Br[M+H]^+$, *m/z* 363.08 $^{37}Cl^{79}Br[M+H]^+$/ $^{35}Cl^{81}Br[M+H]^+$, m/z 365.08 $^{37}Cl^{81}Br[M+H]^+$.

*3-Bromo-5-(pyridin-4-yl)-6-(4-bromophenyl)pyrazin-2-amine (**77**)*:

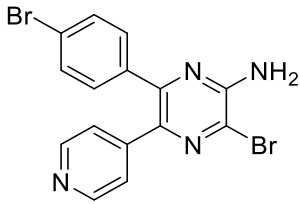

Yellow solid, yield 24%. ^{1}H NMR (400 MHz, DMSO-d_6) δ 8.48 – 8.44 (m, 2H), 7.68 – 7.65 (m, 2H), 7.49 – 7.42 (m, 2H), 7.22 – 7.19 (m, 2H), 7.19 – 7.16 (m, 1H). Calculated mass for $C_{15}H_{10}Br_2N_4$: 404.93 g/mol $^{79}Br[M+H]^+$, 406.93 g/mol $^{79}Br^{81}Br[M+H]^+$, 408.93 g/mol $^{81}Br[M+H]^+$. ESI-MS (methanol): *m/z* 405.00 $^{79}Br[M+H]^+$, *m/z* 407.00 $^{79}Br^{81}Br[M+H]^+$, *m/z* 409.00 $^{81}Br[M+H]^+$.

*3-bromo-5-(pyridine-4-yl)-6-(4-nitrophenyl)pyrazin-2-amine (**79**):*

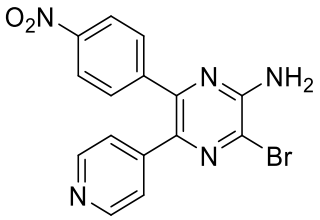

Pale yellow solid, yield 46 %.^{1}H NMR (400 MHz, DMSO-d_6) δ 8.50 – 8.43 (m, 2H), 8.25 – 8.19 (m, 2H), 7.65 – 7.59 (m, 2H), 7.30 (s, 2H), 7.24 – 7.18 (m, 2H).

*4-(6-amino-5-bromo-3-(pyridin-4-yl)pyrazin-2-yl)benzonitrile (**78**):*

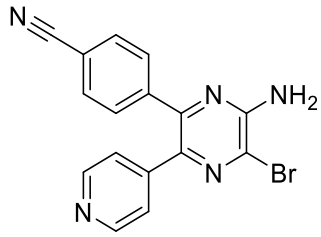

Pale yellow-white solid, yield 48 %. ^{1}H NMR (400 MHz, DMSO-d_6) δ 8.50 – 8.42 (m, 2H), 7.86 – 7.82 (m, 2H), 7.56 – 7.50 (m, 2H), 7.26 (s, 2H), 7.22 – 7.16 (m, 2H).

*General procedure for the synthesis of 6-substituted-3-morpholin-5-Pyridin-Pyrazin-2-Amines (**60-62**, **80-83**):*

To a solution of 1 equivalent of 6-subtsituted-3-bromo-5-pyridin-pyrazin-2-amine (**57-59**, **76-79**) in ethanol was added 3 equivalents of morpholine. The reaction mixture was heated at 110 °C for 4 days. After completion, the solvent was removed under reduced pressure, and the resulting solid was purified by column chromatography. Elution was initially carried out with a 6:4 mixture of ethyl acetate/petroleum ether, gradually increasing the polarity of the eluent to a 8:2 ratio. The fractions containing the desired product were collected, and the solvent was removed under reduced pressure. The crude product was further purified by precipitation using a mixture of ethyl acetate and petroleum ether to afford the final product as a purified solid.

*3-morpholino-5-(pyridin-4-yl)-6-(3-fluorophenyl)pyrazin-2-amine (**60**):*

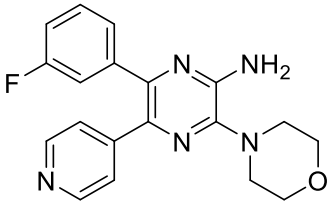

Yellow solid, yield 95 %. Melting Point 256°C. ^{1}H NMR (400 MHz, DMSO-d_6) δ 8.42 (dd, J = 4.3, 1.7 Hz, 2H), 7.37 – 7.31 (m, 1H), 7.26 (dd, J = 4.3, 1.7 Hz, 2H), 7.20 – 7.13 (m, 2H), 7.09 (dt, J = 7.7, 1.1 Hz, 1H), 6.56 (s, 2H), 3.80 (d, J = 4.6 Hz, 4H), 3.18 (d, J = 4.5 Hz, 4H). ^{13}C NMR (101 MHz, DMSO-d_6) δ 161.91 (d, $^{1}J_{CF}$ = 243.4 Hz), 149.26, 147.00, 146.45, 143.77, 142.23 (d, $^{4}J_{CF}$ = 2.3 Hz), 141.35 (d, $^{3}J_{CF}$ = 7.7 Hz), 133.16, 130.11 (d, $^{3}J_{CF}$ = 8.5 Hz), 125.61, 123.58, 116.02 (d, $^{2}J_{CF}$ = 22.0 Hz), 114.81 (d, $^{2}J_{CF}$ = 20.8 Hz), 65.89, 48.11. HRMS-ESI (methanol) $C_{19}H_{18}FN_5O$: calculated *m/z* 352.1568. $[M+H]^+$, experimental *m/z* 352.1569 $[M+H]^+$. Δ = 0.0001. Purity HPLC 99 %.

*3-morpholino-5-(pyridin-4-yl)-6-(2-fluorophenyl)pyrazin-2-amine (**61**):*

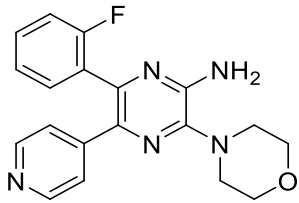

Pale yellow solid, yield 78 %. Melting Point 226 °C. 1H NMR (400 MHz, DMSO-d6) δ 8.38 (dd, J = 4.3, 1.6 Hz, 2H), 7.50 – 7.40 (m, 2H), 7.30 – 7.25 (m, 1H), 7.21 (dd, J = 4.3, 1.6 Hz, 2H), 7.16 – 7.10 (m, 1H), 6.58 (s, 2H), 3.81 (t, J = 4.8, 4.3 Hz, 4H), 3.19 (t, J = 4.6 Hz, 4H). ^{13}C NMR (101 MHz, DMSO-d_6) δ 158.90 (d, $^{1}J_{CF}$ = 245.6 Hz), 149.23, 147.46, 146.28, 144.12, 138.36, 134.13, 131.84, 130.58 (d, $^{3}J_{CF}$ = 8.0 Hz), 127.00 (d, $^{2}J_{CF}$ = 15.2 Hz), 124.66, 122.30, 115.68 (d, $^{3}J_{CF}$ = 21.9 Hz), 65.91, 48.12. HRMS-ESI (methanol) $C_{19}H_{18}FN_5O$: calculated *m/z* 352.1568. $[M+H]^+$, experimental *m/z* 352.1567 $[M+H]^+$, Δ = 0.0001. Purity HPLC 100%.

*3-morpholino-5-(pyridin-4-yl)-6-(4-(trifluoromethyl)phenyl)pyrazin-2-amine (**62**):*

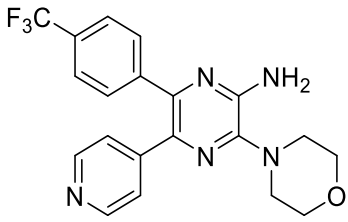

White solid, yield 87 %. Melting point 209 °C. ^{1}H NMR (400 MHz, DMSO-d_6) δ 8.43 (dd, J = 4.5, 1.7 Hz, 2H), 7.69 (d, J =

8.1 Hz, 2H), 7.54 (d, J = 8.0 Hz, 2H), 7.25 (dd, J = 4.4, 1.6 Hz, 2H), 6.60 (s, 2H), 3.81 (t, J = 5.0, 4.0 Hz, 4H), 3.19 (d, J = 4.6 Hz, 4H). Calculated mass for $C_{20}H_{18}F_3N_5O$: *m/z* 402.1536 $[M+H]^+$. HRMS-ESI (methanol): *m/z* 402.1532 $[M+H]^+$. Δ = 0.0004. Purity HPLC 98%.

*3-morpholino-5-(pyridin-4-yl)-6-(4-chlorophenyl)pyrazin-2-amine (**80**):*

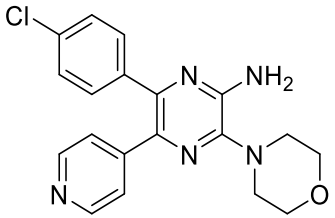

Yellow solid, yield 96 %. Melting point 226 °C. ^{1}H NMR (400 MHz, DMSO-d_6) δ 8.42 (dd, J = 4.3, 1.7 Hz, 2H), 7.42 – 7.36 (m, 2H), 7.36 – 7.31 (m, 2H), 7.25 (dd, J = 4.3, 1.7 Hz, 2H), 6.55 (s, 2H), 3.80 (t, J = 4.3 Hz, 4H), 3.17 (t, J = 4.3 Hz, 4H). ^{13}C NMR (101 MHz, DMSO-d_6) δ 149.75, 147.47, 146.98, 144.11, 142.82, 138.16, 133.52, 133.17, 131.68, 128.68, 124.03, 66.33, 48.56. HRMS-ESI (methanol) $C_{19}H_{18}ClN_5O$: calculated *m/z* 368.1272 $^{35}Cl[M+H]^+$, experimental *m/z* 368.1270 $[M+H]^+$. Δ = 0.0002. Purity HPLC 99 %.

*3-morpholino-5-(pyridin-4-yl)-6-(4-bromophenyl)pyrazin-2-amine (**81**)*:

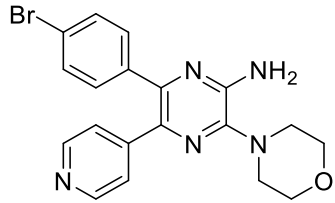

Yellow solid, yield 34 %. Melting point 241 °C. Compound **81** has been further purified using preparative HPLC, using a mixture of water/methanol as elution mixture. HRMS-ESI (methanol): calculated *m/z* 412.0767 ^{79}Br[M+H]$^+$, *m/z* 414.0747 ^{81}Br[M+H]$^+$; experimental *m/z* 412.0763 ^{79}Br[M+H]$^+$, Δ = 0.0004, *m/z* 414.0744 ^{81}Br[M+H]$^+$. Δ = 0.0003. Purity HPLC 91 %.

*4-(6-amino-5-morpholino-3-(pyridin-4-yl)pyrazin-2-yl)benzonitrile (**82**):*

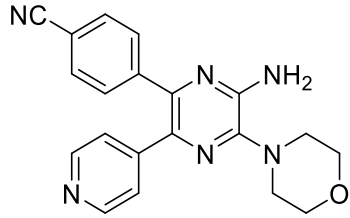

Yellow/orange solid, yield 82%. ^{1}H NMR (400 MHz, DMSO-d_6) δ 8.51 – 8.36 (m, 2H), 7.87 – 7.70 (m, 2H), 7.55 – 7.45 (m, 2H), 7.29 – 7.14 (m, 2H), 6.60 (s, 2H), 3.88 – 3.75 (m, 4H), 3.22 – 3.17 (m, 4H). ^{13}C NMR (101 MHz, DMSO-d_6) δ 149.43, 147.03, 146.25, 144.08, 143.63, 141.65, 133.72, 132.16, 130.42,

123.74, 118.85, 110.48, 65.90, 48.08. HRMS-ESI (methanol) $C_{20}H_{18}N_6O$*:* calculated *m/z* 359.1615 $[M+H]^+$, experimental *m/z* 359.1615 $[M+H]^+$. $\Delta = 0.0000$. Purity HPLC 94 %.

*3-morpholino-6-(4-nitrophenyl)-5-(pyridin-4-yl)pyrazin-2-amine (**83**):*

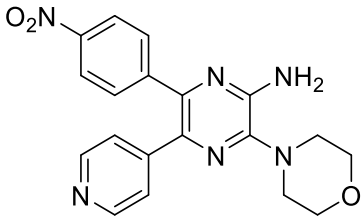

Yellow solid, yield 70%. ^{1}H NMR (400 MHz, DMSO-d_6) δ 8.50 – 8.39 (m, 2H), 8.19 (d, *J* = 8.8 Hz, 2H), 7.60 (d, *J* = 8.8 Hz, 2H), 7.32 – 7.21 (m, 2H), 6.65 (s, 2H), 3.84 – 3.78 (m, 4H), 3.24 – 3.17 (m, 4H). HRMS-ESI (methanol) $C_{19}H_{18}N_6O_3$: calculated *m/z* 379.1513 $[M+H]^+$, experimental *m/z* 379.1516 $[M+H]^+$. $\Delta =$ 0.0003. Purity HPLC 95 %.

*General procedure for the synthesis of tert-butyl 4-(3-amino-5-substituted-6-(pyridin-4-yl)pyrazin-2-yl)amino)piperidine-1-carboxylate **(63-65, 84-86):***

To a solution of 1 equivalent of 6-aryl-3-bromo-5-pyridin-pyrazin-2-amine (**57-59**, **76-79**) in ethanol was added 3 equivalents of tert-butyl 4-aminopiperidine-1-carboxylate (6.5

mL per mmol of starting material). The reaction mixture was heated at 110 °C for 4 days. After completion, the solvent was removed under reduced pressure, and the resulting solid was purified by column chromatography. Elution was initially carried out with a 6:4 mixture of ethyl acetate/petroleum ether, gradually increasing the polarity of the eluent to a 8:2 ratio. The fractions containing the desired product were collected, and the solvent was removed under reduced pressure. The crude product was further purified by precipitation using a mixture of ethyl acetate and petroleum ether to afford the final product as a purified solid.

tert-butyl 4-((3-amino-5-(3-fluorophenyl)-6-(pyridin-4-yl)pyrazin-2-yl)amino)piperidine-1-carboxylate (***63***):

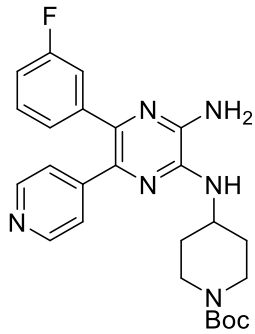

Waxy orange solid, yield 8 %. ^{1}H NMR (400 MHz, DMSO-d_6) δ 8.46 (dd, J = 4.5, 1.7 Hz, 1H), 8.39 (dd, J = 4.6, 1.6 Hz, 1H), 7.65 – 7.52 (m, 3H), 7.43 – 7.35 (m, 2H), 7.33 – 7.23 (m, 4H), 7.23 – 7.18 (m, 3H), 7.14 – 7.09 (m, 1H), 7.09 – 7.04 (m, 1H),

7.01 (dt, J = 7.7, 1.1 Hz, 1H), 6.77 (s, 2H), 6.50 (s, 1H), 6.32 (d, J = 6.6 Hz, 1H), 4.06 – 3.96 (m, 7H), 2.48 – 2.43 (m, 4H), 2.34 – 2.29 (m, 4H), 1.41 (s, 9H). Calculated mass for $C_{25}H_{29}FN_6O_2$: 465.2409 g/mol $[M+H]^+$. ESI-MS (methanol): *m/z* 465.25 $[M+H]^+$.

*tert-butyl 4-((3-amino-5-(2-fluorophenyl)-6-(pyridin-4-yl)pyrazin-2-yl)amino)piperidine-1-carboxylate (**64**):*

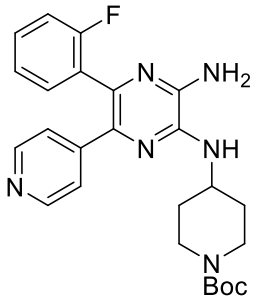

Brown solid, yield 11%. ^{1}H NMR (400 MHz, DMSO-d_6) δ 8.34 (dd, J = 4.6, 1.6 Hz, 2H), 7.41 – 7.33 (m, 2H), 7.24 – 7.19 (m, 1H), 7.18 (dd, J = 4.4, 1.7 Hz, 2H), 7.11 – 7.05 (m, 1H), 6.51 (s, 2H), 6.32 (d, J = 6.8 Hz, 1H), 4.21 – 4.06 (m, 2H), 3.97 – 3.80 (m, 4H), 2.09 – 1.95 (m, 4H), 1.42 (s, 9H). Calculated mass for $C_{25}H_{29}FN_6O_2$: 465.2409 g/mol$[M+H]^+$. ESI-MS (methanol): *m/z* 465.25$[M+H]^+$.

*tert-butyl 4-((3-amino-6-(pyridin-4-yl)-5-(4-(trifluoromethyl)phenyl)pyrazin-2-yl)amino)piperidine-1-carboxylate (**65**):*

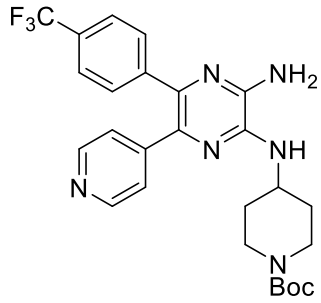

Brown solid, yield 12%. ^{1}H NMR (400 MHz, DMSO-d_6) δ 8.41 (dd, J = 4.5, 1.6 Hz, 2H), 7.62 (d, J = 8.1 Hz, 2H), 7.46 (d, J = 8.0 Hz, 2H), 7.22 (dd, J = 4.2, 1.7 Hz, 2H), 6.53 (s, 2H), 6.38 (d, J = 6.7 Hz, 1H), 4.15 – 4.08 (m, 1H), 3.98 – 3.80 (m, 4H), 2.02 (dd, J = 12.6, 2.9 Hz, 5H), 1.42 (s, 9H). Calculated mass for $C_{26}H_{29}F_3N_6O_2$: 515.2377 g/mol. ESI-MS (methanol): *m/z* 515.2371 $[M+H]^+$.

*tert-butyl 4-((3-amino-5-(4-chlorophenyl)-6-(pyridin-4-yl)pyrazin-2-yl)amino)piperidine-1-carboxylate (**84**):*

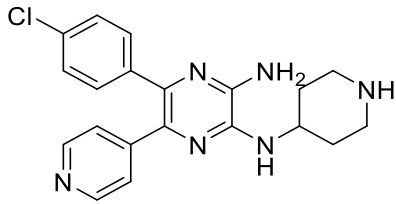

Yellow powder, yield 23%. The reaction led to the deprotected derivative. ^{1}H NMR (400 MHz, DMSO-d_6) δ 8.48 – 8.38 (m, 3H), 7.42 – 7.30 (m, 4H), 7.27 – 7.23 (m, 2H), 6.52 (d, *J* = 16.4 Hz, 3H), 3.06 – 2.99 (m, 2H), 2.99 – 2.88 (m, 1H), 2.61 – 2.51

(m, 2H), 1.85 – 1.72 (m, 2H), 1.40 – 1.26 (m, 2H). ESI-MS (methanol): m/z 381.23. HRMS-ESI (methanol) $C_{20}H_{21}ClN_6$: calculated *m/z* 381.1589 $^{35}[M+H]^+$, *m/z* 383.1560 $^{37}[M+H]^+$; experimental 381.1589 $^{35}[M+H]^+$, Δ=0.0000, *m/z* 383.1556 $^{37}[M+H]^+$ Δ=0.0004. Purity HPLC 95%.

*tert-butyl 4-((3-amino-5-(4-cyanophenyl)-6-(pyridin-4-yl)pyrazin-2-yl)amino)piperidine-1-carboxylate (**85**):*

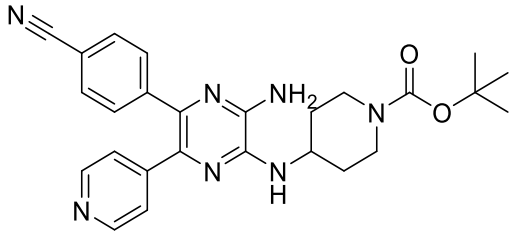

Yellow powder, yield 25%. ^{1}H NMR (400 MHz, DMSO-d_6) δ 8.51 – 8.40 (m, 2H), 7.88 – 7.78 (m, 2H), 7.59 – 7.50 (m, 2H), 7.26 (s, 2H), 7.21 – 7.13 (m, 2H), 4.69 (s, 1H), 3.71 – 3.55 (m, 1H), 2.99 – 2.87 (m, 4H), 1.74 – 1.59 (m, 2H), 1.38 (s, 9H), 1.29 – 1.15 (m, 2H). Calculated mass for $C_{26}H_{29}N_7O_2$: 472.2455 g/mol $[M+H]^+$. ESI-MS (methanol) *m/z* 472.30 $[M+H]^+$.

*tert-butyl 4-((3-amino-5-(4-nitrophenyl)-6-(pyridin-4-yl)pyrazin-2-yl)amino)piperidine-1-carboxylate (**86**):*

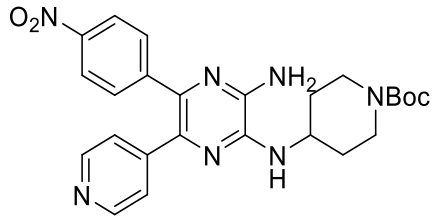

Yellow solid, yield 53%. ^{1}H NMR (400 MHz, DMSO-d_6) δ 8.45 – 8.40 (m, 2H), 8.15 – 8.10 (m, 2H), 7.53 – 7.48 (m, 2H), 7.26 – 7.22 (m, 2H), 6.58 (s, 2H), 6.48 (d, J = 6.7 Hz, 1H), 4.17 – 4.07 (m, 1H), 3.94 – 3.86 (m, 2H), 3.04 – 2.87 (m, 2H), 2.05 – 1.99 (m, 2H), 1.41 (s, 11H).

*General procedure for the tert-butoxycarbonyl group removal (**66-68, 87-89**):*

*5-(3-fluorophenyl)-N^2-(piperidin-4-yl)-6-(pyridin-4-yl)pyrazine-2,3-diamine hydrochloride (**66**)*

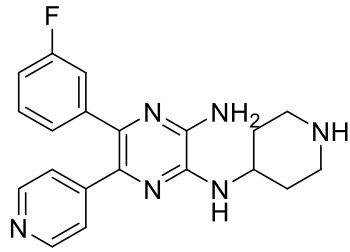

Brown solid, yield 79 %. Melting Point 129 °C. ^{1}H NMR (400 MHz, DMSO-d_6) δ 9.29 (s, 2H), 9.04 (d, J = 10.3 Hz, 2H), 8.74 – 8.70 (m, 2H), 8.46 (s, 5H), 7.76 – 7.73 (m, 2H), 7.48 – 7.12 (m, 7H), 4.22 – 3.68 (m, 2H), 3.00 – 2.85 (m, 4H), 1.86 – 1.71

(m, 4H). ^{13}C NMR (101 MHz, Methanol-d_4) δ 162.03 (d, J = 244.1 Hz), 152.90, 151.84 (d, J = 6.9 Hz), 150.57, 141.81, 141.57, 139.25, 132.35 (d, J = 11.5 Hz), 131.39 (d, J = 8.2 Hz), 130.84, 125.58, 116.48 (d, J = 20.1 Hz), 116.18, 45.03, 41.18, 26.36. HRMS-ESI (methanol) $C_{20}H_{21}FN_6$: calculated *m/z* 365.1884 $[M+H]^+$, experimental *m/z* 365.1882 $[M+H]^+$. Δ = 0.0002. Purity HPLC 83%.

*5-(2-fluorophenyl)-N2-(piperidin-4-yl)-6-(pyridin-4-yl)pyrazine-2,3-diamine hydrochloride (**67**):*

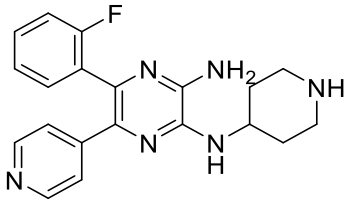

Brown solid, yield 74 %. Melting point 147 °C. ^{1}H NMR (400 MHz, DMSO-d_6) δ 9.09 (s, 1H), 8.99 (d, J = 9.5 Hz, 1H), 8.63 (d, J = 6.9 Hz, 2H), 7.79 (d, J = 6.9 Hz, 2H), 7.53 – 7.47 (m, 2H), 7.38 – 7.29 (m, 3H), 7.25 – 7.16 (m, 2H), 4.32 – 4.24 (m, 2H), 3.47 – 3.27 (m, 3H), 2.26 – 2.08 (m, 3H). ^{13}C NMR (101 MHz, DMSO-d_6) δ 159.05 (d, J = 245.0 Hz), 156.02, 144.99, 141.21, 141.09, 135.26, 132.16 (d, J = 2.8 Hz), 131.64 (d, J = 8.0 Hz), 131.03, 126.30 (d, J = 14.7 Hz), 125.78 (d, J = 3.2 Hz), 124.70, 116.41 (d, J = 21.5 Hz), 45.75, 42.83, 28.25. HRMS-ESI (methanol) $C_{20}H_{21}FN_6$: calculated *m/z* 365.1884 $[M+H]^+$,

experimental *m/z* 365.1886 $[M+H]^+$, Δ = 0.0002. Purity HPLC 96%.

N^2-(piperidin-4-yl)-6-(pyridin-4-yl)-5-(4-(trifluoromethyl)phenyl)pyrazine-2,3-diamine hydrochloride ***(68)***

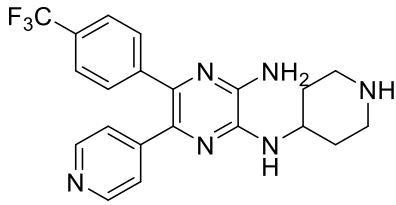

Brown solid, yield 64 %. Melting point 174 °C. ^{1}H NMR (400 MHz, DMSO-d_6) δ 9.07 (s, 1H), 8.98 (d, J = 9.1 Hz, 1H), 8.63 (d, J = 6.9 Hz, 2H), 7.80 (d, J = 6.9 Hz, 2H), 7.72 (d, J = 8.2 Hz, 2H), 7.57 (d, J = 8.0 Hz, 2H), 7.32 (s, 2H), 4.31 – 4.19 (m, 2H), 3.11 – 2.89 (m, 4H), 1.92 – 1.69 (m, 4H). HRMS-ESI (methanol) $C_{21}H_{21}F_3N_6$: calculated *m/z* 415.1853 $[M+H]^+$, experimental *m/z* 415.1852 $[M+H]^+$. Δ = 0.0001. Purity HPLC 99%.

*5-(4-chlorophenyl)-N^2-(piperidin-4-yl)-6-(pyridin-4-yl)pyrazine-2,3-diamine (**87**):*

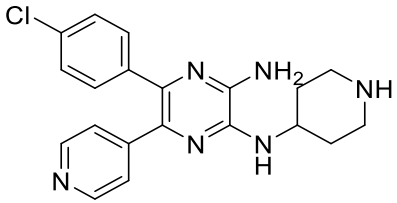

Orange/brown solid, yield 83%. ^{1}H NMR (400 MHz, DMSO-d_6) δ 8.46 – 8.41 (m, 2H), 7.42 – 7.37 (m, 2H), 7.35 – 7.30 (m, 2H), 7.27 – 7.19 (m, 3H), 6.54 (s, 1H), 6.49 (s, 2H), 3.08 – 2.99 (m, 2H), 2.99 – 2.89 (m, 1H), 2.62 – 2.53 (m, 2H), 1.84 – 1.68 (m, 2H), 1.40 – 1.26 (m, 2H). HRMS-ESI (methanol) $C_{20}H_{21}ClFN_6$: calculated *m/z* 381.1589 $[M+H]^+$, experimental *m/z* 381.1589 $[M+H]^+$. Δ= 0.0000. Purity HPLC 95 %.

*4-(6-amino-5-(piperidin-4-ylamino)-3-(pyridin-4-yl)pyrazin-2-yl)benzonitrile (**88**):*

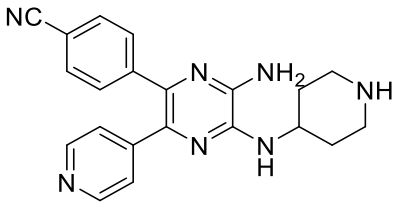

Brown solid, yield 88%. ^{1}H NMR (400 MHz, DMSO-d_6) δ 8.91 – 8.78 (m, 2H), 8.61 (d, *J* = 6.5 Hz, 2H), 7.81 (d, *J* = 8.2 Hz, 2H), 7.75 (d, *J* = 6.5 Hz, 2H), 7.53 (d, *J* = 8.2 Hz, 2H), 7.10 (d, *J* = 6.3 Hz, 1H), 4.30 – 4.19 (m, 2H), 3.12 – 3.00 (m, 3H), 2.23 – 2.10 (m, 2H), 1.89 – 1.75 (m, 4H). HRMS-ESI (methanol)

$C_{21}H_{21}N_7$: calculated *m/z* 372.1931 $[M+H]^+$, experimental *m/z* 372.1933. Δ=0.0002. Purity HPLC 100%.

5-(4-nitrophenyl)-N2-(piperidin-4-yl)-6-(pyridin-4-yl)pyrazine-2,3-diamine ***(89)****:*

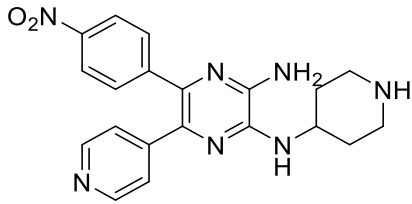

Orange solid, yield 74%. ^{1}H NMR (400 MHz, DMSO-d_6) δ 9.06 – 8.84 (m, 2H), 8.62 (d, *J* = 6.1 Hz, 2H), 8.20 (d, *J* = 8.4 Hz, 2H), 7.78 (d, *J* = 6.0 Hz, 2H), 7.61 (d, *J* = 8.4 Hz, 2H), 7.24 (d, *J* = 6.4 Hz, 1H), 4.25 (s, 1H), 3.16 – 2.95 (m, 4H), 2.23 – 2.11 (m, 2H), 1.92 – 1.78 (m, 3H). ^{13}C NMR (101 MHz, DMSO-d_6) δ 146.79, 145.46, 144.38, 141.52, 141.49, 140.73, 130.81, 130.42, 125.52, 123.69, 45.32, 41.92, 27.76. Purity HPLC 86 %.

4.2. Biochemistry

4.2.1.CK1δ - Enzymatic assay

The compounds were tested on truncated CK1δ (1–294 aa), purchased from Merck-Sigma Aldrich, and compounds activities were measured using two methods: the Kinase-Glo® Luminescent Kinase Assay (Promega) and the ADP-Glo™ Kinase Assay (Promega). The assays were carried out in white, flat-bottom 96-well FluoroNunc plates. Compounds were

initially screened to evaluate residual enzymatic activity, using the Kinase-Glo® assay kit. For each compound two independent experiments were carried out, each concentration seeded in technical duplicate. Starting from a 10 mM stock solution in DMSO, compounds were diluted in aqueous buffer, whose composition is reported in Table 11.

Table 11: composition of the aqueous buffer used during the enzymatic assay

Component	Final concentration
HEPES, pH 7.5	50 mM
EDTA	1 mM
EGTA	1 mM
$MgCl_2$	15 mM

In each well were introduced 10 µL of the tested compound, 10 µL of an enzyme solution (CK1δ truncated enzyme 1–294 aa supplied at 2.27 mg/mL) at a final concentration of 6.5 nM and a solution of ATP and Casein (2 µM and 0.1% in aqueous buffer).

Two reference controls were included in the assay. The positive control consisted of PF-670462, tested at the same concentration as the investigated inhibitors, and was used to define 0% residual enzymatic activity. The negative control, corresponding to 100% residual activity, was represented by

enzyme samples incubated in the absence of inhibitors. The residual activity of each tested compound was calculated relative to these reference controls.

Once the compounds were introduced in the plate this was incubated for one hour at 30°C. Terminated the incubation time 40 µL of Kinase Glo Reagent were added to each well to stop the kinase reaction, the plate was kept in the dark for 8 minutes and the luminescence was registered using Tecan Infinite M1000 Pro plate reader.

The Kinase-Glo® assay exploits a luciferase-based luminescent reaction to quantify the amount of ATP remaining after the kinase reaction. In this system, luciferase catalyzes the oxidation of luciferin to oxyluciferin, releasing light that can be detected as a measure of ATP concentration. Since the emitted luminescence reflects the ATP that has not been consumed by the kinase, the signal intensity is inversely related to enzymatic activity. The percentage of residual kinase activity is then calculated by comparing the luminescence values of inhibitor-treated samples with those of the control wells lacking inhibitors, which define the reference level for total ATP content.

Compounds that exhibit a residual enzymatic activity percentage lower than 50% when tested at a concentration of 10

μM were considered active, and their IC_{50} values were subsequently determined.

For the IC_{50}s determination, the ADP-Glo™ Kinase Assay (Promega) was employed, which, unlike the Kinase-Glo® assay, provides a direct measurement of kinase activity. As for the previous assay, the luminescence signal is generated by the luciferase/luciferin system included in the kit, however it contains two different reagents, the firs one (ADP-Glo™ Reagent, volume added equal to reaction volume) is responsible of the remaining ATP removal. The second one (Kinase Detection Reagent, volume added equal to reaction volume + ADP-Glo™ Reagent volume) is responsible for the conversion of the ADP in ATP and contains also the luciferin/luciferase system. In this case, the luminescence signal depends on the amount of ATP converted from ADP and thus is a direct measure of the kinase activity. This system is more sensitive than the Kinase-Glo® assay, as it is less affected by background signal, providing a more accurate determination of kinase inhibition[194].

As for compounds screening, white, flat-bottom 96-well FluoroNunc plates were used for IC_{50} measurement, for each inhibitor three experiments were performed, each replicate measured in technical duplicates. For the IC_{50}s determination, inhibitors were tested at various concentrations. The truncated

CK1δ enzyme was added to a final concentration of 4 nM per well, while ultra-pure ATP (provided in the kit) was diluted with buffer to a final concentration of 1 μM**.** Casein was diluted and mixed with the ATP to a final concentration of 0.05%**.** Negative and positive controls were included in all experiments. Both the negative control and the positive control have the same concentration of the higher concentration of the tested compound.

After the addition of the enzyme, inhibitor, ATP, and Casein solutions, the plate was incubated at 30 °C for 1 hour**.** Subsequently, ADP-Glo™ Reagent was added in a volume equal to that of the reaction mixture, followed by incubation for 40 minutes at room temperature (RT) to deplete any remaining ATP in the reaction. Finally, Kinase Detection Reagent was added in a volume equal to the new reaction mixture, and the plate was incubated for 30 minutes at RT. This final incubation allows the conversion of ADP to ATP and the subsequent luciferase-catalyzed oxidation reaction, generating a luminescent signal. Luminescence was recorded using the Tecan Infinite M1000 Pro instrument. Recorded signals, expressed as Relative Light Units (RLU), were processed and converted into kinase activity data.

$$\%\ inhibition = \frac{x - C_-}{C_+ - C_-} * 100$$

$$\%\, residual\ enzymatic\ activity = 100 - \%inhibition$$

Dose-response curves were built by plotting log[inhibitor] *vs* % residual enzymatic activity. From these plots, a sigmoidal dose–response curve was generated, and the IC_{50} values, along with their standard error and confidence intervals**,** were calculated using GraphPad Prism 8.0.2.

4.3. ATP - Competition Assay

To assess the behavior of the compounds ATP competition assays were performed using the ADPglo system, as described in paragraph 3.2.1. Kinetic experiments to evaluate the ATP-competitive behavior of CK1δ inhibitors were performed using the ADP-Glo™ Kinase Assay (Promega). Reactions were carried out in white 96-well plates by dispensing 6.25 µL of the test compound at the desired concentration (1xIC_{50} and 2xIC_{50}), 6.25 µL of CK1δ enzyme (4 nM), and 6.25 µL of Casein substrate. The enzymatic reaction was initiated by the addition of 6.25 µL of ultra-pure ATP at increasing concentrations (1, 2, 5, 10, 25 and 50 µM). After incubation for 60 min at 30 °C, 25 µL of ADP-Glo™ reagent were added to stop the reaction and deplete the remaining ATP, followed by the addition of 50 µL of ADP-Glo™ Detection Reagent to convert ADP to ATP, which was then detected via the luciferase/luciferin system. Luminescence was recorded after 40 min at 25 °C using a Tecan

Infinite M1000 plate reader. A titration curve of ADP standards was prepared in parallel to correlate luminescence with ADP (and consequently of ATP) concentration (Figure 48); the resulting slope was used to calculate the amount of ADP produced in each reaction. Kinetic parameters were determined by plotting the reciprocal values (1/V vs. 1/[ATP]) in Lineweaver–Burk plots, as reported in figure 34. All the tested compounds demonstrated their ATP-competitive mechanism since the Lineweaver–Burk plots display the same y-intercept ($1/V_{max}$) when the compounds are tested at concentrations equal to their 1xIC_{50}s and 2xIC_{50}s. regarding this, the V_{max} remains constant and the K_m changes depending in the compound's concentration. These results are diagnostic of a competitive inhibition and support the hypothesis of the binding mode of the compounds.

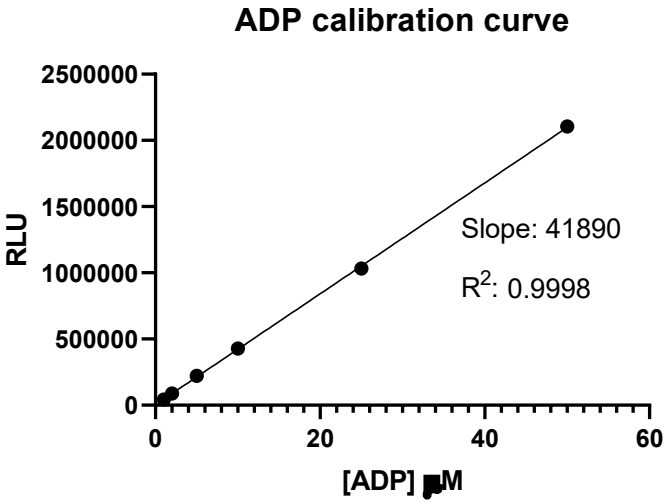

Figure 48: Calibration Curve of the ATP-competition assay

4.4. Biophysical Assays

4.4.1. Thermal Shift Assay – (TSA)

All the biophysical characterization was performed by the group of Paola Storici at Elettra Sincrotrone Trieste. Direct binding experiments were performed using the non-phosphorylated truncated form of CK1δ (residues 1–296; CK1δ-nonPi), previously produced and purified. Assays were carried out in white 96-well plates. The experiments were conducted using Sypro Orange dye (Protein Thermal Shift Dye, Thermo Fisher Scientific®) that was added to each well at a final concentration of 5×, from a 5000× stock prepared in 100% DMSO. Plates were centrifuged again at 100 ×g for 1 min at 4 °C before proceeding

with the thermal shift assay. Thermal shift assays were performed using a real-time PCR instrument (CFX96, Bio-Rad®). Sypro Orange fluorescence was monitored at 560–580 nm, with signal acquisition every 30 s. The temperature program consisted of an initial equilibration at 30 °C for 2 min, followed by a thermal gradient of 2 °C/min up to 110 °C, with a final hold of 40 s at 110 °C. Two controls were included in the experiments, the negative control represented by the presence of only buffer and Sypro Orange, and the positive control consisting in the protein alone (with 2.5% of DMSO) and Sypro Orange.

4.4.2. Crystallization of CK1δ–Inhibitor Complexes

Co-crystallization experiments to obtain CK1δ-inhibitor complexes were performed at Elettra Sincrotrone facilities by the group of Dr. Paola Storici, at Elettra Sincrotrone protein facility, in particular Structure were solved by Dr Andrea Dalle Vedove. X-ray diffraction experiments were performed at the XRD2 beamline of Elettra Sincrotrone Trieste, using monochromatic radiation at 1.00 Å and a Pilatus 6M detector (Dectris). Structures were solved by molecular replacement using the crystal structure model deposited in the Protein Data Bank (PDB ID**:** 6RCH), with the program Molrep (CCP4i suite). Ligand coordinates and geometry restraints (CIF files) were generated using Elbow (Phenix suite). Iterative cycles of

refinement and final validation of the structures were carried out with Refmac5 and WinCoot (CCP4i suite). Final structure visualization and graphical representation were performed using PyMOL (Schrödinger).

4.4.3. Grating Coupled Interferometry (GCI)

Experiments Performed by the Group of Paola Storici at Elettra Sincrotrone- Protein Facility.

Grating-coupled interferometry (GCI) experiments were performed using the WAVE-delta system (Malvern). Binding kinetics and affinities were assessed by reversibly capturing His-tagged CK1δ (100 µg/mL) according to the manufacturer's instructions onto 4PCH-NTA WAVE sensor chips (quasi-planar polycarboxylate surface) that were preconditioned with borate buffer (100 mM sodium borate, pH 9.0, 1 M NaCl). The final immobilization density achieved was 6000–8000 pg/mm². Experiments were conducted at 25°C using a running buffer consisting of PBS supplemented with 0.005% Tween 20 and 3% DMSO using standard waveRAPID parameters optimized for compound **V** and for tight binders in the case of **20**.

4.5. Selectivity

Selectivity profile was performed by Eurofins DiscoverX, compounds **10** and **20** were tested at a concentration of 1 µM on a 100-kinase panel.

IC_{50}s on the other kinases (TTBK1/2, GSK3β, SGK1 and CK1ε) were conducted in the laboratory of Prof. Ana Martinez at the CSIC-CIB Madrid, using the commercially available kinase substrates and the Kinase Glo system, as described in paragraph 4.2.1.

4.6. Pharmacokinetic Evaluation

4.6.1. Parallel Artificial Membrane Permeability Assay (PAMPA-BBB)

Since the aim of the project is to target neurodegeneration, developed compounds were tested for their capability to passively cross the Blood Brain Barrier (BBB). This aspect was evaluated exploiting the Parallel Artificial membrane Permeability Assay – BBB, which consists in an *in vitro* assay that mimics the behavior of the BBB responsible for the passage of the molecules to the Central nervous system to determine whether a compound is permeable or not, a calibration curve was determined using commercial drugs with known behaviors and permeabilities towards the BBB. The compounds considered were atenolol, caffeine, desipramine, enoxacin, hydrocortisone, ofloxacin, piroxicam and verapamil. Their experimental behavior and experimental apparent P_e ($_{app}P_e$) were then compared to the theoretical values found in literature, a linear correlation was found and the cut off values that define the permeability P_e values ranges were determined. These

values allow a classification of the tested compounds in CNS+ (permeable), CNS- (non-permeable) and CNS+/- (intermediated behavior). The calibration curve and corresponding P_e values are shown in Figure 49. To perform the calibration curve and to test the compounds, 1-2 mg of the compounds were solubilized in ethanol (1 mL) and further diluted in a solution composed by PBS/ EtOH (7:3). All the solutions (both for the compounds and the reference drugs) were filtered through hydrophilic PTFE membrane filters, with a 0.45 μm pore size. Compounds and commercial drugs were then seeded in a 96 wells polystyrene plate (180 μL), and their UV absorption was recorded using the plate reader Tecan Infinite M1000 Pro, between 230 and 500 nm, with 2 nm as interval. Control wells, represented by the blanks were also included I the plate. Compounds that presented and absorption outside 0.2 and 1 AU, were further diluted in a 7:3 PBS/EtOH solution. For these compounds, the wavelength corresponding to the maximum and minimum of absorption were selected for the quantification. MultiScreen® filter plates (0.45 μm pore size, PVDF membrane) were used to perform the permeability experiments. The donor plate was coated with 4 μL of porcine brain polar lipid extract (Avanti Polar Lipids, Merck), prepared by weighing 12 mg of the lipid and dissolving it in 600 μL of dodecane. When dried, 180 μL of compounds' solution were added in the donor-plate wells, while in the acceptor plate (MultiScreen 96-well Culture Tray, Merck Millipore) 180 μL of

PBS/EtOH (7:3) solution were introduced. The donor plate was positioned on the acceptor plate in a ‘’sandwich’’ configuration and the system was incubated for 2.5 hours at 25 °C. After the incubation, the acceptor plate was removed and the volume in each well transferred in a polystyrene UV plate, and the absorption was determined at the same wavelength determined in the first step of the assay. Apparent Pe ($_{app}P_e$, expressed as 10^{-6} cm/s) were calculated using the initial absorption of donor plate and the final absorption of the acceptor plate, takin into account the time of the incubation, well volume and membrane area. Results came from two independent experiments and wells were seeded in technical triplicates, and results are represented as mean ± SD.

Table 12: literature P_e of commercial drugs and experimentally determined app P_e.

Commercial drugs	***Literature Pe***	***Experimental app Pe***
Atenolol	0.8	1.1
Caffein	1.3	1.4
Desipramine	12	5.2
Enoxacine	0.8	1.6
Hydrocortinsone	1.9	0.9
Ofloxacine	0.8	1.6
Piroxicam	2.5	4.1
Verapamil	16	6.4

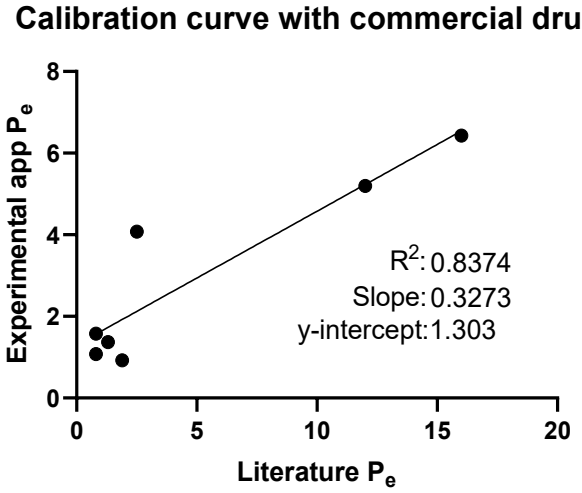

Figure 49:Calibration curve for the PAMPA assay showing the correlation between experimental apparent permeability coefficients (P_e) and literature values for the reference drugs. The linear regression ($R^2 = 0.8374$) was used to define cut-off values for CNS permeability classification.

In literature, PAMPA–BBB permeability cut-off values are conventionally set at Pe = 2×10^{-6} cm/s and Pe = 4×10^{-6} cm/s, where compounds with Pe < 2×10^{-6} cm/s are classified as CNS– (non-permeable to the blood–brain barrier), and those with Pe > 4×10^{-6} cm/s as CNS+ (permeable). Intermediate values between 2 and 4×10^{-6} cm/s are considered borderline.

To establish experimental cut-off values for this study, the linear correlation obtained from reference drugs with known BBB permeability (experimental Pe values vs. literature data) was

used. According to the regression equations, the experimental upper and lower cut-off limits were calculated as follows:

$$Upper\ cut-off = (slope * 4) + q$$
$$= 0.3273 * 4) + 1.303 = 2.6122$$

$$Lower\ cut-off = (slope * 2) + q$$
$$= 0.3273 * 2) + 1.303 = 1.9576$$

These values were subsequently used to classify the tested compounds as CNS+, CNS–, or borderline according to their experimentally determined permeability coefficients. PAMPA experiments were conducted in duplicate and the apparent Permeability values (app P_e), expressed in cm/s were calculated using the following equation:

$$Pe = \frac{Vd * Vr}{(Vd * Vr) * S * t} * \frac{100 * Vd}{100Vd - \%T(Vd * Vr)}$$

$$\%T = \frac{Vr * Ar}{Ad * Vd} * 100$$

Where $\underline{V_d}$ and $\underline{V_r}$ are volumes of donor and acceptor solution (0.180 mL = 0.180 cm^3), $\underline{S}$ is the membrane area (0.266 cm^2), time of incubation (2.5 h ¼ = 9000 s), $\underline{A_r}$ is the absorbance of the receptor plate after the experiment and A_d is the absorbance in the donor compartment before incubation. Results are reported as means of the two experiments +/- standard deviation.

4.6.2. Microsomal stability

Compounds were sent to *Nuvisan – the Science CRO*, to be tested for their *in vitro* microsomal stability.

The assay utilizes liver microsomes from mice and consists in compounds incubation and degradation evaluation at different times using an LC-MS/MS approach. The experiments were carried out including an internal control, midazolam, with known clearance. The experiments outcomes are compound half-life ($t_{1/2}$) and in vitro intrinsic clearance (CL_{int}).

4.7. Biological evaluation

4.7.1. MTT assay – cytotoxicity experiments

SH-SY5Y human neuroblastoma cells were cultured in Dulbecco's Modified Eagle Medium (DMEM) supplemented with 10% fetal bovine serum (FBS), 2 mM L-glutamine, 1% non-essential amino acids, and 1% penicillin–streptomycin, under 5% CO_2 at 37 °C. When cells reached near-confluence, they were detached, counted, and seeded into 96-well plates at a density of 6×10^4 cells per well. After a 24-hour stabilization period, the test molecules were added to the wells at final concentrations of 1, 3, and 10 µM by diluting DMSO stock solutions in fresh medium. After another 24 hours of incubation, the culture medium was replaced with MTT reagent (3-[4,5-dimethylthiazol-2-yl]-2,5-diphenyltetrazolium bromide) at a

final concentration of 20 mg/mL. After 2 hours of incubation, the media was removed and the formazan crystals solubilized in 200 µL of DMSO. Plate's absorbance was recorded with GloMax Discover Microplate Reader (Promega) at 560 nm, and the percentage of viable cells was determined relative to untreated controls (average of three replicates). All treatments were performed in triplicate in three independent experiments, and data were analyzed using GraphPad Prism 8.0 with one-way ANOVA for each plate and Student's *t*-test to compare experimental sets.

4.7.2. Neuroprotection experiments – immunoblotting assay

SH-SY5Y human neuroblastoma cells were maintained in DMEM supplemented with 10% fetal bovine serum (FBS), 2 mM L-glutamine, 1% non-essential amino acids, and 1% penicillin–streptomycin, in a humidified 5% CO_2 incubator at 37 °C. Once the cultures reached approximately 80% confluence, cells were harvested, counted, and seeded at 2×10^6 cells per well in six-well plates. After a 24 h recovery period, test compounds were administered at a final concentration of 5 µM by diluting DMSO stock solutions in fresh culture medium. One hour later, ethacrynic acid (EA) was added at a final concentration of 70 µM, and cells were further incubated for 24 h. After incubation time, medium was removed cells were rinsed

with ice-cold PBS and lysed using RIPA buffer supplemented with protease and phosphatase inhibitors. Lysates were maintained in ice for 30 min and then centrifuged at 4 °C for 15 min. Total protein content was quantified using the BCA protein assay. Equal amounts of protein (30 µg) were separated on SDS–PAGE gels and transferred onto PVDF membranes (Millipore). Membranes were blocked with 5% bovine serum albumin (BSA) in Tris-Buffered Saline with Tween 20 (TBST) for 1 h at room temperature and then incubated overnight at 4 °C with the following primary antibodies: anti-TDP-43 (mouse, Proteintech, 67345-1-Ig, 1:1000) and anti–p-TDP-43 (Ser409/410) (rabbit, Proteintech, 22309-1-AP, 1:1000). The following day, membranes were washed and incubated for 1 hour at room temperature with horseradish peroxidase (HRP) conjugated secondary antibodies (goat anti-mouse and goat anti-rabbit IgG, Bio-Rad, 1:5000 in TBST). Protein bands were visualized using a chemiluminescent detection system, and signal intensity was quantified through densitometric analysis with ImageLab (Bio-Rad). GAPDH was used as an internal loading control for normalization.

4.7.3.In vivo experiments – drosophila model

In vivo experiments, including lifespan experiments, climbing assays and western blot analysis on Drosophilae were conducted by the group of Professor Marco Bisaglia, at the university of

Padua, Biology department. *Drosophila* w^{1118} (BDSC#5905), repo-GAL4 (BDSC#7415), GMR-GAL4 (BDSC#8605), UAS-TDP43(37M) (BDSC#79587), and UAS-TDP43-YFP (BDSC#79589) fly lines were obtained from the Bloomington *Drosophila* Stock Center. All strains were grown using food composed of 0.85% agar, 8% sugar, 5% yeast, 7% corn flour, 0.3% propionic acid and 0.27% nipagin in a temperature-controlled incubator at 25°C on a 12 hour light/dark cycle.

For lifespan experiments the number of dead flies was counted daily. The percentage of survival was calculated at the end of the experiments. Graphs were produced and statistical analyses were performed by using GraphPad Prism software. The climbing assay was performed at different time points, starting the day after the collection. Flies' motility was assessed through a negative geotaxis climbing assay using a counter-current apparatus consisting of two sliding frames with 6 tubes in the lower frame and 5 in the upper frame. Flies were placed in the first plastic vial (1.5 cm diameter and 10 cm height) and gently tapped to the bottom. After 15 seconds, the upper frame was moved to the right, and the flies that passed in the upper tubes during this period were transferred to the next lower tubes by tapping carefully.

5. CONCLUSIONS and FUTURE PERSPECTIVES

This project integrates multiple disciplines: chemical, biochemical, biophysical, and biological, to comprehensively explore and optimize novel inhibitors of CK1δ. The multistep optimization of the initial scaffold led to the identification of several promising compounds, including highly potent derivatives with IC_{50} values in the nanomolar range. This outcome confirms the effectiveness of our structure-based design strategy: the development of tetrasubstituted pyrazine derivatives, inspired by the co-crystal structures of compound **V** and PF-670462, successfully enhanced the inhibitors' potency by promoting more favorable interactions within the active site, particularly with the polar residues located in the solvent-exposed region of the enzyme. Among the developed compounds the most interesting and promising candidates were further investigated for their interaction with ATP, confirming an ATP-competitive inhibition mechanism. Biophysical characterization supported the already hypotized strong affinity of the compounds for the target enzyme.

Crystallographic analyses provided valuable structural insights, clarifying the molecular interactions involved and guiding subsequent optimization strategies. From a biological perspective, the most active compounds demonstrated excellent safety profiles in SH-SY5Y neuronal cells and exhibited a

marked ability to reduce phosphorylated TDP-43 levels, the main pathological hallmark of ALS, thereby supporting a neuroprotective effect.

When tested in vivo, selected compounds showed mild yet consistent neuroprotective effects in Drosophila models of ALS, effectively lowering TDP-43 levels and improving phenotypes such as lifespan and locomotor performance in climbing assays. Pharmacokinetic studies revealed that **21** (IC_{50} = 30 nM) displayed the most favorable microsomal clearance profile, while **20** (IC_{50} = 2.62 nM) also showed good metabolic stability. Importantly, all tested compounds demonstrated the ability to cross the blood–brain barrier, a crucial requirement for CNS-targeting drugs.

Compound **20** emerged as the most selective inhibitor of CK1δ over CK1ε, displaying approximately 100-fold selectivity in favor of the δ isoform. Such evidence encourages deeper investigation into the factors governing this selectivity, to guide the rational design of next-generation inhibitors with improved specificity within kinome and in particular within the CK1 kinase family, an ongoing hot topic in kinase research. This makes compound **20** a particularly valuable candidate finally obtaining a chemical tool for the selective modulation of CK1δ and for specifically investigating its pathological roles, which remain difficult to disentangle to date.

Regarding future perspectives, analysis of the co-crystal structure of compound **20** reveals the protrusion of the amino-piperidine moiety toward the solvent-exposed region of the binding site as well as a strong interaction with polar aminoacids such as Asp91 and Asp132. The orientation of the compound and its associated binding-site interactions, coupled with the presence of a reactive functional group, offers opportunities for further chemical elaboration and new design strategies. For instance, conjugates could be developed by introducing optimized linkers and attaching functional groups such as fluorescent probes, enabling studies on CK1δ localization and mechanism of action. Alternatively, PROteolysis TArgeting Chimera (PROTAC) derivatives could be designed to promote targeted degradation of CK1δ by recruiting the cellular ubiquitination system. Finally, multitarget tools could be developed by linking compound **20** to other active molecules. Altogether, these possibilities highlight the versatility and potential of these compounds for future applications.

6. REFERENCES

(1) Lord, J. M.; Bunce, C. M.; Brown, G. The Role of Protein Phosphorylation in the Control of Cell Growth and Differentiation. *Br J Cancer* 1988, *58* (5), 549. https://doi.org/10.1038/BJC.1988.256.

(2) Cohen, P. The Origins of Protein Phosphorylation. *Nat Cell Biol* 2002, *4* (5), E127–E130. https://doi.org/10.1038/NCB0502-E127;KWRD=LIFE+SCIENCES.

(3) Hanks, S. K.; Hunter, T. The Eukaryotic Protein Kinase Superfamily: Kinase (Catalytic) Domain Structure and Classification1. *The FASEB Journal* 1995, *9* (8), 576–596. https://doi.org/10.1096/FASEBJ.9.8.7768349.

(4) Manning, G.; Whyte, D. B.; Martinez, R.; Hunter, T.; Sudarsanam, S. The Protein Kinase Complement of the Human Genome. *Science (1979)* 2002, *298* (5600), 1912–1934. https://doi.org/10.1126/SCIENCE.1075762,.

(5) Duong-Ly, K. C.; Peterson, J. R. The Human Kinome and Kinase Inhibition. *Curr Protoc Pharmacol* 2013, *60* (1), 2.9.1-2.9.14. https://doi.org/10.1002/0471141755.PH0209S60.

(6) Cheek, S.; Zhang, H.; Grishin, N. V. Sequence and Structure Classification of Kinases. *J Mol Biol* 2002, *320* (4), 855–881. https://doi.org/10.1016/S0022-2836(02)00538-7.

(7) Venerando, A.; Bustos, V. H.; Pinna, L. A.; Cozza, G. Editorial: Casein Kinases in Human Diseases. *Frontiers in Molecular Biosciences*. Frontiers Media S.A.

December 2, 2022. https://doi.org/10.3389/fmolb.2022.1094922.

(8) Endicott, J. A.; Noble, M. E. M.; Johnson, L. N. The Structural Basis for Control of Eukaryotic Protein Kinases. *Annu Rev Biochem* 2012, *81*, 587–613. https://doi.org/10.1146/ANNUREV-BIOCHEM-052410-090317.

(9) Ardito, F.; Giuliani, M.; Perrone, D.; Troiano, G.; Muzio, L. Lo. The Crucial Role of Protein Phosphorylation in Cell Signaling and Its Use as Targeted Therapy (Review). *Int J Mol Med* 2017, *40* (2), 271. https://doi.org/10.3892/IJMM.2017.3036.

(10) Lahiry, P.; Torkamani, A.; Schork, N. J.; Hegele, R. A. Kinase Mutations in Human Disease: Interpreting Genotype-Phenotype Relationships. *Nat Rev Genet* 2010, *11* (1), 60–74. https://doi.org/10.1038/NRG2707,.

(11) Roskoski, R. Classification of Small Molecule Protein Kinase Inhibitors Based upon the Structures of Their Drug-Enzyme Complexes. *Pharmacol Res* 2016, *103*, 26–48. https://doi.org/10.1016/j.phrs.2015.10.021.

(12) Zuccotto, F.; Ardini, E.; Casale, E.; Angiolini, M. Through the "Gatekeeper Door": Exploiting the Active Kinase Conformation. *J Med Chem* 2010, *53* (7), 2681–2694. https://doi.org/10.1021/JM901443H,.

(13) Zhao, Z.; Bourne, P. E. Overview of Current Type I/II Kinase Inhibitors. *Next Generation Kinase Inhibitors: Moving Beyond the ATP Binding/Catalytic Sites* 2020, 13–28. https://doi.org/10.1007/978-3-030-48283-1_2.

(14) Davis, M. I.; Hunt, J. P.; Herrgard, S.; Ciceri, P.; Wodicka, L. M.; Pallares, G.; Hocker, M.; Treiber, D. K.; Zarrinkar, P. P. Comprehensive Analysis of Kinase

Inhibitor Selectivity. *Nat Biotechnol* 2011, *29* (11), 1046–1051. https://doi.org/10.1038/NBT.1990;SUBJMETA=154,191,275,45,607,61,631;KWRD=DRUG+DISCOVERY,FUNCTIONAL+GENOMICS,KINASES.

(15) Kufareva, I.; Abagyan, R. Type-II Kinase Inhibitor Docking, Screening, and Profiling Using Modified Structures of Active Kinase States. *J Med Chem* 2008, *51* (24), 7921–7932. https://doi.org/10.1021/JM8010299/SUPPL_FILE/JM8010299_SI_001.PDF.

(16) Vijayan, R. S. K.; He, P.; Modi, V.; Duong-Ly, K. C.; Ma, H.; Peterson, J. R.; Dunbrack, R. L.; Levy, R. M. Conformational Analysis of the DFG-out Kinase Motif and Biochemical Profiling of Structurally Validated Type II Inhibitors. *J Med Chem* 2015, *58* (1), 466–479. https://doi.org/10.1021/JM501603H/SUPPL_FILE/JM501603H_SI_007.PDF.

(17) Garuti, L.; Roberti, M.; Bottegoni, G. Non-ATP Competitive Protein Kinase Inhibitors. *Curr Med Chem* 2010, *17* (25), 2804–2821. https://doi.org/10.2174/092986710791859333,.

(18) Mancini, M.; Yarden, Y. Mutational and Network Level Mechanisms Underlying Resistance to Anti-Cancer Kinase Inhibitors. *Semin Cell Dev Biol* 2016, *50*, 164–176. https://doi.org/10.1016/J.SEMCDB.2015.09.018,.

(19) Martinez, R.; Defnet, A.; Shapiro, P. Avoiding or Co-Opting ATP Inhibition: Overview of Type III, IV, V, and VI Kinase Inhibitors. *Next Generation Kinase Inhibitors: Moving Beyond the ATP Binding/Catalytic Sites* 2020, 29–59. https://doi.org/10.1007/978-3-030-48283-1_3/FIGURES/13.

(20) Lu, X.; Smaill, J. B.; Ding, K. New Promise and Opportunities for Allosteric Kinase Inhibitors. *Angewandte Chemie International Edition* 2020, *59* (33), 13764–13776. https://doi.org/10.1002/ANIE.201914525.

(21) Yueh, C.; Rettenmaier, J.; Xia, B.; Hall, D. R.; Alekseenko, A.; Porter, K. A.; Barkovich, K.; Keseru, G.; Whitty, A.; Wells, J. A.; Vajda, S.; Kozakov, D. Kinase Atlas: Druggability Analysis of Potential Allosteric Sites in Kinases. *J Med Chem* 2019, *62* (14), 6512–6524. https://doi.org/10.1021/ACS.JMEDCHEM.9B00089/ASSET/IMAGES/LARGE/JM-2019-00089C_0007.JPEG.

(22) Lamba, V.; Ghosh, I. New Directions in Targeting Protein Kinases: Focusing Upon True Allosteric and Bivalent Inhibitors. *Curr Pharm Des* 2012, *18* (20), 2936–2945. https://doi.org/10.2174/138161212800672813,.

(23) Parang, K.; Cole, P. A. Designing Bisubstrate Analog Inhibitors for Protein Kinases. *Pharmacol Ther* 2002, *93* (2–3), 145–157. https://doi.org/10.1016/S0163-7258(02)00184-5.

(24) Abdeldayem, A.; Raouf, Y. S.; Constantinescu, S. N.; Moriggl, R.; Gunning, P. T. Advances in Covalent Kinase Inhibitors. *Chem Soc Rev* 2020, *49* (9), 2617–2687. https://doi.org/10.1039/C9CS00720B.

(25) Choi, J. Y.; Noguchi, Y.; Alburger, J. M.; Bayle, S.; Chung, E.; Grant, W.; Chaikuad, A.; Knapp, S.; Duckett, D. R.; Roush, W. R. Structure-Based Development of Isoform-Selective Inhibitors of Casein Kinase 1ϵ vs Casein Kinase 1δ. *J Med Chem* 2023, *66*

(11), 7162–7178. https://doi.org/10.1021/acs.jmedchem.2c01180.

(26) Long, N. H.; Lee, S. J. Targeting Casein Kinase 1 for Cancer Therapy: Current Strategies and Future Perspectives. *Frontiers in Oncology*. Frontiers Media SA 2023. https://doi.org/10.3389/fonc.2023.1244775.

(27) Sunkari, Y. K.; Meijer, L.; Flajolet, M. The Protein Kinase CK1: Inhibition, Activation, and Possible Allosteric Modulation. *Front Mol Biosci* 2022, *9*, 916232. https://doi.org/10.3389/fmolb.2022.916232.

(28) Cheong, J. K.; Virshup, D. M. Casein Kinase 1: Complexity in the Family. *International Journal of Biochemistry and Cell Biology* 2011, *43* (4), 465–469. https://doi.org/10.1016/j.biocel.2010.12.004.

(29) Knippschild, U.; Gocht, A.; Wolff, S.; Huber, N.; Löhler, J.; Stöter, M. The Casein Kinase 1 Family: Participation in Multiple Cellular Processes in Eukaryotes. *Cell Signal* 2005, *17* (6), 675–689. https://doi.org/10.1016/j.cellsig.2004.12.011.

(30) Fulcher, L. J.; Sapkota, G. P. Functions and Regulation of the Serine/Threonine Protein Kinase CK1 Family: Moving beyond Promiscuity. *Biochemical Journal* 2020, *477* (23), 4603–4621. https://doi.org/10.1042/BCJ20200506.

(31) Cullati, S. N.; Chaikuad, A.; Chen, J. S.; Gebel, J.; Tesmer, L.; Zhubi, R.; Navarrete-Perea, J.; Guillen, R. X.; Gygi, S. P.; Hummer, G.; Dötsch, V.; Knapp, S.; Gould, K. L. Kinase Domain Autophosphorylation Rewires the Activity and Substrate Specificity of CK1 Enzymes. *Mol Cell* 2022, *82* (11), 2006-2020.e8. https://doi.org/10.1016/j.molcel.2022.03.005.

(32) Knippschild, U.; Krüger, M.; Richter, J.; Xu, P.; Balbina García-Reyes; Peifer, C.; Halekotte, J.; Bakulev, V.; Bischof, J. The CK1 Family: Contribution to Cellular Stress Response and Its Role in Carcinogenesis. *Front Oncol* 2014, *4 MAY*. https://doi.org/10.3389/fonc.2014.00096.

(33) Wee Ling Eng, G.; Virshup, D. M. Site-Specific Phosphorylation of Casein Kinase 1 δ (CK1δ) Regulates Its Activity towards the Circadian Regulator PER2. *PLoS One* 2017, *12* (5). https://doi.org/10.1371/journal.pone.0177834.

(34) Etchegaray, J.-P.; Machida, K. K.; Noton, E.; Constance, C. M.; Dallmann, R.; Napoli, M. N. Di; DeBruyne, J. P.; Lambert, C. M.; Yu, E. A.; Reppert, S. M.; Weaver, D. R. Casein Kinase 1 Delta Regulates the Pace of the Mammalian Circadian Clock. *Mol Cell Biol* 2009, *29* (14), 3853–3866. https://doi.org/10.1128/MCB.00338-09.

(35) Smadja Storz, S.; Tovin, A.; Mracek, P.; Alon, S.; Foulkes, N. S.; Gothilf, Y. Casein Kinase 1δ Activity: A Key Element in the Zebrafish Circadian Timing System. *PLoS One* 2013, *8* (1), e54189. https://doi.org/10.1371/JOURNAL.PONE.0054189.

(36) Meng, Q. J.; Maywood, E. S.; Bechtold, D. A.; Lu, W. Q.; Li, J.; Gibbs, J. E.; Dupré, S. M.; Chesham, J. E.; Rajamohan, F.; Knafels, J.; Sneed, B.; Zawadzke, L. E.; Ohren, J. F.; Walton, K. M.; Wager, T. T.; Hastings, M. H.; Loudon, A. S. I. Entrainment of Disrupted Circadian Behavior through Inhibition of Casein Kinase 1 (CK1) Enzymes. *Proc Natl Acad Sci U S A* 2010, *107* (34), 15240–15245. https://doi.org/10.1073/PNAS.1005101107/SUPPL_FILE/PNAS.201005101SI.PDF.

(37) Sprouse, J.; Reynolds, L.; Swanson, T. A.; Engwall, M. Inhibition of Casein Kinase i ε/δ Produces Phase Shifts in the Circadian Rhythms of Cynomolgus Monkeys. *Psychopharmacology (Berl)* 2009, *204* (4), 735–742. https://doi.org/10.1007/S00213-009-1503-X/FIGURES/5.

(38) Gybeľ, T.; Čada, Š.; Klementová, D.; Schwalm, M. P.; Berger, B. T.; Šebesta, M.; Knapp, S.; Bryja, V. Splice Variants of CK1α and CK1α-like: Comparative Analysis of Subcellular Localization, Kinase Activity, and Function in the Wnt Signaling Pathway. *Journal of Biological Chemistry* 2024, *300* (7). https://doi.org/10.1016/j.jbc.2024.107407.

(39) Delehouzé, C.; Godl, K.; Loaëc, N.; Bruyère, C.; Desban, N.; Oumata, N.; Galons, H.; Roumeliotis, T. I.; Giannopoulou, E. G.; Grenet, J.; Twitchell, D.; Lahti, J.; Mouchet, N.; Galibert, M. D.; Garbis, S. D.; Meijer, L. CDK/CK1 Inhibitors Roscovitine and CR8 Downregulate Amplified MYCN in Neuroblastoma Cells. *Oncogene 2014 33:50* 2013, *33* (50), 5675–5687. https://doi.org/10.1038/onc.2013.513.

(40) Perez, D. I.; Gil, C.; Martinez, A. Protein Kinases CK1 and CK2 as New Targets for Neurodegenerative Diseases. *Med. Res. Rev.* 2011, *31*, 924.

(41) Schwab, C.; Demaggio, A. J.; Ghoshal, N.; Binder, L. I.; Kuret, J.; Mcgeer, P. L. Casein Kinase 1 Delta Is Associated with Pathological Accumulation of Tau in Several Neurodegenerative Diseases. *Neurobiol Aging* 2000, *21* (4), 503–510. https://doi.org/10.1016/S0197-4580(00)00110-X.

(42) Francucci, B.; Angeloni, S.; Dal Ben, D.; Lambertucci, C.; Ricciutelli, M.; Spinaci, A.; Smirnov, A.; Volpini,

R.; Buccioni, M.; Marucci, G. Dual Anta-Inhibitors Targeting Protein Kinase CK1δ and A2A Adenosine Receptor Useful in Neurodegenerative Disorders. *Molecules 2023, Vol. 28, Page 4762* 2023, *28* (12), 4762. https://doi.org/10.3390/MOLECULES28124762.

(43) Johnson, A. E.; Chen, J.-S.; Gould, K. L. CK1 Is Required for a Mitotic Checkpoint That Delays Cytokinesis. *Current Biology* 2013, *23* (19), 1920–1926. https://doi.org/https://doi.org/10.1016/j.cub.2013.07.077.

(44) Greer, Y. E.; Gao, B.; Yang, Y.; Nussenzweig, A.; Rubin, J. S. Lack of Casein Kinase 1 Delta Promotes Genomic Instability - The Accumulation of DNA Damage and Down-Regulation of Checkpoint Kinase 1. *PLoS One* 2017, *12* (1), 170903. https://doi.org/10.1371/journal.pone.0170903.

(45) Guillen, R. X.; Beckley, J. R.; Chen, J. S.; Gould, K. L. CRISPR-Mediated Gene Targeting of CK1δ/ε Leads to Enhanced Understanding of Their Role in Endocytosis via Phosphoregulation of GAPVD1. *Sci Rep* 2020, *10* (1). https://doi.org/10.1038/s41598-020-63669-2.

(46) Jiang, K.; Liu, Y.; Fan, J.; Epperly, G.; Gao, T.; Jiang, J.; Jia, J. Hedgehog-Regulated Atypical PKC Promotes Phosphorylation and Activation of Smoothened and Cubitus Interruptus in Drosophila. *Proc Natl Acad Sci U S A* 2014, *111* (45), E4842–E4850. https://doi.org/10.1073/pnas.1417147111.

(47) Zhao, B.; Li, L.; Tumaneng, K.; Wang, C.-Y.; Guan, K.-L. A Coordinated Phosphorylation by Lats and CK1 Regulates YAP Stability through SCF B-TRCP. *Genes*

Dev 2010, *24* (1), 72–85. https://doi.org/10.1101/gad.1843810.

(48) Li, S.-S.; Dong, Y.-H.; Liu, Z.-P. Recent Advances in the Development of Casein Kinase 1 Inhibitors. *Curr Med Chem* 2021, *28* (8), 1585–1604. https://doi.org/10.2174/0929867327666200713185413.

(49) Xu, P.; Ianes, C.; Gärtner, F.; Liu, C.; Burster, T.; Bakulev, V.; Rachidi, N.; Knippschild, U.; Bischof, J. Structure, Regulation, and (Patho-)Physiological Functions of the Stress-Induced Protein Kinase CK1 Delta (CSNK1D). *Gene* 2019, *715*. https://doi.org/10.1016/j.gene.2019.144005.

(50) Peifer, C.; Abadleh, M.; Bischof, J.; Hauser, D.; Schattel, V.; Hirner, H.; Knippschild, U.; Laufer, S. 3,4-Diaryl-Isoxazoles and -Imidazoles as Potent Dual Inhibitors of P38α Mitogen Activated Protein Kinase and Casein Kinase 1δ. *J Med Chem* 2009, *52* (23), 7618–7630. https://doi.org/10.1021/JM9005127,.

(51) Gross, S. D.; Anderson, R. A. Casein Kinase I: Spatial Organization and Positioning of a Multifunctional Protein Kinase Family. *Cell Signal* 1998, *10* (10), 699–711. https://doi.org/10.1016/S0898-6568(98)00042-4.

(52) Graves, P. R.; Roach, P. J. Role of COOH-Terminal Phosphorylation in the Regulation of Casein Kinase Iδ. *Journal of Biological Chemistry* 1995, *270* (37), 21689–21694. https://doi.org/10.1074/jbc.270.37.21689.

(53) Gietzen, K. F.; Virshup, D. M. Identification of Inhibitory Autophosphorylation Sites in Casein Kinase I ε. *Journal of Biological Chemistry* 1999, *274* (45),

32063–32070.
https://doi.org/10.1074/jbc.274.45.32063.

(54) Rivers, A.; Gietzen, K. F.; Vielhaber, E.; Virshup, D. M. Regulation of Casein Kinase I ε and Casein Kinase I δ by an in Vivo Futile Phosphorylation Cycle. *Journal of Biological Chemistry* 1998, *273* (26), 15980–15984. https://doi.org/10.1074/jbc.273.26.15980.

(55) Green, C. L.; Bennett, G. S. Identification of Four Alternatively Spliced Isoforms of Chicken Casein Kinase I Alpha That Are All Expressed in Diverse Cell Types. *Gene* 1998, *216* (1), 189–195. https://doi.org/10.1016/S0378-1119(98)00291-1.

(56) Vielhaber, E. L.; Duricka, D.; Ullman, K. S.; Virshup, D. M. Nuclear Export of Mammalian PERIOD Proteins. *Journal of Biological Chemistry* 2001, *276* (49), 45921–45927. https://doi.org/10.1074/JBC.M107726200.

(57) Walton, K. M.; Fisher, K.; Rubitski, D.; Marconi, M.; Meng, Q. J.; Sládek, M.; Adams, J.; Bass, M.; Chandrasekaran, R.; Butler, T.; Griffor, M.; Rajamohan, F.; Serpa, M.; Chen, Y.; Claffey, M.; Hastings, M.; Loudon, A.; Maywood, E.; Ohren, J.; Doran, A.; Wager, T. T. Selective Inhibition of Casein Kinase 1ε Minimally Alters Circadian Clock Period. *Journal of Pharmacology and Experimental Therapeutics* 2009, *330* (2), 430–439. https://doi.org/10.1124/JPET.109.151415,.

(58) Meng, Q. J.; Logunova, L.; Maywood, E. S.; Gallego, M.; Lebiecki, J.; Brown, T. M.; Sládek, M.; Semikhodskii, A. S.; Glossop, N. R. J.; Piggins, H. D.; Chesham, J. E.; Bechtold, D. A.; Yoo, S. H.; Takahashi, J. S.; Virshup, D. M.; Boot-Handford, R. P.; Hastings,

M. H.; Loudon, A. S. I. Setting Clock Speed in Mammals: The CK1ε Tau Mutation in Mice Accelerates Circadian Pacemakers by Selectively Destabilizing PERIOD Proteins. *Neuron* 2008, *58* (1), 78–88. https://doi.org/10.1016/j.neuron.2008.01.019.

(59) Badura, L.; Swanson, T.; Adamowicz, W.; Adams, J.; Cianfrogna, J.; Fisher, K.; Holland, J.; Kleiman, R.; Nelson, F.; Reynolds, L.; Germain, K. S.; Schaeffer, E.; Tate, B.; Sprouse, J. An Inhibitor of Casein Kinase Iε Induces Phase Delays in Circadian Rhythms under Free-Running and Entrained Conditions. *Journal of Pharmacology and Experimental Therapeutics* 2007, *322* (2), 730–738. https://doi.org/10.1124/jpet.107.122846.

(60) Isojima, Y.; Nakajima, M.; Ukai, H.; Fujishima, H.; Yamada, R. G.; Masumoto, K. H.; Kiuchi, R.; Ishida, M.; Ukai-Tadenuma, M.; Minami, Y.; Kito, R.; Nakao, K.; Kishimoto, W.; Yoo, S. H.; Shimomura, K.; Takao, T.; Takano, A.; Kojima, T.; Nagai, K.; Sakaki, Y.; Takahashi, J. S.; Ueda, H. R. CKIε/δ-Dependent Phosphorylation Is a Temperature-Insensitive, Period-Determining Process in the Mammalian Circadian Clock. *Proc Natl Acad Sci U S A* 2009, *106* (37), 15744–15749. https://doi.org/10.1073/PNAS.0908733106,.

(61) Catarzi, D.; Varano, F.; Vigiani, E.; Lambertucci, C.; Spinaci, A.; Volpini, R.; Colotta, V. Casein Kinase 1δ Inhibitors as Promising Therapeutic Agents for Neurodegenerative Disorders. *Curr Med Chem* 2022, *29* (27), 4698–4737. https://doi.org/10.2174/0929867329666220301115124.

(62) Bischof, J.; Randoll, S.-J.; Sü ßner, N.; Henne-Bruns, D.; Pinna, L. A.; Knippschild, U.; Greggio, E. CK1d

Kinase Activity Is Modulated by Chk1-Mediated Phosphorylation. 2013. https://doi.org/10.1371/journal.pone.0068803.

(63) Giamas, G.; Hirner, H.; Shoshiashvili, L.; Grothey, A.; Gessert, S.; Uhl, M. K. ¨; Henne-Bruns, D.; Vorgias, C. E.; Knippschild, U. Phosphorylation of CK1δ: Identification of Ser 370 as the Major Phosphorylation Site Targeted by PKA in Vitro and in Vivo. *Biochem. J* 2007, *406*, 389–398. https://doi.org/10.1042/BJ20070091.

(64) Sillibourne, J. E.; Milne, D. M.; Takahashi, M.; Ono, Y.; Meek, D. W. Centrosomal Anchoring of the Protein Kinase CK1δ Mediated by Attachment to the Large, Coiled-Coil Scaffolding Protein CG-NAP/AKAP450. *J Mol Biol* 2002, *322* (4), 785–797. https://doi.org/10.1016/S0022-2836(02)00857-4.

(65) Ozaki, T.; Nakagawara, A. Role of P53 in Cell Death and Human Cancers. *Cancers 2011, Vol. 3, Pages 994-1013* 2011, *3* (1), 994–1013. https://doi.org/10.3390/CANCERS3010994.

(66) Pei, D.; Zhang, Y.; Zheng, J. Regulation of P53: A Collaboration between Mdm2 and MdmX. *Oncotarget* 2012, *3* (3), 228. https://doi.org/10.18632/ONCOTARGET.443.

(67) Wang, H.; Guo, M.; Wei, H.; Chen, Y. Targeting P53 Pathways: Mechanisms, Structures and Advances in Therapy. *Signal Transduction and Targeted Therapy 2023 8:1* 2023, *8* (1), 1–35. https://doi.org/10.1038/s41392-023-01347-1.

(68) Higashimoto, Y.; Saito, S.; Tong, X. H.; Hong, A.; Sakaguchi, K.; Appella, E.; Anderson, C. W. Human

P53 Is Phosphorylated on Serines 6 and 9 in Response to DNA Damage-Inducing Agents. *Journal of Biological Chemistry* 2000, *275* (30), 23199–23203. https://doi.org/10.1074/jbc.M002674200.

(69) Sakaguchi, K.; Saito, S.; Higashimoto, Y.; Roy, S.; Anderson, C. W.; Appella, E. Damage-Mediated Phosphorylation of Human P53 Threonine 18 through a Cascade Mediated by a Casein 1-like Kinase. Effect on MDM2 Binding. *Journal of Biological Chemistry* 2000, *275* (13), 9278–9283. https://doi.org/10.1074/JBC.275.13.9278,.

(70) Dumaz, N.; Milne, D. M.; Meek, D. W. Protein Kinase CK1 Is a P53-Threonine 18 Kinase Which Requires Prior Phosphorylation of Serine 15. *FEBS Lett* 1999, *463* (3), 312–316. https://doi.org/10.1016/S0014-5793(99)01647-6,.

(71) Winter, M.; Milne, D.; Dias, S.; Kulikov, R.; Knippschild, U.; Blattner, C.; Meek, D. Protein Kinase CK1δ Phosphorylates Key Sites in the Acidic Domain of Murine Double-Minute Clone 2 Protein (MDM2) That Regulate P53 Turnover. *Biochemistry* 2004, *43* (51), 16356–16364. https://doi.org/10.1021/BI0489255.

(72) Desagher, S.; Osen-Sand, A.; Montessuit, S.; Magnenat, E.; Vilbois, F.; Hochmann, A.; Journot, L.; Antonsson, B.; Martinou, J. C. Phosphorylation of Bid by Casein Kinases I and II Regulates Its Cleavage by Caspase 8. *Mol Cell* 2001, *8* (3), 601–611. https://doi.org/10.1016/S1097-2765(01)00335-5,.

(73) Liu, F. T.; Rabinovich, G. A. Galectins as Modulators of Tumour Progression. *Nat Rev Cancer* 2005, *5* (1), 29–41.

https://doi.org/10.1038/NRC1527;KWRD=BIOMEDICINE.

(74) Ma, S.; Meng, Z.; Chen, R.; Guan, K. L. The Hippo Pathway: Biology and Pathophysiology. *Annu Rev Biochem* 2019, *88* (Volume 88, 2019), 577–604. https://doi.org/10.1146/ANNUREV-BIOCHEM-013118-111829/CITE/REFWORKS.

(75) Harvey, K. F.; Zhang, X.; Thomas, D. M. The Hippo Pathway and Human Cancer. *Nature Reviews Cancer 2013 13:4* 2013, *13* (4), 246–257. https://doi.org/10.1038/nrc3458.

(76) Ni, D. The Hippo Pathway in Oral Diseases and Treatments: A Review. *Medicine (United States)* 2024, *103* (45), e40553. https://doi.org/10.1097/MD.0000000000040553.

(77) Beachy, P. A.; Karhadkar, S. S.; Berman, D. M. Tissue Repair and Stem Cell Renewal in Carcinogenesis. *Nature* 2004, *432* (7015), 324–331. https://doi.org/10.1038/NATURE03100;KWRD=SCIENCE.

(78) Lindemann, R. K. Stroma-Initiated Hedgehog Signaling Takes Center Stage in B-Cell Lymphoma. *Cancer Res* 2008, *68* (4), 961–964. https://doi.org/10.1158/0008-5472.CAN-07-5500,.

(79) Wicking, C.; Smyth, I.; Bale, A. The Hedgehog Signalling Pathway in Tumorigenesis and Development. *Oncogene* 1999, *18* (55), 7844–7851. https://doi.org/10.1038/SJ.ONC.1203282,.

(80) Ingham, P. W.; McMahon, A. P. Hedgehog Signaling in Animal Development: Paradigms and Principles. *Genes*

Dev 2001, *15* (23), 3059–3087. https://doi.org/10.1101/GAD.938601,.

(81) Rubin, L. L.; de Sauvage, F. J. Targeting the Hedgehog Pathway in Cancer. *Nat Rev Drug Discov* 2006, *5* (12), 1026–1033. https://doi.org/10.1038/NRD2086;KWRD=BIOMEDICINE.

(82) Varjosalo, M.; Taipale, J. Hedgehog: Functions and Mechanisms. *Genes Dev* 2008, *22* (18), 2454–2472. https://doi.org/10.1101/GAD.1693608,.

(83) Sigafoos, A. N.; Paradise, B. D.; Fernandez-Zapico, M. E. Hedgehog/GLI Signaling Pathway: Transduction, Regulation, and Implications for Disease. *Cancers (Basel)* 2021, *13* (14), 3410. https://doi.org/10.3390/CANCERS13143410.

(84) Cheng, S. Y.; Yue, S. Chapter 2 Role and Regulation of Human Tumor Suppressor SUFU in Hedgehog Signaling. *Adv Cancer Res* 2008, *101*, 29–43. https://doi.org/10.1016/S0065-230X(08)00402-8.

(85) Hayat, R.; Manzoor, M.; Hussain, A. Wnt Signaling Pathway: A Comprehensive Review. *Cell Biol Int* 2022, *46* (6), 863–877. https://doi.org/10.1002/CBIN.11797;REQUESTEDJOURNAL:JOURNAL:10958355;WGROUP:STRING:PUBLICATION.

(86) Peifer, M. β-Catenin as Oncogene: The Smoking Gun. *Science (1979)* 1997, *275* (5307), 1752–1753. https://doi.org/10.1126/SCIENCE.275.5307.1752,.

(87) Rubinfeld, B.; Albert, I.; Porfiri, E.; Fiol, C.; Munemitsu, S.; Polakis, P. Binding of GSK3β to the APC-β-Catenin Complex and Regulation of Complex

Assembly. *Science (1979)* 1996, *272* (5264), 1023–1026. https://doi.org/10.1126/SCIENCE.272.5264.1023,.

(88) Morin, P. J.; Sparks, A. B.; Korinek, V.; Barker, N.; Clevers, H.; Vogelstein, B.; Kinzler, K. W. Activation of β-Catenin-Tcf Signaling in Colon Cancer by Mutations in β-Catenin or APC. *Science (1979)* 1997, *275* (5307), 1787–1790. https://doi.org/10.1126/SCIENCE.275.5307.1787,.

(89) Chae, W. J.; Bothwell, A. L. M. Canonical and Non-Canonical Wnt Signaling in Immune Cells. *Trends Immunol* 2018, *39* (10), 830–847. https://doi.org/10.1016/J.IT.2018.08.006/ASSET/11B4082B-8362-43D8-8F3B-6997D97E9488/MAIN.ASSETS/GR3.JPG.

(90) Qin, K.; Yu, M.; Fan, J.; Wang, H.; Zhao, P.; Zhao, G.; Zeng, W.; Chen, C.; Wang, Y.; Wang, A.; Schwartz, Z.; Hong, J.; Song, L.; Wagstaff, W.; Haydon, R. C.; Luu, H. H.; Ho, S. H.; Strelzow, J.; Reid, R. R.; He, T. C.; Shi, L. L. Canonical and Noncanonical Wnt Signaling: Multilayered Mediators, Signaling Mechanisms and Major Signaling Crosstalk. *Genes Dis* 2023, *11* (1), 103. https://doi.org/10.1016/J.GENDIS.2023.01.030.

(91) Narimatsu, M.; Bose, R.; Pye, M.; Zhang, L.; Miller, B.; Ching, P.; Sakuma, R.; Luga, V.; Roncari, L.; Attisano, L.; Wrana, J. L. Regulation of Planar Cell Polarity by Smurf Ubiquitin Ligases. *Cell* 2009, *137* (2), 295–307. https://doi.org/10.1016/j.cell.2009.02.025.

(92) Yang, Y.; Mlodzik, M. Wnt-Frizzled/Planar Cell Polarity Signaling: Cellular Orientation by Facing the Wind (Wnt). *Annu Rev Cell Dev Biol* 2015, *31* (Volume

31, 2015), 623–646.
https://doi.org/10.1146/ANNUREV-CELLBIO-100814-125315/CITE/REFWORKS.

(93) Hamao, K.; Ono, T.; Matsushita, M.; Hosoya, H. ZIP Kinase Phosphorylated and Activated by Rho Kinase/ROCK Contributes to Cytokinesis in Mammalian Cultured Cells. *Exp Cell Res* 2020, *386* (1), 111707.
https://doi.org/10.1016/J.YEXCR.2019.111707.

(94) Wulff, K.; Porcheret, K.; Cussans, E.; Foster, R. G. Sleep and Circadian Rhythm Disturbances: Multiple Genes and Multiple Phenotypes. *Curr Opin Genet Dev* 2009, *19* (3), 237–246.
https://doi.org/10.1016/j.gde.2009.03.007.

(95) Cajochen, C.; Münch, M.; Kobialka, S.; Kräuchi, K.; Steiner, R.; Oelhafen, P.; Orgül, S.; Wirz-Justice, A. High Sensitivity of Human Melatonin, Alertness, Thermoregulation, and Heart Rate to Short Wavelength Light. *Journal of Clinical Endocrinology and Metabolism* 2005, *90* (3), 1311–1316.
https://doi.org/10.1210/JC.2004-0957,.

(96) Agarwal, R. Regulation of Circadian Blood Pressure: From Mice to Astronauts. *Curr Opin Nephrol Hypertens* 2010, *19* (1), 51–58.
https://doi.org/10.1097/MNH.0B013E3283336DDB,.

(97) Oster, H.; Damerow, S.; Hut, R. A.; Eichele, G. Transcriptional Profiling in the Adrenal Gland Reveals Circadian Regulation of Hormone Biosynthesis Genes and Nucleosome Assembly Genes. *J Biol Rhythms* 2006, *21* (5), 350–361.
https://doi.org/10.1177/0748730406293053,.

(98) Froy, O. Metabolism and Circadian Rhythms - Implications for Obesity. *Endocr Rev* 2010, *31* (1), 1–24. https://doi.org/10.1210/ER.2009-0014,.

(99) Keller, M.; Mazuch, J.; Abraham, U.; Eom, G. D.; Herzog, E. D.; Volk, H. D.; Kramer, A.; Maier, B. A Circadian Clock in Macrophages Controls Inflammatory Immune Responses. *Proc Natl Acad Sci U S A* 2009, *106* (50), 21407–21412. https://doi.org/10.1073/PNAS.0906361106,.

(100) Walker, W. H.; Walton, J. C.; DeVries, A. C.; Nelson, R. J. Circadian Rhythm Disruption and Mental Health. *Translational Psychiatry 2020 10:1* 2020, *10* (1), 1–13. https://doi.org/10.1038/s41398-020-0694-0.

(101) Langmesser, S.; Tallone, T.; Bordon, A.; Rusconi, S.; Albrecht, U. Interaction of Circadian Clock Proteins PER2 and CRY with BMAL1 and CLOCK. *BMC Mol Biol* 2008, *9* (1), 1–16. https://doi.org/10.1186/1471-2199-9-41/FIGURES/8.

(102) Philpott, J. M.; Narasimamurthy, R.; Ricci, C. G.; Freeberg, A. M.; Hunt, S. R.; Yee, L. E.; Pelofsky, R. S.; Tripathi, S.; Virshup, D. M.; Partch, C. L. Casein Kinase 1 Dynamics Underlie Substrate Selectivity and the PER2 Circadian Phosphoswitch. *Elife* 2020, *9*. https://doi.org/10.7554/ELIFE.52343,.

(103) Trott, A. J.; Menet, J. S. Regulation of Circadian Clock Transcriptional Output by CLOCK:BMAL1. *PLoS Genet* 2018, *14* (1), e1007156. https://doi.org/10.1371/JOURNAL.PGEN.1007156.

(104) Reinke, H.; Asher, G. Crosstalk between Metabolism and Circadian Clocks. *Nat Rev Mol Cell Biol* 2019, *20*

(4), 227–241. https://doi.org/10.1038/S41580-018-0096-9,.

(105) Gallego, M.; Virshup, D. M. Post-Translational Modifications Regulate the Ticking of the Circadian Clock. *Nature Reviews Molecular Cell Biology 2007 8:2* 2007, *8* (2), 139–148. https://doi.org/10.1038/nrm2106.

(106) Lee, H.; Lee, J. W. The Roles of CKI in Circadian Rhythm. *Future Med Chem* 2019, *11* (20), 2621–2624. https://doi.org/10.4155/FMC-2019-0179,.

(107) Eng, G. W. L.; Edison; Virshup, D. M. Site-Specific Phosphorylation of Casein Kinase 1 δ (CK1δ) Regulates Its Activity towards the Circadian Regulator PER2. *PLoS One* 2017, *12* (5), e0177834. https://doi.org/10.1371/JOURNAL.PONE.0177834.

(108) Leng, Y.; Musiek, E. S.; Hu, K.; Cappuccio, F. P.; Yaffe, K. Association between Circadian Rhythms and Neurodegenerative Diseases. *Lancet Neurol* 2019, *18* (3), 307–318. https://doi.org/10.1016/S1474-4422(18)30461-7/ASSET/0E2CBA69-E3F6-4A87-9E17-EDD1C9773FBD/MAIN.ASSETS/GR1.JPG.

(109) Hirano, A.; Fu, Y. H.; Ptáek, L. J. The Intricate Dance of Post-Translational Modifications in the Rhythm of Life. *Nat Struct Mol Biol* 2016, *23* (12), 1053–1060. https://doi.org/10.1038/NSMB.3326,.

(110) Zheng, J. C.; Chen, S. Translational Neurodegeneration in the Era of Fast Growing International Brain Research. *Transl Neurodegener* 2022, *11* (1), 1–2. https://doi.org/10.1186/S40035-021-00276-9/METRICS.

(111) Baier, A.; Szyszka, R. CK2 and Protein Kinases of the CK1 Superfamily as Targets for Neurodegenerative Disorders. *Front Mol Biosci* 2022, *9*. https://doi.org/10.3389/fmolb.2022.916063.

(112) Soria Lopez, J. A.; González, H. M.; Léger, G. C. Alzheimer's Disease. *Handb Clin Neurol* 2019, *167*, 231–255. https://doi.org/10.1016/B978-0-12-804766-8.00013-3.

(113) Scheltens, P.; De Strooper, B.; Kivipelto, M.; Holstege, H.; Chételat, G.; Teunissen, C. E.; Cummings, J.; van der Flier, W. M. Alzheimer's Disease. *The Lancet* 2021, *397* (10284), 1577–1590. https://doi.org/10.1016/S0140-6736(20)32205-4/ASSET/638E98FE-6148-4A97-BD1D-B1750C730D5A/MAIN.ASSETS/GR4.JPG.

(114) Naseri, N. N.; Wang, H.; Guo, J.; Sharma, M.; Luo, W. The Complexity of Tau in Alzheimer's Disease. *Neurosci Lett* 2019, *705*, 183–194. https://doi.org/10.1016/J.NEULET.2019.04.022.

(115) Braak, H.; Braak, E. Neuropathological Stageing of Alzheimer-Related Changes. *Acta Neuropathol* 1991, *82* (4), 239–259. https://doi.org/10.1007/BF00308809.

(116) Mandelkow, E. M.; Mandelkow, E. Biochemistry and Cell Biology of Tau Protein in Neurofibrillary Degeneration. *Cold Spring Harb Perspect Biol* 2011, *3* (10), 1–25. https://doi.org/10.1101/CSHPERSPECT.A006247,.

(117) Jesu´, J.; Avila, J.; Lucas, J. J. Role of Tau Protein in Both Physiological and Pathological Conditions. 2004. https://doi.org/10.1152/physrev.00024.2003.-The.

(118) Mukrasch, M. D.; Bibow, S.; Korukottu, J.; Jeganathan, S.; Biernat, J.; Griesinger, C.; Mandelkow, E.; Zweckstetter, M. Structural Polymorphism of 441-Residue Tau at Single Residue Resolution. *PLoS Biol* 2009, *7* (2), e1000034. https://doi.org/10.1371/JOURNAL.PBIO.1000034.

(119) Mandelkow, E.-M.; Mandelkow, E. Biochemistry and Cell Biology of Tau Protein in Neurofibrillary Degeneration. https://doi.org/10.1101/cshperspect.a006247.

(120) Avila, J.; Jiménez, J. S.; Sayas, C. L.; Bolós, M.; Zabala, J. C.; Rivas, G.; Hernández, F. Tau Structures. *Front Aging Neurosci* 2016, *8* (NOV). https://doi.org/10.3389/FNAGI.2016.00262,.

(121) Guo, T.; Noble, W.; Hanger, D. P. Roles of Tau Protein in Health and Disease. *Acta Neuropathol* 2017, *133* (5), 665–704. https://doi.org/10.1007/S00401-017-1707-9,.

(122) Grundke-Iqbal, I.; Iqbal, K.; Tung, Y. C.; Quinlan, M.; Wisniewski, H. M.; Binder, L. I. Abnormal Phosphorylation of the Microtubule-Associated Protein Tau (Tau) in Alzheimer Cytoskeletal Pathology. *Proc Natl Acad Sci U S A* 1986, *83* (13), 4913–4917. https://doi.org/10.1073/PNAS.83.13.4913,.

(123) Lindwall, G.; David Cole, R. THE J O ~ I R N A L OF BIOI.OGICAL CHEMISTRY Phosphorylation Affects the Ability of Tau Protein to Promote Microtubule Assembly*. *Journal of Biological Chemistry* 1984, *259* (8), 5301–5305. https://doi.org/10.1016/S0021-9258(17)42989-9.

(124) Luna-Muñoz, J.; Chávez-Macías, L.; García-Sierra, F.; Mena, R. Earliest Stages of Tau Conformational

Changes Are Related to the Appearance of a Sequence of Specific Phospho-Dependent Tau Epitopes in Alzheimer's Disease. *Journal of Alzheimer's Disease* 2007, *12* (4), 365–375. https://doi.org/10.3233/JAD-2007-12410,.

(125) Augustinack, J. C.; Schneider, A.; Mandelkow, E. M.; Hyman, B. T. Specific Tau Phosphorylation Sites Correlate with Severity of Neuronal Cytopathology in Alzheimer's Disease. *Acta Neuropathol* 2002, *103* (1), 26–35. https://doi.org/10.1007/S004010100423,.

(126) Kimura, T.; Ono, T.; Takamatsu, J.; Yamamoto, H.; Ikegami, K.; Kondo, A.; Hasegawa, M.; Ihara, Y.; Miyamolo, E.; Miyakawa, T. Sequential Changes of Tau-Site-Specific Phosphorylation during Development of Paired Helical Filaments. *Dement Geriatr Cogn Disord* 1996, *7* (4), 177–181. https://doi.org/10.1159/000106875,.

(127) Noble, W.; Hanger, D. P.; Miller, C. C. J.; Lovestone, S. The Importance of Tau Phosphorylation for Neurodegenerative Diseases. *Front Neurol* 2013, *4 JUL*. https://doi.org/10.3389/FNEUR.2013.00083,.

(128) Ballard, C.; Gauthier, S.; Corbett, A.; Brayne, C.; Aarsland, D.; Jones, E. Alzheimer's Disease. *The Lancet* 2011, *377* (9770), 1019–1031. https://doi.org/10.1016/S0140-6736(10)61349-9.

(129) Rissman, R. A.; Poon, W. W.; Blurton-Jones, M.; Oddo, S.; Torp, R.; Vitek, M. P.; LaFerla, F. M.; Rohn, T. T.; Cotman, C. W. Caspase-Cleavage of Tau Is an Early Event in Alzheimer Disease Tangle Pathology. *Journal of Clinical Investigation* 2004, *114* (1), 121–130. https://doi.org/10.1172/JCI20640,.

(130) Hurtado, D. E.; Molina-Porcel, L.; Iba, M.; Aboagye, A. K.; Paul, S. M.; Trojanowski, J. Q.; Lee, V. M. Y. Aβ Accelerates the Spatiotemporal Progression of Tau Pathology and Augments Tau Amyloidosis in an Alzheimer Mouse Model. *American Journal of Pathology* 2010, *177* (4), 1977–1988. https://doi.org/10.2353/ajpath.2010.100346.

(131) Blennow, K.; de Leon, M. J.; Zetterberg, H. Alzheimer's Disease. *Lancet* 2006, *368* (9533), 387–403. https://doi.org/10.1016/S0140-6736(06)69113-7.

(132) Vassar, R.; Bennett, B. D.; Babu-Khan, S.; Kahn, S.; Mendiaz, E. A.; Denis, P.; Teplow, D. B.; Ross, S.; Amarante, P.; Loeloff, R.; Luo, Y.; Fisher, S.; Fuller, J.; Edenson, S.; Lile, J.; Jarosinski, M. A.; Biere, A. L.; Curran, E.; Burgess, T.; Louis, J. C.; Collins, F.; Treanor, J.; Rogers, G.; Citron, M. β-Secretase Cleavage of Alzheimer's Amyloid Precursor Protein by the Transmembrane Aspartic Protease BACE. *Science (1979)* 1999, *286* (5440), 735–741. https://doi.org/10.1126/SCIENCE.286.5440.735,.

(133) Carson, J. A.; Turner, A. J. β-Amyloid Catabolism: Roles for Neprilysin (NEP) and Other Metallopeptidases? *J Neurochem* 2002, *81* (1), 1–8. https://doi.org/10.1046/J.1471-4159.2002.00855.X.

(134) Flajolet, M.; He, G.; Heiman, M.; Lin, A.; Nairn, A. C.; Greengard, P. Regulation of Alzheimer's Disease Amyloid-β Formation by Casein Kinase I. *Proceedings of the National Academy of Sciences* 2007, *104* (10), 4159–4164. https://doi.org/10.1073/PNAS.0611236104.

(135) Jankovic, J. Parkinson's Disease: Clinical Features and Diagnosis. *J Neurol Neurosurg Psychiatry* 2008, *79* (4), 368–376. https://doi.org/10.1136/JNNP.2007.131045.

(136) Marsden, C. D. Parkinson's Disease. *J Neurol Neurosurg Psychiatry* 1994, *57* (6), 672. https://doi.org/10.1136/JNNP.57.6.672.

(137) Goedert, M.; Jakes, R.; Spillantini, M. G. The Synucleinopathies: Twenty Years On. *J Parkinsons Dis* 2017, *7* (s1), S53–S71. https://doi.org/10.3233/JPD-179005,.

(138) Spillantini, M. G.; Schmidt, M. L.; Lee, V. M. Y.; Trojanowski, J. Q.; Jakes, R.; Goedert, M. α-Synuclein in Lewy Bodies [8]. *Nature* 1997, *388* (6645), 839–840. https://doi.org/10.1038/42166,.

(139) Baba, M.; Nakajo, S.; Tu, P. H.; Tomita, T.; Nakaya, K.; Lee, V. M. Y.; Trojanowski, J. Q.; Iwatsubo, T. Aggregation of Alpha-Synuclein in Lewy Bodies of Sporadic Parkinson's Disease and Dementia with Lewy Bodies. *Am J Pathol* 1998, *152* (4), 879.

(140) Wong, Y. C.; Krainc, D. α-Synuclein Toxicity in Neurodegeneration: Mechanism and Therapeutic Strategies. *Nat Med* 2017, *23* (2), 1. https://doi.org/10.1038/NM.4269.

(141) Oueslati, A. Implication of Alpha-Synuclein Phosphorylation at S129 in Synucleinopathies: What Have We Learned in the Last Decade? *J Parkinsons Dis* 2016, *6* (1), 39–51. https://doi.org/10.3233/JPD-160779/ASSET/AF46D80D-A9B6-4F04-BDAF-95A4CDD3C908/ASSETS/GRAPHIC/10.3233_JPD-160779-FIG2.JPG.

(142) Kosten, J.; Binolfi, A.; Stuiver, M.; Verzini, S.; Theillet, F. X.; Bekei, B.; Van Rossum, M.; Selenko, P. Efficient Modification of Alpha-Synuclein Serine 129 by Protein Kinase CK1 Requires Phosphorylation of Tyrosine 125

as a Priming Event. *ACS Chem Neurosci* 2014, *5* (12), 1203–1208. https://doi.org/10.1021/CN5002254/SUPPL_FILE/CN5002254_SI_001.PDF.

(143) Okochi, M.; Walter, J.; Koyama, A.; Nakajo, S.; Baba, M.; Iwatsubo, T.; Meijer, L.; Kahle, P. J.; Haass, C. Constitutive Phosphorylation of the Parkinson's Disease Associated α- Synuclein. *Journal of Biological Chemistry* 2000, *275* (1), 390–397. https://doi.org/10.1074/jbc.275.1.390.

(144) Chakraborty, J.; Basso, V.; Ziviani, E. Post Translational Modification of Parkin. *Biol Direct* 2017, *12* (1). https://doi.org/10.1186/S13062-017-0176-3,.

(145) Feldman, E. L.; Goutman, S. A.; Petri, S.; Mazzini, L.; Savelieff, M. G.; Shaw, P. J.; Sobue, G. Amyotrophic Lateral Sclerosis. *The Lancet* 2022, *400* (10360), 1363–1380. https://doi.org/10.1016/S0140-6736(22)01272-7/ASSET/57CF8EC9-BE26-4E51-BDF5-2865A9041071/MAIN.ASSETS/GR4.JPG.

(146) Masrori, P.; Van Damme, P. Amyotrophic Lateral Sclerosis: A Clinical Review. *Eur J Neurol* 2020, *27* (10), 1918–1929. https://doi.org/10.1111/ENE.14393.

(147) Phukan, J.; Pender, N. P.; Hardiman, O. Cognitive Impairment in Amyotrophic Lateral Sclerosis. *Lancet Neurology* 2007, *6* (11), 994–1003. https://doi.org/10.1016/S1474-4422(07)70265-X,.

(148) Tzeplaeff, L.; Wilfling, S.; Requardt, M. V.; Herdick, M. Current State and Future Directions in the Therapy of ALS. *Cells* 2023, *12* (11). https://doi.org/10.3390/CELLS12111523,.

(149) Buratti, E. Functional Significance of TDP-43 Mutations in Disease. *Adv Genet* 2015, *91*, 1–53. https://doi.org/10.1016/bs.adgen.2015.07.001.

(150) Eck, R. J.; Kraemer, B. C.; Liachko, N. F. Regulation of TDP-43 Phosphorylation in Aging and Disease. *Geroscience* 2021, *43* (4), 1605–1614. https://doi.org/10.1007/S11357-021-00383-5,.

(151) Lukavsky, P. J.; Daujotyte, D.; Tollervey, J. R.; Ule, J.; Stuani, C.; Buratti, E.; Baralle, F. E.; Damberger, F. F.; Allain, F. H. T. Molecular Basis of UG-Rich RNA Recognition by the Human Splicing Factor TDP-43. *Nat Struct Mol Biol* 2013, *20* (12), 1443–1449. https://doi.org/10.1038/NSMB.2698,.

(152) Ayala, Y. M.; Zago, P.; D'Ambrogio, A.; Xu, Y. F.; Petrucelli, L.; Buratti, E.; Baralle, F. E. Structural Determinants of the Cellular Localization and Shuttling of TDP-43. *J Cell Sci* 2008, *121* (22), 3778–3785. https://doi.org/10.1242/JCS.038950.

(153) Budini, M.; Baralle, F. E.; Buratti, E. Targeting TDP-43 in Neurodegenerative Diseases. *Expert Opin Ther Targets* 2014, *18* (6), 617–632. https://doi.org/10.1517/14728222.2014.896905;WGROUP:STRING:PUBLICATION.

(154) Palomo, V.; Tosat-Bitrian, C.; Nozal, V.; Nagaraj, S.; Martin-Requero, A.; Martinez, A. TDP-43: A Key Therapeutic Target beyond Amyotrophic Lateral Sclerosis. *ACS Chem Neurosci* 2019, *10* (3), 1183–1196. https://doi.org/10.1021/ACSCHEMNEURO.9B00026.

(155) Igaz, L. M.; Kwong, L. K.; Chen-Plotkin, A.; Winton, M. J.; Unger, T. L.; Xu, Y.; Neumann, M.; Trojanowski,

J. Q.; Lee, V. M. Y. Expression of TDP-43 C-Terminal Fragments in Vitro Recapitulates Pathological Features of TDP-43 Proteinopathies. *Journal of Biological Chemistry* 2009, *284* (13), 8516–8524. https://doi.org/10.1074/JBC.M809462200.

(156) Suk, T. R.; Rousseaux, M. W. C. The Role of TDP-43 Mislocalization in Amyotrophic Lateral Sclerosis. *Mol Neurodegener* 2020, *15* (1), 1–16. https://doi.org/10.1186/S13024-020-00397-1/FIGURES/2.

(157) Arai, T.; Hasegawa, M.; Nonoka, T.; Kametani, F.; Yamashita, M.; Hosokawa, M.; Niizato, K.; Tsuchiya, K.; Kobayashi, Z.; Ikeda, K.; Yoshida, M.; Onaya, M.; Fujishiro, H.; Akiyama, H. Phosphorylated and Cleaved TDP-43 in ALS, FTLD and Other Neurodegenerative Disorders and in Cellular Models of TDP-43 Proteinopathy. *Neuropathology* 2010, *30* (2), 170–181. https://doi.org/10.1111/J.1440-1789.2009.01089.X.

(158) Hasegawa, M.; Arai, T.; Akiyama, H.; Nonaka, T.; Mori, H.; Hashimoto, T.; Yamazaki, M.; Oyanagi, K. TDP-43 Is Deposited in the Guam Parkinsonism-Dementia Complex Brains. *Brain* 2007, *130* (5), 1386–1394. https://doi.org/10.1093/BRAIN/AWM065,.

(159) Geser, F.; Winton, M. J.; Kwong, L. K.; Xu, Y.; Xie, S. X.; Igaz, L. M.; Garruto, R. M.; Perl, D. P.; Galasko, D.; Lee, V. M. Y.; Trojanowski, J. Q. Pathological TDP-43 in Parkinsonism-Dementia Complex and Amyotrophic Lateral Sclerosis of Guam. *Acta Neuropathol* 2008, *115* (1), 133–145. https://doi.org/10.1007/S00401-007-0257-Y,.

(160) Miklossy, J.; Steele, J. C.; Yu, S.; McCall, S.; Sandberg, G.; McGeer, E. G.; McGeer, P. L. Enduring

Involvement of Tau, β-Amyloid, α-Synuclein, Ubiquitin and TDP-43 Pathology in the Amyotrophic Lateral Sclerosis/Parkinsonism-Dementia Complex of Guam (ALS/PDC). *Acta Neuropathol* 2008, *116* (6), 625–637. https://doi.org/10.1007/S00401-008-0439-2,.

(161) Amador-Ortiz, C.; Lin, W. L.; Ahmed, Z.; Personett, D.; Davies, P.; Duara, R.; Graff-Radford, N. R.; Hutton, M. L.; Dickson, D. W. TDP-43 Immunoreactivity in Hippocampal Sclerosis and Alzheimer's Disease. *Ann Neurol* 2007, *61* (5), 435–445. https://doi.org/10.1002/ANA.21154,.

(162) Tsuji, H.; Arai, T.; Kametani, F.; Nonaka, T.; Yamashita, M.; Suzukake, M.; Hosokawa, M.; Yoshida, M.; Hatsuta, H.; Takao, M.; Saito, Y.; Murayama, S.; Akiyama, H.; Hasegawa, M.; Mann, D. M. A.; Tamaoka, A. Molecular Analysis and Biochemical Classification of TDP-43 Proteinopathy. *Brain* 2012, *135* (11), 3380–3391. https://doi.org/10.1093/BRAIN/AWS230,.

(163) Nonaka, T.; Suzuki, G.; Tanaka, Y.; Kametani, F.; Hirai, S.; Okado, H.; Miyashita, T.; Saitoe, M.; Akiyama, H.; Masai, H.; Hasegawa, M. Phosphorylation of TAR DNA-Binding Protein of 43 KDa (TDP-43) by Truncated Casein Kinase 1δ Triggers Mislocalization and Accumulation of TDP-43. *Journal of Biological Chemistry* 2016, *291* (11), 5473–5483. https://doi.org/10.1074/jbc.M115.695379.

(164) Cuevas, E. P.; Rodríguez-Fernández, A.; Palomo, V.; Martínez, A.; Martín-Requero, Á. TDP-43 Pathology and Prionic Behavior in Human Cellular Models of Alzheimer's Disease Patients. 2022, *10*, 385. https://doi.org/10.3390/biomedicines10020385.

(165) Pongrácová, E.; Buratti, E.; Romano, M. Prion-like Spreading of Disease in TDP-43 Proteinopathies. *Brain Sciences 2024, Vol. 14, Page 1132* 2024, *14* (11), 1132. https://doi.org/10.3390/BRAINSCI14111132.

(166) Morphy, R. Selectively Nonselective Kinase Inhibition: Striking the Right Balance. *J Med Chem* 2009, *53* (4), 1413–1437. https://doi.org/10.1021/JM901132V.

(167) Knight, Z. A.; Shokat, K. M. Features of Selective Kinase Inhibitors. *Chem Biol* 2005, *12* (6), 621–637. https://doi.org/10.1016/j.chembiol.2005.04.011.

(168) Ghoreschi, K.; Laurence, A.; O'Shea, J. J. Selectivity and Therapeutic Inhibition of Kinases: To Be or Not to Be? *Nature Immunology 2009 10:4* 2009, *10* (4), 356–360. https://doi.org/10.1038/ni.1701.

(169) Davies Stephen P.; Reddy Helen; Caivano Matilde; Cohen Philip. Specificity and Mechanism of Action of Some Commonly Used Protein Kinase Inhibitors | Biochemical Journal | Portland Press. *Biochemical Journal* 2000, *1* (351), 95–105.

(170) Bain, J.; Plater, L.; Elliott, M.; Shpiro, N.; Hastie, C. J.; Mclauchlan, H.; Klevernic, I.; Arthur, J. S. C.; Alessi, D. R.; Cohen, P. The Selectivity of Protein Kinase Inhibitors: A Further Update. *Biochem J* 2007, *408* (3), 297–315. https://doi.org/10.1042/BJ20070797.

(171) Wu, P.; Nielsen, T. E.; Clausen, M. H. FDA-Approved Small-Molecule Kinase Inhibitors. *Trends Pharmacol Sci* 2015, *36* (7), 422–439. https://doi.org/10.1016/j.tips.2015.04.005.

(172) Němec, V.; Khirsariya, P.; Janovská, P.; Moyano, P. M.; Maier, L.; Procházková, P.; Kebková, P.; Gybel', T.; Berger, B. T.; Chaikuad, A.; Reinecke, M.; Kuster, B.;

Knapp, S.; Bryja, V.; Paruch, K. Discovery of Potent and Exquisitely Selective Inhibitors of Kinase CK1 with Tunable Isoform Selectivity. *Angewandte Chemie - International Edition* 2023, *62* (11). https://doi.org/10.1002/ANIE.202217532,.

(173) Arey, R.; McClung, C. A. An Inhibitor of Casein Kinase 1 ε/δ Partially Normalizes the Manic-like Behaviors of the ClockΔ19 Mouse. *Behavioural pharmacology* 2012, *23* (4), 392–396. https://doi.org/10.1097/FBP.0B013E32835651FD.

(174) Perreau-Lenz, S.; Vengeliene, V.; Noori, H. R.; Merlo-Pich, E. V.; Corsi, M. A.; Corti, C.; Spanagel, R. Inhibition of the Casein-Kinase-1-Epsilon/Delta Prevents Relapse-Like Alcohol Drinking. *Neuropsychopharmacology 2012 37:9* 2012, *37* (9), 2121–2131. https://doi.org/10.1038/npp.2012.62.

(175) Bibian, M.; Rahaim, R. J.; Choi, J. Y.; Noguchi, Y.; Schürer, S.; Chen, W.; Nakanishi, S.; Licht, K.; Rosenberg, L. H.; Li, L.; Feng, Y.; Cameron, M. D.; Duckett, D. R.; Cleveland, J. L.; Roush, W. R. Development of Highly Selective Casein Kinase 1δ/1ε (CK1δ/ε) Inhibitors with Potent Antiproliferative Properties. *Bioorg Med Chem Lett* 2013, *23* (15), 4374. https://doi.org/10.1016/J.BMCL.2013.05.075.

(176) Deng, C.; Lipstein, M. R.; Scotto, L.; Jirau Serrano, X. O.; Mangone, M. A.; Li, S.; Vendome, J.; Hao, Y.; Xu, X.; Deng, S.-X.; Realubit, R. B.; Tatonetti, N. P.; Karan, C.; Lentzsch, S.; Fruman, D. A.; Honig, B.; Landry, D. W.; O'Connor, O. A. Silencing C-Myc Translation as a Therapeutic Strategy through Targeting PI3Kδ and CK1ε in Hematological Malignancies. *Blood* 2017, *129* (1), 88–99. https://doi.org/10.1182/blood-2016-08-731240.

(177) Walton, K. M.; Fisher, K.; Rubitski, D.; Marconi, M.; Meng, Q. J.; Sládek, M.; Adams, J.; Bass, M.; Chandrasekaran, R.; Butler, T.; Griffor, M.; Rajamohan, F.; Serpa, M.; Chen, Y.; Claffey, M.; Hastings, M.; Loudon, A.; Maywood, E.; Ohren, J.; Doran, A.; Wager, T. T. Selective Inhibition of Casein Kinase 1ϵ Minimally Alters Circadian Clock Period. *Journal of Pharmacology and Experimental Therapeutics* 2009, *330* (2), 430–439. https://doi.org/10.1124/JPET.109.151415.

(178) Cuevas, E. P.; Martinez-Gonzalez, L.; Gordillo, C.; Tosat-Bitrián, C.; Pérez de la Lastra, C.; Sáenz, A.; Gil, C.; Palomo, V.; Martin-Requero, Á.; Martinez, A. Casein Kinase 1 Inhibitor Avoids TDP-43 Pathology Propagation in a Patient-Derived Cellular Model of Amyotrophic Lateral Sclerosis. *Neurobiol Dis* 2024, *192*. https://doi.org/10.1016/j.nbd.2024.106430.

(179) Lee, J. W.; Hirota, T.; Peters, E. C.; Garcia, M.; Gonzalez, R.; Cho, C. Y.; Wu, X.; Schultz, P. G.; Kay, S. A. A Small Molecule Modulates Circadian Rhythms through Phosphorylation of the Period Protein. *Angewandte Chemie International Edition* 2011, *50* (45), 10608–10611. https://doi.org/10.1002/ANIE.201103915.

(180) Alquezar, C.; Salado, I. G.; De La Encarnación, A.; Pérez, D. I.; Moreno, F.; Gil, C.; López De Munain, A.; Martínez, A.; Martín-Requero, Á. Targeting TDP-43 Phosphorylation by Casein Kinase-1δ Inhibitors: A Novel Strategy for the Treatment of Frontotemporal Dementia. 2016. https://doi.org/10.1186/s13024-016-0102-7.

(181) Salado, I. G.; Redondo, M.; Bello, M. L.; Perez, C.; Liachko, N. F.; Kraemer, B. C.; Miguel, L.; Lecourtois,

M.; Gil, C.; Martinez, A.; Perez, D. I. Protein Kinase CK-1 Inhibitors as New Potential Drugs for Amyotrophic Lateral Sclerosis. *J Med Chem* 2014, *57* (6), 2755–2772. https://doi.org/10.1021/JM500065F.

(182) Juhás, M. J.; Zitko, J. Molecular Interactions of Pyrazine-Based Compounds to Proteins. 2020. https://doi.org/10.1021/acs.jmedchem.9b02021.

(183) Fürstner, A.; Leitner, A.; Méndez, M.; Krause, H. Iron-Catalyzed Cross-Coupling Reactions. *J Am Chem Soc* 2002, *124* (46), 13856–13863. https://doi.org/10.1021/JA027190T.

(184) Shah, P.; Westwell, A. D. The Role of Fluorine in Medicinal Chemistry. *J Enzyme Inhib Med Chem* 2007, *22* (5), 527–540. https://doi.org/10.1080/14756360701425014.

(185) Niesen, F. H.; Berglund, H.; Vedadi, M. The Use of Differential Scanning Fluorimetry to Detect Ligand Interactions That Promote Protein Stability. *Nat Protoc* 2007, *2* (9), 2212–2221. https://doi.org/10.1038/NPROT.2007.321.

(186) Boivin, S.; Kozak, S.; Meijers, R. Optimization of Protein Purification and Characterization Using Thermofluor Screens. *Protein Expr Purif* 2013, *91* (2), 192–206. https://doi.org/10.1016/J.PEP.2013.08.002.

(187) Kozma, P.; Hámori, A.; Kurunczi, S.; Cottier, K.; Horvath, R. Grating Coupled Optical Waveguide Interferometer for Label-Free Biosensing. *Sens Actuators B Chem* 2011, *155* (2), 446–450. https://doi.org/10.1016/J.SNB.2010.12.045.

(188) Di, L.; Kerns, E. H.; Fan, K.; McConnell, O. J.; Carter, G. T. High Throughput Artificial Membrane

Permeability Assay for Blood–Brain Barrier. *Eur J Med Chem* 2003, *38* (3), 223–232. https://doi.org/10.1016/S0223-5234(03)00012-6.

(189) Wohnsland, F.; Faller, B. High-Throughput Permeability PH Profile and High-Throughput Alkane/Water Log P with Artificial Membranes. *J Med Chem* 2001, *44* (6), 923–930. https://doi.org/10.1021/JM001020E.

(190) Targett, I. L.; Crompton, L. A.; Conway, M. E.; Craig, T. J. Differentiation of SH-SY5Y Neuroblastoma Cells Using Retinoic Acid and BDNF: A Model for Neuronal and Synaptic Differentiation in Neurodegeneration. *In Vitro Cell Dev Biol Anim* 2024, *60* (9), 1058–1067. https://doi.org/10.1007/S11626-024-00948-6.

(191) Iguchi, Y.; Katsuno, M.; Takagi, S.; Ishigaki, S.; Niwa, J. ichi; Hasegawa, M.; Tanaka, F.; Sobue, G. Oxidative Stress Induced by Glutathione Depletion Reproduces Pathological Modifications of TDP-43 Linked to TDP-43 Proteinopathies. *Neurobiol Dis* 2012, *45* (3), 862–870. https://doi.org/10.1016/J.NBD.2011.12.002.

(192) Harms, E.; Young, M. W.; Saez, L.; Sehgal. CK1 and GSK3 in the Drosophila and Mammalian Circadian Clock. *Novartis Found Symp* 2003, *253*, 267–279. https://doi.org/10.1002/0470090839.CH19;SUBPAGE:STRING:ACCESS.

(193) Choksi, D. K.; Roy, B.; Chatterjee, S.; Yusuff, T.; Bakhoum, M. F.; Sengupta, U.; Ambegaokar, S.; Kayed, R.; Jackson, G. R. TDP-43 Phosphorylation by Casein Kinase Iε Promotes Oligomerization and Enhances Toxicity in Vivo. *Hum Mol Genet* 2014, *23* (4), 1025–1035. https://doi.org/10.1093/HMG/DDT498.

(194) Schröder, M.; Chaikuad, A. Assessing Reversible and Irreversible Binding Effects of Kinase Covalent Inhibitors through ADP-Glo Assays. *STAR Protoc* 2021, *2* (3). https://doi.org/10.1016/j.xpro.2021.100717.